

# Towards analytical applications using SABRE-hyperpolarised benchtop NMR

Ana Inés Silva Terra

PhD

University of York

Chemistry

February 2025



# Abstract

Benchtop NMR spectrometers offer an accessible analytical platform due to their low acquisition and operation costs, as well as their portability. However, their lower magnetic field strength (1 - 3 T) results in reduced sensitivity and chemical shift dispersion compared to high-field systems ( $\geq 7$  T), limiting their widespread use in routine analysis. This thesis explores the potential of benchtop NMR in combination with the hyperpolarisation technique signal amplification by reversible exchange (SABRE), as an accessible and sensitive analytical technique. A special focus is placed on  $^{19}\text{F}$  NMR measurements to mitigate spectral congestion.

Integrating SABRE with the multiplet-refocusing pulse sequence SHARPER led to significant signal-to-noise ratio (SNR) enhancements, as demonstrated in  $^{19}\text{F}$  NMR measurements on a set of fluoropyridines exhibiting diverse scalar coupling patterns. By the combined effects of SABRE and SHARPER, SNR enhancements of up to 5700-fold were achieved. A novel variation of the selective SHARPER pulse sequence enabled simultaneous signal isolation and enhancement for each component of a binary mixture, minimising signal loss compared to previous versions. The boost in signal enhancement afforded by SABRE-SHARPER was harnessed to decrease detection limits for this technique, aided by the use of co-substrates to form a stable polarisation transfer catalyst, resulting in a sub-micromolar limit of detection for a model fluoropyridine target. The use of co-substrates also facilitated the micromolar quantification of this target with an excellent degree of accuracy and precision.

The scope for this technique was further explored by probing a fluoroamine target, which contains exchangeable protons and is susceptible to polarisation deviation *via* SABRE-Relay. Although this unwanted process leads to a sensitivity penalty, which can be minimised by deuteration of the exchangeable protons, low micromolar limits of detection and accurate quantification is shown for this analyte. In contrast, fluorocarboxylic acids posed greater challenges. SABRE enhancements were observed exclusively for their carboxylate forms and remained modest, with operational detection limits in the low millimolar range.

# Contents

|   |           |
|---|-----------|
| <b>Abstract</b>   | <b>3</b>  |
| <b>Contents</b>   | <b>8</b>  |
| <b>List of Tables</b>   | <b>11</b> |
| <b>List of Figures</b>  | <b>31</b> |
| <b>Acknowledgements</b>                                       | <b>32</b> |
| <b>Author Declaration</b>                                     | <b>33</b> |
| <b>List of Abbreviations</b>                                  | <b>34</b> |
| <b>1 Introduction</b>   | <b>37</b> |
| <b>2 Background Theory</b>                                    | <b>45</b> |
| 2.1 Fundamentals of Nuclear Magnetic Resonance . . . . .      | 45        |
| 2.1.1 Zeeman Interaction . . . . .                            | 45        |
| 2.1.2 The Vector Model . . . . .                              | 48        |
| 2.1.3 Polarisation . . . . .                                  | 53        |
| 2.1.4 Low-field NMR Spectroscopy . . . . .                    | 54        |
| 2.2 Hyperpolarisation . . . . .                               | 55        |
| 2.2.1 Principles of Hyperpolarisation . . . . .               | 55        |
| 2.2.2 <i>Para</i> -hydrogen Based Hyperpolarisation . . . . . | 56        |

|          |   |           |
|----------|---|-----------|
| 2.2.2.1  | <i>Para</i> -hydrogen . . . . .   | 56        |
| 2.2.2.2  | <i>Para</i> -hydrogen Induced Polarisation (PHIP) . . . . .   | 59        |
| 2.2.2.3  | Signal Amplification by Reversible Exchange (SABRE) . . . . .   | 61        |
| <b>3</b> | <b>Experimental</b>   | <b>69</b> |
| 3.1      | Sample Preparation . . . . .  | 69        |
| 3.1.1    | Preparation of Standard SABRE Samples . . . . .   | 69        |
| 3.1.2    | Preparation of SABRE Samples Using Air-Sensitive Substrates . . . . .   | 70        |
| 3.2      | Shake-and-Drop Hyperpolarisation Experiments . . . . .  | 70        |
| 3.3      | NMR Data Acquisition in Benchtop NMR . . . . .  | 71        |
| 3.3.1    | Instrumental Setup . . . . .  | 71        |
| 3.3.2    | Pulse-and-Collect Acquisition . . . . .   | 72        |
| 3.3.3    | SHARPER and <i>sel</i> SHARPER Acquisition . . . . .  | 72        |
| 3.4      | NMR Data Post-acquisition Processing . . . . .  | 72        |
| 3.4.1    | Matched Filters . . . . .   | 73        |
| 3.5      | Analysis of Reference Methanol Samples for SABRE-Relay Studies . . . . .  | 73        |
| 3.6      | Hyperpolarised $T_1$ Experiments . . . . .  | 73        |
| 3.7      | Data Analysis and Calculations . . . . .  | 74        |
| 3.7.1    | Signal-to-Noise Ratio and Noise Standard Deviation Calculations . . . . .   | 74        |
| 3.7.2    | SABRE ( $\epsilon_{1H}$ , $\epsilon_{19F}$ ) and SNR ( $\epsilon_{SNR}$ ) Enhancement Factor Calculations . . . . . | 74        |
| 3.7.3    | Mean, Standard Deviation of the Mean, and Uncertainty of the Mean Calculations . . . . .                            | 75        |
| 3.7.4    | Analysis of Anti-phase Signals in Hyperpolarised $T_1$ Experiments . . . . .  | 76        |
| 3.7.5    | Limit of Detection and Quantification Estimation using a Single Sample . . . . .                                    | 77        |
| 3.7.6    | Limit of Detection and Quantification Calculation using a Set of Samples . . . . .                                  | 78        |
| 3.7.7    | Regression Analysis . . . . .   | 78        |
| 3.7.8    | Accuracy Assessment . . . . .   | 78        |

|          |  |            |
|----------|--|------------|
| 3.8      | Characterisation of SABRE Active Complexes using High-field NMR Spectroscopy . . . . .                                       | 79         |
| 3.8.1    | Characterisation of the Main SABRE Active Species in Samples with 3,5-Difluoropyridine and Dimethylsulfoxide . . . . .       | 79         |
| 3.8.2    | Characterisation of the Main SABRE Active Species in Samples with 2,4,6-Trifluorobenzylamine and Dimethylsulfoxide . . . . . | 85         |
| <b>4</b> | <b>Enhancing Low-Field <math>^{19}\text{F}</math> NMR Sensitivity with SABRE-SHARPER</b>                                     | <b>93</b>  |
| 4.1      | Background Theory . . . . .  | 94         |
| 4.1.1    | SHARPER Pulse Sequence . . . . .   | 94         |
| 4.1.2    | Selective SHARPER Pulse Sequence . . . . .   | 95         |
| 4.1.3    | Optimisation of Data Acquisition and Processing . . . . .  | 96         |
| 4.1.3.1  | Optimisation of FID Chunk Acquisition Time . . . . .   | 96         |
| 4.1.3.2  | Improving Signal-to-Noise Ratios with Post-acquisition Processing . . . . .  | 98         |
| 4.2      | Choice of Test System . . . . .  | 98         |
| 4.3      | SABRE Hyperpolarisation of Test Molecules . . . . .  | 100        |
| 4.3.1    | $^1\text{H}$ SABRE Hyperpolarisation . . . . .   | 100        |
| 4.3.2    | $^{19}\text{F}$ SABRE Hyperpolarisation . . . . .  | 105        |
| 4.4      | $^{19}\text{F}$ SABRE-SHARPER on Test Molecules . . . . .  | 107        |
| 4.5      | $^{19}\text{F}$ SABRE- <i>sel</i> SHARPER for Mixture Analysis . . . . .   | 115        |
| 4.6      | Conclusion . . . . .   | 120        |
| <b>5</b> | <b>Low Micromolar Detection and Quantification of Fluoropyridines</b>  | <b>122</b> |
| 5.1      | Background Theory . . . . .  | 124        |
| 5.1.1    | SABRE Hyperpolarisation Using Co-substrates . . . . .  | 124        |
| 5.1.1.1  | Reducing Limits of Detection . . . . .   | 124        |
| 5.1.1.2  | Quantification . . . . .   | 126        |
| 5.1.1.3  | Extending the Scope of Analytes . . . . .  | 127        |
| 5.2      | Choice of Test System . . . . .  | 129        |

|          |  |            |
|----------|--|------------|
| 5.3      | SABRE Hyperpolarisation of the Test Molecule . . . . .                       | 130        |
| 5.3.1    | $^1\text{H}$ and $^{19}\text{F}$ Hyperpolarisation . . . . .                 | 130        |
| 5.3.2    | $^{13}\text{C}$ Hyperpolarisation . . . . .                                  | 142        |
| 5.4      | Limits of Detection with SABRE Hyperpolarisation . . . . .                   | 145        |
| 5.5      | Quantification with SABRE Hyperpolarisation . . . . .                        | 153        |
| 5.6      | Conclusion . . . . .   | 163        |
| <b>6</b> | <b>Low Micromolar Detection and Quantification of Fluoroamines</b>           | <b>164</b> |
| 6.1      | Background Theory . . . . .  | 165        |
| 6.1.1    | SABRE Hyperpolarisation of Amines . . . . .                                  | 165        |
| 6.1.2    | SABRE-Relay . . . . .  | 166        |
| 6.2      | Choice of Test System . . . . .  | 168        |
| 6.3      | SABRE Hyperpolarisation of the Test Molecule . . . . .                       | 169        |
| 6.4      | SABRE-Relay Activity of the Test Molecule . . . . .                          | 183        |
| 6.5      | Analytical Performance in Inactive SABRE-Relay Conditions . . . . .          | 190        |
| 6.5.1    | Limits of Detection and Quantification . . . . .                             | 190        |
| 6.5.2    | Quantification . . . . .   | 192        |
| 6.6      | Analytical Performance in Active SABRE-Relay Conditions . . . . .            | 197        |
| 6.6.1    | Limits of Detection and Quantification . . . . .                             | 197        |
| 6.6.2    | Quantification . . . . .   | 198        |
| 6.7      | Conclusions . . . . .  | 202        |
| <b>7</b> | <b>Analysis of Fluorocarboxylic Acids with SABRE Hyperpolarisation</b>       | <b>204</b> |
| 7.1      | Background Theory . . . . .  | 205        |
| 7.1.1    | Environmental Relevance of Fluorinated Carboxylic Acids . . . . .            | 205        |
| 7.1.2    | SABRE Hyperpolarisation of Carboxylic Acids . . . . .                        | 208        |
| 7.2      | Choice of Test Systems . . . . .   | 210        |
| 7.3      | SABRE Hyperpolarisation of Difluoroacetic Acid and Difluoroacetate . . . . . | 212        |
| 7.3.1    | Hyperpolarisation of Difluoroacetic Acid . . . . .                           | 212        |
| 7.3.2    | Hyperpolarisation of Difluoroacetate . . . . .                               | 215        |

|          |  |            |
|----------|--|------------|
| 7.4      | SABRE Hyperpolarisation of Trifluoroacetic Acid and Trifluoroacetate . . . | 230        |
| 7.4.1    | Hyperpolarisation of Trifluoroacetic Acid . . . . .                        | 230        |
| 7.4.2    | Hyperpolarisation of Trifluoroacetate . . . . .                            | 232        |
| 7.5      | Conclusions . . . . .  | 235        |
| <b>8</b> | <b>Conclusions and Future Work</b>   | <b>238</b> |
| <b>A</b> | <b>List of Compounds</b>   | <b>246</b> |
|          | <b>References</b>  | <b>272</b> |

# List of Tables

|     |  |     |
|-----|--|-----|
| 3.1 | Experimental parameters for NMR experiments used in the characterisation of the sample containing 3,5-difluoropyridine and dimethylsulfoxide. . . . .  | 80  |
| 3.2 | High-field NMR characterisation of the SABRE active complex containing 3,5-difluoropyridine and dimethylsulfoxide. Repeated from Chapter 5 Section 5.3.1 for convenience. . . . .  | 81  |
| 3.3 | Experimental parameters for NMR experiments used in the characterisation of the sample containing 2,4,6-trifluorobenzylamine and dimethylsulfoxide. .  | 88  |
| 3.4 | High-field NMR characterisation results for the SABRE active complex containing 2,4,6-trifluorobenzylamine and dimethylsulfoxide. Repeated from Chapter 6 Section 6.3 for convenience. . . . .   | 89  |
| 4.1 | $T_2^S$ and $\Delta_{1/2}^S$ values for single-component samples . . . . .   | 110 |
| 4.2 | $T_2^S$ and $\Delta_{1/2}^S$ values for the mixture sample . . . . .   | 119 |
| 5.1 | High-field NMR characterisation of the SABRE active complex containing DFP and DMSO. . . . .   | 135 |
| 5.2 | $T_1$ values in seconds for $^{19}\text{F}$ hyperpolarised signals detected in SABRE experiments (Section 3.6, Chapter 3). $T_1$ values are a mean of triplicate measurements and their standard uncertainties ( $k=1$ ) were calculated according to Section 3.7.3 (Chapter 3). The relative proportion of each signal profile (anti-phase or in-phase) is shown as an area percentage. . . . . | 139 |

|     |  |     |
|-----|--|-----|
| 5.3 | Comparison of signal-to-noise (SNR) ratio, standard deviation of the noise ( $s_{noise}$ ) and height values for SABRE-hyperpolarised $^{19}\text{F}$ NMR signal corresponding to DFP after background correction and/or removing the imaginary part as post-acquisition processing. Experiments were performed on a sample containing 221 $\mu\text{M}$ of DFP, 25 mM of DMSO, and 5 mM of $[\text{IrCl}(\text{COD})(\text{IMes})]$ . SNR and $s_{noise}$ values were calculated according to Section 3.7.1 in Chapter 3. . . . . | 151 |
| 5.4 | Variation of limit of detection (LOD) values for $^{19}\text{F}$ NMR measurements at 1 T with $[\text{IrCl}(\text{COD})(\text{IMes})]$ concentration and FID chunk length ( $\tau$ , in ms) in SHARPER experiments. Samples were prepared in methanol and contained 25 mM of DMSO and either 14 $\mu\text{M}$ (A) or 800 nM (B-D) of DFP and $[\text{IrCl}(\text{COD})(\text{IMes})]$ concentrations as listed on the Table. . . . .   | 153 |
| 5.5 | Predicted concentrations, recovery values and relative standard deviation of the samples using $^1\text{H}$ SABRE, $^{19}\text{F}$ SABRE and $^{19}\text{F}$ SABRE-SHARPER measurements using a PTF of 6 mT. Parameters were calculated as described in Sections 3.7.3 and 3.7.8. Recovery values were calculated against the gravimetric reference value 220.6 $\mu\text{M}$ . . . . .  | 161 |
| 6.1 | High-field NMR characterisation results for the SABRE active complex containing TFBA and DMSO. . . . .   | 173 |
| 6.2 | Proton ( $\varepsilon_{^1\text{H}}$ ) and fluorine ( $\varepsilon_{^{19}\text{F}}$ ) enhancement factors for hyperpolarised samples containing 100 mM of TFBA, either no co-substrate or 100 mM of DMSO as a co-substrate, and 5 mM of $[\text{IrCl}(\text{COD})(\text{IMes})]$ in methanol- $d_4$ . Fluorine enhancement factors were estimated using PTF values of 6.2 mT and $\sim 50 \mu\text{T}$ . *ND: signal not detectable. . . . .  | 175 |
| 6.3 | Proton ( $\varepsilon_{^1\text{H}}$ ) enhancement factors for SABRE-hyperpolarised samples containing 10 mM of TFBA, either 25 mM or 100 mM of DMSO as a co-substrate, and 5 mM of $[\text{IrCl}(\text{COD})(\text{IMes})]$ in methanol- $d_1$ . Experiments were conducted using a PTF of 6.2 mT. . . . .   | 183 |

|     |   |     |
|-----|---|-----|
| 6.4 | Predicted concentrations, recovery values and relative standard deviation of the samples analysed <i>via</i> $^{19}\text{F}$ SABRE and $^{19}\text{F}$ SABRE-SHARPER measurements using a PTF of 6.2 mT. Parameters were calculated as described in Sections 3.7.3 and 3.7.8. Recovery values were calculated against the gravimetric reference value 443 $\mu\text{M}$ . . . . . | 195 |
| 6.5 | Predicted concentration, recovery value and relative standard deviation of the sample analysed <i>via</i> $^{19}\text{F}$ SABRE-SHARPER measurements using a PTF of 6.2 mT. Parameters were calculated as described in Sections 3.7.3 and 3.7.8. The recovery value was calculated against the gravimetric reference value 424 $\mu\text{M}$ . . . . .                            | 202 |
| 7.1 | Fluorine enhancement factors ( $\varepsilon_{^{19}\text{F}}$ ) for SABRE-hyperpolarised samples containing 50 mM of $[\text{DFA-H}]^-$ , either 25 mM or 100 mM of DMSO, and 5 mM of $[\text{IrCl}(\text{COD})(\text{IMes})]$ , at three polarisation transfer fields: 6.2 mT, $\sim 50 \mu\text{T}$ , and $\sim 0 \text{ T}$ . . . . .   | 224 |
| 7.2 | Fluorine enhancement factors ( $\varepsilon_{^{19}\text{F}}$ ) for SABRE experiments on samples containing 10 mM of $[\text{DFA-H}]^-$ , 25 mM of co-substrate, and 5 mM of $[\text{IrCl}(\text{COD})(\text{IMes})]$ using a PTF of 6.2 mT. . . . .   | 229 |
| A.1 | Number and name of the compounds mentioned throughout this thesis. . .  | 246 |

# List of Figures

- 2.1 Energy diagram depicting Zeeman splitting for a nucleus with spin  $I = 1/2$  and  $\gamma > 0$ . In the absence of a magnetic field ( $B_0 = 0$ ), the  $2I + 1$  nuclear states are degenerate. Upon application of a magnetic field ( $B_0 \neq 0$ ), the nuclear states become non-degenerate as the magnetic moment may align in a parallel ( $|\alpha\rangle$ ) or anti-parallel ( $|\beta\rangle$ ) direction relative to the external magnetic field. . . . . 47
- 2.2 Energy levels and spectra for an AX-type system consisting of a pair of non-equivalent weakly coupled spin- $\frac{1}{2}$  nuclei with  $\delta_A > \delta_X$ . Spectra shows a pair of doublets, each split by a  $J_{AX}$  ( $J_{AX} > 0$ ) scalar coupling. Letters a - d show the possible transitions for this system.<sup>107</sup> . . . . . 49
- 2.3 Cartoon representations of an ensemble of nuclei with spin- $\frac{1}{2}$  in the absence (a,  $B_0 = 0$ ) and presence (b,  $B_0 \neq 0$ ) of a magnetic field, with the formation of a net nuclear magnetisation ( $\mathbf{M}_z$ ). The precession of the spin magnetic moment ( $\mathbf{\mu}$ ) around the direction of the magnetic field is depicted in c). . . 50

|     |  |    |
|-----|--|----|
| 2.4 | Schematic representation of an NMR experiment. a) The thermal equilibrium longitudinal magnetisation is rotated $90^\circ$ onto the transverse plane by applying a $\mathbf{B}_1$ field on the $-y$ direction, which appears static in the rotating frame of reference (b), but rotates at the Larmor frequency ( $\omega_0$ ) in the laboratory frame (c). This creates an oscillating signal (in Volts, V) with decays following the time constant $T_2^*$ , known as free induction decay (FID). Fourier transformation of the FID produces a spectrum with a signal at the Larmor frequency (e). . . . . | 51 |
| 2.5 | Schematic representation of the hyperpolarisation process. a) Under non-hyperpolarised conditions, nuclear spins are distributed between $ \alpha\rangle$ and $ \beta\rangle$ states following Boltzmann statistics, with a net polarisation on the order of tens of parts per million. b) Hyperpolarisation increases the population difference between $ \alpha\rangle$ and $ \beta\rangle$ states, reaching polarisation levels up to unity.  | 56 |
| 2.6 | Diagram depicting the energy level for the singlet ( $ S_0\rangle$ ) and triplet ( $ T_{+1}\rangle$ , $ T_0\rangle$ and $ T_{-1}\rangle$ ) nuclear spin states of dihydrogen under a magnetic field. Note: the energy gaps are not drawn to scale. . . . .   | 57 |
| 2.7 | <i>Para</i> -hydrogen enrichment in a $\text{H}_2$ sample expressed as a percentage as a function of temperature with $\theta_R = 87.8$ K. Reproduced under a CC-BY license from Ref. [80]. . . . .  | 58 |

|      |   |    |
|------|---|----|
| 2.8  | Schematic representation of the PASADENA (top) and ALTADENA (bottom) experiments. In PASADENA experiments, the initial singlet population from $p\text{-H}_2$ is distributed between the $ \alpha\beta\rangle$ and $ \beta\alpha\rangle$ of the weakly coupling AX spin system created at the high magnetic field inside the NMR spectrometer. A characteristic spectrum containing a pair of enhanced anti-phase doublets is obtained. In ALTADENA conditions, the singlet population is transferred onto a superposition of $ \alpha\beta\rangle$ and $ \beta\alpha\rangle$ states of the strongly coupled AB system created at low magnetic fields. Upon adiabatic transfer into the spectrometer, either the $ \alpha\beta\rangle$ or $ \beta\alpha\rangle$ state becomes overpopulated, resulting in an NMR spectrum containing a pair of enhanced singlets of opposite phase. . . . . | 61 |
| 2.9  | Schematic representation of the SABRE hyperpolarisation process. <i>Para</i> -hydrogen and the substrate, here 3,5-difluoropyridine, reversibly bind to the iridium centre of the polarisation transfer catalyst, enabling polarisation transfer to the substrate. The hyperpolarised substrate (in red) then dissociates from the complex and is replaced by non-hyperpolarised substrate from the available pool in the solvent. . . . .  | 63 |
| 2.10 | Schematic representation of a SABRE three-spin AA'B system. A and A', in green, represent a pair of chemically equivalent ( $\nu_A = \nu_{A'}$ ) and magnetically inequivalent hydrides, with different scalar couplings to B ( $J_{AB} \neq J_{A'B}$ ), a nucleus in the target molecule with Larmor frequency, $\nu_B$ . . . . .  | 64 |
| 2.11 | Energy levels for three possible states in an AA'B spin system as a function of magnetic field with representing level crossing (a, $J_{AB} = J_{A'B} = 0$ ) and level anti-crossing conditions (b, $J_{A'B} = 1 \text{ Hz}$ , $J_{AB} = 0$ ). The subset of states depicted here can undergo mixing at their corresponding LAC conditions, an example of which is shown as a circle in b. Reproduced under a CC-BY license from Ref. [80]. . . . .   | 65 |

|      |   |    |
|------|---|----|
| 2.12 | Comparison of non-hyperpolarised (top) and SABRE-hyperpolarised (bottom) $^1\text{H}$ NMR spectra of pyridine at (a) 9.4 T and (b) 1 T, with unlabelled signals corresponding to the solvent and the iridium complex. Enhancement factors (c) and polarisation levels (d) for experiments at both magnetic fields are plotted against substrate concentration. Samples were prepared in methanol- $d_4$ using 5 mM of $[\text{IrCl}(\text{COD})(\text{IMes})]$ . Reproduced under a CC-BY licence from Ref. [83]. . . . . | 67 |
| 3.1  | Schematic representation of NMR spectra exhibiting an anti-phase doublet (I), an in-phase doublet (II), and their sum (III). Each half of the doublet has been marked as A or B to facilitate analysis. . . . .   | 77 |
| 3.2  | Proposed structure for the active SABRE complex containing 3,5-difluoropyridine and dimethylsulfoxide. Repeated from Chapter 5 Section 5.3.1 for convenience. . . . .   | 82 |
| 3.3  | $^1\text{H}$ NMR spectra of the characterisation sample acquired at 7 T (263 K), zoomed in the hydride ligand signal region ( $\delta$ -9 to -26). Signals corresponding to the main active species (Figure 3.2) are highlighted and amplified in the dashed box. . . . .   | 83 |
| 3.4  | Key couplings observed <i>via</i> $^1\text{H}$ - $^1\text{H}$ 2D NOESY and $^1\text{H}$ - $^1\text{H}$ 2D TOCSY experiments, revealing the connectivity of the ligands in the main active complex. . . . .  | 84 |
| 3.5  | $^1\text{H}$ - $^1\text{H}$ 2D NMR TOCSY data collected at 263 K and at a field of 7 T. Data shows scalar couplings between the hydride ligand signals at $\delta$ -23.3 and -23.7, confirming they belong to the same complex. . . . .   | 85 |
| 3.6  | $^1\text{H}$ - $^1\text{H}$ 2D NMR NOESY data collected at 263 K and at a field of 7 T. Data reveals through-space connections between the aromatic protons in 3,5-difluoropyridine at $\delta$ 8.55 with signals corresponding to the <i>ortho</i> methyl group in IMes ( $\delta$ 2.14) and a methyl group in dimethylsulfoxide ( $\delta$ 2.72). . . . .   | 86 |

|      |  |    |
|------|--|----|
| 3.7  | Proposed structure for the active SABRE complex containing 2,4,6-trifluorobenzylamine and dimethylsulfoxide. Repeated from Chapter 6 Section 6.3 for convenience. . . . .  | 87 |
| 3.8  | $^1\text{H}$ NMR spectra of the characterisation sample acquired at 11.4 T (263 K), zoomed in the hydride ligand signal region ( $\delta$ -9 to -26). Signals corresponding to the main active species (Figure 3.7) are highlighted and amplified in the dashed box. . . . .   | 90 |
| 3.9  | $^1\text{H}$ NMR spectra of the characterisation sample acquired at 11.4 T (263 K), zoomed in the $\delta$ 4.3 to 4.8 region, showing the signal corresponding to HD gas. . . . .  | 90 |
| 3.10 | $^1\text{H}$ - $^1\text{H}$ 2D NMR NOESY data collected at 263 K and at a field of 11.4 T. Data reveals through-space connections between the hydride ligand signals at $\delta$ - 23.2 and - 24.3 with a signal corresponding to the <i>ortho</i> methyl group in IMes ( $\delta$ 2.22) and the methyl signals in dimethylsulfoxide ( $\delta$ 3.19 and 3.22). . . . .  | 91 |
| 3.11 | Key through-space couplings observed <i>via</i> $^1\text{H}$ - $^1\text{H}$ 2D NOESY experiment, revealing the connectivity of the ligands in the main active complex. . . . .   | 92 |
| 4.1  | Original SHARPER pulse sequence proposed by Jones <i>et al.</i> <sup>103</sup> $90^\circ$ and $180^\circ$ pulses are represented by narrow and wide filled rectangles, respectively. Sine-shaped pulsed-field gradients ( $G_0$ ) are applied for 300 $\mu\text{s}$ with a truncation of 1%. The phase cycle is detailed in the original reference. <sup>103</sup> Reproduced under a CC-BY licence from Ref. [103]. . . . . | 95 |
| 4.2  | Original <i>sel</i> SHARPER pulse sequence proposed by Jones <i>et al.</i> <sup>103</sup> $90^\circ$ non-selective pulses are represented by narrow filled rectangles, and $180^\circ$ Gaussian-shaped selective pulses by smoothed empty shapes. The phase cycle and other experimental details are described in the original reference. <sup>103</sup> Reproduced under a CC-BY licence from Ref. [103]. . . . .           | 96 |

|     |  |     |
|-----|--|-----|
| 4.3 | Schematic representation of the use of matched filters during post-acquisition processing. Multiplication of the original FID signal (in Volts, V) by an exponential function with a time decay following $T_2^S(\Delta_{1/2}^S = 1/\pi T_2^S, \text{red})$ (a) produces a new FID with reduced noise as the signal decays (b). . . . .  | 98  |
| 4.4 | Test molecules used for SABRE-SHARPER experiments: 3,5-difluoropyridine (DFP, <b>1</b> ), 3-(difluoromethyl)pyridine (DFMP, <b>2</b> ), and 3,4,5-trifluoropyridine (TFP, <b>3</b> ). . . . .  | 99  |
| 4.5 | Comparison of reference non-hyperpolarised (top) and SABRE-enhanced (bottom) $^1\text{H}$ benchtop (1 T) NMR spectra ( $\delta$ 9 to 6.5) of 100 mM of (A) DFP, (B) DFMP, and (C) TFP with 5 mM SABRE pre-catalyst in methanol. Baseline distortion observed at ca. $\delta$ 6 in non-hyperpolarised spectra arises from the intense hydroxyl signal from the solvent. . . . .   | 101 |
| 4.6 | SABRE hyperpolarised $^1\text{H}$ NMR spectra acquired at 1 T of samples containing 100 mM of either DFP (a), DFMP (b), and TFP, and 5 mM of $[\text{IrCl}(\text{COD})(\text{IMes})]$ in methanol. Highlighted signals correspond to the hydride ligands of the main SABRE active species in each sample. . . . .  | 102 |
| 4.7 | Comparison of $^1\text{H}$ NMR spectra acquired 11.7 T (263K) of samples containing 100 mM of DFP (A), DFMP (B), or TFP (C) and 5 mM of $[\text{IrCl}(\text{COD})(\text{IMes})]$ in methanol- $d_4$ . Signals corresponding to non-deuterated (HH) and partially deuterated (HD) SABRE complexes with equatorially symmetric (I, here represented as a tris-substituted complex) or asymmetric (II) configurations are indicated with arrows. L represents a fluoropyridine ligand (DFP, DFMP, or TFP) and X an alternative ligand such as methanol- $d_4$ . . . . . | 104 |
| 4.8 | Comparison of SABRE-enhanced and thermally-polarised $^{19}\text{F}$ benchtop NMR spectra of samples containing 100 mM of DFP (A), DFMP (B), and TFP (C) and 5 mM of $[\text{IrCl}(\text{COD})(\text{IMes})]$ in methanol. All SABRE spectra were acquired with a single scan. The vertical scale of the thermal spectra was increased to aid visualisation. . . . .   | 106 |

- 4.9 Pulse sequence diagram for SHARPER. The filled and empty rectangles represent  $90^\circ$  and  $180^\circ$  non-selective pulses, respectively. The chunk time is defined as  $\tau = N\delta t$ , where  $N$  is the number of points per chunk and  $\delta t$  is the dwell time. The total acquisition time is  $t_{acq} = (n + 1/2)\tau$ , where  $n$  is the total number of loops.  $\varphi_1 = x$ ;  $\varphi_2 = y$ ;  $\psi = x$ . . . . . 108
- 4.10 Non-hyperpolarised SHARPER  $^{19}\text{F}$  benchtop (1 T) NMR spectra of samples containing 100 mM of DFP (A), DFMP (B), and TFP (C) with 5 mM of  $[\text{IrCl}(\text{COD})(\text{IMes})]$  in methanol. Full width at half maximum values for the SHARPER spectra include the effects of the matched filter.  $\varepsilon_{\text{SNR}}$  values for DFP, DFMP, and TFP are 11, 17 and 4.3, respectively. SHARPER spectra were acquired using the pulse sequence in Figure 4.9 with a chunk time of  $\tau = 3.2$  ms and  $\varphi_1 = 2x, 2(-x), 2y, 2(-y)$ ;  $\varphi_2 = 2(y,-y), 2(x,-x)$ ;  $\psi = \varphi_1$ . . . . . 109
- 4.11 Comparison of SABRE (A-C) and SABRE-SHARPER (D-F)  $^{19}\text{F}$  benchtop (1 T) NMR spectra of samples containing 100 mM of DFP (A, D), DFMP (B, E), or TFP (C, F) and 5 mM of  $[\text{IrCl}(\text{COD})(\text{IMes})]$  in methanol. All spectra were acquired in a single scan and were apodised by a matched exponential filter (Section 3.4.1, Chapter 3). The SNR values represent averages over three repeat experiments. Full width at half maximum values are shown for the SABRE SHARPER spectra. The linewidths are effectively double the fundamental SHARPER linewidth due to the application of the matched filter. Individual traces were magnified as required to aid visualisation. . . . . 110
- 4.12 Comparison of  $^{19}\text{F}$  SABRE-SHARPER FIDs (A, C) and  $^{19}\text{F}$  NMR spectra at 1 T (B, D) of a sample containing 100 mM of TFP with 5 mM OF  $[\text{IrCl}(\text{COD})(\text{IMes})]$  in methanol, acquired with chunk lengths of  $\tau = 3.2$  ms (A, B) and  $\tau = 0.8$  ms (C, D). Spectra were acquired in a single scan and were apodised by matched exponential filters (Section 3.4.1, Chapter 3). The SNR values represent averages over three repeat experiments. Full width at half maximum values are shown for the SABRE-SHARPER spectra and include the effects of apodisation. . . . . 113

|      |   |     |
|------|---|-----|
| 4.13 | Comparison of $^{19}\text{F}$ NMR SABRE-SHARPER spectra acquired with (top) and without (bottom) a second reference scan to remove the effect of off-resonance artefacts that originate from background $^{19}\text{F}$ signals from the probe at $\delta$ -72 (shown with an asterisk). The reference scan is acquired with a change in phase of the refocusing pulses in the loop by $180^\circ$ . . . . .  | 114 |
| 4.14 | Comparison of SABRE-enhanced $^{19}\text{F}$ benchtop (1 T) NMR spectra of samples containing 100 mM of DFP (A), DFMP (B), and TFP (C) with 5 mM $[\text{IrCl}(\text{COD})(\text{IMes})]$ in protio methanol. (top) Standard $^{19}\text{F}$ SABRE acquisition; (bottom) $^{19}\text{F}\{^1\text{H}\}$ SABRE acquisition. . . . .   | 115 |
| 4.15 | Pulse sequence diagrams for A) <i>sel</i> SHARPER and B) <i>sel</i> SHARPER HPT. The filled rectangles represent $90^\circ$ non-selective pulses, while the smoothed empty shape depicts a selective Gaussian $180^\circ$ pulse. The chunk time is defined as $\tau = N\delta t$ , where $N$ is the number of points per chunk and $\delta t$ is the dwell time. The total acquisition time is $t_{acq} = (n + 1/2)\tau$ , where $n$ is the total number of loops. . . . .                                | 117 |
| 4.16 | SABRE- <i>sel</i> SHARPER experiments on a mixture of DFMP (A) and DFP (B) (50 mM of each) with 5 mM of $[\text{IrCl}(\text{COD})(\text{IMes})]$ in methanol. The <i>sel</i> SHARPER experiments were performed using selective pulses inside the loop. SABRE spectra were acquired with (A) $\text{PTF} = 6.2$ mT and (B) $\text{PTF} \sim 50$ $\mu\text{T}$ . Full width at half maximum values for the SHARPER spectra include the effects of the matched filter. (Section 3.4.1, Chapter 3) . . . . . | 118 |

|      |  |     |
|------|--|-----|
| 4.17 | Comparison between SABRE-enhanced $^{19}\text{F}$ benchtop NMR spectra with (A,C) standard and (B,D) <i>selSHARPER</i> HPT acquisition for a mixture containing DFP and DFMP. SABRE spectra were acquired with (A,B) PTF = 6.2 mT and (C,D) PTF $\sim 50 \mu\text{T}$ . SABRE- <i>selSHARPER</i> HPT spectra were acquired with selection of DFMP in B and selection of DFP in D. All spectra were acquired in a single scan and were apodised by a matched exponential filter (Section 3.4.1, Chapter 3). The SNR values represent averages over three repeat experiments. Full width at half maximum values are shown for the SABRE- <i>selSHARPER</i> HPT spectra. Vertical scales were increased as required to aid visualisation. . . . . | 119 |
| 5.1  | Schematic representation of the SABRE polarisation transfer catalysts producing signals enhancements for the target substrate ('Sub') in standard conditions (A) and with addition of co-substrates (B). The binding sites of the iridium complex are filled with three units of the target substrate under standard SABRE conditions, and a mixture of the target substrate and the co-substrate ('Co-S') when this is added to the sample. . . . .   | 125 |
| 5.2  | Chemical structures of the substrate 3,5-difluoropyridine ( <b>1</b> ) and the co-substrate dimethylsulfoxide ( <b>4</b> ). . . . .  | 130 |
| 5.3  | SABRE-hyperpolarised $^1\text{H}$ (A) and $^{19}\text{F}$ (B) NMR spectra of DFP with DMSO as a co-substrate. The sample was prepared with 100 mM of DFP, 100 mM of DMSO, and 5 mM of $[\text{IrCl}(\text{COD})(\text{IMes})]$ in methanol. The spectra shown here were acquired with the PTF that yielded the largest enhancements at this concentration: 6.2 mT for $^1\text{H}$ and $\sim 50 \mu\text{T}$ for $^{19}\text{F}$ . . . . .   | 131 |
| 5.4  | Main SABRE-active species ( <b>5</b> and <b>6</b> ) in SABRE samples containing DFP and DMSO with 5 mM $[\text{IrCl}(\text{COD})(\text{IMes})]$ in protio and deuterated methanol.133  |     |
| 5.5  | Proposed structure for the active SABRE complex containing DFP and DMSO.134  |     |

|     |   |     |
|-----|---|-----|
| 5.6 | <sup>1</sup> H NMR spectra zoomed in to the hydride region ( $\delta$ - 8 to - 27 ) for SABRE samples containing sub-stoichiometric concentrations of DFP (9 mM to 80 $\mu$ M), 100 mM of DMSO, and 5 mM of [IrCl(COD)(IMes)] at 9.4 T (A, non-hyperpolarised, 253 K) and at 1 T (B, hyperpolarised, 301 K). Signals indicated by the orange stars correspond to the hydride ligands of the same SABRE-active species ( <b>5</b> , I) that produces the hyperpolarised signals observed in <sup>19</sup> F NMR spectra, those shown by the green triangles correspond to complex <b>6</b> (II), which at 301 K (B) appear as broad signals due to fast exchange. Signals shown by purple circles in B correspond to a tris-hydride species (III) previously described in the literature. <sup>211</sup> . . . . . | 136 |
| 5.7 | Non-hyperpolarised <sup>1</sup> H (A) and <sup>19</sup> F (B) NMR spectra acquired at 1.4 T for a sample in sub-stoichiometric conditions containing 20 mM of DFP, 50 mM of DMSO and 10 mM of [IrCl(COD)(IMes)]. The difference in chemical shift between pre-activation (top trace) and post-activation (bottom trace) spectra suggested that DFP was present in its bound form ( <b>5</b> ) post activation. <sup>1</sup> H spectra was referenced to the solvent signal and <sup>19</sup> F to the probe signal at $\delta$ -72. . . . .   | 138 |
| 5.8 | Variation of the SABRE-hyperpolarised <sup>1</sup> H (A) and <sup>19</sup> F (B) signals for <b>5</b> when the co-substrate concentration was varied from 5 to 50 equivalents (25 to 250 mM of DMSO). All samples contained a fixed concentration of DFP = 684 $\mu$ M , with a 3% relative variation between samples. . . . .  | 141 |
| 5.9 | A) Variation of <sup>19</sup> F hyperpolarised signal for species A and B when the co-substrate concentration is varied from 5 to 50 equivalents (25 to 250 mM of DMSO). All samples contained a fixed concentration of DFP = 684 $\mu$ M, with a 3% relative variation between samples. B) Hyperpolarised <sup>19</sup> F spectrum at 1 T for a sample containing 695 $\mu$ M of DFP, 256 mM of DMSO, and 5.5 mM of [IrCl(COD)(IMes)]. Extra species A and B, and the signal corresponding to DFP bound in <b>5</b> are marked. . . . .  | 142 |

|      |  |     |
|------|--|-----|
| 5.10 | Comparison of SABRE-enhanced and non-hyperpolarised $^1\text{H}$ (A) and $^{19}\text{F}$ (B) benchtop NMR spectra of 550 $\mu\text{M}$ of DFP, 25 mM of DMSO, and 5 mM $[\text{IrCl}(\text{COD})(\text{IMes})]$ in methanol. All SABRE spectra were acquired with a single scan. The reported values are the mean and standard deviation of three repeat measurements. . . . .   | 143 |
| 5.11 | SABRE-hyperpolarised proton-decoupled $^{13}\text{C}$ NMR spectra acquired at a 1 T field of a sample containing 100 mM of DFP, 100 mM of DMSO, and 5 mM of $[\text{IrCl}(\text{COD})(\text{IMes})]$ in methanol. Experiments were conducted using PTF values of $\sim 0$ T (a), $\sim 50 \mu\text{T}$ (b), and 6.2 mT (c). The signals corresponding to $^{13}\text{C}$ nuclei in <i>ortho</i> and <i>meta</i> positions are shown with blue squares and green circles, respectively. The inset on the right shows an amplified view of all spectra in the region where <i>ortho</i> $^{13}\text{C}$ can be observed. . . . .   | 144 |
| 5.12 | SABRE-hyperpolarised $^{19}\text{F}$ spectra of samples containing 250 $\mu\text{M}$ of DFP, 5 mM of $[\text{IrCl}(\text{COD})(\text{IMes})]$ , and either 100 mM DMSO (a) or no co-substrate (b) in methanol- $d_4$ . SABRE experiments were conducted using a PTF = 6.2 mT. . . . .  | 148 |
| 5.13 | Comparison of $^{19}\text{F}$ spectra for DFP at different concentrations. A) Non-hyperpolarised spectrum for a sample containing 8.1 mM DFP exhibiting a SNR = 3.9 after accumulation of 64 scans. B) SABRE-hyperpolarised spectrum for a sample containing 14 $\mu\text{M}$ of DFP, 25 mM of DMSO, and 5 mM of $[\text{IrCl}(\text{COD})(\text{IMes})]$ . B) SABRE-SHARPER spectrum on the same sample as B. D) SABRE-SHARPER spectrum for a sample containing 800 nM of DFP, 25 mM of DMSO, and 5 mM of $[\text{IrCl}(\text{COD})(\text{IMes})]$ . SHARPER spectra were acquired with background correction and the imaginary part of the spectrum was removed. All samples were prepared in methanol, except for A which was prepared in methanol- $d_4$ . . . . . | 149 |

|      |  |     |
|------|--|-----|
| 5.14 | Comparison of SABRE-SHARPER $^{19}\text{F}$ NMR spectra with (A) and without (B) background correction (Section 4.4) in the sub-stoichiometric regime. Artefact signals arising from the probe dominated the spectrum when analysing a low concentration sample containing DFP ( $5\ \mu\text{M}$ of DFP, $25\ \text{mM}$ of DMSO, and $5\ \text{mM}$ $[\text{IrCl}(\text{COD})(\text{IMes})]$ in methanol). By using background correction these non-targeted signals were eliminated. . . . .  | 152 |
| 5.15 | Calibration curves for $^1\text{H}$ (A) and $^{19}\text{F}$ hyperpolarised (C) NMR measurements of DFP in the $15\ \mu\text{M}$ to $1000\ \mu\text{M}$ range. Residual errors of the linear model are plotted against analyte concentration for $^1\text{H}$ (B) and $^{19}\text{F}$ (D) hyperpolarised calibration curves. . . . .  | 158 |
| 5.16 | Comparison of $^1\text{H}$ (A) and $^{19}\text{F}$ (B) NMR SABRE-hyperpolarised calibration curves using fresh (blue diamonds) and aged (orange circles) calibration samples. . . . .  | 160 |
| 5.17 | Calibration curves for $^1\text{H}$ SABRE (A), $^{19}\text{F}$ SABRE (B) and $^{19}\text{F}$ SABRE-SHARPER (C) experiments and accuracy test. Black markers correspond to the signal arising from calibration solutions and the white squares, those from the test samples. Each sample, either calibration or test, was analysed in triplicate and standard deviation of the mean values were used as error bars. Coefficients of determination, $R^2$ , are shown for each curve. Insets show the spectra obtained for the test sample in each case, along with its nominal concentration, the signal-to-noise ratio of the measurement and the number of scans. . . . . | 162 |
| 6.1  | Schematic representation of SABRE-Relay hyperpolarisation. Direct hyperpolarisation of a substrate with exchangeable protons, here exemplified by $\text{R}_1\text{NH}_2$ , results in a hyperpolarised transfer agent once released into solution. A second molecule ( $\text{R}_2\text{OH}$ ) then becomes indirectly hyperpolarised after proton exchange with the polarisation transfer agent. . . . .   | 166 |
| 6.2  | Chemical structure of the substrate 2,4,6-trifluorobenzylamine (TFBA, <b>7</b> ). . . . .  | 169 |

|     |   |     |
|-----|---|-----|
| 6.3 | Comparison between non-hyperpolarised (top trace) and SABRE- hyperpolarised (bottom trace) $^1\text{H}$ NMR spectra for samples containing 100 mM of TFBA, 5 mM of $[\text{IrCl}(\text{COD})(\text{IMes})]$ , and either no co-substrate (A) or 100 mM of DMSO (B) in methanol- $d_4$ . Spectra are zoomed in to show the organic ( $\delta$ 8.5 to $\delta$ 0) and hydride ( $\delta$ -21 to $\delta$ -27) regions. Hyperpolarised experiments were conducted using a polarisation transfer field of 6.2 mT. Signals corresponding to the exchangeable protons ('-OH') and DMSO ('DMSO') are indicated with labels. Inset C shows the hyperpolarised hydride ligand signal detected for this sample, which is thought to correspond to the trisubstituted species $[\text{IrCl}(\text{H})_2(\text{IMes})_3]$ . Inset D shows a comparison of the hyperpolarised hydride signals detected for the sample with co-substrate (II) and the those detected on a non-hyperpolarised experiment of this sample at 1.4 T by signal averaging for 4096 scans (I). . . . . | 171 |
| 6.4 | Main SABRE-active species ( <b>8</b> ) in samples containing TFBA, DMSO, and 5 mM of $[\text{IrCl}(\text{COD})(\text{IMes})]$ . . . . .   | 172 |
| 6.5 | Proposed structure for the active SABRE complex containing TFBA and DMSO. . . . .   | 172 |
| 6.6 | Typical 1 T $^{19}\text{F}$ hyperpolarised spectra for samples with 100 mM TFBA, either 100 mM (a and c) or no (b and d) DMSO and 5 mM $[\text{IrCl}(\text{COD})(\text{IMes})]$ in methanol- $d_4$ . SABRE experiments were conducted using a polarisation transfer field of 6.2 mT (a and b) or $\sim 50 \mu\text{T}$ (c and d). . . . .   | 178 |
| 6.7 | SABRE-hyperpolarised $^1\text{H}$ NMR spectra acquired at 1 T of samples containing 250 $\mu\text{M}$ to 1000 $\mu\text{M}$ of TFBA, 100 mM of DMSO, and 5 mM of $[\text{IrCl}(\text{COD})(\text{IMes})]$ in methanol- $d_4$ (A) or methanol (B), using a PTF = 6.2 mT. Spectra are zoomed in to show the hydride ligand signal region ( $\delta$ -7 to -27). Orange squares show the main active species containing TFBA ( <b>8</b> ), green triangles show <b>6</b> , and purple circles a trihydride species containing DMSO. . . . .  | 180 |

|      |  |     |
|------|--|-----|
| 6.8  | Comparison of $^{19}\text{F}$ spectra of TFBA samples at 1 T. The samples contained 700 mM of TFBA (top), 100 mM of TFBA, 100 mM of DMSO and 5 mM of $[\text{IrCl}(\text{COD})(\text{IMes})]$ (middle) or 870 $\mu\text{M}$ of TFBA, 100 mM of DMSO and 5 mM of $[\text{IrCl}(\text{COD})(\text{IMes})]$ (bottom). All samples were prepared in methanol- $d_4$ and all spectra acquired with a single scan. . . . .   | 182 |
| 6.9  | SABRE-hyperpolarised $^1\text{H}$ spectra acquired at 1 T using $\text{PTF} = 6.2$ mT of samples containing 10 mM of TFBA, either 25 mM (black) or 100 mM (red) of DMSO, and 5 mM of $[\text{IrCl}(\text{COD})(\text{IMes})]$ in methanol- $d_1$ . Insets show spectra zoomed in to the aromatic (A, yellow square) and methylene (B, purple circle) signals of TFBA, and the hydride ligand region of the spectra (C). Hydride ligand signals shown in inset C correspond to $[\text{IrCl}(\text{H})_2(\text{IMes})(\mathbf{4})_2]$ (green triangles) and $[\text{IrCl}(\text{H})_2(\text{IMes})(\mathbf{7})(\mathbf{4})]$ (orange squares). . . . .  | 184 |
| 6.10 | SABRE-hyperpolarised $^{19}\text{F}$ spectra at 1 T of samples containing 10 mM TFBA, either 25 mM (black) or 100 mM (red) DMSO, and 5 mM $[\text{IrCl}(\text{COD})(\text{IMes})]$ in methanol- $d_1$ . . . . .  | 185 |
| 6.11 | Comparison between non-hyperpolarised (black trace) and hyperpolarised (blue) $^1\text{H}$ (A) and $^{19}\text{F}$ (B) NMR spectra of TFBA at 1 T. The sample contained 870 $\mu\text{M}$ TFBA, 100 mM DMSO and 5 mM $[\text{IrCl}(\text{COD})(\text{IMes})]$ in methanol- $d_4$ . Insets show regions of the spectra zoomed in the aromatic proton region (left), and the hydride ligand region corresponding to $[\text{Ir}(\text{H})_3(\text{IMes})(\mathbf{4})_2]$ (middle) and the main active species $[\text{IrCl}(\text{H})_2(\text{IMes})(\mathbf{7})(\mathbf{4})]$ (right). It was not possible to determine an enhancement factor for the aromatic protons of TFBA due to peak overlap with hyperpolarised signals from IMes, shown with an asterisk, or for the methylene signals due to poor baseline separation. . . . . | 186 |

|      |   |     |
|------|---|-----|
| 6.12 | Variation of SABRE-hyperpolarised solvent signals in $^1\text{H}$ NMR (1 T) during sample activation for samples containing either 10 mM of TFBA, 100 mM of DMSO, and 5 mM of $[\text{IrCl}(\text{COD})(\text{IMes})]$ in methanol- $d_4$ (green marker) or 1.3 mM of TFBA, 100 mM of DMSO, and 5 mM of $[\text{IrCl}(\text{COD})(\text{IMes})]$ in methanol (orange markers). The first activation step was set as time = 0 s. Hyperpolarised signals are phased negatively. . . . . | 187 |
| 6.13 | Schematic representation of SABRE-Relay hyperpolarisation with TFBA as a polarisation transfer carrier and either methanol (A) or methanol- $d_4$ (B) as recipients of this polarisation. The amine protons in TFBA exchange with the labile protons of methanol, transferring hyperpolarisation to the solvent in a continuous way. In methanol- $d_4$ , TFBA becomes rapidly deuterated and polarisation loss to the solvent is minimised. . . . .                                  | 188 |
| 6.14 | A) Variation in the hyperpolarised signal of exchangeable protons (-OH from methanol) as a response to [TFBA] for protio (orange circles) and deuterated methanol (green squares). B) Comparison of $^{19}\text{F}$ SABRE SHARPER signals for TFBA using protio methanol (orange circles) and deuterated methanol (green squares). Error bars for protio methanol measurements are present but smaller than markers (square), therefore not visible. . . . .                          | 189 |
| 6.15 | SABRE (A) and SABRE-SHARPER (B) $^{19}\text{F}$ NMR spectra acquired at 1 T for a sample containing 254 $\mu\text{M}$ of TFBA, 100 mM of DMSO, and 5 mM of $[\text{IrCl}(\text{COD})(\text{IMes})]$ in methanol- $d_4$ . . . . .  | 192 |
| 6.16 | Calibration curves for $^{19}\text{F}$ SABRE (A) and $^{19}\text{F}$ SABRE SHARPER (C) measurements of TFBA in the 250 $\mu\text{M}$ to 900 $\mu\text{M}$ range in SABRE-Relay inactive conditions (methanol- $d_4$ ). Residual errors of the linear model are plotted against analyte concentration for $^{19}\text{F}$ SABRE (B) and $^{19}\text{F}$ SABRE SHARPER (D) hyperpolarised calibration curves. . . . .   | 194 |

|      |  |     |
|------|--|-----|
| 6.17 | Calibration curves for $^{19}\text{F}$ SABRE (A) and $^{19}\text{F}$ SABRE SHARPER (B) experiments and accuracy test. Black markers correspond to the signal arising from calibration solutions and the white squares, those from the test samples. Each sample, either calibration or test, was analysed in triplicate and the standard deviation of the mean values were used as error bars. Coefficients of determination, $R^2$ , are shown for each curve. Insets show the spectra obtained for the test sample in each case, along with its nominal concentration, the signal-to-noise ratio of the measurement and the number of scans. . . . | 196 |
| 6.18 | SABRE (A) and SABRE-SHARPER (B) $^{19}\text{F}$ NMR spectra acquired at 1 T for a sample containing 267 $\mu\text{M}$ of TFBA, 100 mM of DMSO, and 5 mM of $[\text{IrCl}(\text{COD})(\text{IMes})]$ in methanol. . . . .   | 198 |
| 6.19 | Calibration curves for $^{19}\text{F}$ SABRE (A) and $^{19}\text{F}$ SABRE SHARPER (C) measurements of TFBA in the 270 $\mu\text{M}$ to 990 $\mu\text{M}$ range in SABRE-Relay active conditions (protio methanol). Residual errors of the linear model are plotted against analyte concentration for $^{19}\text{F}$ SABRE (B) and $^{19}\text{F}$ SABRE SHARPER (D) hyperpolarised calibration curves. . . . .   | 200 |
| 6.20 | Calibration curves for $^{19}\text{F}$ SABRE SHARPER experiments and accuracy test in SABRE-Relay active conditions. Black markers correspond to the signal arising from calibration solutions and the white squares, those from the test samples. Each sample, either calibration or test, was analysed in triplicate and the standard deviation of the mean values were used as error bars. Coefficients of determination, $R^2$ , are shown for each curve. The inset shows the spectrum corresponding to the test sample, along with its nominal concentration, the signal-to-noise ratio of the measurement and the number of scans. . . . .    | 201 |
| 7.1  | Chemical structures of perfluorooctanesulfonic acid and perfluorooctanoic acid, two commonly encountered perfluoroalkyl substances. . . . .  | 206 |

|     |  |     |
|-----|--|-----|
| 7.2 | Chemical structures of fluorinated carboxylic acids under investigation in Chapter 7: difluoroacetic acid (DFA, <b>9</b> ) and trifluoroacetic acid (TFA, <b>10</b> ).   | 210 |
| 7.3 | Chemical structure of the co-substrates dimethylsulfoxide (DMSO, <b>4</b> ), here shown again for convenience, pyridine (PYR, <b>11</b> ), 4-methylpyridine (4MPYR, <b>12</b> ), and 1-methyl-1,2,3-triazole (MTZ, <b>13</b> ).  | 211 |
| 7.4 | Chemical structures of fluorinated carboxylates under investigation in Chapter 7: difluoroacetate ( $[\text{DFA-H}]^-$ , <b>14</b> ) and trifluoroacetate ( $[\text{TFA-H}]^-$ , <b>15</b> ).  | 211 |
| 7.5 | Comparison of SABRE-enhanced $^1\text{H}$ spectra for samples containing 100 mM of pyridine and either 100 mM of difluoroacetic acid (a) or no additional substrate (b), and 5 mM of $[\text{IrCl}(\text{COD})(\text{IMes})]$ . Spectra is zoomed in to show the organic ( $\delta$ 1 to 10) and the hydride ligand ( $\delta$ -19 to -27) regions of the spectra. Hyperpolarised signals corresponding to pyridine and pyridinium are highlighted in the dashed box, other signals correspond to the hydroxyl and methyl signals of methanol ( $\delta$ 3 to 5) and the hydride ligands of a symmetric iridium complex containing pyridine ( $\delta$ - 22.8). Spectra was amplified as specified to aid visualisation. | 214 |
| 7.6 | Comparison of SABRE-enhanced $^{19}\text{F}$ spectra for difluoroacetate at polarisation transfer fields of 6.2 mT (a), $\sim 50 \mu\text{T}$ (b) and $\sim 0 \text{ T}$ (c) with non-hyperpolarised spectra (d). The sample contained 100 mM of $[\text{DFA-H}]^-$ (as a lithium salt), 100 mM of PYR, and 5 mM of $[\text{IrCl}(\text{COD})(\text{IMes})]$ in methanol- $d_4$ . The doublet at $\delta$ -125.8 corresponds to the fluorine resonance in the difluoromethyl group.  | 216 |

|      |  |     |
|------|--|-----|
| 7.7  | Comparison of SABRE-enhanced (black trace) and non-hyperpolarised (red trace) $^1\text{H}$ NMR spectra for difluoroacetate at 1 T using dimethylsulfoxide ('DMSO') as a co-substrate. The sample contained 100 mM of lithium difluoroacetate, 100 mM of dimethylsulfoxide, and 5 mM $[\text{IrCl}(\text{COD})(\text{IMes})]$ in methanol- $d_4$ . Insets show an expanded view within the organic region of the spectra ( $\delta$ 4 to 8, A) showing the signal for the proton resonance in the difluoromethyl group of $[\text{DFA-H}]^-$ at $\delta$ 5.71, and the hydride region of the spectra ( $\delta$ -12 to -28, B). . . . . | 218 |
| 7.8  | Comparison of $^{19}\text{F}$ NMR non-hyperpolarised (a) and hyperpolarised spectra acquired at 6.2 mT (b,e), $\sim 50 \mu\text{T}$ (c) or $\sim 0$ T (d) using pulse-and-collect (a-d) or SHARPER (e) acquisition of a sample containing 100 mM of difluoroacetate (as a lithium salt), 100 mM of DMSO, and 5 mM of $[\text{IrCl}(\text{COD})(\text{IMes})]$ in methanol- $d_4$ . All spectra were acquired with a single scan. Main doublet signal (orange square) corresponds to the difluoromethyl group ( $\delta$ -125.8), signals shown with asterisks in c) correspond to carbon satellites. . . . .                           | 220 |
| 7.9  | Comparison of $^{13}\text{C}\{^1\text{H}\}$ NMR SABRE-hyperpolarised spectra acquired using a polarisation transfer field of $\sim 0$ T (a), 6.2 mT (b), or $\sim 50 \mu\text{T}$ (c). The sample contained 100 mM $[\text{DFA-H}]^-$ , 100 mM of DMSO, and 5 mM of $[\text{IrCl}(\text{COD})(\text{IMes})]$ in methanol- $d_4$ . The highlighted signal at $\delta$ -108.7 (t, $J=249$ Hz) corresponds to the carbon in the difluoromethyl group ( $-\text{CF}_2\text{H}$ ) of difluoroacetate. . . . .   | 222 |
| 7.10 | Comparison of fluorine enhancement factors ( $\varepsilon_{^{19}\text{F}}$ ) for SABRE experiments on samples containing 50 mM of $[\text{DFA-H}]^-$ ( <b>14</b> ), either 25 mM or 100 mM of DMSO ( <b>4</b> ), and 5 mM of $[\text{IrCl}(\text{COD})(\text{IMes})]$ at PTF values of 6.2 mT, $\sim 50 \mu\text{T}$ , and $\sim 0$ T. $\varepsilon_{^{19}\text{F}}$ were estimated as the average of triplicate measurements, with the standard deviation shown as error bars. . . . .  | 223 |

|      |   |     |
|------|---|-----|
| 7.11 | Comparison of $^{19}\text{F}$ NMR hyperpolarised spectra acquired at 6.2 mT using pulse-and-collect (a) or SHARPER (b) acquisition of a sample containing 50 mM of difluoroacetate (as a lithium salt), 25 mM of DMSO, and 5 mM of $[\text{IrCl}(\text{COD})(\text{IMes})]$ in methanol- $d_4$ . All spectra were acquired with a single scan. Main doublet signal (orange square) corresponds to the difluoromethyl group ( $\delta$ -125.8). . . . .  | 224 |
| 7.12 | Comparison of post activation non-hyperpolarised $^1\text{H}$ NMR spectra at 1.4 T of samples containing 50 mM of $[\text{DFA-H}]^-$ , either 25 mM (red trace) or 100 mM (black trace) of DMSO, and 5 mM of $[\text{IrCl}(\text{COD})(\text{IMes})]$ in methanol- $d_4$ . Spectra are zoomed in to show the hydride region of the spectra ( $\delta$ - 10 to $\delta$ -31). Chemical shift values for detected hydride signals are shown above each peak. . . . .  | 225 |
| 7.13 | Comparison of SABRE-hyperpolarised $^1\text{H}$ spectra for samples containing 50 mM (black), 10 mM (green), or 1 mM (orange) of $[\text{DFA-H}]^-$ , 25 mM of DMSO, and 5 mM of $[\text{IrCl}(\text{COD})(\text{IMes})]$ in methanol- $d_4$ . Inset shows a zoom in portion of the spectra in the $\delta$ -12 to $\delta$ -27 region. . . . .   | 227 |
| 7.14 | Comparison of SABRE-hyperpolarised spectra corresponding to samples containing either 10 mM of $[\text{DFA-H}]^-$ , 25 mM of DMSO (black trace) or 100 mM of TFA, 100 mM of DMSO (red trace), and 5 mM of $[\text{IrCl}(\text{COD})(\text{IMes})]$ in methanol- $d_4$ . The left side of the figure shows the organic region of the spectra ( $\delta$ 9 to 0) whilst the right side is zoomed in to show the hydride region ( $\delta$ - 8 to - 30) and is amplified by a factor of 200 to aid visualisation. Chemical shift values for the main hyperpolarised hydride signals are shown above the spectra. . . . . | 232 |
| 7.15 | Comparison of SABRE-enhanced $^1\text{H}$ spectra for samples containing 100 mM of either sodium trifluoroacetate (a) or trifluoroacetic acid (b), 100 mM of dimethylsulfoxide, and 5 mM of $[\text{IrCl}(\text{COD})(\text{IMes})]$ in methanol- $d_4$ . Spectra are zoomed in to display the relevant hydride region ( $\delta$ -6 to $\delta$ - 34). . . . .   | 233 |

|  |     |
|--|-----|
| 7.16 Comparison of fluorine enhancement factors ( $\varepsilon_{^{19}\text{F}}$ ) for SABRE experiments on samples containing 100 mM of either difluoroacetate ([DFA-H] <sup>-</sup> , <b>14</b> , stripes) or trifluoroacetate ([TFA-H] <sup>-</sup> , <b>15</b> , filled), 100 mM of DMSO, and 5 mM of [IrCl(COD)(IMes)] in methanol- <i>d</i> <sub>4</sub> . Enhancement factors were compared at three polarisation transfer fields: 6.2 mT, $\sim 50 \mu\text{T}$ , and $\sim 0 \text{ T}$ , and were estimated as the average of triplicate measurements, with the standard deviation shown as error bars. . . . . | 235 |
|--|-----|

# Acknowledgements

I would like to thank my supervisor Dr Meghan Halse for giving me the opportunity to carry out this project. I have learnt so much from your guidance and support, you have challenged me to become a better researcher.

I would like to extend my thanks to the members of the Halse, CHyM, and Phys Chem groups, past and present, for all their support and making my time at York so enjoyable: Alastair, Matheus, Izzy, Laura, James, Vicky, Helena, Pav, Ben C., Ben T., Claire, Keiran, Alex, Clara, Amy, Katya, Sophie, Giuseppina, Cate and Barby. A special thank you to Aminata for being a great friend. Dan, I am very grateful to you for the technical and emotional support, as well as for sharing a passion for caffeine. To my top-tier friend Callum, thank you for being there to hear my crazy ideas and help me become a better researcher. It has been a privilege to share this journey with you.

I would also like extend my gratitude to Dr Tony Wild for funding my PhD project and giving me this opportunity. I am very thankful to Prof. Simon Duckett for access to the facilities in CHyM, and the invaluable support of Dr Victoria Annis on technical and not-so-technical aspects.

To my dear friends and family, both in Uruguay and England, I would not have accomplished this without your unwavering support and belief that I could somehow pull this off. To my parents and sister, thank you for your encouragement and endless support. To Alison, I am forever grateful that our paths crossed. Your friendship has kept me sane through this process.

Finally, I would like to thank my husband, James. Thank you for your support throughout this PhD. I could not have asked for a better partner for our adventures.

# Author Declaration

I declare that this thesis is a presentation of original work and I am the sole author. This work has not previously been submitted for an award at this, or any other, University. All sources are acknowledged as References. Some of the work detailed in this thesis has been presented in the publications listed below.

## List of Publications

- [A. I. Silva Terra](#), M. Rossetto, C. L. Dickson, G. Peat, D. Uhrín and M. E. Halse, *ACS Measurement Science Au*, 2023, **3**, 73–81.
- [A. I. Silva Terra](#), D. A. Taylor and M. E. Halse, *Progress in Nuclear Magnetic Resonance Spectroscopy*, 2024, **144-145**, 153–178.
- [A. I. Silva Terra](#) and M. E. Halse, *Chemistry-Methods*, 2025, e202400094.

# Abbreviations

|                          |  |
|--------------------------|--|
| <i>o</i> -H <sub>2</sub> | <i>ortho</i> -hydrogen.  |
| <i>p</i> -H <sub>2</sub> | <i>para</i> -hydrogen.   |
| <i>sel</i> SHARPER       | Selective Sensitive, Homogeneous, And Resolved PEaks in Real time.                       |
| <i>sel</i> SHARPER HPT   | Selective Sensitive, Homogeneous, And Resolved PEaks in Real time with Hard Pulse Train. |
| ALTADENA                 | Adiabatic Longitudinal Transport After Dissociation Engenders Nuclear Alignment.         |
| COSY                     | Correlation Spectroscopy.  |
| CPMG                     | Carr-Purcell-Meiboom-Gill.   |
| dDNP                     | Dissolution Dynamic Nuclear Polarisation.  |
| DMSO                     | Dimethylsulfoxide.   |
| DPSO                     | Diphenylsulfoxide.   |
| EPR                      | Electron Paramagnetic Resonance.   |
| EXSY                     | Exchange Spectroscopy.   |
| FID                      | Free Induction Decay.  |

|          |  |
|----------|--|
| HMQC     | Heteronuclear Multiple Quantum Coherence.  |
| HSQC     | Heteronuclear Single Quantum Coherence.  |
| Hz       | Hertz.   |
| IMes     | 1,3-bis(2,4,6-trimethylphenyl)imidazole-2-ylidene.                                 |
| K        | Kelvin.  |
| LAC      | Level Anti-Crossing.   |
| LC/MS/MS | Liquid Chromatography with tandem Mass Spectrometry.                               |
| LOD      | Limit of Detection.  |
| MeOD     | Methanol- <i>d</i> <sub>4</sub> .  |
| MeOH     | Methanol.  |
| mtz      | 1-methyl-1,2,3-triazole.   |
| NMR      | Nuclear Magnetic Resonance.  |
| NOESY    | Nuclear Overhauser Effect Spectroscopy.  |
| ODNP     | Overhauser Dynamic Nuclear Polarisation.   |
| PASADENA | <i>Para</i> hydrogen And Synthesis Allows Dramatically Enhanced Nuclear Alignment. |
| PFAS     | Per- and polyfluoroalkyl substances.   |
| PFG      | Pulsed Field Gradient.   |
| PFOA     | Perfluorooctanoic acid.  |
| PFOS     | Perfluorooctane sulfonic acid.   |
| PHIP     | <i>Para</i> Hydrogen Induced Polarisation.   |

|          |   |
|----------|---|
| PHIP-SAH | <i>Para</i> -hydrogen Induced Polarisation with Side-Arm Hydrogenation. |
| PTF      | Polarisation Transfer Field.  |
| r.f.     | radio frequency.  |
| SABRE    | Signal Amplification by Reversible Exchange.                            |
| SAM      | Standard Addition Method.   |
| SHARPER  | Sensitive, Homogeneous, And Resolved PEaks in Real time.                |
| SIMes    | 1,3-bis(2,4,6-trimethylphenyl)-4,5-dihydroimidazole-2-ylidene.          |
| SNR      | Signal-to-Noise Ratio.  |
| SPE      | Solid-Phase Extraction.   |
| T        | Tesla.  |
| TOCSY    | Total Correlation Spectroscopy.   |
| TOF      | Total Organic Fluorine.   |
| TOP      | Total Oxidisable Precursor.   |

# Chapter 1

## Introduction

Nuclear Magnetic Resonance (NMR) spectroscopy is a powerful analytical technique capable of providing high-quality information about chemical and biological systems. Its strength lies not only in facilitating qualitative structural analysis, but also in enabling accurate quantitative measurements in a non-destructive manner. In fact, quantification using NMR has been proposed as a potential primary measurement method by the BIPM (International Bureau of Weights and Measures) given the direct relationship between the detected signal and the number of nuclei contributing to it.<sup>1,2</sup> Despite its potential, the widespread adoption of high-field ( $\geq 7$  T) NMR spectroscopy remains constrained by the significant costs associated with instrument acquisition and operation, as well as the substantial requirements in terms of infrastructure and expertise.<sup>3,4</sup>

Benchtop NMR spectrometers operating at a lower magnetic field (1 - 3 T) represent a more economic alternative to their high-field analogues, as they employ permanent magnets or resistive electromagnets instead of cryogen-cooled superconducting magnets.<sup>5,6</sup> These instruments are also portable, making them well-suited for use beyond traditional laboratory settings, including on workbenches, in clinical environments, or within industrial applications. Examples of such applications include reaction monitoring,<sup>7-12</sup> automated synthesis optimisation,<sup>13,14</sup> point-of-care diagnosis,<sup>15,16</sup> and industrial process monitoring.<sup>17-19</sup> The lower operational costs of benchtop NMR spectrometers are primarily due to their minimal maintenance requirements, particularly the absence of periodic cryogenic liquid refills. This

makes them a more sustainable alternative to high-field NMR spectrometers, as helium, which is commonly used in cryogenic cooling, is in limited global supply, which has led to a substantial increase in price.<sup>20</sup> Consequently, benchtop NMR spectrometers offer a more accessible analytical solution, both in terms of affordability and flexibility in measurement location.

However, the lower magnetic field of benchtop NMR spectrometers negatively affects both sensitivity and chemical shift dispersion. The latter is particularly problematic for  $^1\text{H}$  measurements, as protons have a narrower chemical shift range than other NMR-active nuclei, often leading to signal overlap. As a result, the applicability of this technique is limited to a reduced scope of applications that rely on samples with higher concentrations and relatively simple spectra. To address these limitations, efforts have been made to enhance sensitivity and mitigate the reduced chemical shift dispersion associated with low-field NMR measurements

One of the most successful approaches to overcome sensitivity limitations is the use of hyperpolarisation. This term is used to refer to a group of techniques which aim to increase the population difference between Zeeman energy levels, *i.e.* the polarisation level, beyond what is dictated by Boltzmann statistics (polarisation levels in parts per million). Several hyperpolarisation techniques have been developed, including: spin-exchange optical pumping (SEOP),<sup>21</sup> dynamic nuclear polarisation (DNP),<sup>22,23</sup> chemically induced dynamic nuclear polarisation (CIDNP),<sup>24</sup> and *para*-hydrogen induced polarisation (PHIP).<sup>25,26</sup> These techniques differ in terms of enhancement factors, applicability scope, and instrumentation requirements. It is these differences that inform the selection of a hyperpolarisation technique for a specific analytical application.

In spin-exchange optical pumping, the angular momentum of laser photons is transferred to the electrons of an alkali metal vapour, *e.g.* Rb, to increase its electronic polarisation. This polarisation is then transferred to the nuclei of noble gases, such as  $^3\text{He}$  and  $^{129}\text{Xe}$ , *via* spin exchange collisions mediated by Fermi contact hyperfine interactions.<sup>21</sup> Polarisation levels close to unity may be obtained *via* this approach.<sup>21,27</sup> Several interesting applications using this hyperpolarisation technique have been developed, including *in vivo* lung

imaging,<sup>28</sup> targeted biosensors,<sup>29,30</sup> and material science and engineering studies.<sup>27,31</sup>

The high polarisation levels achieved by SEOP, as well as the possibility to store and transport polarised gases to be used off-site,<sup>21,27</sup> make this hyperpolarisation technique a good complement to benchtop NMR measurements as its portability is not sacrificed. This has motivated the combination of SEOP with benchtop NMR,<sup>32,33</sup> demonstrating *ca.* 50 % polarisation for <sup>129</sup>Xe, as recently reported.<sup>33</sup> Nevertheless, the applicability of this hyperpolarisation technique is restricted to noble gases, so it is of little use in routine liquid-state analytical applications.

Dynamic nuclear polarisation exploits the high gyromagnetic ratio of electrons ( $\gamma_e/\gamma_n \simeq 658$ ), which leads to significantly larger thermal equilibrium population differences that can be used as a source of nuclear polarisation. The electronic population difference of species with unpaired electrons, typically stable radical species, is equalised by applying microwave irradiation at the electron paramagnetic resonance (EPR) frequency.<sup>22</sup> The electronic polarisation is then transferred to nuclei, either in the liquid state *via* the Overhauser effect (ODNP),<sup>34,35</sup> or in the solid state by additional mechanisms including the solid effect,<sup>36,37</sup> cross effect, and thermal mixing<sup>38–42</sup> in magic-angle spinning (MAS) DNP<sup>43</sup> and dissolution DNP<sup>23</sup> (dDNP). The diversity of polarisation transfer mechanisms thus broadens the applicability scope of DNP in comparison to SEOP.

ODNP applications include the study of hydration dynamics in biomolecules,<sup>44</sup> as well as, polymers, ionic liquids and viscous liquids, in combination with field-cycling NMR.<sup>45</sup> In dissolution DNP, solid-state transfer at low temperatures ( $1.2 < T < 4.2$  K) in a strong magnetic field ( $3.35 < B_0 < 10$  T) is followed by rapid dissolution and liquid-state detection.<sup>23</sup> Hyperpolarisation by dDNP has been widely explored for *in vivo* applications, particularly in real-time MRI studies of cancerous tumours,<sup>46–49</sup> as well as reaction monitoring and metabolomics using NMR.<sup>50–52</sup> As for MAS-DNP experiments, these involve solid-state detection and require low temperatures, and reported applications include solid-state protein analysis,<sup>53,54</sup> and material science studies.<sup>55,56</sup>

These approaches show vast differences in terms of the enhancement levels that can be achieved in liquid-state applications: whilst dDNP can reach polarisation levels on the order

of tens of percent,<sup>27,57,58</sup> those for ODNP are below 1 %.<sup>59,60</sup> Nevertheless, ODNP presents an advantage in that instrumentation requirements are less stringent, and integration with benchtop NMR has shown to be possible at relative low costs.<sup>61</sup> Whilst dDNP experiments are compatible with low-field NMR detection, they require the use of complex and costly instrumentation to create the polarisation conditions, *i.e.* cryogenic temperatures and moderate magnetic fields (a few Tesla), compromising the accessibility and portability of benchtop NMR spectrometers. Despite recent efforts to improve on these limitations,<sup>62</sup> the development of portable and accessible dDNP still remains in its infancy.

Perhaps a better compromise between achievable enhancements and accessibility may be provided by CIDNP. Chemically induced dynamic nuclear polarisation involves an excited initiating molecule, *e.g.* a photosensitiser excited by light irradiation in photo-CIDNP, which accepts an electron from the target molecule to form a radical pair. Following spin sorting processes and recombination of this radical pair, a non-Boltzmann population is obtained for the molecule under investigation.<sup>24</sup> This cyclical process regenerates the starting material, enabling repeated measurements to be obtained for the same sample, though it is ultimately limited by dye bleaching. This facilitates scan averaging to further enhance measurement sensitivity beyond the polarisation levels delivered by this technique, typically below 1 %.<sup>27</sup> The simplicity of this technique and low instrumentation requirements, *i.e.* the addition of a photosensitiser to the sample followed by light irradiation, has made it particularly attractive for integration with portable low-field NMR spectrometers.<sup>63–65</sup> For example, this approach has been recently exploited for drug fragment screening using photo-CIDNP benchtop NMR.<sup>65</sup> A limitation presented by this approach is the scope of molecules that can be hyperpolarised. Unlike DNP, which can be considered almost universal in its application, photo-CIDNP is mostly applicable to a subset of heteroaromatic molecules<sup>24,66–68</sup> currently covering a chemical space of a few thousand analytes.<sup>69</sup>

*Para*-hydrogen-based hyperpolarisation techniques exploit the high spin order of *para*-hydrogen ( $p\text{-H}_2$ ) as a source of nuclear polarisation. Through a chemical reaction, the high symmetry of  $p\text{-H}_2$  is broken and polarisation is transferred onto a target molecule. Hyperpolarisation techniques using  $p\text{-H}_2$  are collectively known as *para*-hydrogen induced polarisa-

tion (PHIP). *Para*-hydrogen may be incorporated into an unsaturated molecule *via* hydrogenation, resulting in an irreversible chemical transformation (hydrogenative PHIP).<sup>25,70</sup> Alternatively, the symmetry of *p*-H<sub>2</sub> may be broken by transiently binding to a metal centre to which the target molecule is also bound. In this variation, termed signal amplification by reversible exchange (SABRE), hyperpolarisation is continuously produced through the reversible exchange of both *p*-H<sub>2</sub> and target molecule with an iridium-based complex which facilitates polarisation transfer.<sup>26</sup>

PHIP, in particular the SABRE variant, shows the most promise as it provides a compromise between low instrumentation requirements, with its easiest implementation requiring a simple liquid-nitrogen-cooled hydrogen supply system<sup>71–74</sup> and a hand-held magnet,<sup>75</sup> and large signal enhancement levels, reaching values above 50 %.<sup>76</sup> In terms of the scope of applicability, whilst still restricted, it shows more versatility than photo-CIDNP, provided the target molecules exhibit a lone pair of electrons to act as ligands,<sup>26,77</sup> or exchangeable protons for the SABRE-Relay variation.<sup>78,79</sup> Besides extending the scope of possible analytes, SABRE offers higher enhancement factors than traditional PHIP experiments and the ability to continuously produce hyperpolarised signals as a result of the reversible nature of this process.<sup>26</sup>

Nevertheless, the development of real-life applications using SABRE-hyperpolarised benchtop NMR is still in its early stages and several challenges remain.<sup>80</sup> One challenge is the loss of the inherent quantitative nature of NMR, as signal enhancement occurs in a non-homogeneous way across the nuclei in a molecule. Although this issue could be addressed through the use of external calibration, a common procedure in most analytical methods, the complex interplay of exchange processes involved in SABRE renders this solution non-trivial. The use of co-substrates has been shown to alleviate this issue, whilst also expanding the range of molecules that can be probed and enabling low-concentration analysis, as demonstrated for high-field <sup>1</sup>H NMR measurements.<sup>81,82</sup>

Another significant obstacle in SABRE-hyperpolarised benchtop NMR spectroscopy is signal overlap. One simple way to overcome this limitation is to probe alternative NMR-active nuclei possessing wider chemical shift ranges, hence being less likely to suffer from

peak overlap. This solution is evidently limited by the presence of alternative nuclei in the sample. For instance,  $^{13}\text{C}$ , and to a lesser extent  $^{15}\text{N}$ , may be found in many analytical targets in organic and biochemical analysis. SABRE-hyperpolarisation of these heteronuclei has been reported before in 1D,<sup>83–85</sup> as well as in 2D NMR studies,<sup>86</sup> further mitigating spectral congestion. However, this approach comes with a further reduction in sensitivity compared to  $^1\text{H}$  measurements due to their lower gyromagnetic ratio and natural abundance. In contrast, heteronuclei such as  $^{19}\text{F}$  and  $^{31}\text{P}$  are more sensitive and 100 % naturally abundant,<sup>87,88</sup> and, while not ubiquitous, these nuclei are present in a wide range of molecules of interest. Furthermore, chemical labelling with these nuclei, particularly  $^{19}\text{F}$ ,<sup>89</sup> is a well developed strategy, with many known applications in protein studies,<sup>90–92</sup> offering a sensitive, well-resolved analysis without background signals.

Amongst other strategies commonly employed to overcome spectral overlap and simplify spectra is the use of pure shift and selective excitation methods to remove splitting due to homonuclear couplings and/or isolate a target signal in a mixture.<sup>93–97</sup> Some of these approaches have been successfully implemented in benchtop NMR spectrometers.<sup>98,99</sup> While useful for analysing complex spectra, these techniques are linked to a further loss in sensitivity, which has motivated their combination with hyperpolarisation techniques.<sup>100–102</sup> An alternative approach to spectral simplification is the use of the Sensitive, Homogeneous, And Resolved PEaks in Real time (SHARPER) pulse sequence, initially developed for high-field NMR spectroscopy,<sup>103</sup> but recently implemented on a benchtop NMR spectrometer.<sup>104</sup> By removing peak splitting and reducing field inhomogeneity effects, this pulse sequence is able to create simpler spectra, most importantly, whilst increasing signal-to-noise ratios.

This thesis aims to explore the potential of SABRE-hyperpolarised  $^{19}\text{F}$  benchtop NMR for the development of analytical applications. The collective effect of strategies such as the use of SHARPER and co-substrates is investigated to aid low-concentration detection and quantification of a set of molecules presenting increasing amounts of challenge. The background theory covering fundamental concepts of NMR and *para*-hydrogen-based hyperpolarisation techniques is presented in Chapter 2. Chapter 3 covers relevant experimental details for the measurements presented in Chapters 4 to 7.

In Chapter 4, the combination of the multiplet-refocusing pulse sequence SHARPER with SABRE experiments is explored for  $^{19}\text{F}$  NMR experiments. Studies on a set of fluoropyridines with diverse scalar coupling configurations, including  $^{19}\text{F}$  homonuclear and  $^1\text{H}$ - $^{19}\text{F}$  heteronuclear couplings, are presented, aiming to explore the applicability scope for SHARPER. Key factors having an impact on sensitivity and spectral quality are covered, including the optimisation of both SABRE experimental parameters and SHARPER acquisition and post-processing tools. Gains in signal-to-noise ratio introduced by SHARPER are explored for each sample and compared to proton-decoupling experiments, a common approach to remove  $^1\text{H}$ - $^{19}\text{F}$  scalar couplings. Finally, a selective version of SHARPER is applied to SABRE-hyperpolarised spectra to investigate its performance in a mixture sample.

Chapter 5 explores the use of co-substrates to facilitate the sensitive analysis of one of the fluoropyridines explored in Chapter 4: 3,5-difluoropyridine. The efficiency of hyperpolarisation for this target is compared with and without the use of a co-substrate, as well as at low concentrations of target molecule, where the co-substrate plays a crucial role in creating a stable SABRE system. Signal-to-noise ratios are used to establish the limit of detection for this approach, focusing on the impact on detectability introduced by the use of SHARPER. In addition, the potential for quantification is tested for SABRE-enhanced  $^{19}\text{F}$  NMR measurements, and their comparability to analogous  $^1\text{H}$  NMR measurements assessed, followed by a study on the impact of SHARPER acquisition on analytical performance.

In Chapter 6, the strategy presented in Chapter 5 is expanded to a more challenging fluoroamine substrate, 2,4,6-trifluorobenzylamine, which participates in a SABRE-Relay<sup>78,79</sup> polarisation transfer process with the solvent. The impact of this loss of hyperpolarisation to the solvent on the sensitivity gains for this test molecule are evaluated, and an approach to minimise the sensitivity penalty is presented. The effects of SABRE-Relay on the overall analytical performance of SABRE-enhanced benchtop NMR is assessed by comparing limits of detection and quantification accuracy in experimental conditions where the SABRE-Relay process is either favoured or minimised.

Chapter 7 investigates the limitations of SABRE-hyperpolarised benchtop NMR spectroscopy for analysing fluorinated analytes, focusing on fluorinated carboxylic acids due to their environmental significance. This chapter covers the hyperpolarisation feasibility of two simple fluorocarboxylic acids with the aim to find optimal hyperpolarisation conditions.

The main conclusions of this thesis are presented in Chapter 8 along with potential areas for future research.

## Chapter 2

# Background Theory

### 2.1 Fundamentals of Nuclear Magnetic Resonance

#### 2.1.1 Zeeman Interaction

Nuclear Magnetic Resonance (NMR) spectroscopy relies on the interaction between nuclear spins and a magnetic field. Many atomic nuclei possess spin, an intrinsic form of angular momentum,  $\hat{I}$ , characterised by the nuclear spin quantum number,  $I$ , which can take half-integer values from zero. Nuclear isotopes containing an even number of protons and an even number of neutrons, *e.g.*  $^{12}\text{C}$  and  $^{16}\text{O}$ , have no intrinsic angular momentum ( $I = 0$ ) and are therefore NMR inactive.<sup>105</sup>

Non-zero spin nuclei ( $I > 0$ ) exhibit an associated magnetic moment  $\hat{\mu}$ , as described in Equation 2.1. Magnetic moment and spin are related by the gyromagnetic ratio,  $\gamma$ , which may take positive or negative values. For most atomic nuclei, the gyromagnetic ratio is positive, and as a result the magnetic moment and the spin angular momentum are parallel, whilst in some cases  $\gamma < 0$  and they are antiparallel.<sup>105</sup>

$$\hat{\mu} = \gamma\hat{I} \tag{2.1}$$

A nucleus with spin  $I$  possesses  $(2I + 1)$  degenerate energy levels, each described by the azimuthal quantum number  $m$ , with values spanning from  $-I$  to  $+I$  in integer steps.

For example, spin- $\frac{1}{2}$  nuclei, such as  $^1\text{H}$  and  $^{13}\text{C}$ , have two energy states described by  $m = +\frac{1}{2}$  and  $m = -\frac{1}{2}$ . Upon application of an external magnetic field  $\mathbf{B}_0$ , the degeneracy of these states is broken in a phenomenon known as Zeeman splitting (Figure 2.1). The magnetic moment of a nucleus may become aligned to the external magnetic field, in a state commonly known as  $|\alpha\rangle$  ( $m = +\frac{1}{2}$ ), or oppose the magnetic field in a  $|\beta\rangle$  ( $m = -\frac{1}{2}$ ) state. The energy of each level depends on the quantum number  $m$  as well as the gyromagnetic ratio,  $\gamma$ , and the magnitude of the applied magnetic field,  $B_0$  (Equation 2.2).<sup>105</sup>

NMR selection rules dictate that signal is only observed for transitions between states with  $\Delta m = \pm 1$ , which is the case for transitions between  $|\alpha\rangle$  and  $|\beta\rangle$  states. The energy associated with the transition from  $|\alpha\rangle$  to  $|\beta\rangle$ ,  $\Delta E$ , is proportion to the Larmor frequency,  $\omega_0$ , as shown in Equations 2.3 and 2.4. The Larmor frequency represents the precession rate of the magnetic moment around the external magnetic field. This value is proportional to the gyromagnetic ratio and the external magnetic field, and may be expressed in angular frequency ( $\omega$ ) in radians  $s^{-1}$  as shown in Equation 2.4 or in frequency in Hertz ( $\nu$ ), using the conversion  $\omega = 2\pi\nu$ . By applying electromagnetic radiation at the Larmor frequency (radio-frequency region of the electromagnetic spectrum), the resonance condition which promotes transitions between  $|\alpha\rangle$  and  $|\beta\rangle$  states is met.<sup>105</sup> This is the underlying mechanism of NMR spectroscopy.

$$E_m = -m\hbar\gamma B_0$$

$$E_\alpha = -\frac{1}{2}\hbar\gamma B_0 \tag{2.2}$$

$$E_\beta = \frac{1}{2}\hbar\gamma B_0$$

$$\Delta E_{\alpha \rightarrow \beta} = E_\beta - E_\alpha = \hbar\gamma B_0 \tag{2.3}$$

$$\omega_0 = -\gamma B_0 \tag{2.4}$$

The Larmor frequency is specific for each type of nucleus. For example, at 9.4 T  $^1\text{H}$  nuclear spins precess at a frequency close to 400 MHz. The specific resonating frequency for a nucleus is determined by the electronic environment surrounding it. The external magnetic field induces an electric current resulting in an opposing magnetic field which

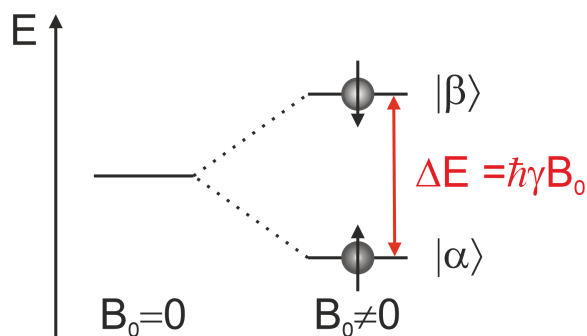


Figure 2.1: Energy diagram depicting Zeeman splitting for a nucleus with spin  $I = 1/2$  and  $\gamma > 0$ . In the absence of a magnetic field ( $B_0 = 0$ ), the  $2I + 1$  nuclear states are degenerate. Upon application of a magnetic field ( $B_0 \neq 0$ ), the nuclear states become non-degenerate as the magnetic moment may align in a parallel ( $|\alpha\rangle$ ) or anti-parallel ( $|\beta\rangle$ ) direction relative to the external magnetic field.

shields the nucleus from the external magnetic field. As a result, the resonating frequency for this nucleus is shifted from the expected value for a bare nucleus without surrounding electrons, as described in Equation 2.5, where  $\sigma$  is the shielding constant.<sup>106</sup> In this way, NMR spectroscopy is able to probe the chemical environment surrounding each nucleus. Since the variation in Larmor frequency for two nuclei with different chemical surroundings is significantly smaller than their resonating frequency, it is customary to describe these signals in terms of frequency differences rather than absolute frequencies. These differences, expressed relative to a set reference in parts per million, are commonly referred to as chemical shift values ( $\delta$ ) and are calculated as defined in Equation 2.6.<sup>105</sup> By using chemical shift values, it is possible to describe resonances in a spectrum in a field-independent way, thus facilitating spectra comparison irrespective of the magnetic field.

$$\omega_0 = -\gamma B_0(1 - \sigma) \quad (2.5)$$

$$\delta = \frac{\omega_0 - \omega_{0,ref}}{\omega_{0,ref}} 10^6 \quad (2.6)$$

Another important source of information about the chemical environment of each nuclear spin is scalar spin-spin couplings, or  $J$  couplings. This indirect interaction occurs between

bonded nuclei and it is mediated by the electrons participating in this bond. As a result,  $J$  coupling provides insights into the connectivity of NMR-active nuclei within the same molecule, with larger  $J$  coupling values typically observed for nuclei that are closer together.<sup>106</sup> Notably, this coupling is independent of the applied magnetic field.<sup>105</sup>

The concepts of chemical shift and  $J$  coupling may be better understood by considering a pair of  $^1\text{H}$  spins, A and X, with different chemical environments. Such spins possess different deviations from the Larmor frequency for this nucleus type. Thus, a spectrum containing a pair of peaks with different chemical shift values,  $\delta_A$  and  $\delta_X$ , would be observed in the absence of scalar coupling. In the scenario where these spins are coupled, then each peak is split by the  $J_{AX}$  coupling constant. This may be explained as follows: the magnetic moment of A will affect that of X, and *vice versa*. For instance, if A is in the  $|\alpha\rangle$  state, X may either be in the  $|\alpha\rangle$  state, reinforcing  $\mathbf{B}_0$ , or the  $|\beta\rangle$  state, partially cancelling this field. As a result, A spins will precess at either a lower or higher frequency than that observed in the absence of coupling. As the reciprocal situation holds true, this will result in a spectrum in which both signals for A and X are split in two (doublets) (Figure 2.2).<sup>107</sup> In a more general case, the multiplicity of the splitting of A will be given by  $2nI + 1$ , with  $n$  being the number of chemically equivalent nuclei (*i.e.* possessing the same  $\delta$ ) coupled to A, and  $I$  being the spin quantum number of the X spins. For example, in an  $AX_2$  system, where X has  $I = \frac{1}{2}$ , the signal corresponding to A will be three equally spaced peaks with an intensity ratio of 1:2:1 (triplet).<sup>107</sup>

The situation described so far applies to weak coupling conditions, *i.e.* when the difference in frequencies for A and X is much larger than the scalar coupling between these nuclei ( $|\Delta\nu_{AX}| \gg |J_{AX}|$ ). In contrast, strong coupling, *i.e.* when both magnitudes are comparable ( $|\Delta\nu_{AX}| \approx |J_{AX}|$ ), produces complex second-order splitting, a situation more often encountered at lower  $B_0$ .<sup>106</sup>

### 2.1.2 The Vector Model

The description presented so far has focused on a single spin or spin pair and its interaction with  $\mathbf{B}_0$ . However, NMR samples contain a large ensemble of spins that collectively con-

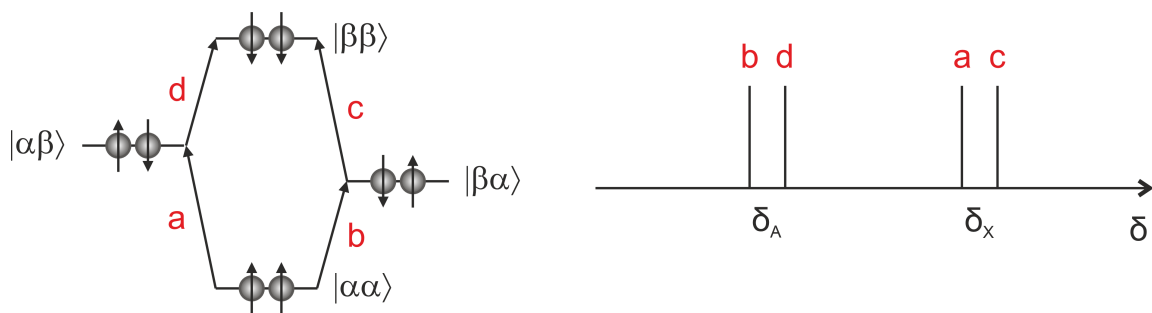


Figure 2.2: Energy levels and spectra for an AX-type system consisting of a pair of non-equivalent weakly coupled spin- $\frac{1}{2}$  nuclei with  $\delta_A > \delta_X$ . Spectra shows a pair of doublets, each split by a  $J_{AX}$  ( $J_{AX} > 0$ ) scalar coupling. Letters a - d show the possible transitions for this system.<sup>107</sup>

tribute to a detectable signal. In the absence of an external magnetic field, this collection of spins exhibits an isotropic distribution of spin angular momentum, *i.e.* these vectors point in every direction (Figure 2.3a). However, when a magnetic field is applied, the spin magnetic moment of each nucleus starts precessing around  $\mathbf{B}_0$  with varying cone angles (Figure 2.3 b and c). The spin angular momentum vector can be represented using a set of  $x$ ,  $y$ ,  $z$  Cartesian coordinates, where the  $z$ -axis is parallel to  $\mathbf{B}_0$  by convention. The  $z$ -component or longitudinal component of the spin angular momentum of each nucleus will then be parallel ( $|\alpha\rangle$ ) or anti-parallel ( $|\beta\rangle$ ) to the magnetic field. As the parallel alignment is more energetically favourable, there will be a larger number of nuclei presenting this configuration. This results in a net nuclear magnetic moment or magnetization along the  $z$ -axis, termed  $\mathbf{M}_z$ , which increases over time after  $\mathbf{B}_0$  is switched on. This value will stabilise over time to reach a net magnetisation value at thermal equilibrium,  $\mathbf{M}_0$ . The magnitude of  $\mathbf{M}_0$  is proportional to the difference in population between the lower-energy  $|\alpha\rangle$  state and the higher-energy  $|\beta\rangle$  state. In contrast, the  $x$  and  $y$  (transverse) components of the individual magnetic moments rotate in the  $x$ - $y$  plane due to the precession motion. At thermal equilibrium, the spins precess with a random distribution of phases and as a result, the  $x$  and  $y$  components cancel out and there is no net transverse magnetisation ( $M_{x,y} = 0$ ). Following this treatment, it is possible to describe the behaviour of an entire

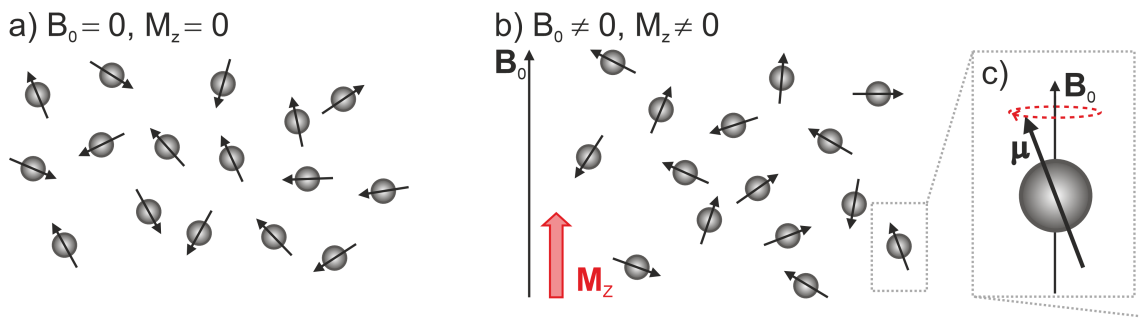


Figure 2.3: Cartoon representations of an ensemble of nuclei with spin- $\frac{1}{2}$  in the absence (a,  $B_0 = 0$ ) and presence (b,  $B_0 \neq 0$ ) of a magnetic field, with the formation of a net nuclear magnetisation ( $M_z$ ). The precession of the spin magnetic moment ( $\mu$ ) around the direction of the magnetic field is depicted in c).

collection of nuclei in terms of a bulk magnetisation vector  $\mathbf{M}$  and its components along  $x$ ,  $y$ ,  $z$ -axes, in a model known as the Bloch vector model. Although overly simplistic, this model is sufficient to understand the behaviour of non-interacting spin- $\frac{1}{2}$  nuclei during NMR experiments.<sup>105,108</sup>

A typical NMR experiment involves the manipulation of the initial bulk magnetisation ( $\mathbf{M}_0$ ) through the application of a radio-frequency (r.f.) pulse, followed by the detection of the signal produced by the evolving system. At the start of the experiment, the initial magnetisation vector corresponds to the net magnetisation along the  $z$  axis,  $M_z$ , arising from the difference in population between  $|\alpha\rangle$  and  $|\beta\rangle$  states (Figure 2.4a). This magnetisation is then subjected to a magnetic field oscillating at the Larmor frequency,  $\mathbf{B}_1$ , which is applied on the transverse plane. To aid understanding of the effect of this pulse on the initial magnetisation, it is convenient to use the rotating frame of reference.<sup>108</sup>

The rotating frame of reference relies on the decomposition of  $\mathbf{B}_1$  into two magnetic vectors rotating in the  $x$ - $y$  plane in opposite directions at the same frequency. One of these components is then considered to be aligned and fixed to either the  $x$  or  $y$  axis which rotates at the same frequency of  $\mathbf{B}_1$ , whilst the other component is ignored. By using this approach,  $\mathbf{B}_1$  appears to be static if observed from a set of  $x'$ ,  $y'$ ,  $z'$  axes rotating at the same frequency as  $\mathbf{B}_1$ , *i.e.* the rotating frame of reference (Figure 2.4a). As this precessional

motion arises from the effect of the external magnetic field,  $\mathbf{B}_0$ , it is not represented in this frame of reference. By using the rotating frame of reference, the interaction between  $\mathbf{B}_1$  and  $\mathbf{M}_0$  can then be simplified as the former imposing a torque on the latter, resulting in a rotation of the bulk magnetisation vector towards the  $x'-y'$  plane. The nutation angle in degrees generated by a r.f. pulse is proportional to the amplitude of  $\mathbf{B}_1$  and its duration  $t$ , as described in Equation 2.7.<sup>108</sup>

$$\theta = 360 \frac{\gamma}{2\pi} B_1 t \quad (2.7)$$

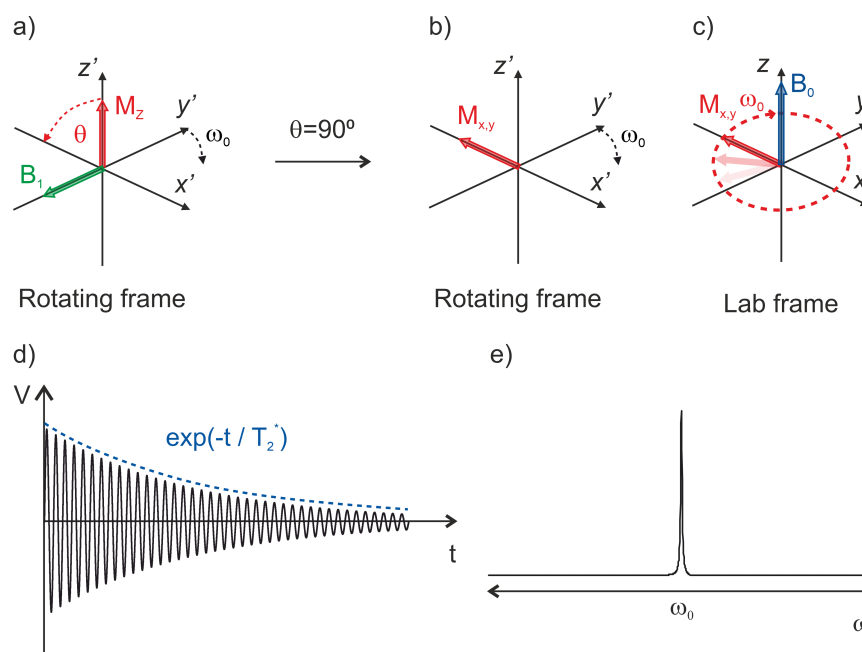


Figure 2.4: Schematic representation of an NMR experiment. a) The thermal equilibrium longitudinal magnetisation is rotated  $90^\circ$  onto the transverse plane by applying a  $\mathbf{B}_1$  field on the  $-y$  direction, which appears static in the rotating frame of reference (b), but rotates at the Larmor frequency ( $\omega_0$ ) in the laboratory frame (c). This creates an oscillating signal (in Volts, V) with decays following the time constant  $T_2^*$ , known as free induction decay (FID). Fourier transformation of the FID produces a spectrum with a signal at the Larmor frequency (e).

As the nutation angle increases, so does the transverse component of the bulk magnetisation ( $M_{x,y}$ ), whilst the longitudinal component ( $M_z$ ) decreases following Equation 2.8. At  $90^\circ$ , the transverse magnetisation reaches its largest value ( $M_{x,y} = M_0$ ), whilst the longitudinal magnetisation is null (Figure 2.4b), representing a situation in which  $|\alpha\rangle$  and  $|\beta\rangle$  states are equally populated. The evolution of the created transverse magnetisation can be understood differently depending on the frame of reference. In the laboratory frame of reference, this transverse magnetisation will be subjected to a torque by  $\mathbf{B}_0$ , causing it to precess at the Larmor frequency as described in Equations 2.9 (Figure 2.4c), whilst in the rotating frame of reference, this transverse magnetisation will appear static (Figure 2.4b). The rotating magnetisation observed in the laboratory frame will produce an oscillating electric current that can be detected by a nearby coil, such as the one producing the r.f. pulse (Figure 2.4d).<sup>108</sup>

$$M_{xy} = M_0 \sin(\theta) \quad (2.8)$$

$$M_x(t) = M_{xy} \cos(\omega_0 t) \quad (2.9)$$

$$M_y(t) = -M_{xy} \sin(\omega_0 t)$$

The magnitude of the longitudinal and transverse magnetisation vectors will vary during the evolution of the spin system due to two distinct phenomena. Firstly, the population difference between  $|\alpha\rangle$  and  $|\beta\rangle$  states, which was modified *via* r.f. pulsing, must return to its initial equilibrium value thus restoring the original longitudinal magnetisation. This phenomenon is known as longitudinal or spin-lattice relaxation, which describes the variation in  $M_z$  as a function of a time constant  $T_1$  (Equation 2.10).<sup>109</sup> Secondly, the magnitude of the net transverse magnetisation vector will decrease over time due to a loss in phase coherence in a process known as transverse or spin-spin relaxation. Phase decoherence may be understood as a gradual desynchronisation of the individual magnetic moments of each spin on the transverse plane. The dephasing process arises from two primary causes. Firstly, phase coherence may be lost due to random interactions between individual spins resulting in energy exchange. Transverse relaxation due to this process follows a time constant  $T_2$ . Another source of dephasing is field inhomogeneity due to variations in  $B_0$  or different mag-

netic susceptibility within the sample region, introducing variations in Larmor frequency for individual spins. The combined effect of  $T_2$  and  $B_0$  inhomogeneity is described by the effective transverse relaxation time constant  $T_2^*$  (Equation 2.11),<sup>108,109</sup> which describes the decay of transverse magnetisation (Equation 2.12) and detected signal (Figure 2.4d) over time.

$$M_z(t) = M_0 \left[ 1 - \exp\left(\frac{-t}{T_1}\right) \right] \quad (2.10)$$

$$\frac{1}{T_2^*} = \frac{\gamma \Delta B_0}{2} + \frac{1}{T_2} \quad (2.11)$$

$$M_x(t) = M_{xy} \cos(\omega_0 t) \exp\left(\frac{-t}{T_2^*}\right) \quad (2.12)$$

$$M_y(t) = -M_{xy} \sin(\omega_0 t) \exp\left(\frac{-t}{T_2^*}\right)$$

This relaxation mechanism contributes to the decay of transverse magnetisation (Equations 2.12), and as a consequence, of the induced electrical current. As a result, the signal obtained from an NMR experiment is an electrical signal oscillating at the Larmor frequency of the nuclear spin in the sample that decays over time, referred to as a free induction decay (FID). By applying a Fourier transformation to the FID, a spectrum containing peaks at these frequencies is obtained (Figure 2.4e).

### 2.1.3 Polarisation

As discussed in the previous section, the bulk longitudinal magnetisation vector  $M_z$  is determined by the difference in population of  $|\alpha\rangle$  and  $|\beta\rangle$  energy states, ( $n_\alpha$  and  $n_\beta$ , respectively) given by Equation 2.13. This results in a polarisation of the spins along the z direction.<sup>107</sup>

$$M_z = \frac{1}{2} \hbar \gamma (n_\alpha - n_\beta) \quad (2.13)$$

At thermal equilibrium and in a sample containing  $N$  spins, the population of each energy state may be predicted by the Boltzmann distribution using the Boltzmann constant ( $k_B$ ) at a given temperature,  $T$  (Equation 2.14). Applying the high-temperature approximation, it follows that the longitudinal magnetisation at thermal equilibrium ( $M_z^0$ ) depends on the

energy gap between  $|\alpha\rangle$  and  $|\beta\rangle$  (Equation 2.15).<sup>107</sup> This difference in population between  $|\alpha\rangle$  and  $|\beta\rangle$  states is commonly known as a polarisation value,  $P$ , calculated according to Equation 2.16.

$$\begin{aligned} n_\alpha &= \frac{1}{2}N \exp(-E_\alpha/k_B T) \\ n_\beta &= \frac{1}{2}N \exp(-E_\beta/k_B T) \end{aligned} \quad (2.14)$$

$$M_z^0 \approx \frac{1}{4}\hbar\gamma(E_\beta - E_\alpha) = \frac{\gamma^2\hbar^2NB_0}{4k_B T} \quad (2.15)$$

$$P \approx \frac{\gamma\hbar B_0}{2k_B T} \quad (2.16)$$

As the energy gap is four orders of magnitude smaller than the available thermal energy,<sup>105</sup> the energetic benefit for spins to align to the external magnetic field is negligible. This results in very small polarisation values, typically in tens of parts per million, in NMR experiments performed under standard conditions. As the intensity of the detected signal is directly proportional to the magnitude of  $M_z^0$ , NMR is highly insensitive relative to other analytical techniques. The correlation between  $M_z^0$  and the applied magnetic field (Equation 2.15) has driven the development of NMR spectrometers with increasingly higher operating magnetic fields. However, this progress is accompanied by larger instrument sizes and higher acquisition and operational costs.<sup>109</sup> In contrast, some manufacturers have produced smaller, more affordable instruments that operate at lower magnetic fields, aiming to enhance the accessibility of NMR technology.<sup>110–112</sup>

#### 2.1.4 Low-field NMR Spectroscopy

Benchtop NMR spectrometers employ permanent magnets to generate low magnetic fields ranging from  $B_0 = 1$  to 3 T, in contrast to the cryogen-cooled superconducting magnets used in conventional NMR systems, which typically operate at  $B_0 \geq 7$  T.<sup>111</sup> Consequently, benchtop instruments are more compact and affordable, making them accessible as laboratory tools and suitable for benchtop or field applications.<sup>113</sup> However, the lower field strength of commercially available benchtop NMR spectrometers generally results in a significant reduction in sensitivity compared to high-field spectrometers as nuclear spin polarisation is directly proportional to  $B_0$  (Equation 2.16).<sup>111</sup>

Early prototypes of low-field NMR spectrometers lacked sufficient field homogeneity to enable chemical-shift-resolved NMR analysis and were primarily limited to relaxation and diffusion experiments in the time domain.<sup>110</sup> Advances in Halbach permanent magnet design have since improved field homogeneity, allowing for the development of NMR spectrometers with chemical-shift resolution, available since 2010.<sup>110</sup>

This new generation of benchtop NMR spectrometers offers several advantages, including a reduced dependence on deuterated solvents, maintenance-free operation, portability, and, in high-end models, linewidths comparable to those of high-field systems.<sup>110</sup> These benefits, combined with their lower cost and improved accessibility, have made benchtop NMR spectroscopy an attractive option for industrial applications such as process control and reaction monitoring, as well as for chemical analysis in workbenches or fume hoods.<sup>110,112,113</sup>

## 2.2 Hyperpolarisation

### 2.2.1 Principles of Hyperpolarisation

The inherently low sensitivity of NMR spectroscopy can be addressed through hyperpolarisation techniques. Hyperpolarisation refers to methods that enhance the population difference between energy levels beyond what is achieved under equilibrium conditions dictated by Boltzmann statistics (Figure 2.5). By increasing polarisation values from the typical parts per million to percentages, hyperpolarisation can boost the sensitivity of NMR spectroscopy by orders of magnitude, offering a more efficient solution than increasing the applied magnetic field strength.

Several hyperpolarisation techniques are currently in advanced stages of development and show promising applications.<sup>80</sup> These methods, which vary in their polarisation sources and transfer mechanisms, include spin-exchange optical pumping (SEOP),<sup>21</sup> dynamic nuclear polarisation (DNP),<sup>22,23</sup> chemically induced dynamic nuclear polarisation,<sup>24</sup> and *para*-hydrogen induced polarisation (PHIP).<sup>25,26</sup>

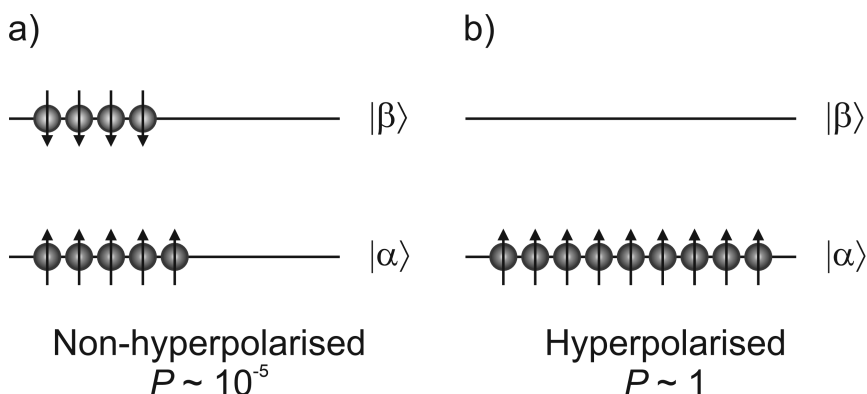


Figure 2.5: Schematic representation of the hyperpolarisation process. a) Under non-hyperpolarised conditions, nuclear spins are distributed between  $|\alpha\rangle$  and  $|\beta\rangle$  states following Boltzmann statistics, with a net polarisation on the order of tens of parts per million. b) Hyperpolarisation increases the population difference between  $|\alpha\rangle$  and  $|\beta\rangle$  states, reaching polarisation levels up to unity.

## 2.2.2 *Para*-hydrogen Based Hyperpolarisation

### 2.2.2.1 *Para*-hydrogen

*Para*-hydrogen and *ortho*-hydrogen (*o*-H<sub>2</sub>) are nuclear spin isomers of dihydrogen. The existence of these two isomers is a consequence of the anti-symmetry requirements for the total wavefunction of fermion particles, such as electrons and protons, according to Pauli's exclusion principle.<sup>114</sup> For this requirement to be fulfilled, the wavefunction of two particles must change signs upon exchange. The total wavefunction of the hydrogen molecule H<sub>2</sub> can be represented as the dot product of the wavefunctions for translational ( $\psi_T$ ), rotational ( $\psi_R$ ), vibrational ( $\psi_V$ ), electronic ( $\psi_E$ ) and nuclear spin ( $\psi_{sn}$ ) components (Equation 2.17).<sup>115,116</sup>

$$\Psi = \psi_T \cdot \psi_R \cdot \psi_V \cdot \psi_E \cdot \psi_N \quad (2.17)$$

As the translational, vibrational, and electronic wavefunctions are symmetrical upon exchange, the anti-symmetry of the total wavefunction must stem from the product of ro-

tational and nuclear wavefunctions ( $\psi_R \cdot \psi_N$ ). In other words, symmetric rotational states may only exist when coupled to anti-symmetric nuclear states and *vice versa*. The wavefunction for rotational motion of the nuclei will be symmetric for even rotational states ( $J=0, 2, 4, \text{etc.}$ ) and anti-symmetric for odd rotational states ( $J = 1, 3, 5, \text{etc.}$ ).<sup>116</sup> As for the nuclear spin wavefunctions, the combination of two nuclear spin states produces four possible states *via* linear combinations of the direct product of the two possible spin orientations for each single spin.<sup>116</sup> These nuclear states, described in Equation 2.18, correspond to the symmetric triplet state of *o*-H<sub>2</sub> ( $|T_{+1}\rangle, |T_0\rangle$  and  $|T_{-1}\rangle$ ), and the singlet anti-symmetric state ( $|S_0\rangle$ ) of *p*-H<sub>2</sub>.

$$\begin{aligned}
 |T_{+1}\rangle &= |\alpha\alpha\rangle \\
 |T_0\rangle &= \frac{1}{\sqrt{2}}(|\alpha\beta\rangle + |\beta\alpha\rangle) \\
 |T_{-1}\rangle &= |\beta\beta\rangle \\
 |S_0\rangle &= \frac{1}{\sqrt{2}}(|\alpha\beta\rangle - |\beta\alpha\rangle)
 \end{aligned}
 \tag{2.18}$$

To meet anti-symmetry requirements, the singlet nuclear state must combine with even rotational states, whilst the triplet nuclear state combines with odd rotational states, giving rise to *para*-hydrogen and *ortho*-hydrogen, respectively. As the singlet state combines with the lowest energy rotational state ( $J=0$ ), *para*-hydrogen corresponds to the lowest energy nuclear spin isomer (Figure 2.6).

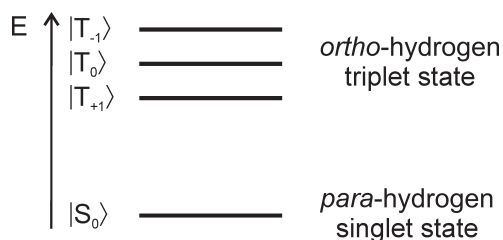


Figure 2.6: Diagram depicting the energy level for the singlet ( $|S_0\rangle$ ) and triplet ( $|T_{+1}\rangle, |T_0\rangle$  and  $|T_{-1}\rangle$ ) nuclear spin states of dihydrogen under a magnetic field. Note: the energy gaps are not drawn to scale.

The absolute populations of *o*-H<sub>2</sub> ( $N_o$ ) and *p*-H<sub>2</sub> ( $N_p$ ) in a sample of H<sub>2</sub> will depend on

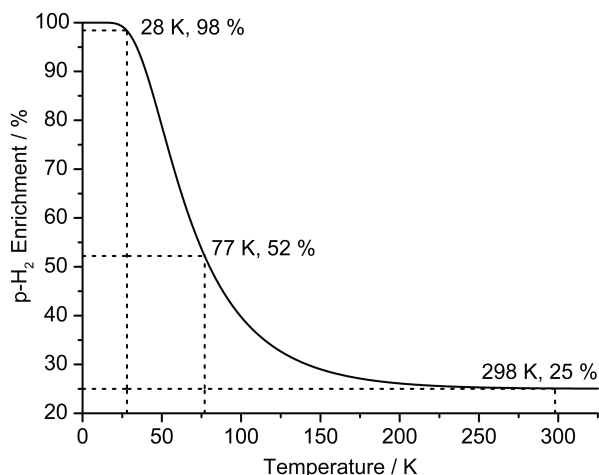


Figure 2.7: *Para*-hydrogen enrichment in a H<sub>2</sub> sample expressed as a percentage as a function of temperature with  $\theta_R = 87.8$  K. Reproduced under a CC-BY license from Ref. [80].

its temperature (T), as stipulated by Boltzmann statistics (Equation 2.19,  $\theta_R$ : rotational constant of the molecule), from which *o*-H<sub>2</sub> and *p*-H<sub>2</sub> fractions may be derived (Figure 2.7). At room temperature in thermal equilibrium conditions, the *p*-H<sub>2</sub> population is  $\approx 25$  %. As the temperature of the sample decreases, the fraction of *p*-H<sub>2</sub> increases, reaching  $\approx 98$  % at 28 K.

$$\begin{aligned}
 N_p &= \sum_{J=\text{even}} (2J+1) e^{-\frac{J(J+1)\theta_R}{T}} \\
 N_o &= 3 \sum_{J=\text{odd}} (2J+1) e^{-\frac{J(J+1)\theta_R}{T}}
 \end{aligned}
 \tag{2.19}$$

Whilst simply cooling a sample of H<sub>2</sub> would appear to suffice to create large *p*-H<sub>2</sub> enrichments, this is in practice inefficient as *o*-H<sub>2</sub>/*p*-H<sub>2</sub> interconversion is symmetry forbidden. This process can be accelerated by introducing a spin isomer interconversion catalyst to facilitate nuclear spin reorientation.<sup>71,116,117</sup> Suitable catalyst typically fall within two classes: paramagnetic species creating local field inhomogeneities to break the symmetry of H<sub>2</sub> (*e.g.* iron (III) oxide) and adsorption/desorption surfaces enabling H<sub>2</sub> dissociation and recombination (*e.g.* activated charcoal).<sup>118</sup> *Para*-hydrogen-enriched samples generated using low temperatures and interconversion catalysts may then be stored at room tempera-

ture for periods up to months,<sup>119,120</sup> provided the sample is isolated from any material that may induce conversion back to *ortho*-hydrogen. Various *p*-H<sub>2</sub> generation methods exist, including systems cooled by liquid nitrogen (*p*-H<sub>2</sub> enrichment  $\approx 52\%$ ),<sup>71–74</sup> or the more costly closed-cycle helium (*p*-H<sub>2</sub> enrichment  $> 98\%$ ).<sup>121–123</sup>

The null nuclear spin of *para*-hydrogen results in a lack of Zeeman splitting under a magnetic field, and as a result it is NMR invisible. Nevertheless, the high spin order of *p*-H<sub>2</sub> can be harnessed as a source of polarisation provided its symmetry is broken. This is typically achieved when *p*-H<sub>2</sub> is involved in a chemical reaction, resulting in large enhancements of NMR signals. Differing in the nature of this chemical reaction, there exists two primary *p*-H<sub>2</sub>-based techniques: hydrogenative (Section 2.2.2.2) and non-hydrogenative (Section 2.2.2.3) *para*-hydrogen induced polarisation. These techniques, referred to as PHIP and SABRE from this point onwards, will be described in the following sections.

#### 2.2.2.2 *Para*-hydrogen Induced Polarisation (PHIP)

The hydrogenative variation of *para*-hydrogen induced polarisation involves the incorporation of *p*-H<sub>2</sub> into an unsaturated molecule, upon which its symmetry is broken. This was first predicted by Bowers and Weitekamp in 1986,<sup>25</sup> who proposed that if hydrogenation reactions were performed using *p*-H<sub>2</sub>-enriched hydrogen gas, NMR signal enhancements would be observed. Such a hypothesis was confirmed experimentally by two independent groups in 1987,<sup>70,124</sup> by simply storing the hydrogenation samples at low temperatures, thus increasing *p*-H<sub>2</sub> enrichment, before conducting NMR experiments. This experiment was named by Bowers and Weitekamp using the acronym PASADENA (*para*-hydrogen and synthesis allows dramatically enhanced nuclear alignment).<sup>70</sup> A variation of this experiment was subsequently proposed by Pravica and Weitekamp termed adiabatic longitudinal transport after dissociation engenders nuclear alignment (ALTADENA).<sup>125</sup> In this experiment, the hydrogenation reaction was performed outside the NMR spectrometer, which they found to produce differences in the form of the enhanced NMR signals.

In PASADENA experiments, the hydrogenation reaction occurs at the high magnetic field inside the spectrometer (Figure 2.8, top). Upon incorporation of *p*-H<sub>2</sub> into the un-

saturated molecule, the hydrogen pair transitions from a magnetically equivalent  $A_2$  spin system (Pople’s notation<sup>126</sup>) to a magnetically inequivalent weakly coupling AX system ( $|\Delta\nu_{AX}| \gg |J_{AX}|$ ). In this process, the initial population of the  $|S_0\rangle$  state is distributed almost equally amongst the near-degenerate  $|\alpha\beta\rangle$  and  $|\beta\alpha\rangle$  states of the AX system (Section 2.1.1). The allowed transitions from these overpopulated states to the  $|\alpha\alpha\rangle$  and  $|\beta\beta\rangle$  states results in a characteristic pair of anti-phase doublets with greatly enhanced signals.

In contrast, hydrogenation reactions in ALTADENA conditions are performed outside the bore of the NMR instrument at low magnetic fields, followed by adiabatic transfer of the sample into the spectrometer. At this low magnetic field, the frequency difference between both hydrogen nuclei is comparable to their scalar coupling, thus creating a strongly-coupled AB spin system ( $|\Delta\nu_{AX}| \approx |J_{AX}|$ ). In this scenario, the initial population of the singlet state overpopulates a superposition of the  $|\alpha\beta\rangle$  and  $|\beta\alpha\rangle$  states. As the sample is adiabatically introduced into the spectrometer, weakly coupling conditions are created (AX) with either the  $|\alpha\beta\rangle$  or  $|\beta\alpha\rangle$  state becoming overpopulated. The transitions from the overpopulated state to  $|\alpha\alpha\rangle$  and  $|\beta\beta\rangle$  produce a spectrum containing a pair of singlets of opposite phase (Figure 2.8, bottom).

PHIP as a signal enhancement technique is limited to unsaturated molecules which can undergo hydrogenation. Variations on this approach have been developed to alleviate this restriction on the chemical space of molecules that are suitable to PHIP hyperpolarisation. For instance, Reineri *et al.* developed the *para*-hydrogen induced polarisation with side-arm hydrogenation technique (PHIP-SAH) in which a saturated target molecule may be hyperpolarised through an unsaturated side arm, which is cleaved post polarisation.<sup>127</sup> Other alternatives include PHIP-X,<sup>128</sup> or PHIP-Relay,<sup>129</sup> in which an unsaturated molecule containing exchangeable protons facilitates the hyperpolarisation of a secondary saturated target molecule. Once the first molecule is hydrogenated and hyperpolarised, it acts as a polarisation transfer agent by hyperpolarising the target molecule *via* proton exchange.

Another limitation of hydrogenative PHIP is that attainable signal enhancements are limited by the irreversible chemical transformation occurring in the experiment. In other words, signal enhancements will only be seen provided there remains unsaturated target

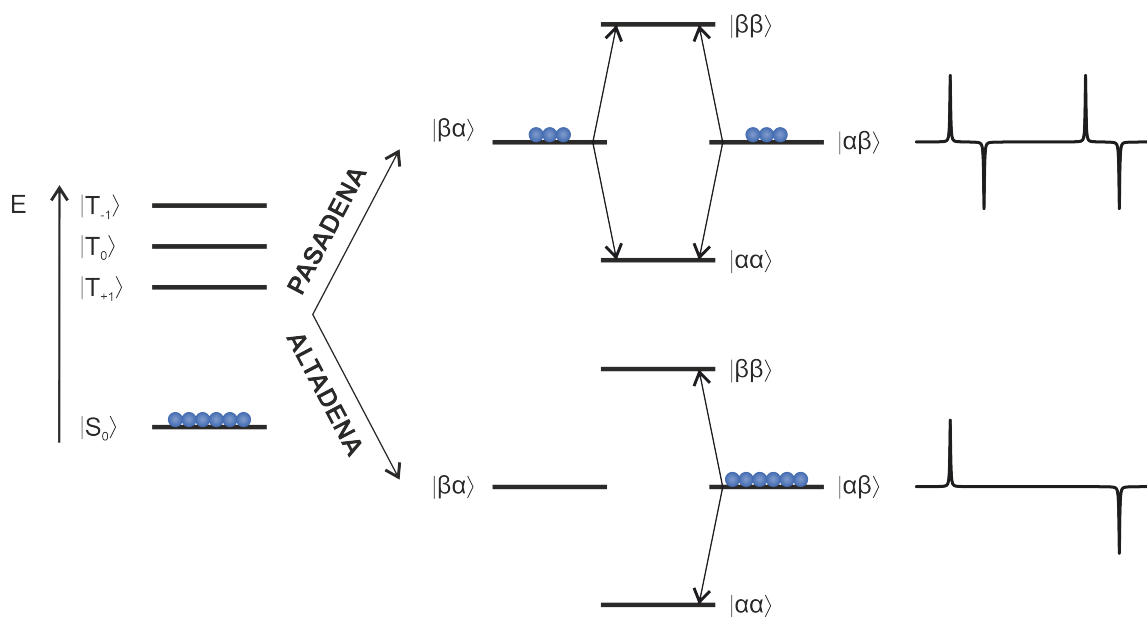


Figure 2.8: Schematic representation of the PASADENA (top) and ALTADENA (bottom) experiments. In PASADENA experiments, the initial singlet population from  $p$ -H<sub>2</sub> is distributed between the  $|\alpha\beta\rangle$  and  $|\beta\alpha\rangle$  of the weakly coupling AX spin system created at the high magnetic field inside the NMR spectrometer. A characteristic spectrum containing a pair of enhanced anti-phase doublets is obtained. In ALTADENA conditions, the singlet population is transferred onto a superposition of  $|\alpha\beta\rangle$  and  $|\beta\alpha\rangle$  states of the strongly coupled AB system created at low magnetic fields. Upon adiabatic transfer into the spectrometer, either the  $|\alpha\beta\rangle$  or  $|\beta\alpha\rangle$  state becomes overpopulated, resulting in an NMR spectrum containing a pair of enhanced singlets of opposite phase.

in solution. As this transformation is irreversible, the sample can only be probed a finite number of times. The non-hydrogenative PHIP variation, SABRE, lifts those limitations and, as a result, is more attractive for analytical applications.

### 2.2.2.3 Signal Amplification by Reversible Exchange (SABRE)

The hyperpolarisation technique SABRE was introduced in 2009 as an alternative to hydrogenative PHIP.<sup>26</sup> In SABRE,  $p$ -H<sub>2</sub> and the target molecule to hyperpolarise, also referred to

as the substrate, reversibly bind to a transient polarisation transfer catalyst. This is typically an iridium octahedral complex with the general structure  $[\text{Ir}(\text{H})_2(\text{NHC})(\text{substrate})_3]^+$ , where NHC is a N-heterocyclic carbene such as 1,3-bis(2,4,6-trimethylphenyl)-imidazol-2-ylidene (IMes). Although SABRE hyperpolarisation using alternative complexes has been explored,<sup>130,131</sup> iridium-based catalyst remain the most widely used. The binding of *p*-H<sub>2</sub> to this polarisation transfer catalyst breaks its symmetry by creating chemical and/or magnetic non-equivalence. The network of scalar couplings connecting the *p*-H<sub>2</sub>-derived hydrides and the substrate in the iridium complex acts as a conduit for polarisation to be transferred. As both *p*-H<sub>2</sub> and the substrate exchange with the available pool in solution, the polarisation cycle is continuously repeated to create a build-up of hyperpolarised analyte in solution. Large signal enhancements are consequently achieved for the target ( $P_{1\text{H}}$  of up to 63%,<sup>76</sup>) without resulting in its chemical modification, thus enabling repeated experiments on the same sample. This process is shown schematically in Figure 2.9.

Signal enhancement has been successfully achieved in substrates using a wide range of binding groups, provided they can act as ligands. For example, SABRE has been successfully applied to N-heterocycles,<sup>26,132–140</sup> nitriles,<sup>141–143</sup> Schiff bases,<sup>144</sup> nitrites,<sup>145</sup> amino acids and oligopeptides,<sup>146–148</sup> thiophenes,<sup>149</sup> and phosphines.<sup>150</sup> It is also possible to hyperpolarise heteronuclei within the target molecule: signal enhancements of <sup>13</sup>C, <sup>15</sup>N, <sup>19</sup>F and <sup>31</sup>P have been reported.<sup>83,132,138,150–153</sup> An interesting variation of SABRE that allows for a more diverse array of hyperpolarised target molecules is SABRE-Relay. In this technique, hyperpolarisation is transferred from *para*-hydrogen to a polarisation transfer agent that binds to the iridium centre, commonly amines, and then to another substrate through exchange of labile hydrogens.<sup>79</sup> This new strategy has extended the range of substrates and has been successfully applied to amines (primary and secondary), carboxylic acids and alcohols (primary, secondary and tertiary).<sup>78,79,154</sup>

Experimentally, SABRE studies start by the activation of the polarisation transfer catalyst precursor  $[\text{Ir}(\text{IMes})(\text{COD})\text{Cl}]$  (where COD: 1,5-cyclooctadiene) by adding substrate and *p*-H<sub>2</sub>. This process involves the oxidative addition of *p*-H<sub>2</sub> to the iridium centre and the full hydrogenation of COD resulting in its dissociation and substitution by substrate

units.<sup>26,135,155</sup> Once the pre-catalyst is activated, SABRE experiments can be conducted by adding  $p\text{-H}_2$  to the headspace of the sample and shaking said sample under a weak magnetic field (nT to mT). Sample shaking facilitates the dissolution of  $p\text{-H}_2$  into the solution, whilst applying a weak magnetic field, known as polarisation transfer field, creates the conditions for polarisation transfer to occur.<sup>26</sup>

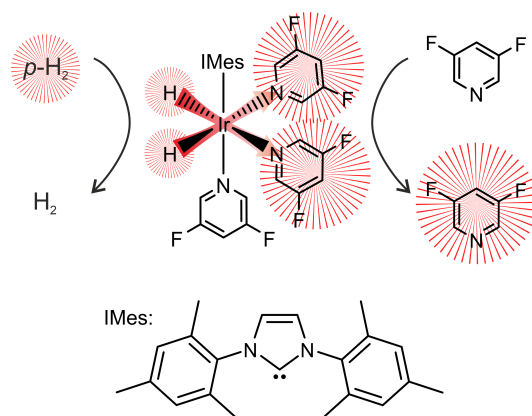


Figure 2.9: Schematic representation of the SABRE hyperpolarisation process. *Para*-hydrogen and the substrate, here 3,5-difluoropyridine, reversibly bind to the iridium centre of the polarisation transfer catalyst, enabling polarisation transfer to the substrate. The hyperpolarised substrate (in red) then dissociates from the complex and is replaced by non-hyperpolarised substrate from the available pool in the solvent.

Spontaneous polarisation transfer from hydrides to nuclei in the target substrate is mediated by the strong coupling conditions created upon application of a weak magnetic field. This is most easily understood by following the level anti-crossing (LAC) model proposed by Ivanov and co-workers.<sup>156</sup> According to this model, in a level anti-crossing the intersection of the energy levels of two spin states is avoided due to their strong coupling, which results in the mixing of such states.

To illustrate this theory, the simplest SABRE three-spin system  $AA'B$  will be considered, where  $AA'$  correspond to the magnetically inequivalent hydrides, and  $B$  a nucleus in the target molecule (Figure 2.10). The hydrides in this system are chemically equivalent ( $\nu_A = \nu_{A'}$ ) but magnetically inequivalent as they exhibit scalar couplings of different

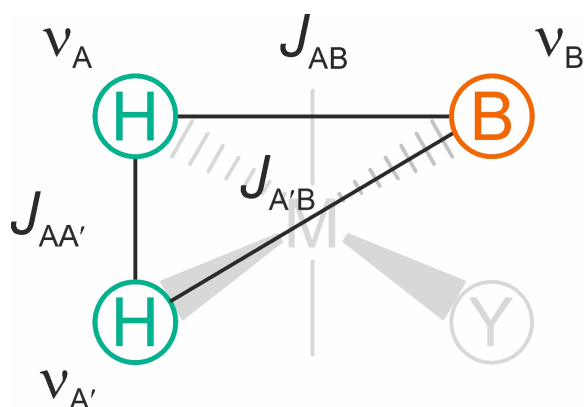


Figure 2.10: Schematic representation of a SABRE three-spin AA'B system. A and A', in green, represent a pair of chemically equivalent ( $\nu_A = \nu_{A'}$ ) and magnetically inequivalent hydrides, with different scalar couplings to B ( $J_{AB} \neq J_{A'B}$ ), a nucleus in the target molecule with Larmor frequency,  $\nu_B$ .

magnitudes to B ( $J_{AB} \neq J_{A'B}$ ). The energy states of this system may be described as a combination of the singlet-triplet basis used to describe *p*-H<sub>2</sub> ( $|S_0\rangle, |T_{+1}\rangle, |T_0\rangle, |T_{-1}\rangle$ ) and  $|\alpha\rangle$  and  $|\beta\rangle$  for spin B. For hyperpolarisation to take place, one of the mixing states must include the singlet state of *p*-H<sub>2</sub>, for example, when  $|S_0\alpha\rangle$  and  $|T_{+1}\beta\rangle$  are mixed. As proposed in the LAC theory and illustrated in Figure 2.11a, the energy levels for  $|S_0\alpha\rangle$  and  $|T_{+1}\beta\rangle$  intersect in the absence of a strong coupling between hydrides and target B ( $J_{AB} = J_{A'B} = 0$ ). In contrast, when there is a strong coupling between hydrides and B, the crossing is avoided and  $|S_0\alpha\rangle$  and  $|T_{+1}\beta\rangle$  mix (Figure 2.11b). As a result, the  $|\beta\rangle$  state of the target nuclei B is overpopulated, leading to hyperpolarised signals.

The mixing of these states occurs at a specific magnetic field, the polarisation transfer field, at which the LAC conditions are met. A LAC takes place when strong coupling conditions are created by matching the difference in resonating frequency between hydrides and B ( $\Delta\nu_{AB}$ ) with the effective scalar coupling of the system ( $J_{eff}$ ).<sup>157</sup> The effective scalar coupling is a combination of the *J* couplings of the system and may be estimated as the largest scalar coupling,<sup>77</sup> which is typically the scalar coupling between hydrides,  $J_{AA'}$  (Equation 2.20). Whilst resonating frequencies vary with the applied magnetic field, scalar

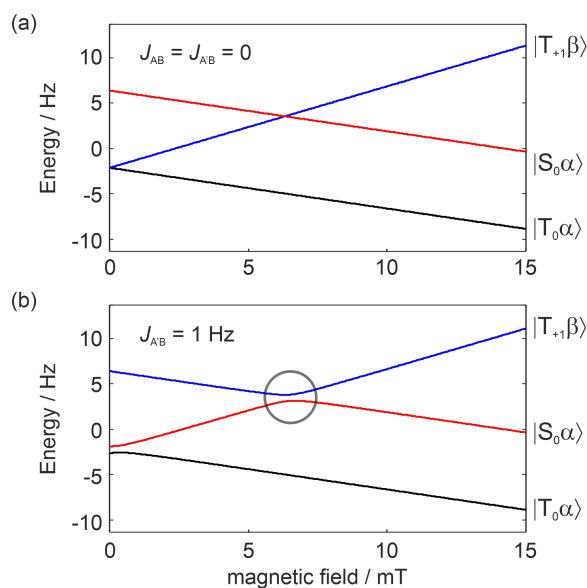


Figure 2.11: Energy levels for three possible states in an AA'B spin system as a function of magnetic field with representing level crossing (a,  $J_{AB} = J_{A'B} = 0$ ) and level anti-crossing conditions (b,  $J_{A'B} = 1$  Hz,  $J_{AB} = 0$ ). The subset of states depicted here can undergo mixing at their corresponding LAC conditions, an example of which is shown as a circle in b. Reproduced under a CC-BY license from Ref. [80].

couplings remain unchanged. This makes it possible to match the frequency difference between hydrides and target nuclei with the effective scalar coupling by applying a selected magnetic field,  $B_{PTF}$ .

$$\Delta\nu_{AB} = J_{\text{eff}} \approx J_{AA'} \quad (2.20)$$

For  $^1\text{H}$  experiments,  $B_{PTF}$  may be calculated by converting the frequency difference into a chemical shift difference,  $\Delta\delta$ , as shown in Equation 2.21. In a typical SABRE system using the pre-catalyst  $[\text{IrCl}(\text{COD})(\text{IMes})]$  and pyridine as a substrate, the optimum polarisation transfer field according to Equation 2.21 is  $\sim 6.5$  mT. In contrast, polarisation transfer to heteronuclei (Equation 2.22) typically requires lower magnetic fields (nT to  $\mu\text{T}$ ) as the difference in resonating frequencies between hydrides and the target heteronuclei is considerably larger, stemming from the difference in gyromagnetic ratios between  $^1\text{H}$  ( $\gamma_{^1\text{H}}$ )

and the heteronucleus, X ( $\gamma_X$ ).

$$B_{\text{PTF}} = 2\pi \frac{J_{AA'}}{\gamma_{^1\text{H}} \Delta\delta} \quad (2.21)$$

$$B_{\text{PTF}} = 2\pi \frac{J_{AA'}}{\gamma_{^1\text{H}}(1 - \delta_{^1\text{H}}) - \gamma_X(1 - \delta_X)} \quad (2.22)$$

One of the key factors controlling SABRE efficiency is thought to be the residence time of the target molecule on the iridium complex.<sup>158</sup> It is desirable to strike a balance between sufficient residence time for polarisation build-up and minimising relaxation while the molecule remains bound.<sup>159,160</sup> This is directly influenced by both *p*-H<sub>2</sub> and substrates exchange rates.<sup>76,158</sup> In fact, an optimal substrate dissociation rate of  $\sim 4.5 \text{ s}^{-1}$  has been theoretically proposed,<sup>159</sup> and experimentally verified,<sup>158</sup> for efficient <sup>1</sup>H hyperpolarisation. The dissociation rate of substrates may be modified by changing the NHC and/or the temperature of the experiment,<sup>76,158,159,161,162</sup> as well as by using an auxiliary co-substrate. Steric hinderance has also been shown to have an impact on substrate dissociation rates,<sup>163</sup> which in extreme cases might hinder hyperpolarisation altogether as stable complexes may not form.<sup>139</sup> Some strategies reported to achieve hyperpolarisation in sterically demanding substrates include the use of bidentate ligands such as [Ir(COD)(Phox)]PF<sub>6</sub> (where Phox: 2-(2-(diphenylphosphanyl)phenyl)-4,5-dihydrooxazole),<sup>164</sup> using asymmetric NHC ligands,<sup>165</sup> and co-substrates<sup>142,163,166</sup>.

The higher sensitivity afforded by SABRE has been exploited in biomedical applications, such as biochemical analysis in biological fluids,<sup>167–169</sup> protein-ligand binding studies,<sup>170</sup> and preclinical metabolic imaging,<sup>171,172</sup> as well as in reaction monitoring<sup>145,173</sup> and low concentration analysis of complex mixtures.<sup>133,174</sup> The signal enhancement capabilities of SABRE have also been exploited in benchtop NMR analysis to overcome the reduced sensitivity produced by lower-field spectrometers. SABRE-hyperpolarised <sup>1</sup>H, <sup>13</sup>C, <sup>13</sup>C{<sup>1</sup>H}, and <sup>19</sup>F spectra have been acquired in a single-shot in benchtop NMR spectrometers.<sup>83,86,175–178</sup>

For example, Richardson *et al.* reported 17000-fold <sup>1</sup>H signal enhancements in a single-shot experiment at 1 T, resulting in signal-to-noise ratio (SNR) values that would otherwise require acquisition times of several hours, higher concentrations or isotopically labelling

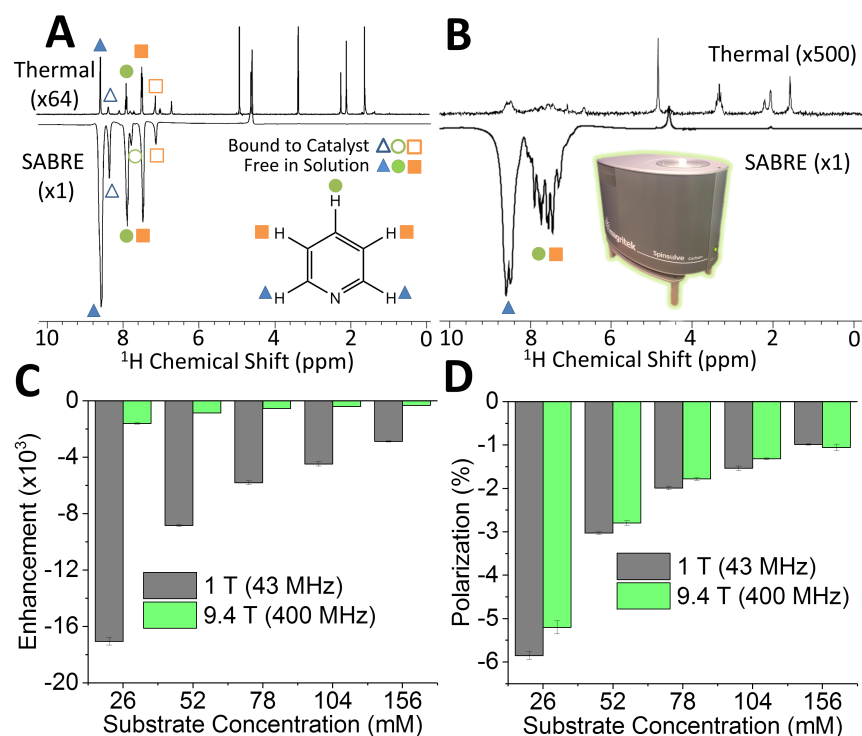


Figure 2.12: Comparison of non-hyperpolarised (top) and SABRE-hyperpolarised (bottom)  $^1\text{H}$  NMR spectra of pyridine at (a) 9.4 T and (b) 1 T, with unlabelled signals corresponding to the solvent and the iridium complex. Enhancement factors (c) and polarisation levels (d) for experiments at both magnetic fields are plotted against substrate concentration. Samples were prepared in methanol- $d_4$  using 5 mM of  $[\text{IrCl}(\text{COD})(\text{IMes})]$ . Reproduced under a CC-BY licence from Ref. [83].

in thermally polarised samples.<sup>83</sup> This study also revealed that the efficacy of SABRE hyperpolarisation is field independent, yielding comparable polarisation values at 1 T and 9.4 T (Figure 2.12).

Added to the previously mentioned benefits of benchtop NMR spectrometers, SABRE measurements in low-field NMR often show longer hyperpolarised lifetimes.<sup>175</sup> Moreover, they allow for the use of protonated solvents as these usually exhibit low signals, thus rendering the use of costly deuterated solvents and time consuming sample preparation steps unnecessary.<sup>83</sup> Automated flow systems that regenerate hyperpolarisation and ultra-

fast single-shot experiments have also enabled the acquisition of 2D NMR spectra.<sup>83,86,133</sup>  
The combination of SABRE hyperpolarisation and benchtop NMR, and in particular its potential for analytical applications, will be the focus of this thesis.

## Chapter 3

# Experimental

### 3.1 Sample Preparation

#### 3.1.1 Preparation of Standard SABRE Samples

Standard SABRE samples were prepared by adding the substrate to make up the desired concentration and 2.24 mg of pre-catalyst [IrCl(COD)(IMes)] (where COD: *cis,cis*-1,5-cyclooctadiene and IMes: 1,3-bis(2,4,6-trimethyl-phenyl)imidazole-2-ylidene in 0.7 mL of either HPLC-grade methanol (Fisher Scientific) or methanol- $d_4$  ( $\geq 99.8$  % D, Merck). The pre-catalyst ([IrCl(COD)(IMes)]) was synthesised by Dr Victoria Annis following published procedures.<sup>76,179</sup> The substrates were sourced from Fluorochem (3,5-difluoropyridine, 3-(difluoromethyl)pyridine, 3,4,5-trifluoropyridine, difluoroacetic acid, lithium difluoroacetate, and 1-methyl-1,2,3-triazole), Fisher Scientific (trifluoroacetic acid, 4-methylpyridine, and dimethylsulfoxide AR), Aldrich (pyridine), or Avantor (sodium trifluoroacetate) and used without further modification. The samples thus prepared were then sonicated to aid dissolution of the pre-catalyst and solid substrates, if any, and then introduced into a 5 mm NMR tube with a J-Young valve using a syringe. Following this, the samples were de-gassed using a three-stage freeze/pump/thaw method using a Schlenk line and an acetone and dry-ice bath. The de-gassing step was included to improve the dissolution of  $p$ -H<sub>2</sub> and to remove dissolved oxygen.

### 3.1.2 Preparation of SABRE Samples Using Air-Sensitive Substrates

Samples containing air-sensitive substrates such as 2,4,6-trifluorobenzylamine were prepared and transferred into a 5 mm NMR tube fitted with a J-Young valve inside a glovebox. To do so, the pre-catalyst was weighed (2.24 mg) into a glass vial and introduced into the glovebox after three cycles of vacuum/ $\text{N}_2$ . The substrates were sourced from Fluorochem (2,4,6-trifluorobenzylamine) and Merck (anhydrous dimethylsulfoxide,  $\geq 99.9\%$ ). The solvents and substrates were introduced into the glovebox following the same procedure either sealed (methanol- $d_4 \geq 99.8\%$  D, Merck, substrate and co-substrate) or after de-gassing and drying (methanol and methanol- $d_1$ ) using a Schlenk line and a 3 Å molecular sieve (Merck). As these samples were prepared inside the glovebox, the de-gassing step was not required.

## 3.2 Shake-and-Drop Hyperpolarisation Experiments

In shake-and-drop experiments, the headspace of the NMR tube containing the SABRE sample was filled with 4 bar of  $p\text{-H}_2$ , which was generated with a helium-cooled system operating at 28 K to produce *ca.* 98 %  $p\text{-H}_2$  enrichment, as described previously.<sup>180</sup> The tube was then shaken for 10 s at the desired polarisation transfer field (PTF), and then introduced into the spectrometer for FID acquisition. Typical sample transfer times were *ca.* 2 s. The target PTF was achieved either by shaking the sample inside a hand-held magnetic array with an average field of 6.2 mT,<sup>75</sup> in the ambient Earth's magnetic field adjacent to the spectrometer (PTF  $\sim 50\ \mu\text{T}$ ), or inside a  $\mu$ -metal shield that reduces the ambient field by a factor of  $\sim 300$ -fold to achieve a PTF  $\sim 0.2\ \mu\text{T}$ . Between shake-and-drop repetitions, the  $p\text{-H}_2$  in the sample was refreshed by evacuating the headspace of the NMR tube and re-filling with fresh  $p\text{-H}_2$ . Samples were analysed in triplicate, from which corresponding mean and standard deviation values were calculated according to Section 3.7.3. The manual nature of shake-and-drop experiments results in typical variations of 5% when using a hand-held magnet, or 10% when using the ambient magnetic field.<sup>75</sup> As this step is believed to be the largest source of measurement variability, the standard deviation obtained

from replicate measurements is considered to be a good estimator of standard measurement uncertainty. Once hyperpolarised experiments were concluded, a non-hyperpolarised spectrum was collected as a reference for enhancement factor calculations (Section 3.7.2) using the same spectrometer parameters but averaging enough scans to detect the target signal. When low sensitivity precluded the acquisition of non-hyperpolarised spectra with detectable signals in a reasonable amount of time, these reference values were estimated *via* extrapolation from a calibration curve, as described in Section 3.7.2.

In order to obtain SABRE hyperpolarised spectra, the pre-catalyst was activated by performing a set of preliminary shake-and-drop experiments. The activation of the pre-catalyst consists of the oxidative addition of *p*-H<sub>2</sub> to the iridium centre and the full hydrogenation of cyclooctadiene (COD) resulting in its dissociation and substitution by substrate units. The activation of the SABRE pre-catalyst was conducted and monitored by repeating shake-and-drop experiments until the intermediate products were no longer detected and the intensity of hyperpolarised signals was consistent, which typically required 4 to 6 repetitions.

### 3.3 NMR Data Acquisition in Benchtop NMR

#### 3.3.1 Instrumental Setup

Low-field NMR spectra were acquired using a Spinsolve 43 Carbon spectrometer (Magritek) operating at 1 T or a Spinsolve 60 Multi-X Ultra spectrometer (Magritek) operating at 1.4 T, both equipped with <sup>1</sup>H/<sup>19</sup>F and <sup>13</sup>C channels. Locking, shimming and frequency calibrations were performed on a reference sample containing a H<sub>2</sub>O:D<sub>2</sub>O mixture (10%:90%) before data was collected. All experiments were conducted at 301.5 K. Data was acquired using the Spinsolve Expert software (V 1.41) and processed either by Prospa (V 3.63), MestReNova (V 14.1.2.25024), or Matlab (V R2020a).

### 3.3.2 Pulse-and-Collect Acquisition

$^1\text{H}$ ,  $^{19}\text{F}$ , and  $^{19}\text{F}\{^1\text{H}\}$  experiments utilised full power  $90^\circ$  and  $180^\circ$  pulses of  $9.35\ \mu\text{s}$  and  $24.2\ \mu\text{s}$  respectively for  $^1\text{H}$  measurements and  $100\ \mu\text{s}$  and  $225\ \mu\text{s}$  for  $^{19}\text{F}$  measurements in the Spinsolve 43 Carbon spectrometer. For  $^1\text{H}$  and  $^{19}\text{F}$  experiments at a 1.4 T field, full power  $90^\circ$  pulses of  $13.9\ \mu\text{s}$  and  $119\ \mu\text{s}$  were used, respectively.  $^{13}\text{C}\{^1\text{H}\}$  experiments were preceded by a WALTZ-16<sup>181</sup> NOE enhancement step, followed by a  $45^\circ$   $^{13}\text{C}$  pulse and WALTZ-16<sup>181</sup> proton-decoupled acquisition, using a -5.4 dB power level for  $30\ \mu\text{s}$  for the  $45^\circ$   $^{13}\text{C}$  pulse and -16.4 dB for  $120\ \mu\text{s}$ , or multiples of that length, for the  $90^\circ$ ,  $180^\circ$ ,  $270^\circ$ , and  $360^\circ$   $^1\text{H}$  pulses for the NOE enhancing and decoupling steps.

### 3.3.3 SHARPER and *sel*SHARPER Acquisition

Unless otherwise stated in the text, SHARPER (Section 4.9, Chapter 4) and *sel*SHARPER (either fully selective or the hard-pulse train (HPT) version, Section 4.15, Chapter 4) were acquired in two scans for background correction using a chunk time of  $\tau = 3.2\ \text{ms}$  within each echo loop and a  $180^\circ$  pulse duration of  $225\ \mu\text{s}$ . In *sel*SHARPER experiments, a 5 ms  $180^\circ$  Gaussian pulse generated with 1000 steps and 1 % truncation was used as the selective pulse. This Gaussian pulse required the implementation of a correction for non-linearity issues in the r.f. amplitude, which was developed by Dr Matheus Rossetto and described in the literature.<sup>178</sup> Rectangular pulsed field gradients were generated by shifting the shim values along x, y, and z to their maximum value for  $250\ \mu\text{s}$ , and then reverting them to the original values.

## 3.4 NMR Data Post-acquisition Processing

FID data acquired for pulse-and-collect experiments were apodised using an exponential decay filter, zero-filled, and Fourier transformed to produce the spectrum, which was manually phased and baseline corrected as needed. For non-SHARPER experiments, the apodisation filter was chosen so as to optimise SNR without compromising spectral resolution. Apodisation filters for SHARPER experiments were chosen to match the effective relaxation during

the experiment, estimated as described in Section 3.4.1.  $^1\text{H}$  spectra were referenced to the solvent signals (methanol or methanol- $d_4$ ).

### 3.4.1 Matched Filters

The time decay constant ( $T_f$ ) used in matched exponential filters  $\exp(-\frac{t}{T_f})$  was determined from the effective relaxation times during SHARPER experiments, estimated using the ‘t2fit’ function in Prospa (V 3.63).

## 3.5 Analysis of Reference Methanol Samples for SABRE-Relay Studies

In order to gauge hyperpolarisation levels for the hydroxyl group in methanol- $d_4$  through SABRE-Relay effects, it was necessary to establish a baseline of what the typical signal would be in the absence of hyperpolarisation. The shake-and-drop procedure was thought to have an impact on this signal, particularly as a consequence of degassing and the limited time the sample is allowed to build-up magnetisation inside the probe. Therefore, a sample containing only methanol- $d_4$  was analysed following the standard shake-and-drop procedure (*i.e.* degassing,  $p\text{-H}_2$  addition, shaking and dropping into the spectrometer), and the typical area for the -OH signal was estimated by averaging triplicate measurements.

## 3.6 Hyperpolarised $T_1$ Experiments

$T_1$  values for hyperpolarised signals were acquired in triplicate following shake-and-drop experiments using a variable flip angle approach, as reported before.<sup>182</sup> During each experiment, 15 FID spectra were acquired, using repetition time values ranging from 1.5 s to 5 s according to the lifetime of the signal under investigation. Each FID was zero-filled to 256 k points and exponentially apodised with a 1000 ms time filter prior Fourier transformation. Spectra were then manually phased and integrated to produce a signal decay plot *versus* time. Parameters corresponding to the exponential decay rate were obtained using the

‘expfit’ macro in Prospa (V 3.63). Anti-phase signals were processed according to Section 3.7.4.  $T_1$  mean values and their combined uncertainty were calculated according to Section 3.7.3.

## 3.7 Data Analysis and Calculations

### 3.7.1 Signal-to-Noise Ratio and Noise Standard Deviation Calculations

Signal-to-noise ratio (SNR) values were calculated as the ratio of the signal height of the tallest peak ( $H$ ) and twice the standard deviation of the noise ( $s_{noise}$ ), as shown in Equation 3.1. The standard deviation of the noise was calculated on a spectral region without signals according to Equation 3.2 where  $x_i$  is the height of each of the  $N$  points in this region and  $\bar{x}$ , their average.

$$SNR = \frac{H}{2 \times s_{noise}} \quad (3.1)$$

$$s_{noise} = \sqrt{\frac{\sum(x_i - \bar{x})^2}{N}} \quad (3.2)$$

When reference spectra were obtained by averaging more than one scan, the inverse of the square root of the number of scans was used as the correction factor to obtain a signal-to-noise ratio per one scan (Equation 3.3).

$$SNR_{ss} = \frac{SNR}{\sqrt{NS}} \quad (3.3)$$

### 3.7.2 SABRE ( $\varepsilon_{1H}$ , $\varepsilon_{19F}$ ) and SNR ( $\varepsilon_{SNR}$ ) Enhancement Factor Calculations

Enhancement factors for SABRE hyperpolarised experiments were calculated as the ratio of the area of the hyperpolarised signal and the area of the thermal signal at the same concentration, acquired under the same conditions.

$$\varepsilon_{1H/19F} = \frac{Area_{hyp, 1H/19F}}{Area_{thermal, 1H/19F}} \quad (3.4)$$

For SABRE samples with substrate concentrations below the non-hyperpolarised detection limit (*ca.* 10 mM), non-hyperpolarised signal areas were estimated extrapolating from a 3,5-difluoropyridine non-hyperpolarised calibration curve covering a 10 to 100 mM range, which was acquired with the same receiver gain value as hyperpolarised experiments.  $\varepsilon_{1\text{H}}$  and  $\varepsilon_{19\text{F}}$  calculations were done by adding the area values for all the signals in the substrate molecule, *e.g.* *ortho* and *para*  $^1\text{H}$  NMR signals in 3,5-difluoropyridine. This was done for the sake of consistency, as it reflects the effect of SHARPER, and the same approach was taken in limit of detection and quantification studies. When hyperpolarised signals exhibited an anti-phase profile, the overall peak integral was calculated as a the sum of the absolute values of the positive and negative portions of the peak.

Similarly, SNR enhancement factors  $\varepsilon_{\text{SNR}}$  were calculated according to Equation 3.5, using the SNR value of non-hyperpolarised (thermal) spectra as reference.

$$\varepsilon_{\text{SNR}} = \frac{\text{SNR}_{\text{hyp}}}{\text{SNR}_{\text{thermal}}} \quad (3.5)$$

### 3.7.3 Mean, Standard Deviation of the Mean, and Uncertainty of the Mean Calculations

When  $n$  replicates of a measurement were made, the mean ( $\bar{x}$ ) of these results ( $x_i$ , with  $i = 1, 2, \dots, n$ ) was determined according to Equation 3.6. The standard deviation of the mean ( $s_{\text{mean}}$ ) is calculated according to Equation 3.7.<sup>183</sup>

$$\bar{x} = \frac{x_1 + x_2 + \dots + x_n}{n} \quad (3.6)$$

$$s_{\text{mean}} = \frac{1}{\sqrt{n}} \times \sqrt{\frac{\sum (x_i - \bar{x})^2}{(n - 1)}} \quad (3.7)$$

The combined standard uncertainty of a measurement ( $u_c(y)$ ) is typically calculated as as the square root of the sum of the squares of the sensitivity coefficient ( $c_i$ ) and the standard uncertainties ( $u_i$ ), according to Equation 3.8.<sup>184</sup> For a value estimated through a mean value, the combined standard uncertainty ( $u_{\bar{x}}$ ) was calculated as Equation 3.9. When the largest contribution to uncertainty of the individual measurements ( $x_i$ ) was their repeatability, the standard uncertainty for each  $u_{x_1}$  was estimated as  $s_{\text{mean}}$ .

$$u_c(y) = \sqrt{\sum_{i=1,n} c_i^2 u_i^2} \quad (3.8)$$

$$u_{\bar{x}} = \sqrt{\frac{1^2}{n} u_{x_1}^2 + \frac{1^2}{n} u_{x_2}^2 + \dots + \frac{1^2}{n} u_{x_n}^2 + \frac{range}{2\sqrt{6}}} \quad (3.9)$$

$$range = max(x_i) - min(x_i) \quad (3.10)$$

The expanded uncertainty ( $U$ ) was determined by multiplying the combined uncertainty by a coverage factor  $k=2$ , which gives a level of confidence of approximately 95%, according to Equation 3.11.<sup>184</sup>

$$U = k \times u_c(y) \quad (3.11)$$

### 3.7.4 Analysis of Anti-phase Signals in Hyperpolarised $T_1$ Experiments

Hyperpolarised  $T_1$  experiments for 3,5-difluoropyridine samples resulted in a combination of anti-phase and in-phase doublet signals (Figure 3.1 I and II, respectively) exhibiting different relaxation constants. To isolate the in-phase and anti-phase contributions to the detected signal, represented by Figure 3.III, and obtain  $T_1$  values for each one, Equations 3.12 and 3.13, where A and B correspond to each half of the doublet and are assumed to have area values which are equal in II, but opposite in sign in I.

$$A_I = -B_I = \frac{A_{III} - B_{III}}{2} \quad (3.12)$$

$$A_{II} = B_{II} = \frac{A_{III} + B_{III}}{2} \quad (3.13)$$

The resulting area values were plotted against time, where time values were given by the repetition time between scans, and an exponential fit obtained for the anti-phase (I) and in-phase (II) components of the signal.

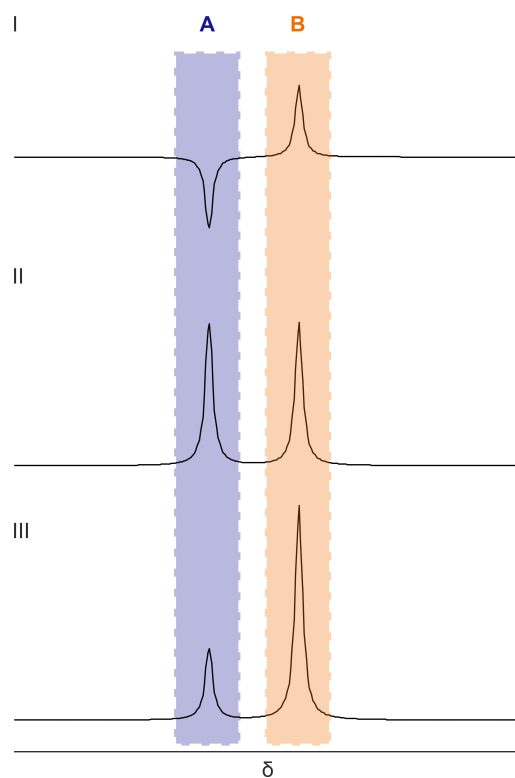


Figure 3.1: Schematic representation of NMR spectra exhibiting and anti-phase doublet (I), an in-phase doublet (II), and their sum (III). Each half of the doublet has been marked as A or B to facilitate analysis.

### 3.7.5 Limit of Detection and Quantification Estimation using a Single Sample

Limit of detection and quantification values were determined according to Equations 3.14 and 3.15, respectively<sup>185–187</sup> using a sample whose concentration ( $C$ ) exhibits a signal-to-noise ratio ( $SNR$ ) that closely matches that of the expected LOD concentration.<sup>183</sup>

$$LOD = 3 \times \frac{C}{SNR} \quad (3.14)$$

$$LOQ = 10 \times \frac{C}{SNR} \quad (3.15)$$

When the LOD value of a non-hyperpolarised sample was obtained through signal averaging of several scans ( $NS$ ), the LOD on a single-scan basis ( $LOD_{ss}$ ) was calculated

using a scan-corrected SNR ( $SNR_{ss}$ ) according to Equations 3.16 and 3.3 (Section 3.7.1) to facilitate the direct comparison with hyperpolarised single-scan experiments.

$$LOD_{ss} = 3 \times \frac{C}{SNR_{ss}} \quad (3.16)$$

### 3.7.6 Limit of Detection and Quantification Calculation using a Set of Samples

When large variability in SNR values led to unreliable estimations of LOD and LOQ values, as was the case for 2,4,6-trifluorobenzylamine samples (Chapter 6), a set of samples with concentration values within the sub-stoichiometric regime were tested and LOD/LOQ estimations were performed on each of them, as described in Section 3.7.5. The overall LOD/LOQ values were estimated as the mean value of these results, following Section 3.7.3.

### 3.7.7 Regression Analysis

Regression statistics (OLS) for calibration curves, including regression coefficients and their standard error were calculated using the Data Analysis package in Microsoft Excel 2019. Residual plots showing the difference between experimental signal areas and signal areas predicted by the linear model were also obtained using this package.

### 3.7.8 Accuracy Assessment

To assess the quantification accuracy, recovery factors ( $R$ ) and relative standard deviations ( $RSD$ ) expressed as percentages were calculated.<sup>188</sup> To estimate the measurement bias, a test sample whose reference concentration was established through gravimetric preparation ( $C_{grav}$ ) was quantified through external calibration (calibration curve,  $C$ ). The recovery value was then calculated according to Equation 3.17 for each result and an average and standard deviation of the recovery were estimated according to Section 3.7.3. To assess the precision under repeatability conditions for said quantification, the  $RSD$  was calculated according to Equation 3.18 using the standard deviation of the mean value of the triplicate

measurements ( $s_{mean,C}$ , Equation 3.7) and the mean value of the predicted concentrations ( $\bar{C}$ , Equation 3.6).

$$R(\%) = \frac{C}{C_{grav}} \times 100 \quad (3.17)$$

$$RSD(\%) = \frac{s_{mean,C}}{\bar{C}} \times 100 \quad (3.18)$$

## 3.8 Characterisation of SABRE Active Complexes using High-field NMR Spectroscopy

### 3.8.1 Characterisation of the Main SABRE Active Species in Samples with 3,5-Difluoropyridine and Dimethylsulfoxide

The characterisation of the main SABRE active species in the sub-stoichiometric regime for samples containing 3,5-difluoropyridine and dimethylsulfoxide was carried out at 263 K in a 7 T NMR spectrometer (300 MHz Fourier Bruker Avance III console, BBO probe). The sample used for characterisation studies contained 20 mM of 3,5-difluoropyridine, 50 mM of dimethylsulfoxide, and 10 mM of [IrCl(COD)(IMes)] in methanol- $d_4$ . This concentration was chosen as it is close to the upper boundary of the sub-stoichiometric regime. All concentrations were doubled relative to typical concentrations to increase the SNR of the measurements. The characterisation experiments comprised  $^1\text{H}$  and  $^{19}\text{F}$  pre- and post-activation pulse-and-collect experiments, as well as,  $^1\text{H}$ - $^1\text{H}$  COSY,  $^1\text{H}$ - $^1\text{H}$  NOESY,  $^1\text{H}$ - $^1\text{H}$  TOCSY and  $^1\text{H}$ - $^{13}\text{C}$  HSQC experiments. Experiments were generally conducted using standard acquisition parameters from Bruker, with specific parameters shown in Table 3.1.

The characterisation of the principal active species containing 3,5-difluoropyridine and dimethylsulfoxide was achieved through a series of low-temperature multinuclear NMR experiments. As an initial step, the hydride ligand region of the 1D  $^1\text{H}$  NMR spectrum was examined to assess the diversity and relative abundance of hydride-containing complexes present in the sample. Figure 3.3 displays two prominent pairs of hydride ligand signals:

Table 3.1: Experimental parameters for NMR experiments used in the characterisation of the sample containing 3,5-difluoropyridine and dimethylsulfoxide.

| Experiment   | Parameters  | F1   | F2  |
|--|---|--|---|
| $^1\text{H}$<br>pulse-and-collect                                      | pulse programme:<br>zg                                    | Nuclei: $^1\text{H}$ , spectral<br>width: 50 ppm,<br>transmitter freq. offset:<br>-10 ppm, acq. time: 8.7 s      | -   |
| $^1\text{H}$ - $^1\text{H}$ 2D COSY                                    | pulse programme:<br>cosygpppqf                            | Nuclei: $^1\text{H}$ , spectral<br>width: 10 ppm,<br>transmitter- freq. offset:<br>5 ppm, acq. time: 0.34 s      | Nuclei: $^1\text{H}$ , spectral<br>width: 10 ppm,<br>transmitter freq. offset:<br>5 ppm, acq. time: 0.17 s                  |
| $^1\text{H}$ - $^{13}\text{C}$ 2D HSQC<br>aliphatic/aromatic<br>region | pulse programme:<br>hsqcetgpsi2,<br>coupling: 145 Hz      | Nuclei: $^1\text{H}$ , spectral<br>width: 4/4 ppm,<br>transmitter freq. offset:<br>2/8 ppm, acq. time:<br>0.25 s | Nuclei: $^{13}\text{C}$ , spectral<br>width: 100/100 ppm,<br>transmitter freq. offset:<br>50/150 ppm, acq. time:<br>0.034 s |
| $^1\text{H}$ - $^1\text{H}$ 2D<br>TOCSY                                | pulse programme:<br>mlevphpp                              | Nuclei: $^1\text{H}$ , spectral<br>width: 50 ppm,<br>transmitter freq. offset:<br>-10 ppm, acq. time: 0.55<br>s  | Nuclei: $^1\text{H}$ , spectral<br>width: 50 ppm,<br>transmitter freq. offset:<br>-10 ppm, acq. time: 0.55<br>s             |
| $^1\text{H}$ - $^1\text{H}$ 2D<br>NOESY                                | pulse programme:<br>noesygpphpp,<br>mixing time: 0.3<br>s | Nuclei: $^1\text{H}$ , spectral<br>width: 10 ppm,<br>transmitter freq. offset:<br>5 ppm, acq. time: 0.34 s       | Nuclei: $^1\text{H}$ , spectral<br>width: 10 ppm,<br>transmitter freq. offset:<br>5 ppm, acq. time: 0.17 s                  |

Table 3.2: High-field NMR characterisation of the SABRE active complex containing 3,5-difluoropyridine and dimethylsulfoxide. Repeated from Chapter 5 Section 5.3.1 for convenience.

| Resonance number | $\delta$ $^1\text{H}$ | $\delta$ $^{13}\text{C}$ | $\delta$ $^{19}\text{F}$ |
|------------------|-----------------------|--------------------------|--------------------------|
| 1                | -                     | 159.64                   | -                        |
| 2                | -                     | -                        | -                        |
| 3                | 7.16                  | 122.83                   | -                        |
| 4                | -                     | 138.40                   | -                        |
| 5                | -                     | 136.20                   | -                        |
| 6                | a 6.84/ b 6.77        | a 128.25/ b 128.30       | -                        |
| 7                | -                     | 139.25                   | -                        |
| 8                | a 2.14 / b 2.13       | a 18.51/b 19.00          | -                        |
| 9                | 2.26                  | 20.85                    | -                        |
| 10               | -23.3 (d, 7.9 Hz)     | -                        | -                        |
| 11               | -23.7 (d, 7.9 Hz)     | -                        | -                        |
| 12               | -                     | -                        | -                        |
| 13               | 8.55                  | 139.34                   | -                        |
| 14               | -                     | 159.52                   | -                        |
| 15               | 7.63                  | 111.10                   | -                        |
| 16, 17           | 2.72 / 3.10           | 43.14 / 55.84            | -                        |
| 18, 19           | -                     | -                        | -124.96                  |

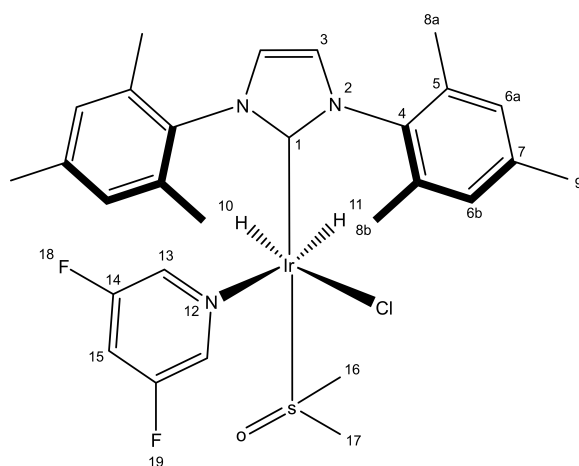


Figure 3.2: Proposed structure for the active SABRE complex containing 3,5-difluoropyridine and dimethylsulfoxide. Repeated from Chapter 5 Section 5.3.1 for convenience.

one set at  $\delta$  -15.5 and -21.5, previously assigned to  $[\text{IrCl}(\text{H})_2(\text{IMes})(\text{DMSO})_2]$  (where DMSO = dimethylsulfoxide), and another set at  $\delta$  -23.3 and -23.7.

The latter pair exhibited hyperpolarisation activity in shake-and-drop experiments conducted at both 1 T and 7 T. A mutual coupling between these hydride resonances was confirmed via  $^1\text{H}$ - $^1\text{H}$  2D TOCSY experiments (Figures 3.5 and 3.4). This observation, together with the agreement of chemical shift values with those reported for analogous species formed with 3,5-dihalogenopyridine ligands,<sup>189</sup> strongly supports the assignment of these hydride signals to the species of interest. In each case, a singlet appearing at a higher chemical shift relative to the corresponding hydride signals was attributed to the HD isotopologue, as discussed in Chapter 4, Section 4.3. This assignment is further corroborated by the presence of a triplet at  $\delta$  4.6 with  $J = 43$  Hz.

A 2D  $^1\text{H}$ - $^1\text{H}$  NOESY experiment was employed to investigate through-space interactions between ligands, with key correlations illustrated in Figure 3.4. This experiment revealed nuclear Overhauser effect (NOE) correlations between the aromatic proton signals of 3,5-difluoropyridine at  $\delta$  8.55 and resonances corresponding to the ortho methyl group of the IMes ligand ( $\delta$  2.14), as well as a methyl group of dimethylsulfoxide ( $\delta$  2.72), as shown in Figure 3.6. The structure of these ligands was confirmed by comparison with previously

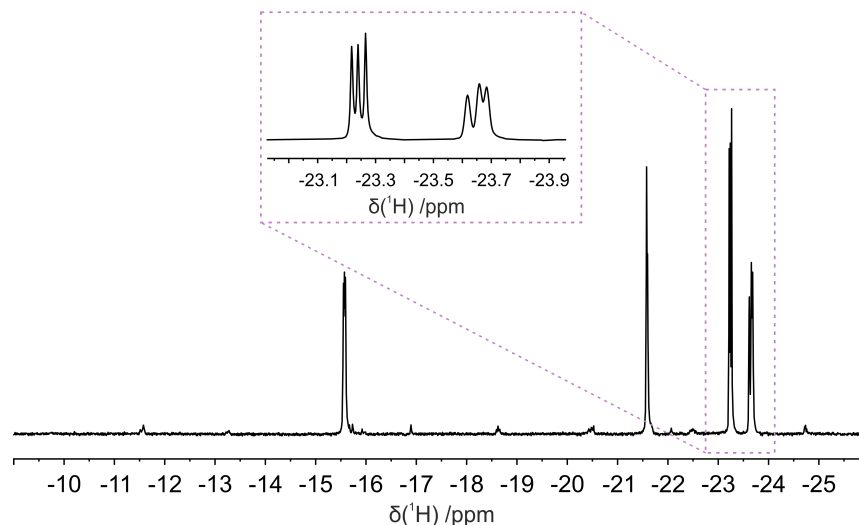


Figure 3.3:  $^1\text{H}$  NMR spectra of the characterisation sample acquired at 7 T (263 K), zoomed in the hydride ligand signal region ( $\delta$  -9 to -26). Signals corresponding to the main active species (Figure 3.2) are highlighted and amplified in the dashed box.

reported chemical shift values,<sup>189</sup> and were further corroborated by  $^1\text{H}$ - $^1\text{H}$  2D COSY and  $^1\text{H}$ - $^{13}\text{C}$  2D HSQC experiments. Taken together, these data support the presence of IMes, 3,5-difluoropyridine, and dimethylsulfoxide as ligands within the species under investigation, in addition to the hydride ligands previously identified and proposed to be responsible for the observed hyperpolarisation of 3,5-difluoropyridine.

No cross-peaks were observed between the signals corresponding to IMes and the methyl groups of dimethylsulfoxide, suggesting that these ligands are positioned *trans* to one another. Furthermore, the absence of any additional NOE correlations involving the hydride ligands, 3,5-difluoropyridine, or dimethylsulfoxide with a fourth, unidentified ligand implies that the ligand *cis* to 3,5-difluoropyridine is chloride. This assignment is further supported by the close similarity between the chemical shift values of the hydride ligand *cis* to 3,5-difluoropyridine and those reported by Tickner *et al.* for analogous complexes.<sup>189</sup>  $^{19}\text{F}$  NMR signals were assigned by comparison with a reference sample of 3,5-difluoropyridine (70 mM in methanol- $d_4$ ).

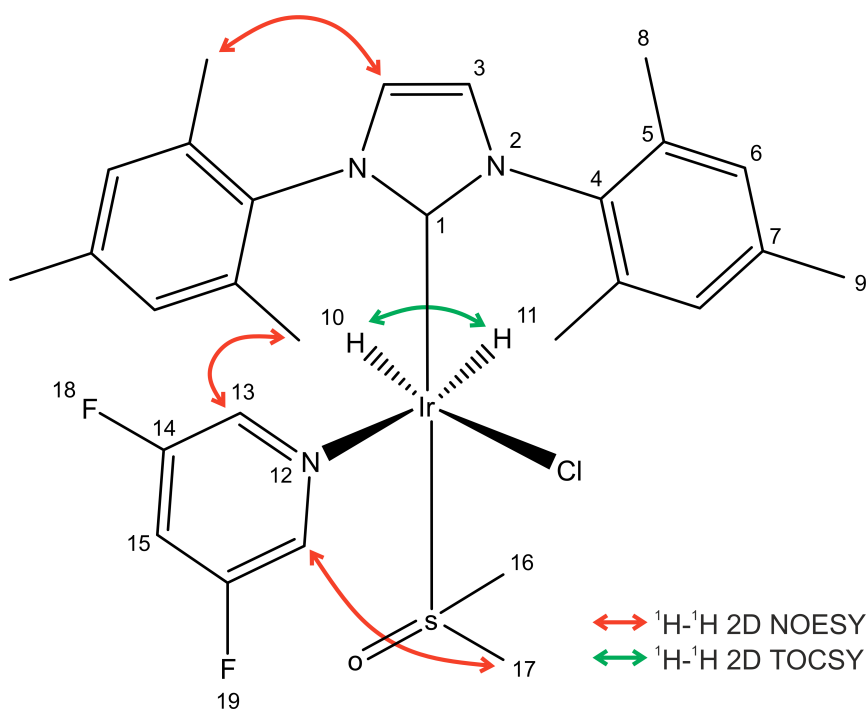


Figure 3.4: Key couplings observed *via*  $^1\text{H}$ - $^1\text{H}$  2D NOESY and  $^1\text{H}$ - $^1\text{H}$  2D TOCSY experiments, revealing the connectivity of the ligands in the main active complex.

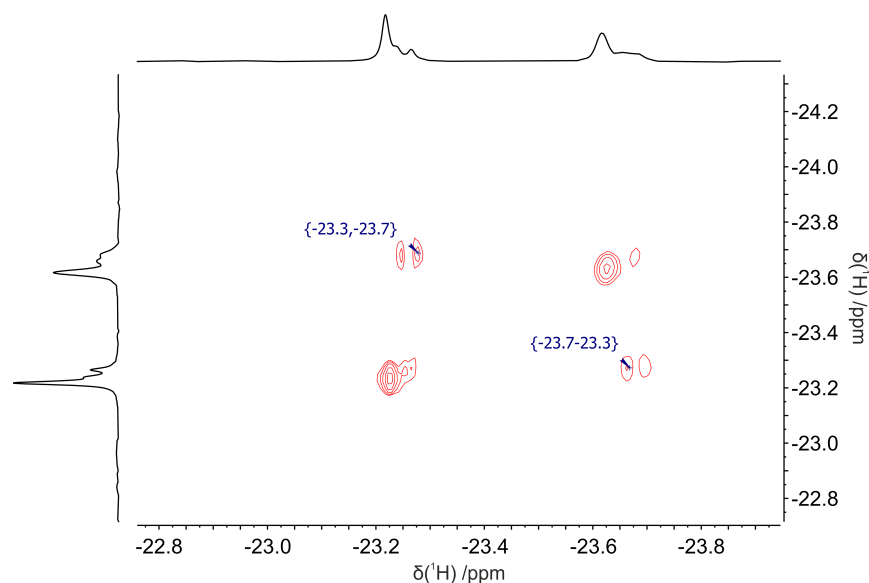


Figure 3.5:  $^1\text{H}$ - $^1\text{H}$  2D NMR TOCSY data collected at 263 K and at a field of 7 T. Data shows scalar couplings between the hydride ligand signals at  $\delta$  - 23.3 and -23.7, confirming they belong to the same complex.

### 3.8.2 Characterisation of the Main SABRE Active Species in Samples with 2,4,6-Trifluorobenzylamine and Dimethylsulfoxide

The characterisation of the main SABRE active species in the sub-stoichiometric regime for samples containing 2,4,6-trifluorobenzylamine and dimethylsulfoxide was carried out at 263 K in a 11.7 T NMR spectrometer (500 MHz Ascend Bruker Avance III HD console, BBI probe) and a 7 T NMR spectrometer (300 MHz Fourier Bruker Avance III console, BBO probe). The sample used for characterisation studies contained 20 mM of 2,4,6-trifluorobenzylamine, 200 mM of dimethylsulfoxide, and 10 mM of  $[\text{IrCl}(\text{COD})(\text{IMes})]$  in methanol- $d_4$ . This concentration was chosen as it is close to the upper boundary of the sub-stoichiometric regime. All concentrations were doubled relative to typical concentrations to increase the SNR of the measurements. The characterisation experiments comprised  $^1\text{H}$  pre- and post-activation pulse-and-collect experiments,  $^1\text{H}$ - $^1\text{H}$  COSY,  $^1\text{H}$ - $^1\text{H}$  NOESY and  $^1\text{H}$ - $^{13}\text{C}$  HMQC experiments conducted at 11.7 T and  $^{19}\text{F}$  pre- and post-activation pulse-and-collect experiments conducted at 7 T to assign fluorine resonances. Experiments

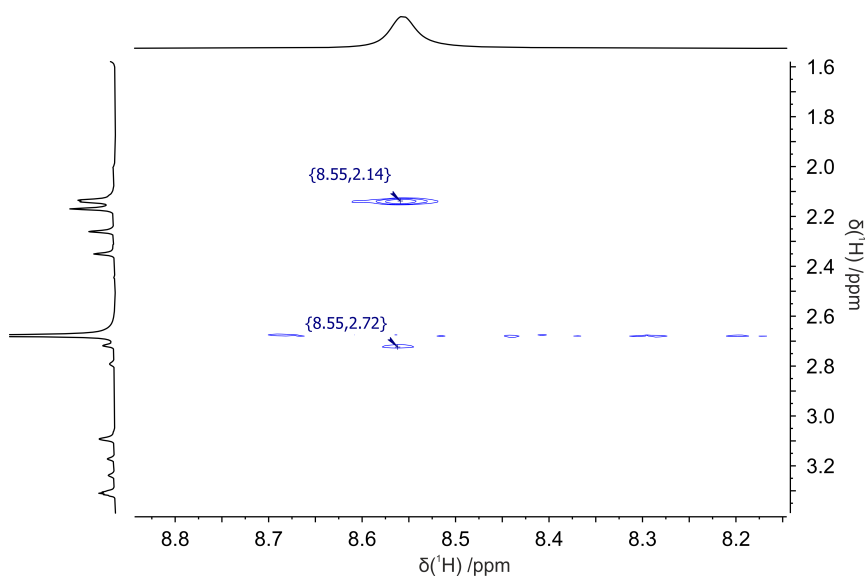


Figure 3.6:  $^1\text{H}$ - $^1\text{H}$  2D NMR NOESY data collected at 263 K and at a field of 7 T. Data reveals through-space connections between the aromatic protons in 3,5-difluoropyridine at  $\delta$  8.55 with signals corresponding to the *ortho* methyl group in IMes ( $\delta$  2.14) and a methyl group in dimethylsulfoxide ( $\delta$  2.72).

were generally conducted using standard acquisition parameters from Bruker, and specific parameters shown in Table 3.3.

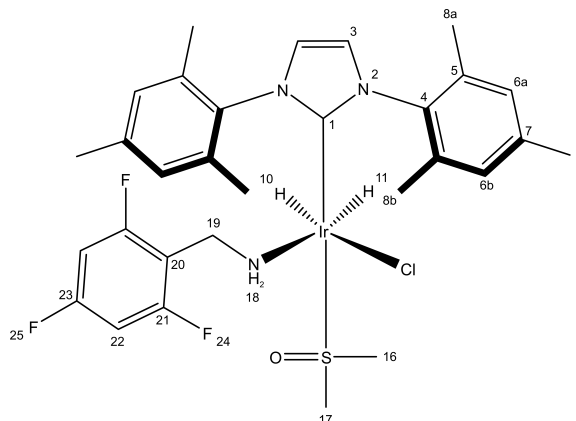


Figure 3.7: Proposed structure for the active SABRE complex containing 2,4,6-trifluorobenzylamine and dimethylsulfoxide. Repeated from Chapter 6 Section 6.3 for convenience.

To characterise the SABRE-active catalyst responsible for the  $^{19}\text{F}$  NMR hyperpolarised signals of 2,4,6-trifluorobenzylamine, a series of low-temperature multinuclear NMR experiments was undertaken. The investigation began by examining the connectivity of the hydride ligand signals corresponding to the active species, observed at  $\delta$   $-23.2$  and  $-24.3$  ppm (Figure 3.8). These signals had been previously identified in hyperpolarised experiments conducted at both 1 T and 11.4 T. As noted earlier (Chapter 4, Section 4.3), the singlet at a higher chemical shift relative to the hydride resonances was attributed to the HD isotopologue for this complex, further supported by the observation of a triplet at  $\delta$  4.6 ppm with  $J = 43$  Hz (Figure 3.9).

To explore through-space interactions involving these hydride ligands, a 2D  $^1\text{H}$ - $^1\text{H}$  NOESY experiment was conducted. It revealed NOE correlations with the *ortho* methyl protons of the mesityl group in IMes and the methyl groups of dimethylsulfoxide. The identity of these ligands was assigned based on their chemical shift values and supported by  $^1\text{H}$ - $^1\text{H}$  2D COSY experiments, along with both short-range and long-range ( $J = 145$  Hz and 12 Hz, respectively)  $^1\text{H}$ - $^{13}\text{C}$  2D HMQC experiments. Key NOE correlations between these ligands are illustrated in Figure 3.11.

Table 3.3: Experimental parameters for NMR experiments used in the characterisation of the sample containing 2,4,6-trifluorobenzylamine and dimethylsulfoxide.

| Experiment  | Parameters  | F1  | F2  |
|---|---|---|---|
| $^1\text{H}$<br>pulse-and-collect   | pulse programme:<br>zg30                                  | Nuclei: $^1\text{H}$ , spectral<br>width: 50 ppm,<br>transmitter freq. offset:<br>-10 ppm, acq. time: 2 s               | -   |
| $^1\text{H}$ - $^1\text{H}$ 2D COSY   | pulse programme:<br>cosygpppqf                            | Nuclei: $^1\text{H}$ , spectral<br>width: 10 ppm,<br>transmitter freq. offset:<br>4.5 ppm, acq. time: 0.25<br>s         | Nuclei: $^1\text{H}$ , spectral<br>width: 10 ppm,<br>transmitter freq. offset:<br>4.5 ppm, acq. time:<br>0.057 s                |
| $^1\text{H}$ - $^{13}\text{C}$ 2D<br>HMQC (long<br>range)                                   | pulse programme:<br>hmqcgpq,<br>coupling: 12 Hz           | Nuclei: $^1\text{H}$ , spectral<br>width: 10 ppm,<br>transmitter freq. offset:<br>5 ppm, acq. time: 0.25 s              | Nuclei: $^{13}\text{C}$ , spectral<br>width: 200 ppm,<br>transmitter freq. offset:<br>100 ppm, acq. time:<br>0.014 s            |
| $^1\text{H}$ - $^{13}\text{C}$ 2D<br>HMQC (short<br>range)<br>aliphatic/aromatic<br>regions | pulse programme:<br>hmqcgpq,<br>coupling: 145 Hz          | Nuclei: $^1\text{H}$ , spectral<br>width: 10/10 ppm,<br>transmitter freq. offset:<br>5/5 ppm, acq. time:<br>0.25/0.25 s | Nuclei: $^{13}\text{C}$ , spectral<br>width: 70/50 ppm,<br>transmitter freq. offset:<br>35/115 ppm, acq. time:<br>0.029/0.041 s |
| $^1\text{H}$ - $^1\text{H}$ 2D<br>NOESY   | pulse programme:<br>noesygpqhpp,<br>mixing time: 0.4<br>s | Nuclei: $^1\text{H}$ , spectral<br>width: 34 ppm,<br>transmitter freq. offset:<br>-8 ppm, acq. time: 0.40 s             | Nuclei: $^1\text{H}$ , spectral<br>width: 34 ppm,<br>transmitter freq. offset:<br>-8 ppm, acq. time:<br>0.030 s                 |

Table 3.4: High-field NMR characterisation results for the SABRE active complex containing 2,4,6-trifluorobenzylamine and dimethylsulfoxide. Repeated from Chapter 6 Section 6.3 for convenience.

| Resonance number | $\delta$ $^1\text{H}$ | $\delta$ $^{13}\text{C}$ | $\delta$ $^{19}\text{F}$ |
|------------------|-----------------------|--------------------------|--------------------------|
| 1                | -                     | 160.29                   | -                        |
| 2                | -                     | -                        | -                        |
| 3                | 7.21                  | 122.69                   | -                        |
| 4                | -                     | 139.90                   | -                        |
| 5                | -                     | 136.49/138.44            | -                        |
| 6                | 6.94/6.96             | 128.58/128.72            | -                        |
| 7                | -                     | 140.59                   | -                        |
| 8                | 2.13/2.22             | 18.94/17.95              | -                        |
| 9                | 2.20                  | 20.45                    | -                        |
| 10               | -23.2 (d, J = 7.6 Hz) | -                        | -                        |
| 11               | -24.3 (d, J = 7.6 Hz) | -                        | -                        |
| 16, 17           | 3.19/3.21             | 58.15/46.73              | -                        |
| 18               | 5.15                  | -                        | -                        |
| 19               | 3.90                  | 32.34                    | -                        |
| 20               | -                     | 112.98                   | -                        |
| 21               | -                     | 161.26                   | -                        |
| 22               | 6.97                  | 100.03                   | -                        |
| 23               | -                     | 163.22                   | -                        |
| 24               | -                     | -                        | -112.45                  |
| 25               | -                     | -                        | -106.45/ -110.77         |

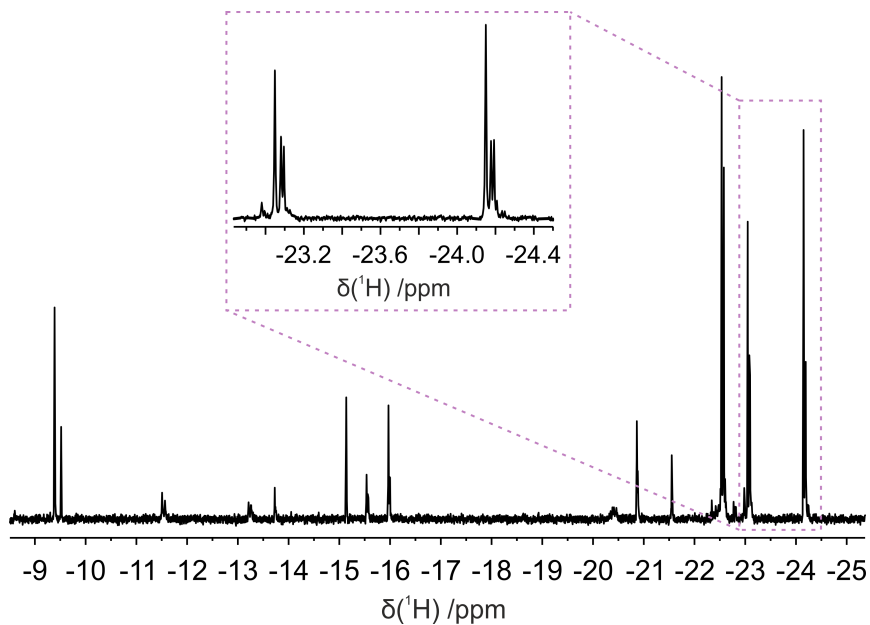


Figure 3.8:  $^1\text{H}$  NMR spectra of the characterisation sample acquired at 11.4 T (263 K), zoomed in the hydride ligand signal region ( $\delta$  -9 to -26). Signals corresponding to the main active species (Figure 3.7) are highlighted and amplified in the dashed box.

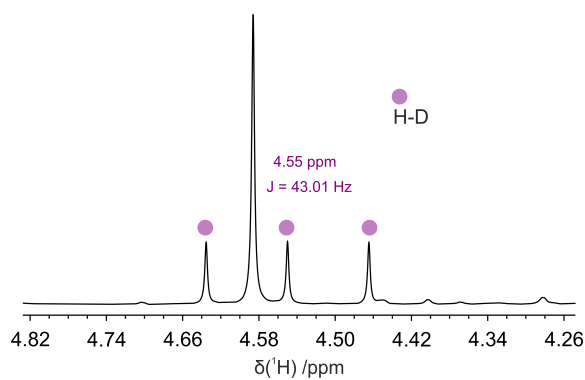


Figure 3.9:  $^1\text{H}$  NMR spectra of the characterisation sample acquired at 11.4 T (263 K), zoomed in the  $\delta$  4.3 to 4.8 region, showing the signal corresponding to HD gas.

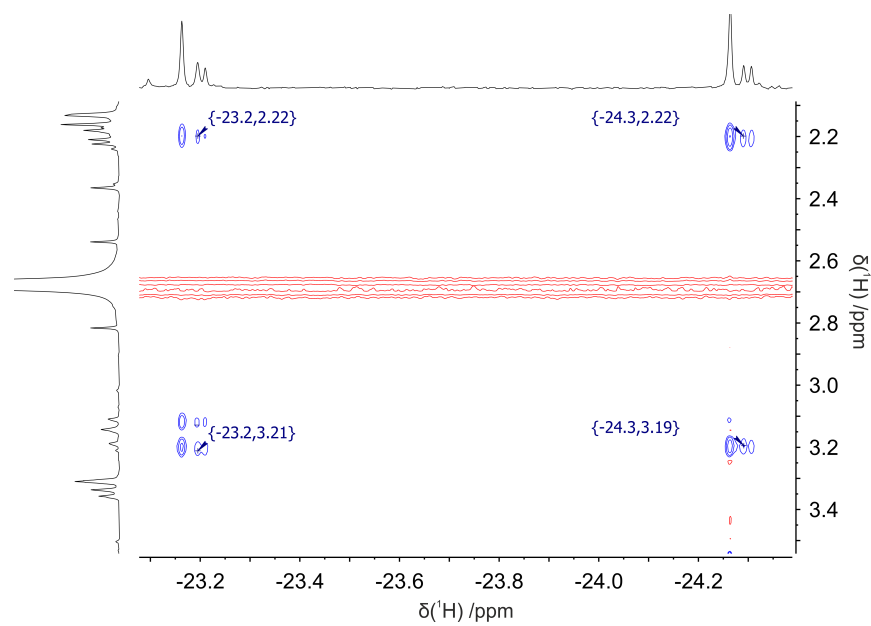


Figure 3.10:  $^1\text{H}$ - $^1\text{H}$  2D NMR NOESY data collected at 263 K and at a field of 11.4 T. Data reveals through-space connections between the hydride ligand signals at  $\delta$  - 23.2 and - 24.3 with a signal corresponding to the *ortho* methyl group in IMes ( $\delta$  2.22) and the methyl signals in dimethylsulfoxide ( $\delta$  3.19 and 3.22).

Additionally, the NOESY spectrum revealed through-space connectivity between the *ortho* methyl groups in IMes and a resonance at  $\delta$  3.90. This signal was assigned to the methylene group of 2,4,6-trifluorobenzylamine based on hyperpolarised experiments, further corroborated by both  $^1\text{H}$ - $^1\text{H}$  2D COSY and  $^1\text{H}$ - $^{13}\text{C}$  2D HMQC experiments (short- and long-range,  $J = 145$  Hz and 12 Hz, respectively).

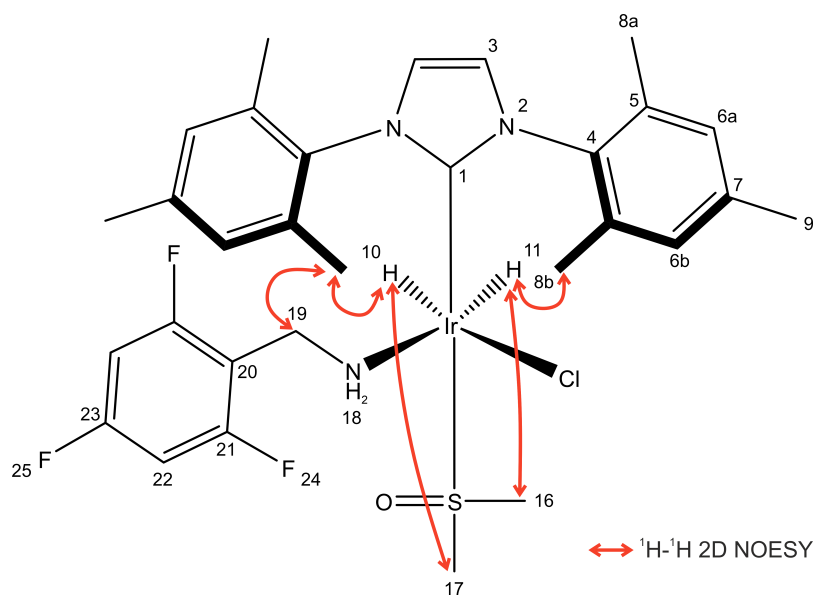


Figure 3.11: Key through-space couplings observed *via*  $^1\text{H}$ - $^1\text{H}$  2D NOESY experiment, revealing the connectivity of the ligands in the main active complex.

As with the system containing 3,5-difluoropyridine (Section 3.8.1), no NOE correlations were observed between the IMes and dimethylsulfoxide ligands, suggesting these occupy *trans* positions. Furthermore, the absence of NOE couplings between the hydride ligands, 2,4,6-trifluorobenzylamine, or dimethylsulfoxide with any additional ligands implies that the ligand *cis* to 2,4,6-trifluorobenzylamine is chloride. This assignment is supported by the similarity of the hydride ligand chemical shift values to those observed in the 3,5-difluoropyridine system and those reported by Tickner *et al.* for analogous complexes.<sup>189</sup>  $^{19}\text{F}$  NMR signals were assigned by comparison with a reference sample of 2,4,6-trifluorobenzylamine (60 mM in methanol- $d_4$ ).

## Chapter 4

# Enhancing Low-Field $^{19}\text{F}$ NMR Sensitivity with SABRE-SHARPER

In this chapter, the combination of SABRE with the multiplet refocusing pulse sequence SHARPER (Sensitive, Homogeneous, And Resolved PEaks in Real time)<sup>103</sup> will be explored as a strategy to further improve the sensitivity of benchtop NMR. This study was done on a set of test molecules presenting homonuclear and/or heteronuclear  $J$  couplings of small to large magnitudes.  $^1\text{H}$  and  $^{19}\text{F}$  SABRE hyperpolarisation of the test molecules is explored prior to the combination of  $^{19}\text{F}$  SABRE SHARPER. The gains in signal-to-noise ratio and reduction of peak linewidth will be covered, along with a discussion of the use of matched filters and background correction tools. The performance of this pulse sequence is compared to that of proton-decoupled fluorine experiments ( $^{19}\text{F}\{^1\text{H}\}$ ), a common approach to eliminate peak splitting produced by heteronuclear  $J$  coupling. In the last section of this chapter, the application of a selective variation of SHARPER, *sel*SHARPER, to a mixture of analytes will be discussed. The results presented in this chapter have been published and can be found in reference.<sup>178</sup>

## 4.1 Background Theory

### 4.1.1 SHARPER Pulse Sequence

The SHARPER pulse sequence developed by Jones *et al.*<sup>103</sup> improves the sensitivity of NMR measurements by eliminating peak splitting due to heteronuclear couplings and producing narrower linewidths. SHARPER was originally postulated as a tool to improve the efficiency of reaction monitoring, allowing for smaller sample sizes and more frequent sampling.<sup>103</sup> In this pulse sequence, a radio frequency pulse is applied at the chemical shift of the target signal, after which a short portion of the FID (referred to as an ‘FID chunk’) is acquired. This is followed by a train of 180° refocusing pulses which are interleaved with half-chunk acquisition steps. In this way, heteronuclear scalar coupling evolution, and the resulting peak splitting, are prevented.<sup>106</sup>

One of the advantages of this pulse sequence is that it is able to compensate for pulse imperfections and magnetic field inhomogeneity ( $\Delta B_0$ ), thus reducing peak linewidths. This is achieved by acquiring the FID chunks through a Carr-Purcell-Meiboom-Gill (CPMG) pulse train.<sup>190,191</sup> As the contribution of  $\Delta B_0$  to the effective transverse relaxation time constant ( $T_2^*$ ) is reduced, SHARPER peaks approach their natural linewidths in the absence of chemical exchange. By removing peak splitting and improving linewidths, SHARPER significantly increases the signal-to-noise ratio of target peaks.

Another advantage of this pulse sequence is that it eliminates the need for an X-channel to pulse on the non-active nucleus, making it less hardware demanding. This is particularly useful for <sup>19</sup>F NMR, as independent <sup>1</sup>H and <sup>19</sup>F channels or probes that can pulse at both frequencies simultaneously are seldom seen on benchtop NMR spectrometers. Additionally, as SHARPER only involves pulsing on the active nucleus, scalar couplings arising from any other heteronuclei affecting the detected nucleus can be simultaneously eliminated.<sup>103</sup>

In its original version designed for high-field implementation (Figure 4.1), shaped pulsed field gradients (PFG) were applied surrounding the non-selective 180° pulse inside each spin echo. In some cases, this posed a limitation as not all benchtop NMR spectrometers have the capacity to perform PFGs.<sup>3</sup> Dickson *et al.* proposed an adaptation of this pulse sequence

for benchtop NMR spectrometers that renders the use of PFGs unnecessary by adjusting the phase cycle of the train of  $180^\circ$  pulses.<sup>104</sup> This not only facilitated the application of SHARPER on benchtop NMR spectrometers, it also reduced the duration of the spin echoes, and as a consequence, signal loss due to relaxation.

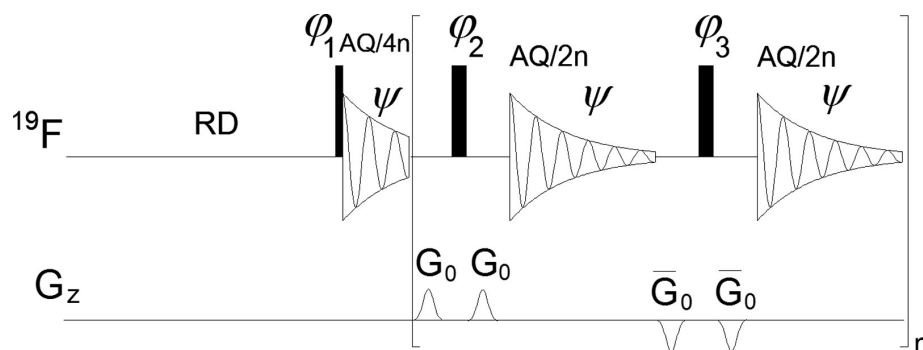


Figure 4.1: Original SHARPER pulse sequence proposed by Jones *et al.*<sup>103</sup>  $90^\circ$  and  $180^\circ$  pulses are represented by narrow and wide filled rectangles, respectively. Sine-shaped pulsed-field gradients ( $G_0$ ) are applied for  $300 \mu\text{s}$  with a truncation of 1%. The phase cycle is detailed in the original reference.<sup>103</sup> Reproduced under a CC-BY licence from Ref. [103].

#### 4.1.2 Selective SHARPER Pulse Sequence

The application of the previously described SHARPER pulse sequence to a mixture of components results in the collapse of all resonances into a single peak. In other words, chemical shift information of each compound is lost. While this approach may be useful in certain applications, such as determining the total content of a specific group of chemicals, it is often necessary to differentiate between species in a sample, making it an undesirable outcome. To avoid this, selective  $180^\circ$  pulses surrounded by PFGs may be applied prior to chunk acquisition in the initial step and throughout the pulse train (Figure 4.2).<sup>103</sup> In this approach termed *sel*SHARPER, the target signal is selected at the initial step and refocused throughout the pulse train, whilst off-resonance signals are de-phased by the pulsed field gradients. As a result, only the targeted signal remains after the application of

*sel*SHARPER.

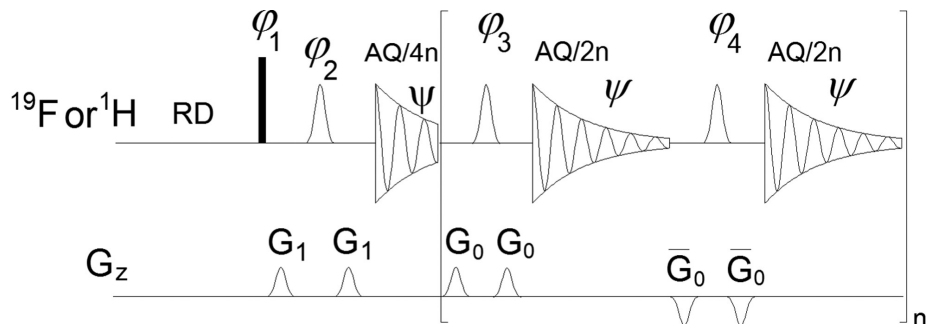


Figure 4.2: Original *sel*SHARPER pulse sequence proposed by Jones *et al.*<sup>103</sup> 90° non-selective pulses are represented by narrow filled rectangles, and 180° Gaussian-shaped selective pulses by smoothed empty shapes. The phase cycle and other experimental details are described in the original reference.<sup>103</sup> Reproduced under a CC-BY licence from Ref. [103].

In the adaptation of *sel*SHARPER to benchtop NMR spectrometers, Dickson *et al.* removed the need for PFGs by either using two scans to remove artefacts arising from off-resonance signals, or by using a more selective 270° Gaussian pulse.<sup>104</sup> Although both of these approaches proved to be effective in artefact removal, the achieved SNR levels were *ca.* 50% of those obtained for the non-selective version. This signal loss can be attributed to relaxation, and affects both low- and high-field NMR versions of this pulse sequence,<sup>103,104</sup> demonstrating that chemical-shift differentiation comes with a sensitivity penalty.

### 4.1.3 Optimisation of Data Acquisition and Processing

#### 4.1.3.1 Optimisation of FID Chunk Acquisition Time

A consequence of the piece-like collection of FID chunks is the formation of spectral artefacts, which are observed at  $\pm n/\tau$  (Hz) intervals from the target frequency, with  $\tau$  being the chunk acquisition time and  $n$  an integer number ( $n = 1, 2, 3, \text{etc.}$ ). These arise from the periodic drop in amplitude of the FID signal in between acquisition steps due to  $T_2$  relaxation, as well as the evolution of scalar couplings during acquisition.

The drop of FID signal is exacerbated by longer pulses within the spin-echo train, as well as by longer acquisition chunks. For example, Jones *et al.* compared the relative intensity of the sidebands (main artefacts on either side of the target signal) and the target signal when increasing the chunk length in *sel*SHARPER experiments.<sup>103</sup> This study showed that sidebands can account for 37% of the combined artefact/target signal area for  $\tau = 40$  ms *versus* 2% for  $\tau = 5$  ms. Interestingly, although the SNR decreased with longer  $\tau$  values, the sum of the integrals of the sidebands and the target signal remained largely unchanged when chunk length varied; it was the proportion of signal leached to the sidebands that increased with chunk length. It is therefore recommended that the sidebands are included in the integration step for quantitative applications.<sup>103</sup>

Careful chunk length optimisation is crucial for molecules containing large  $J$  couplings, as magnetisation evolution due to  $J$  coupling happens quickly during acquisition steps. If this evolution time is restricted by reducing  $\tau$ ,  $J$  coupling splitting can be efficiently removed. In order to achieve this, chunk lengths should comply with Eq. 4.1. When molecules exhibit large  $J$  couplings, this may involve very short chunk lengths resulting in an increase in pulsing frequency. This is more straightforward to achieve at lower magnetic fields, as duty cycle requirements are less stringent due to a decrease in power deposition. Another advantage of shorter chunk lengths is that it can better compensate for magnetic field inhomogeneity effects.<sup>103</sup>

$$\tau < 1/(4J) \tag{4.1}$$

The arguments presented in the previous paragraphs suggest that shorter chunk lengths are beneficial and should be opted for, provided duty cycle requirements are met. There is however a disadvantage of using short  $\tau$  values: it can lead to increased line broadening.<sup>104</sup> This is a consequence of using a greater amount of spin-echos to acquire the same amount of points, during which relaxation takes place. This partially counteracts the linewidth-narrowing quality of SHARPER by adding a contribution to  $T_2$ , resulting in a SHARPER-specific effective transverse relaxation time constant  $T_2^S$  ( $T_2^S > T_2$ ). The use of longer selective pulses during the spin-echo pulse train exacerbates this problem. It becomes evident that a balance must be struck between SNR gains and line broadening.

### 4.1.3.2 Improving Signal-to-Noise Ratios with Post-acquisition Processing

Another strategy used to increase the SNR of SHARPER signals is the use of matched filters. This post-processing tool involves multiplying the obtained FID by an exponential function with a time decay matching that of the FID envelope.<sup>192</sup> In this way, the FID is weighted in a way that minimises the noise contribution towards the end of the acquisition window, thus producing an increase in SNR. For SHARPER experiments, Dickson *et al.* proposed the use of a matched filter following  $T_2^S$  as a time decay ( $\exp(-\pi t \Delta_{1/2}^S)$ , where  $\Delta_{1/2}^S = 1/\pi T_2^S$ ) to maximise SNR (Figure 4.3).<sup>104</sup>

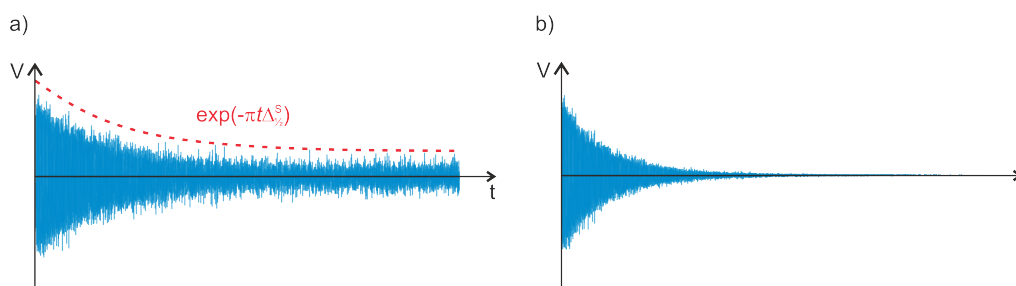


Figure 4.3: Schematic representation of the use of matched filters during post-acquisition processing. Multiplication of the original FID signal (in Volts, V) by an exponential function with a time decay following  $T_2^S$  ( $\Delta_{1/2}^S = 1/\pi T_2^S$ , red) (a) produces a new FID with reduced noise as the signal decays (b).

A further  $\sqrt{2}$ -fold SNR improvement can be achieved by removing the imaginary part of the spectrum. This approach requires adjusting the receiver phase of the spectrometer to acquire the real part of the spectrum. By doing so, only noise is collected through the imaginary channel which can be discarded post acquisition. Not only does this increase SNR, but it also reduces the intensity of SHARPER artefacts.<sup>104</sup>

## 4.2 Choice of Test System

The compounds used to test the efficacy of SABRE-SHARPER, shown in Figure 4.4, were chosen as they represent diverse scalar coupling scenarios. For example, fluorine spectra for

3,5-difluoropyridine (DFP, **1**) revealed a medium strength heteronuclear coupling constant of  ${}^3J_{HF} = 9$  Hz (*meta*- ${}^{19}\text{F}$  and *para*- ${}^1\text{H}$ ), whereas 3-(difluoromethyl)pyridine (DFMP, **2**) exhibited a larger heteronuclear coupling constant of  ${}^2J_{HF} = 55$  Hz ( ${}^{19}\text{F}$  and  ${}^1\text{H}$  in  $-\text{CF}_2\text{H}$  group), as determined by pulse-and-collect  ${}^1\text{H}$  and  ${}^{19}\text{F}$  NMR experiments at 1 T (Chapter 3, Section 3.3). The more complex system 3,4,5-trifluoropyridine (TFP, **3**) revealed two distinct  ${}^{19}\text{F}$  resonances with both homonuclear and heteronuclear  $J$  couplings:  ${}^3J_{HF} = 8$  Hz (*ortho*- ${}^1\text{H}$  and *meta*- ${}^{19}\text{F}$ ) and  ${}^3J_{FF} = 18$  Hz ( ${}^{19}\text{F}$  nuclei in *meta* and *para* positions). The diversity of  $J$  coupling regimes in this set of test molecules was ideal to assess the robustness of SHARPER.

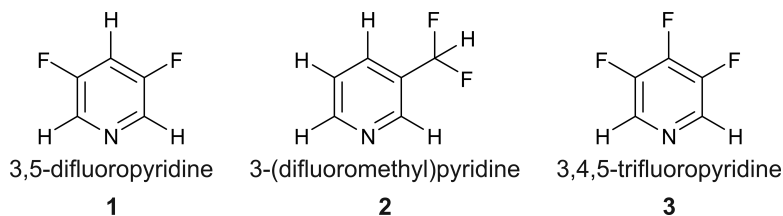


Figure 4.4: Test molecules used for SABRE-SHARPER experiments: 3,5-difluoropyridine (DFP, **1**), 3-(difluoromethyl)pyridine (DFMP, **2**), and 3,4,5-trifluoropyridine (TFP, **3**).

A second factor that led to this choice of test molecules was that they were expected to hyperpolarise through SABRE in an efficient way. Efficient  ${}^1\text{H}$  and  ${}^{19}\text{F}$  SABRE hyperpolarisation of a range of fluoropyridines has been demonstrated before.<sup>134,152,193</sup> The position of the fluoro substituents has been shown to be a determinant factor on hyperpolarisation efficiency, as substituents in the *ortho* position can prevent binding to the catalyst due to steric hinderance.<sup>193</sup> Therefore only *meta* and *para* substituted pyridines were chosen. Additionally, as these molecules exhibit vastly different scalar couplings, the effective  $J$  coupling of the active SABRE complex was expected to vary, leading to different optimal hyperpolarisation conditions.

## 4.3 SABRE Hyperpolarisation of Test Molecules

### 4.3.1 $^1\text{H}$ SABRE Hyperpolarisation

Prior to the application of SHARPER, the SABRE activity of DFP, DFMP and TFP was tested. Samples containing 100 mM of substrate (either DFP, DFMP or TFP) and 5 mM of the standard SABRE pre-catalyst  $[\text{IrCl}(\text{COD})(\text{IMes})]$  in methanol were prepared according to the procedure described in Section 3.1.1 (Chapter 3). SABRE-hyperpolarised spectra of these samples were obtained through standard shake-and-drop experiments followed by benchtop NMR acquisition at 1T, as described in Sections 3.2 and 3.3 (Chapter 3). Experimental parameters such as substrate and pre-catalyst concentrations or sample shaking time were chosen based on what is common practice and known to be suitable for efficient polarisation.<sup>83,135</sup> A polarisation transfer field of 6.2 mT was chosen for  $^1\text{H}$  SABRE experiments as this is within the field region shown to be effective for this nucleus, as discussed in Section 2.2.2.3. Under these conditions, all three molecules exhibited good  $^1\text{H}$  SABRE hyperpolarisation levels as evidenced by their area enhancement factors,  $\varepsilon_{1\text{H}}$  (Section 3.7.2, Chapter 3). These values were  $(3000 \pm 300)$ ,  $(1740 \pm 60)$  and  $(720 \pm 60)$  for DFP, DFMP, and TFP, respectively as shown in Figure 4.5. Although it was deemed unnecessary based on these results, optimisation of experimental parameters such as substrate and pre-catalyst concentration has been shown to improve enhancement levels.<sup>135,151,158,194</sup>

Although the efficiency of SABRE, and other hyperpolarisation methods, is typically measured in terms of an area enhancement factor ( $\varepsilon$ ), this metric would not demonstrate the benefit of using SHARPER accurately as SHARPER improves signal height but preserves signal area. In order to describe the sensitivity-enhancing properties of both SABRE and SHARPER in similar terms, signal-to-noise ratio enhancement factors ( $\varepsilon_{\text{SNR}}$ , Sections 3.7.1 and 3.7.2, Chapter 3) were used. This translates to  $\varepsilon_{\text{SNR}}$  values of 1200, 600, and 1400 for DFP, DFMP, and TFP respectively, relative to non-hyperpolarised spectra.

Inspection of the hydride section of the  $^1\text{H}$  NMR spectrum in SABRE experiments acquired at 1 T (Figure 4.6) revealed a single hyperpolarised species appearing in each case. For DFMP and TFP, these species appeared as broad singlets at  $\delta$  -22.9 and  $\delta$  -24.6,

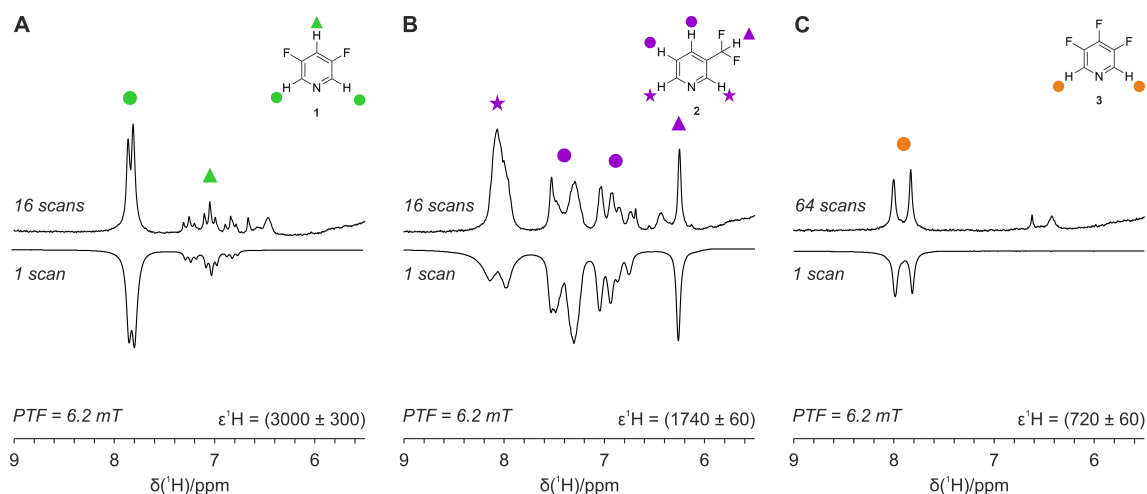


Figure 4.5: Comparison of reference non-hyperpolarised (top) and SABRE-enhanced (bottom)  $^1\text{H}$  benchtop (1 T) NMR spectra ( $\delta$  9 to 6.5) of 100 mM of (A) DFP, (B) DFMP, and (C) TFP with 5 mM SABRE pre-catalyst in methanol. Baseline distortion observed at ca.  $\delta$  6 in non-hyperpolarised spectra arises from the intense hydroxyl signal from the solvent.

respectively. These correspond to an equatorially symmetric complex, such as the trisubstituted species of general formula  $[\text{Ir}(\text{H})_2(\text{IMes})(\text{L})_3]^+$  (L: DFMP or TFP). In contrast, the active SABRE species corresponding to DFP appeared to be a partially overlapped pair of anti-phase doublets, for which chemical shift values of  $\delta$  -24.2 and -24.8 were estimated. The presence of a pair of doublets is indicative of chemically non-equivalent hydride ligands, suggesting that an equatorially asymmetric complex, *i.e.* one containing two different ligands in the equatorial plane, was present.

Non-hyperpolarised high-field NMR experiments at lower temperatures (11.7 T, 263 K, Figure 4.7) were conducted on analogous samples prepared in methanol- $d_4$  and activated as described in Section 3.2 (Chapter 3). These experiments revealed the presence of additional hydride signals, which were likely not observed at 1 T due to their reduced SABRE activity. Furthermore, these experiments provided information on the relative amount of each species in solution. For example, a symmetric species was the main product only when DFMP was used as a substrate (HH-I, Figure 4.7B). Conversely, in samples containing DFP and TFP there was a relatively even distribution of the symmetric complex (HH-I) and additional

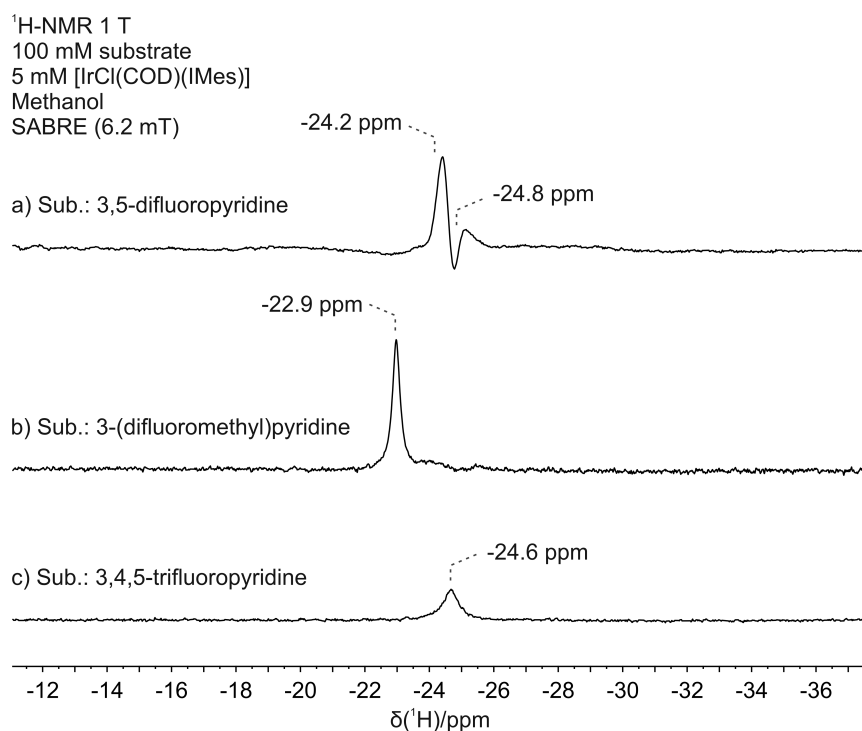


Figure 4.6: SABRE hyperpolarised <sup>1</sup>H NMR spectra acquired at 1 T of samples containing 100 mM of either DFP (a), DFMP (b), and TFP, and 5 mM of [IrCl(COD)(IMes)] in methanol. Highlighted signals correspond to the hydride ligands of the main SABRE active species in each sample.

equatorially asymmetric species (HH-II, Figure 4.7A and C).

The formation of asymmetric species was reported by Olaru and co-workers when using DFP and other fluoropyridines as substrates, who proposed  $[\text{Ir}(\text{H})_2(\text{IMes})(\text{L})_2(\text{MeOH})]^+$  (L: DFP, 3-fluoropyridine or 5-fluoropyridine-3-carboxylic acid, MeOH: methanol) as its formula.<sup>193</sup> SABRE species containing methanol as a ligand have been reported before when pyridine was used as a substrate.<sup>81,161,195,196</sup> Similar hydride signals were observed in a SABRE study carried out by Tickner *et al.* which explored 3,5-dichloro- and 3,5-dibromopyridine as substrates.<sup>189</sup> However, the signals reported in this work were attributed to the formation of the neutral complex  $[\text{IrCl}(\text{H})_2(\text{IMes})(\text{L})_2]$  (L: 3,5-dichloro- or 3,5-dibromopyridine).

The presence of a singlet at higher chemical shift values relative to each hydride signal is indicative of the formation of a  $[\text{Ir}(\text{H})(\text{D})(\text{IMes})(\text{L})_3]^+$  species, further supported by the formation of HD gas (triplet at  $\delta$  4.6 with  $J = 43$  Hz).<sup>146,157,197</sup> As the only source of deuterium in solution is methanol- $d_4$ , this suggests that a species with the formula  $[\text{Ir}(\text{H})_2(\text{IMes})(\text{L})_2(\text{MeOD})]^+$  (where MeOD is methanol- $d_4$ ) was indeed formed, driving the hydrogen isotope exchange process. Such behaviour has been previously reported and has been linked to deuteration of pyridine based substrates.<sup>182,198</sup> The relative proportion of HD to HH in samples containing DFP and TFP *versus* that containing DFMP is consistent with this analysis: more H/D exchange is expected when the methanol- $d_4$ -containing species is prevalent. The formation of methanol containing complexes has been linked to a decrease in SABRE activity. Eshuis *et al.* observed that pyridine hyperpolarisation was reduced when the formation of the methanol containing species was favoured at lower pyridine to catalyst ratios in high-field NMR spectroscopy.<sup>81</sup> Interestingly,  $^1\text{H}$  NMR SABRE experiments with DFP at 1 T using *protio* methanol showed hyperpolarisation only for the equatorially asymmetric species containing methanol, demonstrating this species is SABRE active. In fact, DFP showed the highest  $\varepsilon_{1\text{H}}$  out of the tested fluoropyridines, suggesting that hyperpolarisation was not hindered by the presence of methanol. One potential explanation for this discrepancy is that while methanol- $d_4$ , commonly used as a solvent in high-field NMR experiments, would induce deuteration of the substrates resulting in a decrease in SABRE activity, *protio* methanol would not.

The preferential formation of the methanol-containing species for samples containing DFP and TFP is presumably a result of the lower stability of the tris-substituted species. One factor that may lead to instability in the tris-substituted species is weaker iridium-substrate binding due to a lower electron density on the binding atom. The electron density of aromatic rings with halogen substituents directly attached to them is influenced by two opposing effects. On one hand, the high electronegativity of halogen atoms results in an electron-withdrawing inductive effect, which is exacerbated as the number of substituents increase.<sup>199</sup> On the other hand, the presence of substituents with a lone pair of electrons (*e.g.* fluorine) directly attached to the ring can increase the electronic density through

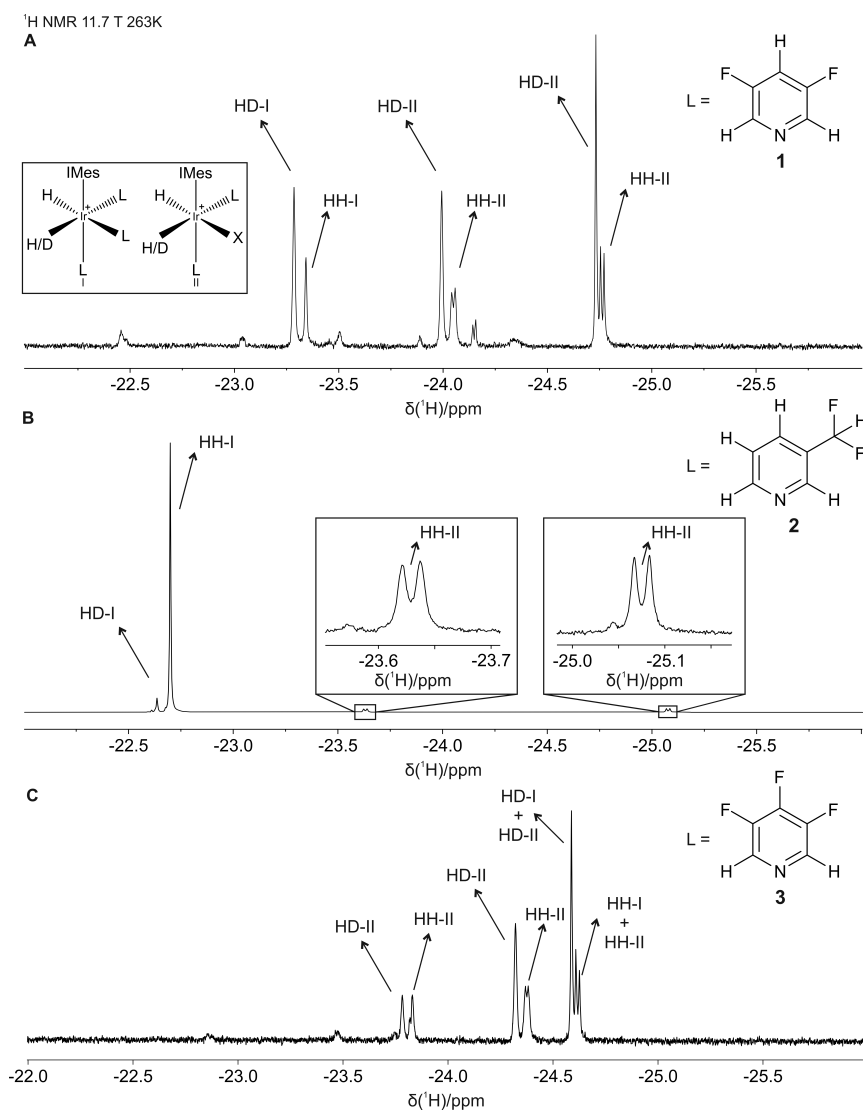


Figure 4.7: Comparison of <sup>1</sup>H NMR spectra acquired 11.7 T (263K) of samples containing 100 mM of DFP (A), DFMP (B), or TFP (C) and 5 mM of [IrCl(COD)(IMes)] in methanol-*d*<sub>4</sub>. Signals corresponding to non-deuterated (HH) and partially deuterated (HD) SABRE complexes with equatorially symmetric (I, here represented as a tris-substituted complex) or asymmetric (II) configurations are indicated with arrows. L represents a fluoropyridine ligand (DFP, DFMP, or TFP) and X an alternative ligand such as methanol-*d*<sub>4</sub>.

conjugation.<sup>199</sup> This favours a higher electronic density in the *para* position relative to the substituent, which would increase the electron density on the binding nitrogen in TFP. Given the high electronegativity of fluorine, the inductive effect outbalances the conjugating effect,<sup>199</sup> making DFP and TFP electron-poor ligands. In the case of DFMP, as the fluorine substituents are further removed from the ring, their effect is less significant. The lack of a conjugated system connecting the lone pair of electrons in fluorine and the aromatic ring hinders electron donation, and inductive effects are weaker as bond distances increase. This may explain why the formation of the tris-substituted species is not favoured for DFP and TFP, as opposed to DFMP (HH-I, Figure 4.7).

Despite the structural similarities of the tested substrates,  $\varepsilon_{1\text{H}}$  values for DFP, DFMP and TFP were vastly different. A key factor in terms of SABRE efficiency, as described in Section 2.2.2.3 (Chapter 2), is the substrate dissociation rate constant,  $k_D$ , which should be close to  $4.5 \text{ s}^{-1}$  for optimal  $^1\text{H}$  enhancements.<sup>158,159</sup> This dissociation rate constant can be greatly affected by electronic and steric effects in the SABRE complex, such as the ones described above.<sup>76,158,194</sup> In order to better understand the compounded impact of electronic and steric effects on  $^1\text{H}$  hyperpolarisation efficiency for all three substrates, determining dissociation rates *via* exchange spectroscopy (EXSY) experiments would be necessary. However, this was considered beyond the scope of the current study.

### 4.3.2 $^{19}\text{F}$ SABRE Hyperpolarisation

In order to optimise  $^{19}\text{F}$  hyperpolarisation conditions for these substrates, fluorine-detected SABRE experiments following the previously outlined procedure (Sections 3.1.1 and 3.2, Chapter 3) were carried out using three different polarisation transfer fields: 6.2 mT, the Earth's magnetic field outside the spectrometer ( $\sim 50 \mu\text{T}$ ), and the field inside a  $\mu$ -metal shield. Figure 4.8 presents SABRE-enhanced  $^{19}\text{F}$  benchtop NMR spectra for DFP, DFMP, and TFP using the optimal polarisation transfer field for each substrate. Fluorine enhancement factors ( $\varepsilon_{^{19}\text{F}}$ , Section 3.7.2, Chapter 3) at these PTFs were as follows:  $(270 \pm 20)$  for DFP,  $(200 \pm 10)$  for DFMP, and  $(1080 \pm 30)$  for TFP. Expressed as SNR gains,  $^{19}\text{F}$   $\varepsilon_{\text{SNR}}$  values of  $210 \pm 10$ ,  $240 \pm 20$ , and  $360 \pm 40$  were observed for DFP, DFMP, and TFP,

respectively. While the presented proton and fluorine enhancement factors did not follow the same trend relative to the chemical structure of the substrates, it is noted that as the optimised conditions under which these were obtained varied in each case, a direct comparison is not possible. Nevertheless, a comparison between fluorine enhancement factors is presented in the next paragraph.

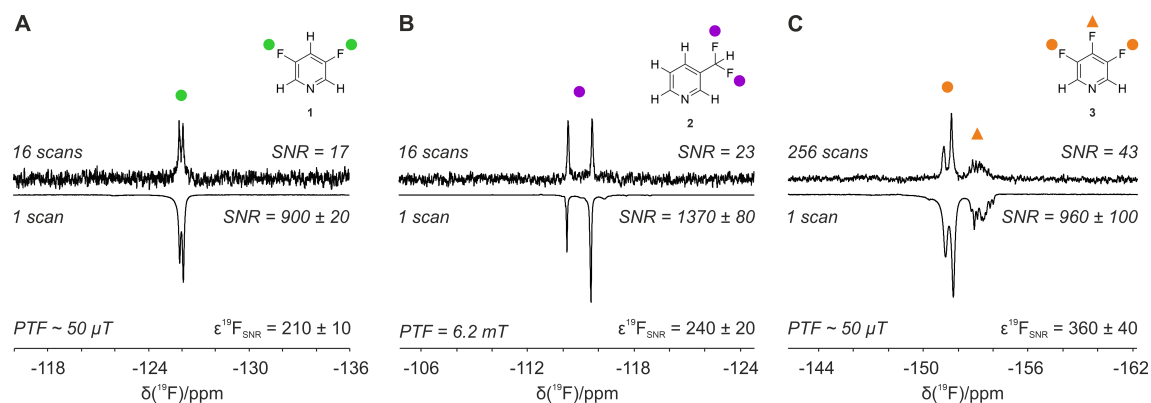


Figure 4.8: Comparison of SABRE-enhanced and thermally-polarised  $^{19}\text{F}$  benchtop NMR spectra of samples containing 100 mM of DFP (A), DFMP (B), and TFP (C) and 5 mM of  $[\text{IrCl}(\text{COD})(\text{IMes})]$  in methanol. All SABRE spectra were acquired with a single scan. The vertical scale of the thermal spectra was increased to aid visualisation.

For DFP and TFP, optimal polarisation transfer took place at the Earth's magnetic field. These findings are in agreement with reports by Chukanov *et al.* who studied SABRE polarisation transfer mechanisms for 3-fluoropyridine and proposed that at milli-tesla fields (*e.g.* 6.2 mT), the polarisation is transferred from the hydrides to the protons of the substrate and then relayed to the fluorine nuclei, which is highly inefficient. When using micro-tesla fields, such as  $50 \mu\text{T}$ , polarisation transfers from the hydrides to  $^{19}\text{F}$  nuclei directly, yielding higher signal enhancements.<sup>134</sup>

Interestingly, results for DFMP did not follow this trend, which showed an optimal PTF of 6.2 mT. At the Earth's magnetic field, enhancements for DFMP were lower and presented an anti-phase profile (Figure 4.17). This discrepancy may be explained by the presence of a large  $^2J_{\text{H},\text{F}}$  coupling (55 Hz) found in the difluoromethyl group in DFMP, which results

in a larger effective  $J$  coupling ( $J_{eff}$ ) for this system. As discussed in Section 2.2.2.3 (Chapter 2), polarisation transfer occurs most efficiently at a PTF for which the difference in frequency between hydrides and the target nuclei is matched to  $J_{eff}$ . Therefore, larger signal enhancements may be expected for DFMP at higher PTFs.

Generally speaking,  $^1\text{H}$  enhancement factors were significantly larger than those observed for  $^{19}\text{F}$ . Similar results were obtained in high-field  $^{19}\text{F}$  SABRE hyperpolarisation experiments.<sup>134,152,193</sup> For example, Shchepin *et al.* reported proton enhancement factors for 3-fluoropyridine at 9.4 T that were more than twice as high as those observed for fluorine:  $\varepsilon_{^1\text{H}} = 215$  *vs.*  $\varepsilon_{^{19}\text{F}} = 93$ .<sup>152</sup> This is likely a reflection of a less efficient polarisation transfer pathway from the hydrides ligands to the fluorine nuclei, *versus* the proton ones. Direct polarisation transfer from hydrides ligands to fluorine is mediated through a 5 (or 6 for DFMP) bond  $J$  coupling, which is expected to be small ( $^5J_{\text{HF}} \sim 0.34$  Hz in 3-fluoropyridine<sup>134</sup>), making polarisation transfer inefficient.

Remarkably, TFP exhibited a  $^{19}\text{F}$  enhancement factor surpassing not only its proton equivalent,  $\varepsilon_{^1\text{H}}$ , but also  $\varepsilon_{^{19}\text{F}}$  values for DFP and DFMP. One simple explanation for this could be that TFP has the lowest ratio of  $^1\text{H} / ^{19}\text{F}$  nuclei, which would minimise spin dilution and  $^{19}\text{F}$  to  $^1\text{H}$  cross polarisation for this substrate. It is also possible that the larger enhancement factor observed for TFP is a result of the additional fluorine atom in this substrate, creating electronic effects that improve SABRE efficiency for this system, as discussed in Section 4.3.1.

Further signal-to-noise ratio improvements could be achieved for these test molecules if peak splitting due to scalar coupling and field inhomogeneity effects were removed by SHARPER. In the next section, SABRE-SHARPER is investigated as a route to achieve further SNR gains in  $^{19}\text{F}$  NMR measurements.

## 4.4 $^{19}\text{F}$ SABRE-SHARPER on Test Molecules

The combined signal-enhancing effects of SABRE and SHARPER were evaluated by replacing the pulse-and-collect acquisition scheme used in the SABRE shake-and-drop protocol

(described in the previous section) with a SHARPER acquisition scheme. The SHARPER pulse sequence was based on the benchtop NMR version published by Dickson *et al.*<sup>104</sup> and is shown in Figure 4.9. Experimental parameters for this pulse sequence can be found in Section 3.3.3 (Chapter 3). Importantly, it was only possible to implement SHARPER for  $^{19}\text{F}$  measurements. This is due to the fact that  $^1\text{H}$  NMR spectra of SABRE samples contain signals from sources other than the target molecule, *e.g.* catalyst and solvent signals. As SHARPER is non-selective, its application to  $^1\text{H}$  would result in the collapse of all signals, irrespective of their origin, into a single peak. In contrast,  $^{19}\text{F}$  NMR spectra for SABRE samples containing DFP, DFMP, or TFP only exhibit signals from the test molecule, making it ideal to evaluate the performance of SABRE-SHARPER. In Section 4.5, a strategy to differentiate signals from different molecules is presented.

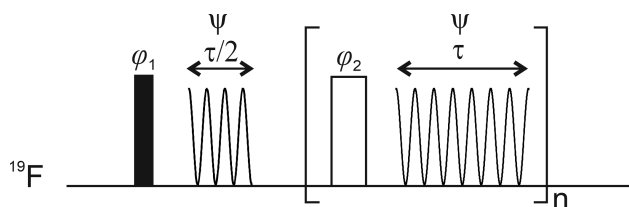


Figure 4.9: Pulse sequence diagram for SHARPER. The filled and empty rectangles represent  $90^\circ$  and  $180^\circ$  non-selective pulses, respectively. The chunk time is defined as  $\tau = N\delta t$ , where  $N$  is the number of points per chunk and  $\delta t$  is the dwell time. The total acquisition time is  $t_{acq} = (n + 1/2)\tau$ , where  $n$  is the total number of loops.  $\varphi_1 = x$ ;  $\varphi_2 = y$ ;  $\psi = x$ .

The performance of SHARPER was initially tested on non-hyperpolarised samples of DFP, DFMP, and TFP using  $\tau = 3.2$  ms. As shown in Figure 4.10, peak splitting was removed to yield a single peak for all three test molecules. As a result, SHARPER resulted in signal-to-noise enhancement factors of 11, 17 and 4.3 for DFP, DFMP, and TFP, respectively. It is worth noting that for TFP, not only were heteronuclear couplings ( $J_{HF}$ ) removed, but also peak splitting due to homonuclear scalar coupling ( $J_{FF}$ ) and chemical shift differentiation of the *meta* and *para* fluorine atoms.

A matched filter corresponding to  $T_2^S$  was applied to the SHARPER spectra to maximise SNR gains.  $T_2^S$  and linewidth values ( $\Delta_{1/2}^S$ ) obtained prior to the application of the matched

filter are shown in Table 4.1 (Section 3.4.1, Chapter 3). In most cases (DFP and DFMP), linewidths were extremely low, suggesting a value close to their natural linewidths was achieved. Although application of the matched filters doubles the linewidth ( $\Delta_{1/2}^S$ ), as shown in Figure 4.10, these values were still very low compared to typical optimal linewidths achieved for the benchtop NMR spectrometer ( $\sim 0.5$  Hz). The comparatively larger  $\Delta_{1/2}^S$  observed for TFP was thought to be a consequence of the complex combination of effects producing the peak splitting ( $J_{HF}$ ,  $J_{FF}$ , and chemical shift differences).

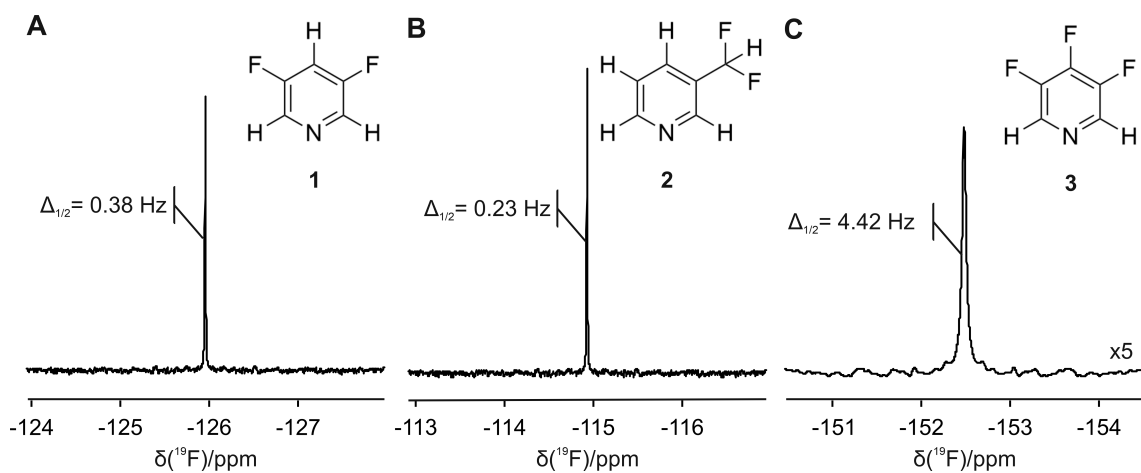


Figure 4.10: Non-hyperpolarised SHARPER  $^{19}\text{F}$  benchtop (1 T) NMR spectra of samples containing 100 mM of DFP (A), DFMP (B), and TFP (C) with 5 mM of  $[\text{IrCl}(\text{COD})(\text{IMes})]$  in methanol. Full width at half maximum values for the SHARPER spectra include the effects of the matched filter.  $\varepsilon_{\text{SNR}}$  values for DFP, DFMP, and TFP are 11, 17 and 4.3, respectively. SHARPER spectra were acquired using the pulse sequence in Figure 4.9 with a chunk time of  $\tau = 3.2$  ms and  $\varphi_1 = 2x, 2(-x), 2y, 2(-y)$ ;  $\varphi_2 = 2(y,-y), 2(x,-x)$ ;  $\psi = \varphi_1$ .

The combination of SABRE and SHARPER on samples containing DFP, DFMP, and TFP is shown in Figure 4.11. Similarly to what was observed in non-hyperpolarised experiments, all splitting was removed from the SABRE-hyperpolarised signals to produce a single resonance. A comparison of the SNR with SABRE (Figure 4.11 A-C) and with SABRE-SHARPER (Figure 4.11 D-F) shows that SHARPER provides SNR enhancement factors in SABRE experiments that are on the same order as those observed for non-hyperpolarised

Table 4.1:  $T_2^S$  and  $\Delta_{1/2}^S$  values for single-component samples

| Experiment        | <b>1</b>      |                  | <b>2</b>      |                  | <b>3</b>    |                  | <b>3*</b>    |                  |
|-------------------|---------------|------------------|---------------|------------------|-------------|------------------|--------------|------------------|
|                   | $T_2^S$       | $\Delta_{1/2}^S$ | $T_2^S$       | $\Delta_{1/2}^S$ | $T_2^S$     | $\Delta_{1/2}^S$ | $T_2^S$      | $\Delta_{1/2}^S$ |
|                   | /ms           | /Hz              | /ms           | /Hz              | /ms         | /Hz              | /ms          | /Hz              |
| SHARPER           | $1860 \pm 30$ | 0.17             | $3330 \pm 40$ | 0.10             | $146 \pm 7$ | 2.18             | $470 \pm 10$ | 0.68             |
| SABRE-<br>SHARPER | $328 \pm 2$   | 0.97             | $1694 \pm 2$  | 0.19             | $153 \pm 2$ | 2.07             | $545 \pm 2$  | 0.58             |

\*  $\tau = 0.8$  ms

experiments: 8.9 for DFP, 17 for DFMP, and 7.2 for TFP.

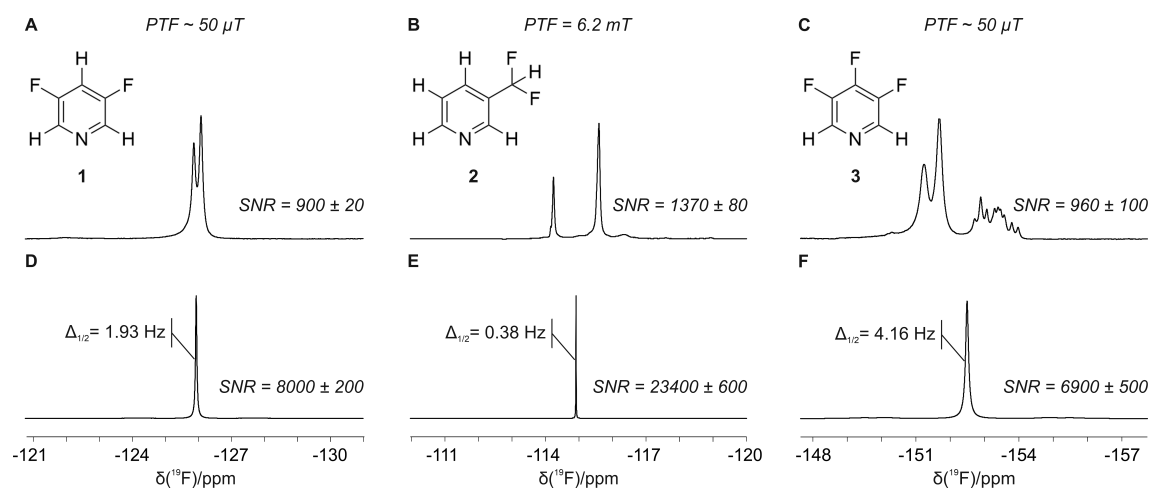


Figure 4.11: Comparison of SABRE (A-C) and SABRE-SHARPER (D-F)  $^{19}\text{F}$  benchtop (1 T) NMR spectra of samples containing 100 mM of DFP (A, D), DFMP (B, E), or TFP (C, F) and 5 mM of  $[\text{IrCl}(\text{COD})(\text{IMes})]$  in methanol. All spectra were acquired in a single scan and were apodised by a matched exponential filter (Section 3.4.1, Chapter 3). The SNR values represent averages over three repeat experiments. Full width at half maximum values are shown for the SABRE SHARPER spectra. The linewidths are effectively double the fundamental SHARPER linewidth due to the application of the matched filter. Individual traces were magnified as required to aid visualisation.

Generally speaking, the linewidths obtained for SABRE-SHARPER experiments were larger than those observed for non-hyperpolarised SHARPER experiments. For example, when performing SABRE-SHARPER on samples containing DFP, a linewidth of 0.97 Hz is obtained prior to applying a matched filter. This is roughly 5 times larger than the linewidth obtained for non-hyperpolarised experiments on DFP (0.17 Hz, Table 4.1). This line broadening effect could be explained by the chemical exchange of the substrates between their catalyst-bound and free states. Additionally, line broadening could potentially be due to the presence of hyperpolarised higher-order spin states (*e.g.* two-spin order  $^{19}\text{F}$ - $^1\text{H}$  states) arising from the *p*- $\text{H}_2$  singlet state. Such spin states behave differently under the train of pulses, meaning their refocusing may be less effective, therefore contributing to a broader signal. Despite this, an impressive 1900-fold increase in SNR was achieved by the combined effects of SABRE and SHARPER.

As for DFMP, the application of SABRE-SHARPER produces an extremely narrow linewidth of 0.19 Hz. This value is only marginally greater than the one obtained for non-hyperpolarised experiments (0.10 Hz, Table 4.1), implying that the hyperpolarisation process has a minimal line-broadening effect. Remarkably, a small linewidth was obtained even when a large 55 Hz heteronuclear scalar coupling was present, highlighting the robustness of SHARPER. Overall, an SNR enhancement by a factor of 4100 was obtained by SABRE-SHARPER relative to thermally-polarised spectra.

In the case of TFP, SHARPER removed the chemical shift difference (1.9 ppm, 75 Hz) between *meta* and *para* fluorine resonances, as well as the splitting due to heteronuclear ( $J_{HF}$ ) and homonuclear ( $J_{FF}$ ) scalar couplings. The removal of the homonuclear scalar coupling was unexpected for the non-selective version of SHARPER, as these are not refocused by spin-echo structures, unlike heteronuclear couplings.<sup>106</sup> However, if the period of time during which evolution under  $J_{FF}$  (*i.e.* chunk length) is minimised, splitting would be reduced. The broad linewidths observed for TFP in hyperpolarised and non-hyperpolarised SHARPER experiments (2.18 Hz and 2.08 Hz respectively), were thus attributed to the incomplete refocusing of the large homonuclear  $J$  coupling ( $^3J_{FF} = 18$  Hz), in addition to chemical shift evolution.

To test the validity of this, a SABRE-SHARPER spectrum for TFP was acquired using a much shorter chunk time of  $\tau = 0.8$  ms. It is worth noting that by reducing chunk length, the time between r.f. pulses is also reduced, making energy dissipation during the pulse train less efficient. However, as r.f. pulses require less power in low-field NMR, less stringent duty cycle requirements are needed compared to high-field NMR. SABRE-SHARPER FIDs and spectra for TFP using chunk lengths of  $\tau = 3.2$  ms and  $\tau = 0.8$  ms are shown in Figure 4.12. An increase in the effective relaxation time  $T_2^S$  from 154 ms to 547 ms was observed when decreasing chunk lengths. This translates to a reduction of linewidth from  $\Delta_{1/2}^S = 2.10$  Hz to  $\Delta_{1/2}^S = 0.58$  Hz, prior to the application of matched filters. Interestingly, Peat *et al.* conducted a comparable study examining the relationship between chunk length in SHARPER and effective relaxation, concluding that longer chunk durations result in larger  $T_2^S$  values.<sup>200</sup> As the chunk times employed in their work ( $\tau = 0.1$  to 0.4 ms) were significantly shorter than those used in the present work, the discrepancy in findings is proposed to stem from differing sources of line broadening. While Peat *et al.* suggested that extended chunk times enhance  $T_2^S$  by reducing relaxation losses associated with more frequent pulsing,<sup>200</sup> the broader linewidths observed in Figure 4.12 are thought to reflect incomplete refocusing of the strong homonuclear  $J$  coupling in this system when using comparatively longer chunk times ( $\tau = 3.2$  ms). Notably, reducing the chunk duration more than doubled the SNR of SABRE-SHARPER for TFP, increasing from  $(6900 \pm 500)$  to  $(15000 \pm 1000)$ , and yielding an overall 5700-fold SNR enhancement relative to a standard  $^{19}\text{F}$  pulse-and-collect experiment. This is the largest observed SNR gain out of the set of test molecules, which is unsurprising given that this molecule exhibits a complex splitting pattern which greatly diminishes the SNR in a  $^{19}\text{F}$  NMR experiment. It is worth noting, that no additional SNR gains were observed for DFP or DFMP when chunk length was decreased below 3.2 ms.

Generally speaking, the use of short chunk lengths for samples containing DFP, DFMP, and TFP contributed to the appearance of fewer chunking artefacts. Such a strategy was however not effective against off-resonance artefacts arising from a  $^{19}\text{F}$  background signal at  $\delta -72$  introduced by the probe of the spectrometer employed in these experiments.

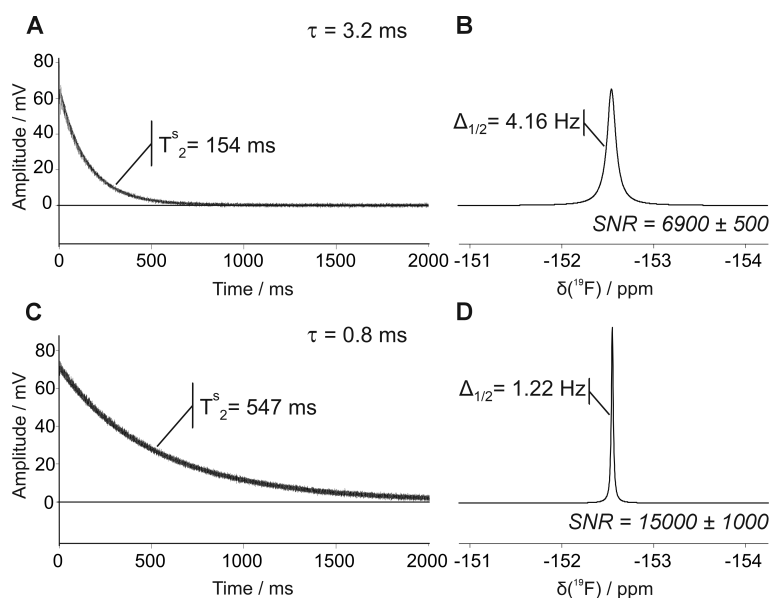


Figure 4.12: Comparison of  $^{19}\text{F}$  SABRE-SHARPER FIDs (A, C) and  $^{19}\text{F}$  NMR spectra at 1 T (B, D) of a sample containing 100 mM of TFP with 5 mM OF  $[\text{IrCl}(\text{COD})(\text{IMes})]$  in methanol, acquired with chunk lengths of  $\tau = 3.2$  ms (A, B) and  $\tau = 0.8$  ms (C, D). Spectra were acquired in a single scan and were apodised by matched exponential filters (Section 3.4.1, Chapter 3). The SNR values represent averages over three repeat experiments. Full width at half maximum values are shown for the SABRE-SHARPER spectra and include the effects of apodisation.

As stated in Section 4.1, scan averaging with adequate phase cycling can help reduce the appearance of such artefacts,<sup>104</sup> but this approach is incompatible with shake-and-drop experiments. Nevertheless, the transient nature of SABRE-hyperpolarised signals can be exploited to remove off-resonance artefacts from non-hyperpolarised signals. By acquiring a non-hyperpolarised reference scan with opposite phase and averaging with the hyperpolarised spectrum in post-processing, such artefacts are effectively removed as seen in Figure 4.13. For this strategy to be successful, the SNR of the non-hyperpolarised SHARPER signal must be much smaller than the hyperpolarised one, otherwise partial cancellation of this signal can be expected. Additionally, as the reference scan contributes in noise but not in hyperpolarised signal, the overall SNR after background correction will

necessarily be lower. Therefore, this strategy should only be applied when background signals produce a significant interference in the SABRE-SHARPER spectrum.

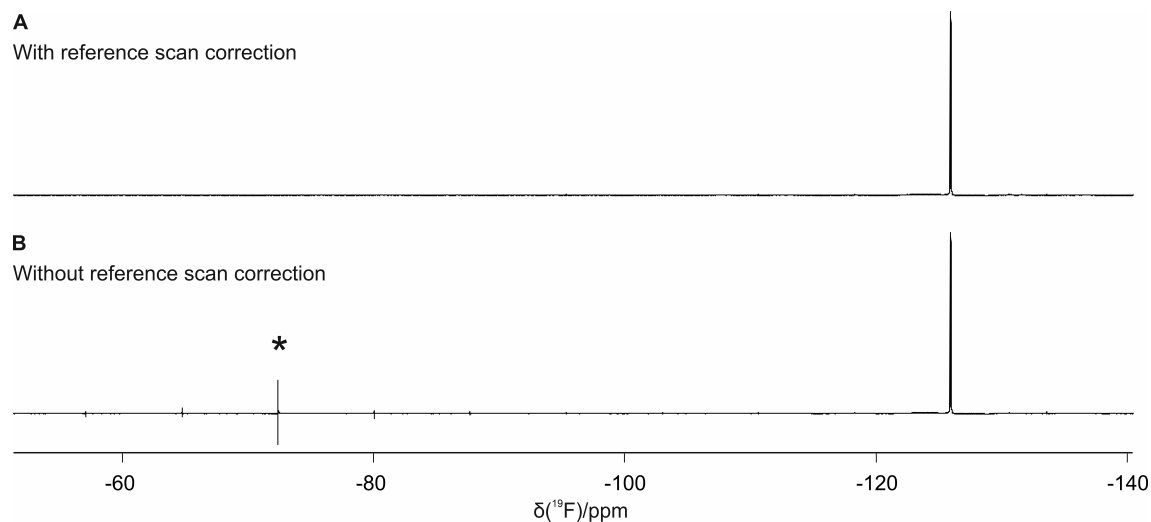


Figure 4.13: Comparison of  $^{19}\text{F}$  NMR SABRE-SHARPER spectra acquired with (top) and without (bottom) a second reference scan to remove the effect of off-resonance artefacts that originate from background  $^{19}\text{F}$  signals from the probe at  $\delta$  -72 (shown with an asterisk). The reference scan is acquired with a change in phase of the refocusing pulses in the loop by  $180^\circ$ .

It is common practice to simplify spectra by removing heteronuclear scalar coupling through decoupling of the nucleus responsible for the splitting. In this case, that would involve doing proton decoupling to  $^{19}\text{F}$  measurements, which is not straightforward to achieve in benchtop NMR as it requires simultaneous pulsing at proton and fluorine frequencies using the same coil. Nevertheless,  $^{19}\text{F}\{^1\text{H}\}$  can be achieved by interleaving proton decoupling using an MLEV sequence<sup>201</sup> and fluorine detection. In order to compare this approach with SHARPER, SABRE-enhanced  $^{19}\text{F}\{^1\text{H}\}$  spectra were acquired for DFP, DFMP, and TFP, as shown in Figure 4.14. Although these results show that spectra are indeed simplified by proton decoupling, it did not result in SNR gains. It is also worth noting that, unlike SHARPER, this approach to spectral simplification is only effective when heteronuclear  $J$  couplings are the only source of peak splitting. In addition to that, this implementation of

$^{19}\text{F}\{^1\text{H}\}$  was found to be lacking as spectra showed significant peak and baseline distortions for DFP and DFMP, which could not be minimised by parameter optimisation.

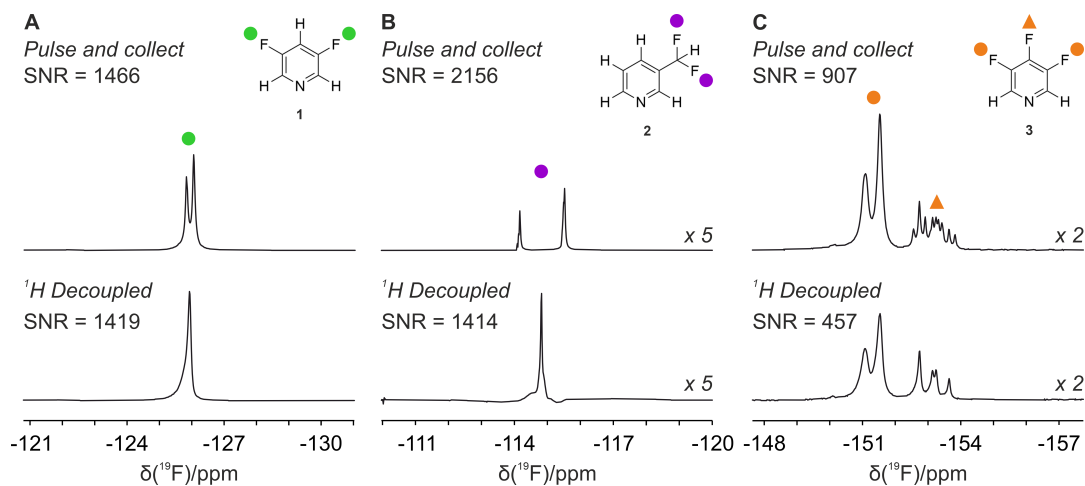


Figure 4.14: Comparison of SABRE-enhanced  $^{19}\text{F}$  benchtop (1 T) NMR spectra of samples containing 100 mM of DFP (A), DFMP (B), and TFP (C) with 5 mM  $[\text{IrCl}(\text{COD})(\text{IMes})]$  in protio methanol. (top) Standard  $^{19}\text{F}$  SABRE acquisition; (bottom)  $^{19}\text{F}\{^1\text{H}\}$  SABRE acquisition.

#### 4.5 $^{19}\text{F}$ SABRE-*sel*SHARPER for Mixture Analysis

The usefulness of the non-selective SHARPER version discussed so far is applicable to a limited set of analytical problems. The collapse of peak splitting in resonances from a single compound to increase SNR is an example of such, as shown in the previous section. This approach could also be highly advantageous when all resonances in the spectra belong to a class of chemically related compounds and a determination of the total content of such a class is sought. In most other cases, the spectra show an assortment of resonances arising from different compounds in the sample and differentiation of these is crucial. This can be accomplished by using the selective variation of SHARPER, termed *sel*SHARPER, which can selectively excite the target resonance before SHARPER is applied.<sup>103,104</sup> In this section, the results of the combination of *sel*SHARPER and SABRE hyperpolarisation on

a mixture of DFP and DFMP is presented.

As discussed in Section 4.1, the original *sel*SHARPER pulse sequence (Figure 4.2) introduces two modifications to the non-selective variation. First, it utilises a PFG spin echo structure with a selective  $180^\circ$  instead of the initial  $90^\circ$  pulse. Secondly, it utilises a train of selective inversion pulses surrounded by PFGs which is interleaved with FID chunk acquisition.<sup>103</sup> The first modification selects the target signal to refocus, whilst the train of selective pulses preserves this resonance, de-phasing off-resonance signals, and refocuses homonuclear couplings.

Dickson *et al.* proposed adaptations of this pulse sequence, which either restricted the use of PFGs to just the initial selection step, or removed them altogether. The latter variation makes *sel*SHARPER better suited to benchtop NMR spectrometers without PFG capabilities.<sup>104</sup> By removing PFGs within the train of inversion pulses (Figure 4.15A), a shorter delay can be used between chunk acquisition steps, minimising relaxation effects leading to improved line narrowing and minimising signal loss. Although the sensitivity of these variations was better than the original version with PFGs inside the acquisition loop, a *ca.* 50% loss of SNR relative to the non-selective version was observed in all cases.<sup>104</sup>

The *sel*SHARPER variation without PFGs inside the pulse train (Figure 4.15A) and a 5 ms Gaussian pulse was tested on a SABRE sample containing 50 mM each of DFP and DFMP and 5 mM of  $[\text{IrCl}(\text{COD})(\text{IMes})]$  in methanol. The sample was prepared and hyperpolarised using the shake-and-drop technique following the procedure detailed in the previous section. Signal-to-noise enhancements for DFP and DFMP were less than half of the values observed for non-selective SHARPER: 2.7-fold for DFP and 7.3-fold for DFMP (Figure 4.16). Added to this, linewidth values increased from 0.97 Hz to 3.24 Hz for DFP and from 0.19 Hz to 1.11 Hz for DFMP when compared to non-selective SHARPER (Tables 4.1 and 4.2). This is a clear reflection of an increased effective relaxation (lower  $T_2^S$ , Table 4.2) resulting from the long selective pulses inside the acquisition loops, which also cause signal loss.

Signal loss and line broadening could then be reduced if non-selective inversion pulses were used in the refocusing pulse train (Figure 4.15B). As this variation, termed

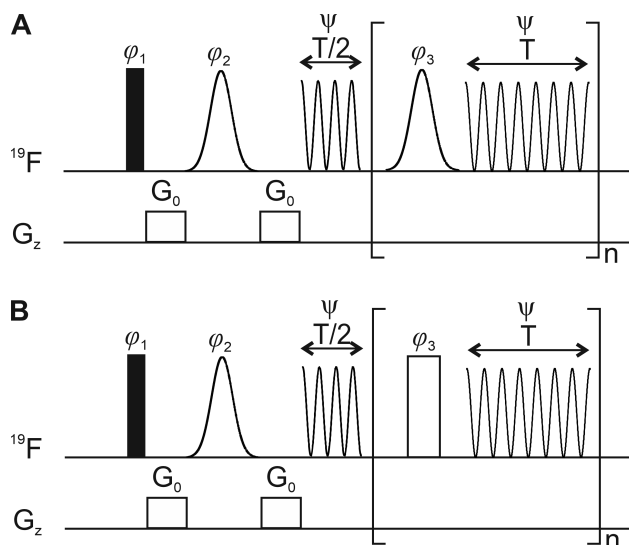


Figure 4.15: Pulse sequence diagrams for A) *selSHARPER* and B) *selSHARPER HPT*. The filled rectangles represent  $90^\circ$  non-selective pulses, while the smoothed empty shape depicts a selective Gaussian  $180^\circ$  pulse. The chunk time is defined as  $\tau = N\delta t$ , where  $N$  is the number of points per chunk and  $\delta t$  is the dwell time. The total acquisition time is  $t_{acq} = (n + 1/2)\tau$ , where  $n$  is the total number of loops.

*selSHARPER HPT* for clarity (HPT: hard-pulse train), retains the inversion Gaussian pulse in the first step, the selective properties for this pulse sequence are preserved, making it suitable for mixture analysis. A fully non-selective variation of SHARPER using a similar hard-pulse train for diffusion-ordered NMR spectroscopy experiments has been published.<sup>200</sup> Additionally, the selectivity of *selSHARPER HPT* can be adapted to more challenging mixtures, *i.e.* signals in close proximity, by increasing the duration of the initial selective pulse. As this only increases the duration of the first inversion pulse, the sensitivity penalty would be far less to that observed for the fully selective SHARPER version. The selective pulses inside the pulse train serve the additional purpose of removing homonuclear  $J$  couplings. However, as seen for the case of TFP in the previous section, by keeping chunk length sufficiently small the same refocusing effect can be achieved using *selSHARPER HPT* without the sensitivity penalty.

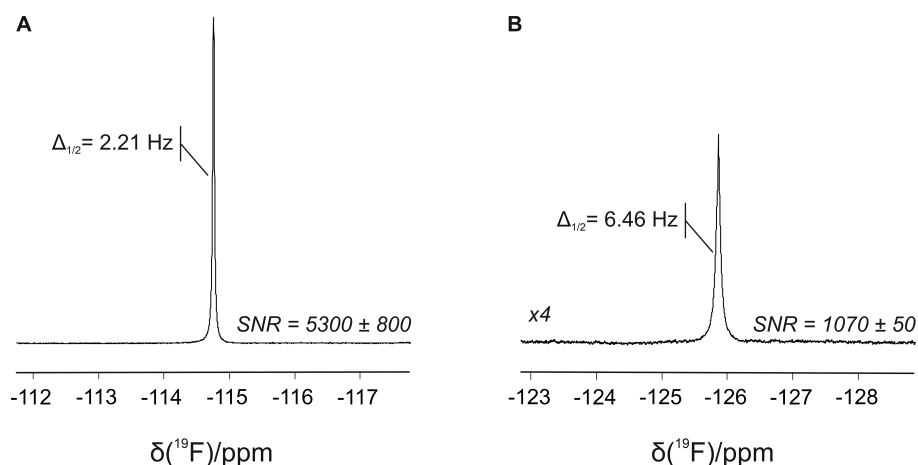


Figure 4.16: SABRE-*sel*SHARPER experiments on a mixture of DFMP (A) and DFP (B) (50 mM of each) with 5 mM of  $[\text{IrCl}(\text{COD})(\text{IMes})]$  in methanol. The *sel*SHARPER experiments were performed using selective pulses inside the loop. SABRE spectra were acquired with (A)  $\text{PTF} = 6.2 \text{ mT}$  and (B)  $\text{PTF} \sim 50 \mu\text{T}$ . Full width at half maximum values for the SHARPER spectra include the effects of the matched filter. (Section 3.4.1, Chapter 3)

The results showing the performance of *sel*SHARPER HPT with the SABRE-enhanced mixture of DFP and DFMP described previously are shown in Figure 4.17. The signals arising from these molecules are separated by 11.1 ppm ( $\sim 450 \text{ Hz}$  at 1 T), providing a good selectivity test. As only one signal can be targeted in each scan, the shake-and-drop experiment was repeated twice to collect spectra for both DFP and DFMP. This could be simplified by using automated bubbling setups to perform multiple scans.<sup>75,83,86</sup> This would be straightforward to implement as SHARPER was previously shown to minimise signal distortion due to bubbling.<sup>103</sup>

Given that these molecules hyperpolarised most efficiently at different polarisation transfer fields (6.2 mT for DFMP and  $\sim 50 \mu\text{T}$  for DFP), the choice of magnetic field during shake-and-drop experiments provided an additional layer of selectivity. For example, when using  $\text{PTF} = 6.2 \text{ mT}$  signals from DFMP are greatly enhanced, whilst minimal enhancement is seen for DFP (Figure 4.17 A), facilitating the removal of off-resonance

Table 4.2:  $T_2^S$  and  $\Delta_{1/2}^S$  values for the mixture sample

| Experiment                    | 1               |                      | 2             |                      |
|-------------------------------|-----------------|----------------------|---------------|----------------------|
|                               | $T_2^S$ \ms     | $\Delta_{1/2}^S$ \Hz | $T_2^S$ \ms   | $\Delta_{1/2}^S$ \Hz |
| SABRE- <i>sel</i> SHARPER     | $98 \pm 1$      | 3.24                 | $287 \pm 1$   | 1.11                 |
| SABRE- <i>sel</i> SHARPER HPT | $277.5 \pm 0.4$ | 1.15                 | $1170 \pm 20$ | 0.27                 |

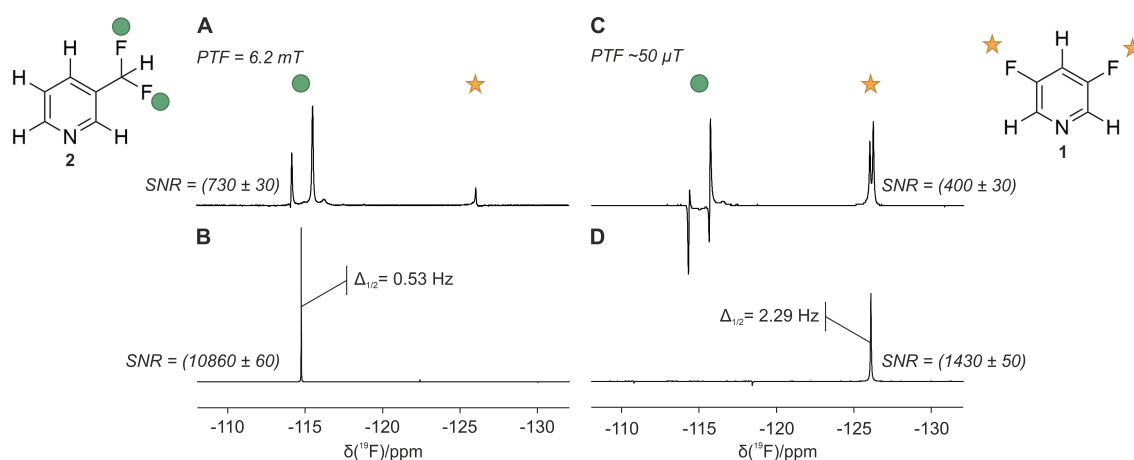


Figure 4.17: Comparison between SABRE-enhanced  $^{19}\text{F}$  benchtop NMR spectra with (A,C) standard and (B,D) *sel*SHARPER HPT acquisition for a mixture containing DFP and DFMP. SABRE spectra were acquired with (A,B)  $\text{PTF} = 6.2 \text{ mT}$  and (C,D)  $\text{PTF} \sim 50 \mu\text{T}$ . SABRE-*sel*SHARPER HPT spectra were acquired with selection of DFMP in B and selection of DFP in D. All spectra were acquired in a single scan and were apodised by a matched exponential filter (Section 3.4.1, Chapter 3). The SNR values represent averages over three repeat experiments. Full width at half maximum values are shown for the SABRE-*sel*SHARPER HPT spectra. Vertical scales were increased as required to aid visualisation.

signals introduced by DFP. In contrast, when the sample was shaken under the Earth's magnetic field ( $\sim 50 \mu\text{T}$ ), a significant signal contribution from DFMP remained. As this

signal presented a strong anti-phase component, it was anticipated that the application of SHARPER would result in the partial cancellation of this signal, thus assisting in the selection process. Upon the application of *sel*SHARPER, the signal from DFP was preserved and collapsed with minimal presence of off-resonance artefacts.

The incomplete removal of artifacts achieved with *sel*SHARPER HPT may be a reasonable compromise to achieve improved sensitivity. Signal-to-noise enhancement factors for DFP and DFMP were 3.6-fold and 15-fold respectively, a significant improvement compared to those obtained for the fully selective version, in particular for DFMP. This is a reflection of the reduced effective relaxation seen when using a hard pulse train. Indeed,  $T_2^S$  values obtained with *sel*SHARPER HPT for the mixture of DFP and DFMP were only marginally larger than those obtained with the non-selective SHARPER pulse sequence (Tables 4.1 and 4.2).

## 4.6 Conclusion

In this chapter, the signal enhancing properties obtained by combining SABRE and the multiplet-refocusing pulse sequence SHARPER were explored on a benchtop NMR (1 T) spectrometer. The technique was tested on a set of fluorinated pyridines possessing a range of homo- and heteronuclear  $J$  couplings: 3,5-difluoropyridine, 3-(difluoromethyl)pyridine, and 3,4,5-trifluoropyridine. Signal-to-noise ratio enhancements of up to 360 were obtained for  $^{19}\text{F}$  NMR measurements by applying SABRE under optimised polarisation transfer field conditions. By applying SHARPER, a further SNR improvement of up to 17 times was achieved by removing peak splitting due to heteronuclear  $J$  couplings and broadening due to field inhomogeneity. Through the use of shorter chunk lengths, SHARPER was also able to remove homonuclear  $J$  couplings and chemical shift differences in 3,4,5-trifluoropyridine, producing a SNR gain by a factor of 5700 compared to a standard pulse-and-collect experiment.

A sensitivity optimised selective variation of SHARPER, *sel*SHARPER HPT, was tested on a mixture of 3,5-difluoropyridine and 3-(difluoromethyl)pyridine. This variation min-

imised the use of pulsed field gradients and selective refocusing pulses compared to other selective SHARPER pulse sequences.<sup>103,104</sup> As a result, signal loss due to relaxation between acquisition steps was minimised and narrower linewidths were obtained. The use of SABRE-*sel*/SHARPER HPT enabled the isolation of each of the target signals and resulted in SNR enhancements of 630-fold and 4300-fold for 3,5-difluoropyridine and 3-difluoromethylpyridine, respectively.

In the next chapter, the sensitivity enhancing properties of SABRE-SHARPER will be applied to reduce detection limits in the quantitative analysis of low concentration samples of 3,5-difluoropyridine.

## Chapter 5

# Low Micromolar Detection and Quantification of Fluoropyridines

In the previous chapter, the combination of SABRE and the multiplet refocusing pulse sequence SHARPER was explored as a strategy to enhance the sensitivity of  $^{19}\text{F}$  benchtop NMR measurements. This approach produced up to 5700-fold SNR enhancements for molecules exhibiting peak splitting due to heteronuclear and/or homonuclear  $J$  couplings and chemical shift differentiation. By drastically improving its sensitivity, SABRE-SHARPER makes  $^{19}\text{F}$  benchtop NMR measurements better suited to the analysis of low-concentration samples. The sensitivity required for these low-concentration measurements often demands the use of high-cost and high-maintenance instrumentation. By breaking the link between instrumentation cost and sensitivity, SABRE-SHARPER makes such measurements more accessible.

In practice, there are a few obstacles that need to be addressed for SABRE-enhanced benchtop NMR spectroscopy to gain widespread use in analytical applications. For example, the minimum concentration of a target molecule that can be probed under standard SABRE conditions is set not by the sensitivity of the measurement system, but by the concentration of pre-catalyst used in the sample preparation. Such a restriction arises from the activation requirements of the SABRE complex: at least three units of target molecule need to be

present per unit of pre-catalyst to form a stable complex.<sup>81,155</sup> This constraint makes the exploration of limits of detection more challenging.<sup>81</sup>

The restricted scope of SABRE-compatible molecules presents another impediment for the broad adoption of this approach in analytical applications. In its standard form, SABRE-hyperpolarisation has been shown to be effective for ‘well-behaved’ ligating molecules, most commonly nitrogen-based heterocyclic molecules.<sup>26,132–140</sup> This represents a small proportion of the total chemical space of molecules of analytical interest, restricting the potential use of SABRE-enhanced benchtop NMR to a few localised analytical problems.

A third obstacle limiting the use of SABRE-hyperpolarised NMR in analytical chemistry is that quantification is challenging.<sup>81,82</sup> The intrinsic quantitative nature of NMR is lost in hyperpolarised experiments as the proportionality factor relating signal and number of nuclei is no longer constant. Furthermore, the complex interplay of exchange processes that take place during SABRE mean that the dependence of hyperpolarised signals on analyte concentration cannot be easily modelled in most cases,<sup>82</sup> which is the underlying requirement of quantitative analysis. This restricts the usefulness of SABRE-enhanced benchtop NMR to analytical problems requiring qualitative results, *e.g.* screening methods aiming to detect the presence of an analyte or group of analytes.<sup>177</sup> However, in many cases, it is imperative that measurements produce numerical results as an estimation of how much of an analyte is present to trigger decision making. Such situations cannot be reliably addressed *via* SABRE-enhanced measurements.

Conveniently, the use of an auxiliary substrate, or co-substrate, has been shown to address all three of these limitations. By using a co-substrate, the link between the concentrations of target analyte and pre-catalyst is broken, as the presence of one or more co-substrates facilitates SABRE complex activation.<sup>81</sup> This enables low-concentration detection of target molecules. Additionally, co-substrates have been shown to enable SABRE-hyperpolarisation of weakly-binding, sterically-hindered<sup>163</sup> or bidentate ligands<sup>202,203</sup> that do not form stable SABRE complexes. This greatly extends the scope of analytes that can be probed using SABRE hyperpolarisation. Lastly, the use of co-substrates and sub-stoichiometric amounts of a target analyte, *i.e.* less than three times the concentration of

iridium catalyst, has been previously shown to lead to linear relationships between hyperpolarised signal and the amount of target analyte, making quantification possible.<sup>81,82</sup>

In this chapter, the use of a co-substrate, in particular dimethylsulfoxide, will be investigated in conjunction with the previously studied SABRE substrate DFP to explore the analytical potential of the SABRE-hyperpolarised benchtop NMR technique, particularly in terms of limits of detection and quantification.

## 5.1 Background Theory

### 5.1.1 SABRE Hyperpolarisation Using Co-substrates

#### 5.1.1.1 Reducing Limits of Detection

Eshuis *et al.* proposed the use of co-substrates as a strategy to explore lower limits of detection for hyperpolarised pyridine measurements.<sup>81</sup> The authors found that as the concentration of substrate relative to pre-catalyst is decreased to approach stoichiometric conditions (*i.e.* 3 units of substrate per unit of pre-catalyst), the SABRE-active tris-substituted species decreased in concentration. Instead, the formation of a SABRE-inactive species, which they proposed contained solvent (methanol) as a ligand, was favoured. The formation of such a species was not deemed a consequence of the stronger binding affinity of the solvent to the iridium centre, but a result of the sheer excess of solvent molecules in the sample.<sup>204</sup> Based on these findings they concluded that in order to achieve hyperpolarisation of the substrate at lower (sub-stoichiometric) concentrations, the formation of this SABRE-inactive species ought to be inhibited.

To this end, they proposed the addition of a secondary substrate, or co-substrate, with a stronger binding affinity to the metal centre to out-compete the solvent.<sup>81</sup> As a further requirement, this co-substrate ought to exhibit a binding affinity that is lower or comparable to that of the target molecule, to prevent its complete displacement. Additionally, the ideal co-substrate would form a species containing both the co-substrate and the substrate, as shown in Figure 5.1, with a suitable lifetime for efficient SABRE-hyperpolarisation, and its <sup>1</sup>H signals would not overlap with those of the molecule of interest.

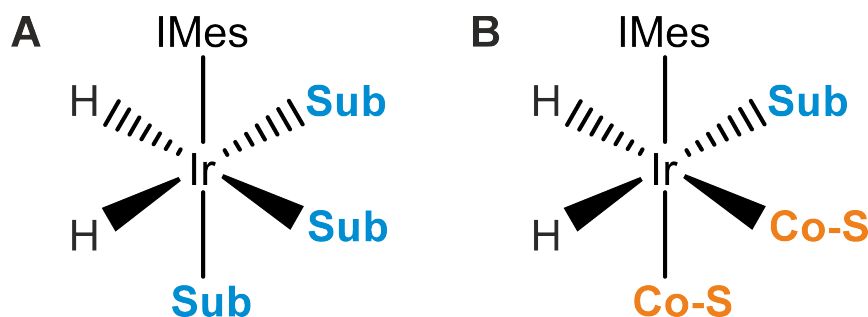


Figure 5.1: Schematic representation of the SABRE polarisation transfer catalysts producing signals enhancements for the target substrate ('Sub') in standard conditions (A) and with addition of co-substrates (B). The binding sites of the iridium complex are filled with three units of the target substrate under standard SABRE conditions, and a mixture of the target substrate and the co-substrate ('Co-S') when this is added to the sample.

The requirements presented in the previous paragraph inform the co-substrate selection process in terms of its chemistry, but other practical aspects should be taken into account for low-concentration detection to be possible. One such aspect is the concentration of co-substrate to be used, as this needs to be present in an excess relative to the amount of pre-catalyst.<sup>81</sup> Presumably, this requirement stems from the need to fill the binding sites of the active hexacoordinated iridium complex with the co-substrate. This role cannot be fulfilled by the target molecule as it is present in sub-stoichiometric amounts. When samples are prepared in methanol, the solvent provides an alternative ligand to complete the coordination sphere, but as previously mentioned, its binding should be inhibited to avoid deactivation of the SABRE complex.

Eshuis *et al.* proposed 1-methyl-1,2,3-triazole (mtz) as a suitable co-substrate that fulfilled the previously mentioned requirements.<sup>81</sup> Using mtz in SABRE experiments at 14.1 T, they were able to detect as low as 2  $\mu$ M of pyridine with a single scan. The hyperpolarised signal detected in this case was produced by an active catalyst species containing two units of mtz and one of pyridine, which took an equatorial position. By switching the NHC in these experiments from IMes to 1,3-bis(2,4,6-trimethylphenyl)-4,5-dihydroimidazole-2-ylidene (SIMes), ligand dissociation rates were optimised and a lower

limit of detection of 0.5  $\mu\text{M}$  was achieved for pyridine. In a real-life application of this approach, Tickner *et al.* reported the analysis of extracted nicotine in electronic cigarettes, detecting 74  $\mu\text{M}$  of nicotine at 9.4 T *via* SABRE.<sup>205</sup>

### 5.1.1.2 Quantification

A further extension of the use of co-substrates when the target analyte is present in sub-stoichiometric concentrations is that a linear relationship between the hyperpolarised signal integral and the analyte concentration can be achieved, as discovered by Eshuis' work using mtz.<sup>81</sup> To rationalise these findings, the authors proposed a model (Eq. 5.1) linking the ratio of free ( $[S]_{free}$ ) to bound ( $[S]_{bound}$ ) analyte concentration in sub-stoichiometric conditions, to the added concentrations of co-substrate ( $C_{cS}$ ) and pre-catalyst ( $C_M$ ), and the relative affinity of substrate and co-substrate to the metal centre ( $K_{eq}$ ).

$$\frac{[S]_{free}}{[S]_{bound}} = 3 \times K_{eq} \frac{[cS]_{free}}{[cS]_{bound}} \approx 3 \times K_{eq} \frac{C_{cS} - 3 \times C_M}{3 \times C_M} \quad (5.1)$$

According to this model, the ratio of free-to-bound analyte is fixed and determined by the concentration of co-substrate in the sample. From this, it follows that when the concentration of free analyte in solution increases, so would the concentration of bound analyte in a linear way, which is expected to be directly proportional to the detected hyperpolarised signal. In this way, a linear relationship between substrate concentration and hyperpolarised signal could be attained at a fixed co-substrate concentration.

Indeed, through this strategy Eshuis *et al.* reported the low-micromolar quantification of aromatic N-heterocycles using SABRE-hyperpolarised  $^1\text{H}$  measurements at 14 T *via* the standard addition method (SAM).<sup>82</sup> In this extension of the original work, the combination of 15 components in low individual concentrations, but which collectively amount to supra-stoichiometric conditions, were used in lieu of a single co-substrate. This allowed them to perform the quantification of four of these components (nicotinamide, pyrazine, isoxazole, and quinazoline) at low micromolar concentrations ( $\sim 10 \mu\text{M}$ ) with a 5 to 20% relative uncertainty in a complex matrix. Remarkably, hyperpolarisation allowed for this quantification process to take place with a series of single-scan experiments to collect the 7 steps of

the standard addition process. This represents a drastic improvement in analytical throughput considering 11 hours of signal-averaging were necessary to acquire a non-hyperpolarised spectrum with adequate signal-to-noise ratio at low micromolar concentrations.

### 5.1.1.3 Extending the Scope of Analytes

An additional benefit of using co-substrates is that they can lead to larger enhancement factors through optimisation of the SABRE process, even when present in supra-stoichiometric concentrations. For example, acetonitrile has been used as a co-substrate during the hyperpolarisation of imidazole, resulting in a 1.6-fold improvement in its  $^1\text{H}$  enhancement factor.<sup>140</sup> The authors attributed this improvement of signal enhancement to an increase in ligand and hydrogen exchange rates, which they linked to an increase in SABRE efficiency. This was further explored by Rayner *et al.* using dimethylsulfoxide (DMSO) and diphenylsulfoxide (DPSO) during 2,5-lutidine hyperpolarisation studies.<sup>163</sup> Although both sulfoxide co-substrates led to SABRE-hyperpolarised signals, enhancement factors were 3 times larger for DPSO ( $\varepsilon_{1\text{H}} = 215$  for DMSO *vs.*  $\varepsilon_{1\text{H}} = 723$  for DPSO in dichloromethane- $d_2$ ). This difference in performance was attributed to a larger substrate exchange rate in the complex formed when using DPSO. As this sulfoxide exhibits a larger cone angle than DMSO, the steric congestion introduced by the co-substrate reduced its binding affinity for the metal centre, which likely contributed to this increased exchange rate. This exchange rate was brought closer to the optimal value ( $k_D = 4.5 \text{ s}^{-1}$ ,<sup>76,158,159</sup>) by reducing the temperature of the experiment, thus increasing signal enhancement factors.<sup>163</sup>

Notably, hyperpolarisation of 2,5-lutidine was not seen under standard SABRE conditions without a co-substrate.<sup>163,206</sup> This is commonly the case for *ortho*-substituted pyridines, as the steric constraint around the binding position prevents the formation of stable tris-substituted species. The use of DPSO to overcome this limitation for a set of 12 sterically-hindered substrates by Rayner *et al.*<sup>163</sup> highlights the additional benefit of using co-substrates: providing a route to form less sterically demanding polarisation transfer complexes. Similar work conducted by Mandal and co-workers using either acetonitrile or allylamine as co-substrates demonstrated the SABRE hyperpolarisation of a series of

*ortho*-substituted N-heterocyclic compounds, which would otherwise hyperpolarise inefficiently or not at all.<sup>166</sup> These relatively small and linear co-substrates were expected to effectively relieve the steric congestion introduced by substitutions adjacent to the binding site or generally bulky ligands.

Co-substrates have further contributed to extending the scope of hyperpolarisable analytes by including multidentate ligands. For example, sulfoxide co-substrates were employed to hyperpolarise bidentate ligands such as pyruvate<sup>173,207,208</sup> and ketoisocaproate<sup>209</sup>. In these cases, the co-substrate stabilises the polarisation transfer complex by completing the coordination sphere. Studies on sulfoxides have shown that these are beneficial co-substrates as they are linked to rapid hydrogen exchange rates,<sup>202</sup> a necessary step to refresh polarisation on the transfer catalyst. Moreover, the sulfoxide moiety is of a moderate to low binding affinity, meaning weakly binding targets such as pyruvate are not out-competed.<sup>208</sup>

Amongst other examples of bidentate ligands whose hyperpolarisation was enabled by co-substrates, it is relevant to mention the case of large sized EGTA-based (EGTA: ethylene glycol-bis( $\beta$ -aminoethyl ether)-*N,N,N',N'*-tetraacetic acid) substrates.<sup>203</sup> Acetonitrile was used to aid the hyperpolarisation of such molecules, which are amongst the largest substrates ( $\sim 500$  Da) to be hyperpolarised by SABRE at the time of writing, showing the true potential of co-substrates to aid with bulky substrates. Another notable example is the hyperpolarisation of amino acids using pyridine as a co-substrate.<sup>167</sup> In this case, co-substrates seem to play a crucial role in continuous  $p$ -H<sub>2</sub> refreshment, which is key to achieve a build-up of hyperpolarised analyte in free solution. As amino acids bind strongly to the iridium centre through the amino- and carboxyl groups, their dissociation is inhibited, and so is the association of fresh  $p$ -H<sub>2</sub>.<sup>210</sup> However, the  $p$ -H<sub>2</sub> refreshment cycle can be activated by the dissociation of the co-substrate, in this case pyridine, when present in an equatorial position.<sup>167</sup>

In light of the several benefits of using co-substrates presented so far, its combination with SABRE-hyperpolarised benchtop NMR spectroscopy can be thought of as advantageous. This line of research, unexplored previously in the literature, will be the focus of the next section.

## 5.2 Choice of Test System

As a model system, 3,5-difluoropyridine (DFP, **1**, Figure 5.2) was investigated as the target analyte. This substrate was chosen as its SABRE hyperpolarisation was studied in the previous chapter (Chapter 4), as well as by others.<sup>193</sup> In Chapter 4, the formation of multiple polarisation transfer catalysts containing DFP was discussed, namely tris-substituted and solvent-containing species. The fact that only one of these species led to hyperpolarisation suggested that the efficiency of this process could be potentially improved by forming a more stable polarisation transfer catalyst using co-substrates. Additionally, as this target molecule exhibits both  $^1\text{H}$  and  $^{19}\text{F}$  hyperpolarised signals, it enables the comparison of analytical performance parameters such as limit of detection and quantification accuracy for both nuclei.

As discussed above, dimethylsulfoxide (DMSO, **4**, Figure 5.2) has been extensively studied for use as a SABRE co-substrate in the literature.<sup>202,207,208</sup> Furthermore, it aligns with the requirements previously stipulated by Eshuis and co-authors,<sup>81</sup> as it is expected to have a stronger binding affinity to the iridium centre than the solvent, but comparable or lower to that of the substrate.<sup>163,208,211</sup> Additionally, the fast ligand dissociation rate of mixed complexes containing DMSO<sup>202</sup> is considered advantageous as it would increase the throughput of the polarisation transfer catalyst. In terms of interference, DMSO would not pose a problem in either  $^{19}\text{F}$  or  $^1\text{H}$  measurements as it is fluorine-free and only produces a singlet signal in  $^1\text{H}$  NMR spectra at *ca.*  $\delta$  2.65 in methanol at room temperature, well removed from the typical aromatic proton region of  $\delta$  7 to 9 where the substrate peaks are expected to appear.

Diphenylsulfoxide was also considered as an alternative co-substrate, as previous reports comparing DMSO and DPSO showed larger enhancement factors were achievable with the latter.<sup>163</sup> However, DPSO was deemed unsuitable for applications in the sub-stoichiometric regime as its larger cone angle (by 10% *vs.* DMSO<sup>212</sup>) deters the formation of bis- or tris-substituted DPSO species.<sup>163</sup> As a consequence, and keeping in mind that the analyte is present in sub-stoichiometric concentrations, pre-catalyst activation would likely be in-

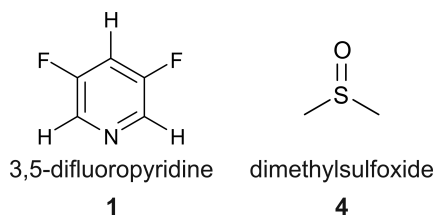


Figure 5.2: Chemical structures of the substrate 3,5-difluoropyridine (**1**) and the co-substrate dimethylsulfoxide (**4**).

complete or favour the formation of SABRE-inactive complexes containing ligated solvent. Therefore, DMSO was not tested as a potential co-substrate.

## 5.3 SABRE Hyperpolarisation of the Test Molecule

### 5.3.1 $^1\text{H}$ and $^{19}\text{F}$ Hyperpolarisation

In order to test the adequacy of the model presented in the previous section, it was necessary to investigate if a SABRE-active species was formed when both DFP and DMSO are combined with the pre-catalyst, as well as, the structure of the species involved in said hyperpolarisation process. Following that, the SABRE activity of this species was studied at progressively decreasing substrate concentrations to understand the behaviour of the hyperpolarised signal in the sub-stoichiometric regime, focusing on  $^1\text{H}$ ,  $^{19}\text{F}$ , and  $^{13}\text{C}$  measurements and the optimal polarisation transfer field for each nucleus.

A sample containing 100 mM (each) of substrate DFP and co-substrate DMSO, and 5 mM of the standard SABRE pre-catalyst  $[\text{IrCl}(\text{COD})(\text{IMes})]$  in methanol was prepared according to the procedure described in Section 3.1.1 (Chapter 3), hyperpolarised using the shake-and-drop technique (Section 3.2, Chapter 3), and probed using pulse-and-collect  $^1\text{H}$  and  $^{19}\text{F}$  NMR experiments at 1 T (Section 3.3, Chapter 3). Enhancement factors for  $^1\text{H}$  and  $^{19}\text{F}$  measurements were calculated as previously described (Section 3.7.2, Chapter 3).

A standard polarisation transfer field of 6.2 mT was used to probe SABRE-hyperpolarised  $^1\text{H}$  signals, allowing for a direct comparison with results from Chapter 4.

Under these conditions,  $^1\text{H}$  SABRE hyperpolarisation yielded an enhancement factor of  $(5840 \pm 60)$ , which represented a *ca.* 2-fold improvement over the results obtained without co-substrates ( $\epsilon_{^1\text{H}} = (3000 \pm 300)$ , Chapter 4). Such a difference in enhancement factor values suggested that a new species was formed that contains both DFP and DMSO, and that this species was more efficient at polarisation transfer to  $^1\text{H}$  nuclei in the substrate. The change in hyperpolarised signal profile (Figure 5.3A) was additional evidence of the formation of a new polarisation transfer catalyst, which led to the hyperpolarisation of new spin terms.

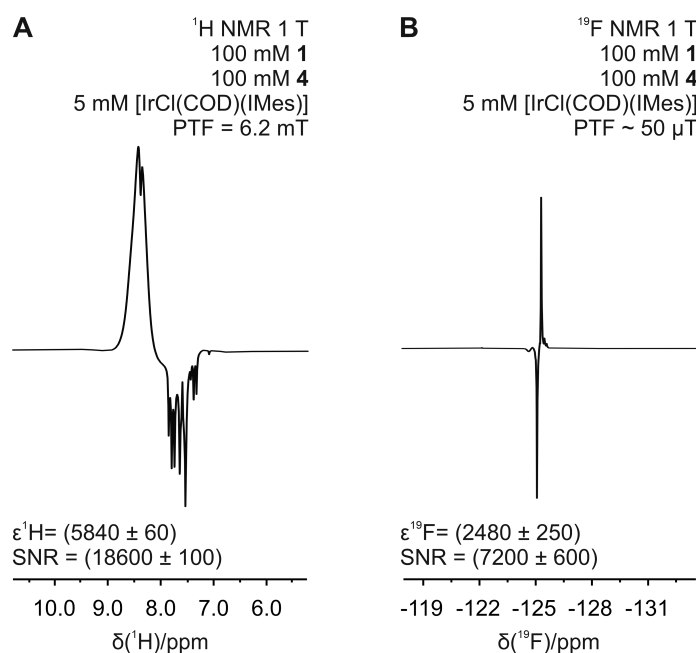


Figure 5.3: SABRE-hyperpolarised  $^1\text{H}$  (A) and  $^{19}\text{F}$  (B) NMR spectra of DFP with DMSO as a co-substrate. The sample was prepared with 100 mM of DFP, 100 mM of DMSO, and 5 mM of  $[\text{IrCl}(\text{COD})(\text{IMes})]$  in methanol. The spectra shown here were acquired with the PTF that yielded the largest enhancements at this concentration: 6.2 mT for  $^1\text{H}$  and  $\sim 50 \mu\text{T}$  for  $^{19}\text{F}$ .

Fluorine-detected SABRE experiments on the same sample using a PTF  $\sim 50 \mu\text{T}$  showed that the system under investigation also exhibited fluorine hyperpolarisation (Figure 5.3B). In a similar way to  $^1\text{H}$  measurements, the addition of DMSO improved SABRE

enhancement factors for  $^{19}\text{F}$ , but in this case the improvement was tenfold ( $\varepsilon_{^{19}\text{F}} = (2480 \pm 250)$  with co-substrates *versus*  $\varepsilon_{^{19}\text{F}} = (270 \pm 20)$  without, Chapter 4). SABRE-enhanced  $^{19}\text{F}$  NMR experiments using DMSO in supra-stoichiometric conditions also exhibited an anti-phase profile as the main detected signal, once again suggesting that the active species producing this hyperpolarised signal is different from the one seen in the absence of a co-substrate.

The increase in both  $^1\text{H}$  and  $^{19}\text{F}$  enhancement factors when using co-substrates suggests that this new species is more effective as a polarisation transfer catalyst than the active methanol-containing species without co-substrates described in Chapter 4 (Section 4.3). As previously discussed, the improvement of SABRE efficiency through the use of co-substrates has been reported before.<sup>140,163,189</sup> Recently, Tickner *et al.*<sup>189</sup> investigated the hyperpolarisation of dichloro- and dibromopyridine at high magnetic fields when using sulfoxide co-substrates. In this work, the authors observed a significant improvement in  $\varepsilon_{^1\text{H}}$  when adding DMSO as a co-substrate. By doing exchange spectroscopy studies (EXSY) they discovered that without co-substrates, the active species (which they proposed followed a  $[\text{IrCl}(\text{H})_2(\text{IMes})(\text{L})_2]$  form) exchanges its ligand at a faster rate than when DMSO is used as a co-substrate. Moreover, they observed that the exchange rate constant with DMSO is much closer to the optimal value of  $4.5 \text{ s}^{-1}$ , which was expected to yield better  $^1\text{H}$  signal enhancements (Section 2.2.2.3, Chapter 2). Although these results were not obtained for fluorinated pyridines, the substrates under investigation are expected to behave similarly as ligands, therefore extrapolation of these results to DFP is a reasonable starting hypothesis.

To confirm that the active species indeed contained both DFP and DMSO, characterisation studies using high-field (7 T) multi-nuclear NMR experiments were conducted, which revealed that the structure of the main active species containing DFP was  $[\text{IrCl}(\text{H})_2(\text{IMes})\text{-}(\mathbf{1})(\mathbf{4})]$  (Figure 5.4, **5**). Characterisation results are presented in Figure 5.5 and Table 5.1 and described in detail in Section 3.8.1 (Chapter 3). Analogous structures were reported when using DMSO as a co-substrates with dibromo- and dichloropyridine<sup>189</sup> and 2,5-lutidine.<sup>163</sup> This structure confirms that the selected test system is suitable for this investigation as it contains both DFP and DMSO, with DFP in an equatorial position,

which is vital for efficient hyperpolarisation to take place.<sup>132,142</sup>

Closer inspection of the active species reveals additional attributes that make this system ideal. For example, the absence of DFP *trans* to IMes means that the entire pool of the target molecule can participate in the hyperpolarisation process. This point is better illustrated if the opposite is considered: units of DFP in the axial position would be locked in place (*i.e.* exchanging slowly) and not subject to polarisation transfer. Thus, the pool of molecules that can be probed is reduced and as a result, so is the effective sensitivity of the measurement. Another relevant attribute of this system is that a chloride ligand occupies the other equatorial position of this species. The absence of complex species without this ligand in equatorial position (Figure 5.6) suggests this ligand exchanges slowly, if at all, possibly as the electrostatic interaction between the positive charge of the iridium centre and the negative charge of the ligand would have to be overcome for dissociation to take place. This is thought to be beneficial as chloride is not expected to hyperpolarise efficiently as <sup>35</sup>Cl and <sup>37</sup>Cl are spin-3/2 nuclei with low gyromagnetic ratio. The use of co-substrates without SABRE-active spins (*e.g.* fully deuterated species) has been reported before and shown to increase enhancement factors for the substrate, as the polarisation is channeled solely to the target.<sup>142,151,213,214</sup>

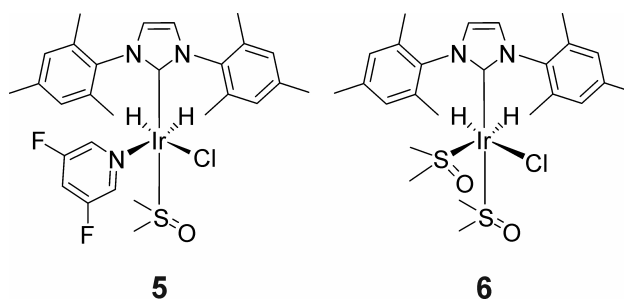


Figure 5.4: Main SABRE-active species (**5** and **6**) in SABRE samples containing DFP and DMSO with 5 mM [IrCl(COD)(IMes)] in protio and deuterated methanol.

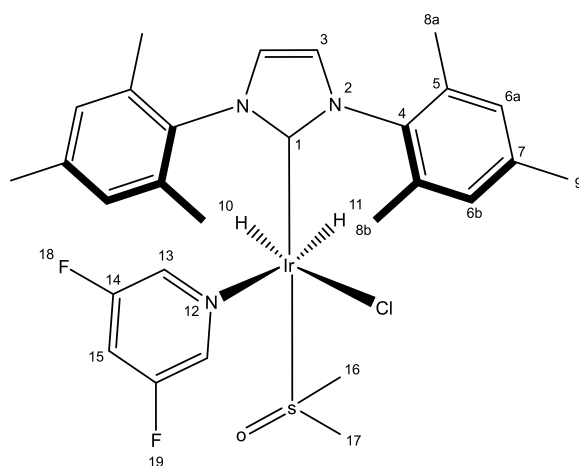


Figure 5.5: Proposed structure for the active SABRE complex containing DFP and DMSO.

In order to explore low limits of detection with this system, it was necessary to establish whether the formation of a suitable species could be observed at sub-stoichiometric concentrations relative to the pre-catalyst. To gain that information, samples with decreasing concentrations of DFP were analysed through high-field (9.4 T)  $^1\text{H}$  NMR and SABRE-enhanced  $^1\text{H}$  benchtop (1 T) NMR measurements. By comparing these two measurements, it was possible to learn which species form and their relative amounts (from non-hyperpolarised high-field NMR measurements), as well as, which species are SABRE active under normal operational conditions (hyperpolarised 1 T measurements).

Inspection of the hydride signal region of the spectra revealed that the main SABRE-active species seen in supra-stoichiometric conditions, **5**, is preserved in the sub-stoichiometric regime (Figure 5.6 A and B, star,  $\delta$  -23.3 and  $\delta$  -23.7). Notably, the signal intensity of the non-hyperpolarised hydride peaks decreases with substrate concentration (Figure 5.6A, star). This is important as it shows that the formation of this active species is sensitive to the amount of substrate present in solution. Furthermore, hyperpolarised signals for **5** follow a similar trend when the concentration of DFP decreases, a behaviour that is crucial for quantitative measurements.

Table 5.1: High-field NMR characterisation of the SABRE active complex containing DFP and DMSO.

| Resonance number | $\delta$ $^1\text{H}$ | $\delta$ $^{13}\text{C}$ | $\delta$ $^{19}\text{F}$ |
|------------------|-----------------------|--------------------------|--------------------------|
| 1                | -                     | 159.64                   | -                        |
| 2                | -                     | -                        | -                        |
| 3                | 7.16                  | 122.83                   | -                        |
| 4                | -                     | 138.40                   | -                        |
| 5                | -                     | 136.20                   | -                        |
| 6                | a 6.84/ b 6.77        | a 128.25/ b 128.30       | -                        |
| 7                | -                     | 139.25                   | -                        |
| 8                | a 2.14 / b 2.13       | a 18.51/b 19.00          | -                        |
| 9                | 2.26                  | 20.85                    | -                        |
| 10               | -23.3 (d, 7.9 Hz)     | -                        | -                        |
| 11               | -23.7 (d, 7.9 Hz)     | -                        | -                        |
| 12               | -                     | -                        | -                        |
| 13               | 8.55                  | 139.34                   | -                        |
| 14               | -                     | 159.52                   | -                        |
| 15               | 7.63                  | 111.10                   | -                        |
| 16, 17           | 2.72 / 3.10           | 43.14 / 55.84            | -                        |
| 18, 19           | -                     | -                        | -124.96                  |

In addition to the signals for **5**, the hydride signal region of the spectrum reveals the presence of a second major species at  $\delta$  -15.5 and  $\delta$  -21.5, corresponding to  $[\text{IrCl}(\text{H})_2(\text{IMes})(\mathbf{4})_2]$  (**6**, green triangles in Figure 5.6), as previously reported.<sup>202</sup> This species decreased in relative intensity when DFP was present in higher concentrations (Figure 5.6A). Such a finding suggests that the formation of **5** is favoured over that of **6**, even when there is an excess of DMSO relative to DFP of up to 1250:1, supporting the assumption that DFP has a higher binding affinity to the metal centre than DMSO.

This secondary species containing DMSO plays an important role when low concen-

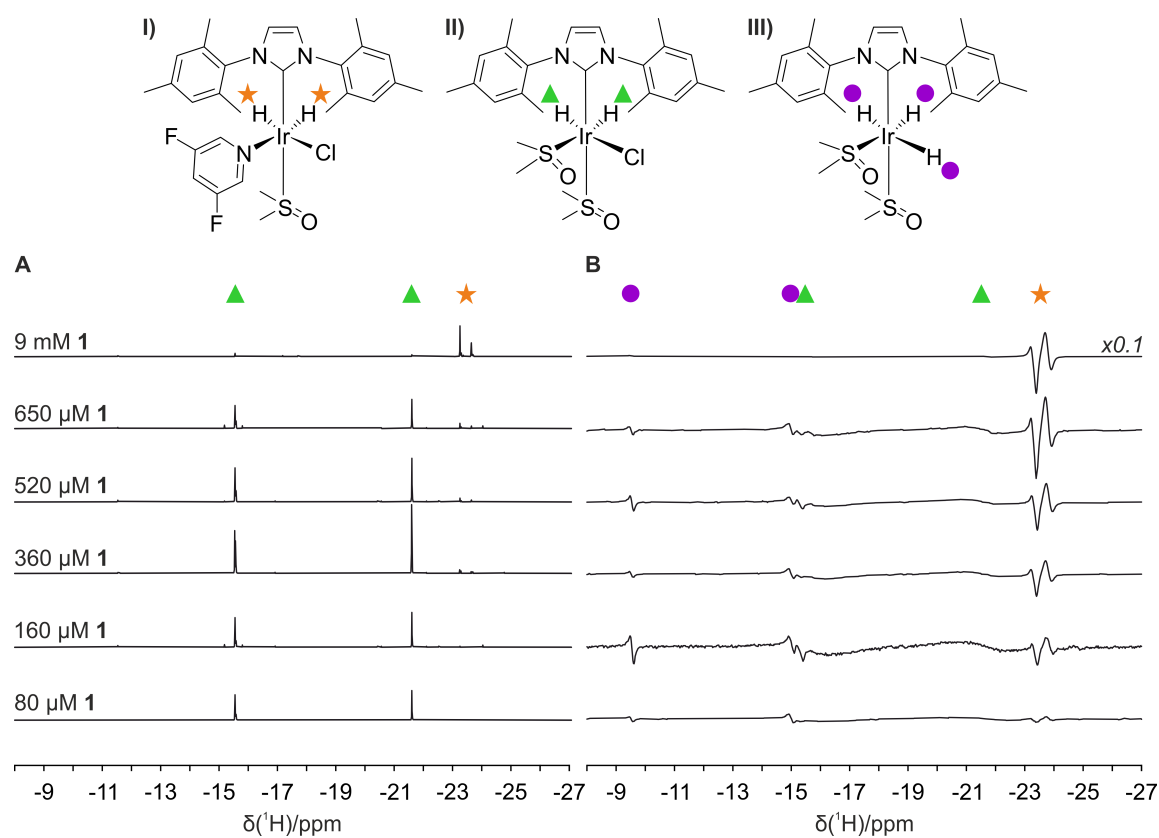


Figure 5.6:  $^1\text{H}$  NMR spectra zoomed in to the hydride region ( $\delta$  - 8 to - 27 ) for SABRE samples containing sub-stoichiometric concentrations of DFP (9 mM to 80  $\mu\text{M}$ ), 100 mM of DMSO, and 5 mM of  $[\text{IrCl}(\text{COD})(\text{IMes})]$  at 9.4 T (A, non-hyperpolarised, 253 K) and at 1 T (B, hyperpolarised, 301 K). Signals indicated by the orange stars correspond to the hydride ligands of the same SABRE-active species (**5**, I) that produces the hyperpolarised signals observed in  $^{19}\text{F}$  NMR spectra, those shown by the green triangles correspond to complex **6** (II), which at 301 K (B) appear as broad signals due to fast exchange. Signals shown by purple circles in B correspond to a tris-hydride species (III) previously described in the literature.<sup>211</sup>

trations of substrate are probed, as it stabilises the transfer catalyst that composes the ‘hyperpolarisation machinery’ of the system. The rapid ligand exchange rate for **6**, evidenced by the broad hydride signals (Figure 5.6B, triangle) and supported by previous reports,<sup>163,202</sup> is key to this. A faster ligand dissociation rate increases the processing rate of the complex, thus probing more molecules per unit of time. The increased throughput of the hyperpolarisation machinery is likely to be beneficial when lower concentrations of the target analyte are used, as it would increase the probability of interaction between the target substrate and the complex.

A third asymmetric species was observed with hydride signals at  $\delta$  -9.5 and -15.3 (purple circles in Figure 5.6B). This species is thought to correspond to a trihydride species of formula  $[\text{Ir}(\text{H})_3(\mathbf{4})_2(\text{IMes})]$ , based on recent studies by Tickner and co-workers.<sup>211</sup> As this species does not contain the target analyte and it is formed in small amounts (not detected in non-hyperpolarised experiments), the formation of this species was not thought to have a significant impact on the performance of SABRE-enhanced benchtop NMR measurements. Nevertheless, as this species was also observed for other target analytes, it is further discussed in Chapter 6.

In the sub-stoichiometric regime, the observed hyperpolarised signal corresponded to that of the bound substrate in **5** and not the free substrate, DFP, as observed in supra-stoichiometric conditions. This was evidenced by the difference in chemical shift seen in samples pre- and post-activation in non-hyperpolarised pulse-and-collect experiments at 1.4 T, a magnetic field chosen as it afforded better sensitivity than 1 T (Figure 5.7). The signals in the sample before activation were largely due to the free substrate, which was in equilibrium with a relatively small amount of the pre-activation complex  $[\text{Ir}(\text{COD})(\text{DFP})\text{IMes}]$  according to high-field NMR characterisation studies. Once the sample is activated, the proton and fluorine chemical shifts change ( $\Delta\delta = 0.34$  ppm for  $^{19}\text{F}$ ,  $\Delta\delta = 0.15$  and  $0.08$  ppm for *o*-/*p*- $^1\text{H}$ , respectively) and match those of the bound substrate in **5**, as seen in Figure 5.7 (bottom trace). This observation is aligned with results seen for a sub-stoichiometric pyridine system employing 1-methyl-1,2,3-triazole as a co-substrate, for which the authors estimated 80% of the available pyridine was in its bound state.<sup>81</sup>

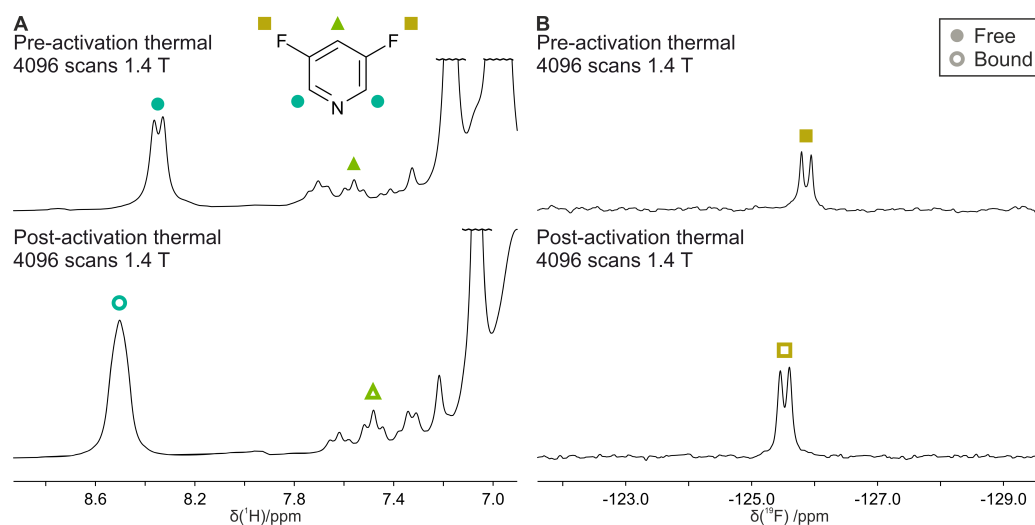


Figure 5.7: Non-hyperpolarised  $^1\text{H}$  (A) and  $^{19}\text{F}$  (B) NMR spectra acquired at 1.4 T for a sample in sub-stoichiometric conditions containing 20 mM of DFP, 50 mM of DMSO and 10 mM of  $[\text{IrCl}(\text{COD})(\text{IMes})]$ . The difference in chemical shift between pre-activation (top trace) and post-activation (bottom trace) spectra suggested that DFP was present in its bound form (**5**) post activation.  $^1\text{H}$  spectra was referenced to the solvent signal and  $^{19}\text{F}$  to the probe signal at  $\delta$  -72.

Interestingly,  $^{19}\text{F}$  enhancement factors for DFP in the sub-stoichiometric regime were optimised when SABRE experiments were conducted using a  $\text{PTF} = 6.2$  mT. This differed from supra-stoichiometric results, irrespective of the use of co-substrates, which showed larger enhancements when using  $\text{PTF} \sim 50$   $\mu\text{T}$ , a PTF that favours direct polarisation of  $^{19}\text{F}$  nuclei.<sup>134</sup> As the active catalyst, and hence the spin system, remained unchanged when moving to the sub-stoichiometric regime, a change in the efficiency of the polarisation transfer mechanism was deemed an unlikely explanation.

A possible explanation for this phenomenon stems from the difference in  $T_1$  relaxation rate for the different hyperpolarised spin terms preferentially formed at each PTF. Table 5.2 summarises  $T_1$  values for the detected hyperpolarised  $^{19}\text{F}$  signal corresponding to DFP, either in free solution in the supra-stoichiometric regime, or bound to the catalyst in the sub-stoichiometric regime, at PTF values of 6.2 mT and  $\sim 50$   $\mu\text{T}$ . Hyperpolarised

variable flip angle  $T_1$  experiments were carried out following the procedure described in Chapter 3, Section 3.6.  $T_1$  experiments conducted in the supra-stoichiometric regime at 6.2 mT revealed the presence of a fast-relaxing anti-phase term, and a slightly larger slow-relaxing in-phase term. Anti-phase signals arise from multi-spin terms which show faster relaxation rates as the number of possible relaxation pathways increases with the number of spins.<sup>215-217</sup>  $T_1$  experiments using PTF  $\sim 50 \mu\text{T}$  also exhibited the presence of both in-phase and anti-phase signals, but at this field the latter was approximately 10 times larger.

Table 5.2:  $T_1$  values in seconds for  $^{19}\text{F}$  hyperpolarised signals detected in SABRE experiments (Section 3.6, Chapter 3).  $T_1$  values are a mean of triplicate measurements and their standard uncertainties ( $k=1$ ) were calculated according to Section 3.7.3 (Chapter 3). The relative proportion of each signal profile (anti-phase or in-phase) is shown as an area percentage.

| [1]                 | Signal profile | PTF = 6.2 mT    |                          | PTF $\sim 50 \mu\text{T}$ |                          |
|---------------------|----------------|-----------------|--------------------------|---------------------------|--------------------------|
|                     |                | Area percentage | $T_1 \setminus \text{s}$ | Area percentage           | $T_1 \setminus \text{s}$ |
| 100 mM<br>(20 eq.)  | Anti-phase     | 42 %            | $(5.34 \pm 0.12)$        | 91 %                      | $(6.423 \pm 0.037)$      |
|                     | In-phase       | 58 %            | $(31.33 \pm 0.44)$       | 9 %                       | $(8.03 \pm 0.35)$        |
| 0.9 mM<br>(0.2 eq.) | Anti-phase     | -               | -                        | 100 %                     | $(1.810 \pm 0.027)$      |
|                     | In-phase       | 100%            | $(5.863 \pm 0.050)$      | -                         | -                        |

When repeating these experiments in the sub-stoichiometric regime (0.79 mM of DFP) at 6.2 mT, the in-phase signal exhibited a 5-fold decrease in hyperpolarised  $T_1$  values ( $T_{1,\text{sub}} = (5.863 \pm 0.050) \text{ s}$  vs  $T_{1,\text{supra}} = (31.33 \pm 0.44) \text{ s}$ ). This behaviour has been reported before,<sup>159</sup> and is consistent with longer residence times of the substrate in the active complex, as the scalar coupling network in the bound species favours longitudinal relaxation. A decrease in  $T_1$  values for signals corresponding to the bound substrate would

explain why  $^{19}\text{F}$  enhancement factors decrease at a PTF  $\sim 50 \mu\text{T}$ . In this case, the relaxation of these already short-lived terms is enhanced ( $T_{1,\text{sub}} = (1.810 \pm 0.027) \text{ s}$ ), thus capping the build up of polarisation that can be detected in solution. As a result, the longer-living in-phase signal detected at 6.2 mT would result in higher  $\varepsilon_{^{19}\text{F}}$ , even if this proton-relayed polarisation transfer mechanism is less efficient than the direct transfer mechanism observed at  $\sim 50 \mu\text{T}$ .<sup>134</sup>

In the seminal work on sub-stoichiometric analysis of substrates using co-substrates, Eshuis and co-workers proposed that the concentration of the co-substrate affects the proportion of target substrate bound to the active catalyst (Eq. 5.1).<sup>81</sup> As the bound proportion of the target substrate in solution is expected to be correlated to the SABRE activity, experiments were conducted to gauge how the concentration of co-substrate may affect hyperpolarisation efficiency of the target molecule. To this end, SABRE samples containing fixed amounts of DFP,  $(684 \pm 20) \mu\text{M}$ , and varying amounts of DMSO (5 to 50 equivalents relative to the pre-catalyst concentration) were prepared, and SABRE-hyperpolarised  $^1\text{H}$  and  $^{19}\text{F}$  spectra recorded.

When the resulting  $^1\text{H}$  and  $^{19}\text{F}$  SABRE-enhanced signals were plotted against the concentration of DMSO, a downward trend was observed at higher co-substrate concentrations (Figure 5.8 A and B). Although the intensity of the  $^1\text{H}$  signal only drops by 2% when the concentration of DMSO increases by 50 mM, the decrease in  $^{19}\text{F}$  hyperpolarised signal is more significant (9%) under equal conditions. Following Eshuis' model (Eq. 5.1), lower concentrations of co-substrate are to expected lead to a smaller free-to-bound substrate ratio. In other words, there are more units of bound substrate as the concentration of DMSO decreases. Given that substrate binding to the catalyst is a necessary step for hyperpolarisation to take place, it is a reasonable hypothesis that the more units of substrate that are bound at any given time, the more hyperpolarisation is expected to be observed.

Smaller equivalents of co-substrate also reduced the appearance of extra species containing DFP. These species, shown in Figure 5.9B as A and B, were thought to contain extra units of DMSO, thus explaining their formation at higher DMSO equivalents (Figure 5.9A). The formation of extra species was undesired as it meant that the amount of available

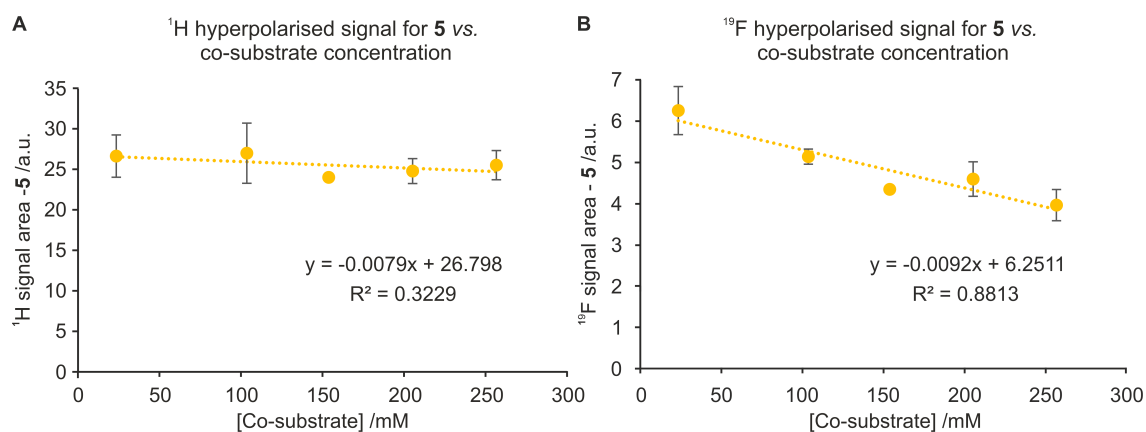


Figure 5.8: Variation of the SABRE-hyperpolarised  $^1\text{H}$  (A) and  $^{19}\text{F}$  (B) signals for **5** when the co-substrate concentration was varied from 5 to 50 equivalents (25 to 250 mM of DMSO). All samples contained a fixed concentration of DFP =  $684 \mu\text{M}$ , with a 3% relative variation between samples.

substrate was distributed amongst several species. This is expected to negatively impact measurements in two ways; in terms of sensitivity, as a smaller fraction of DFP contributes to the target signal, and linearity, due to the presence of several competing exchange processes taking place. As signals from the different species were resolved in  $^{19}\text{F}$  but not in  $^1\text{H}$  NMR spectra, this could explain how the increase of co-substrate concentration led to a more pronounced drop in  $^{19}\text{F}$  enhancements *versus* those for  $^1\text{H}$ . As SABRE-enhanced  $^{19}\text{F}$  signals for the undesired species, A and B, were essentially undetectable when using 25 mM of co-substrate (5 equivalents relative to the pre-catalyst), this was chosen as the optimal concentration for limit of detection and quantification studies.

SABRE experiments performed in the sub-stoichiometric regime after optimisation of the co-substrate concentration produced the results shown in Figure 5.10. As previously stated, in the sub-stoichiometric regime the largest enhancements are observed using a PTF = 6.2 mT, both for  $^1\text{H}$  and  $^{19}\text{F}$  measurements. At this polarisation transfer field, hyperpolarised signals are in-phase, which facilitated processing and, in the case of  $^{19}\text{F}$ , the application of SHARPER for further SNR enhancement, which is discussed in the next section. At the tested concentration ( $[\text{DFP}] = 550 \mu\text{M}$ ), a proton enhancement factor of

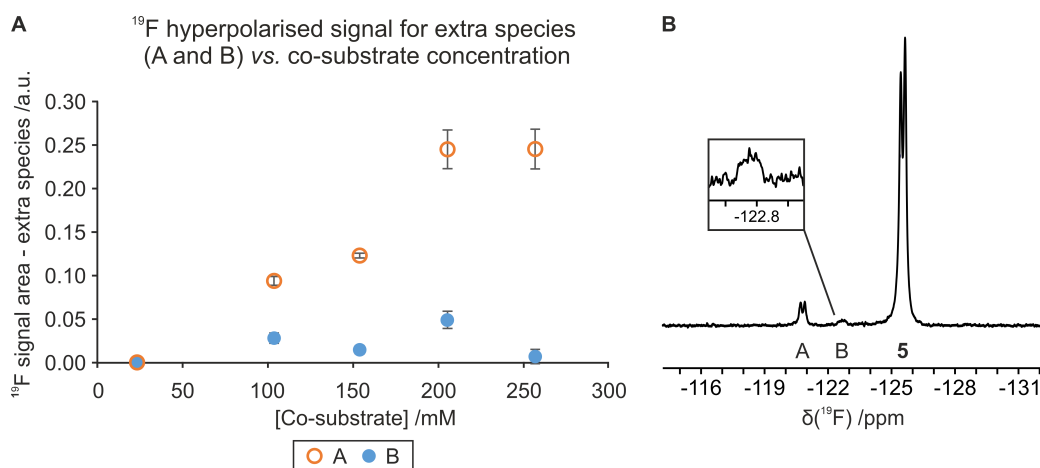


Figure 5.9: A) Variation of  $^{19}\text{F}$  hyperpolarised signal for species A and B when the co-substrate concentration is varied from 5 to 50 equivalents (25 to 250 mM of DMSO). All samples contained a fixed concentration of DFP = 684  $\mu\text{M}$ , with a 3% relative variation between samples. B) Hyperpolarised  $^{19}\text{F}$  spectrum at 1 T for a sample containing 695  $\mu\text{M}$  of DFP, 256 mM of DMSO, and 5.5 mM of  $[\text{IrCl}(\text{COD})(\text{IMes})]$ . Extra species A and B, and the signal corresponding to DFP bound in **5** are marked.

$\varepsilon_{1\text{H}} = (12500 \pm 800)$  was obtained. This value was roughly double of that seen in the supra-stoichiometric regime. In contrast, fluorine enhancement factors decreased from  $\varepsilon_{19\text{F}} = (2480 \pm 250)$  to  $\varepsilon_{19\text{F}} = (940 \pm 40)$  in the sub-stoichiometric regime. This is likely the result of the faster relaxation of hyperpolarised signals in the sub-stoichiometric regime, as previously discussed.

### 5.3.2 $^{13}\text{C}$ Hyperpolarisation

In addition to the signal enhancements observed for  $^1\text{H}$  and  $^{19}\text{F}$  nuclei, hyperpolarised  $^{13}\text{C}$  NMR signals were also observed for this system. Shake-and-drop experiments were performed as described previously but with  $^{13}\text{C} \{^1\text{H}\}$  pulse-and-collect detection (Section 3.3, Chapter 3) on a sample containing 100 mM of DFP, 100 mM of DMSO and 5 mM of  $[\text{IrCl}(\text{COD})(\text{IMes})]$  in methanol at three PTF values:  $\sim 0$  T,  $\sim 50$   $\mu\text{T}$ , and 6.2 mT. Figure 5.11 shows the results for these experiments, revealing hyperpolarised  $^{13}\text{C}$  signals were

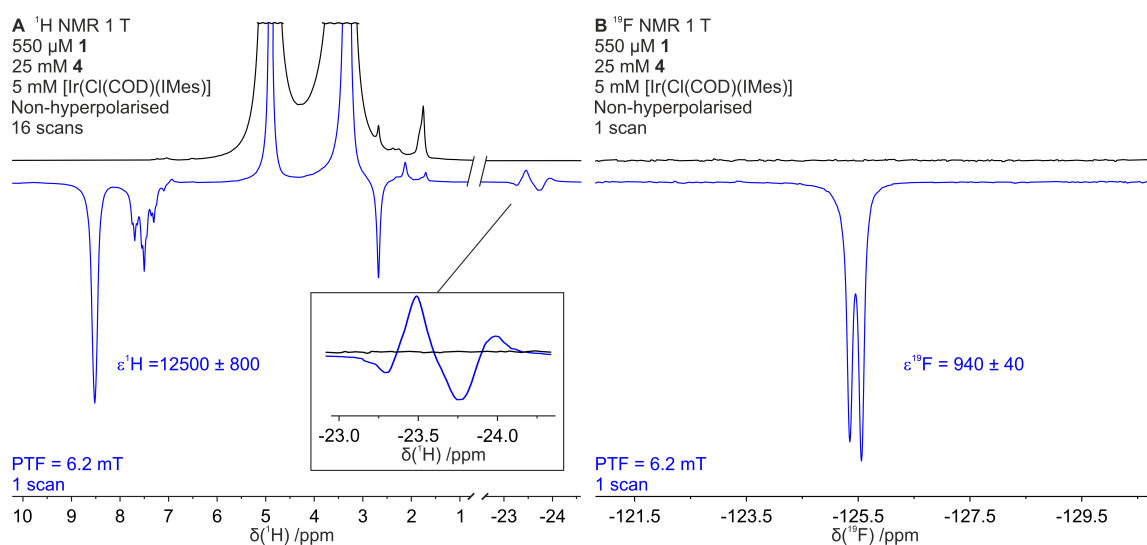


Figure 5.10: Comparison of SABRE-enhanced and non-hyperpolarised  $^1\text{H}$  (A) and  $^{19}\text{F}$  (B) benchtop NMR spectra of 550  $\mu\text{M}$  of DFP, 25 mM of DMSO, and 5 mM  $[\text{IrCl}(\text{COD})(\text{IMes})]$  in methanol. All SABRE spectra were acquired with a single scan. The reported values are the mean and standard deviation of three repeat measurements.

obtained for all tested PTFs. It is worth noting that  $^{13}\text{C}$  NMR signal enhancements for the system using co-substrates were superior to those for the traditional SABRE system. The increase in SABRE performance with co-substrates can be rationalised as a consequence of an optimised substrate dissociation rate and a decrease in spin dilution.

Interestingly, the  $^{13}\text{C}$  NMR signals showing the largest signal enhancement were those directly bound to the fluorine atoms in the *meta* positions, whilst hyperpolarisation of signals in *ortho* positions were significantly lower and those in *para* position did not exhibit hyperpolarisation. This suggests that the fluorine nuclei are key participants in the polarisation transfer mechanism. At a PTF  $\sim 50$   $\mu\text{T}$ , which favours direct polarisation of fluorine atoms and produced the largest  $^{19}\text{F}$  enhancements in supra-stoichiometric conditions,  $^{13}\text{C}$  enhancements were the lowest (Figure 5.11, middle trace). When using a polarisation transfer field in the low micro tesla range, enhancements for *meta*  $^{13}\text{C}$  improved and hyperpolarisation of the *ortho* positions was observed (Figure 5.11, top trace). Interestingly, the largest overall enhancement was obtained at a PTF = 6.2 mT, and only *meta* carbons

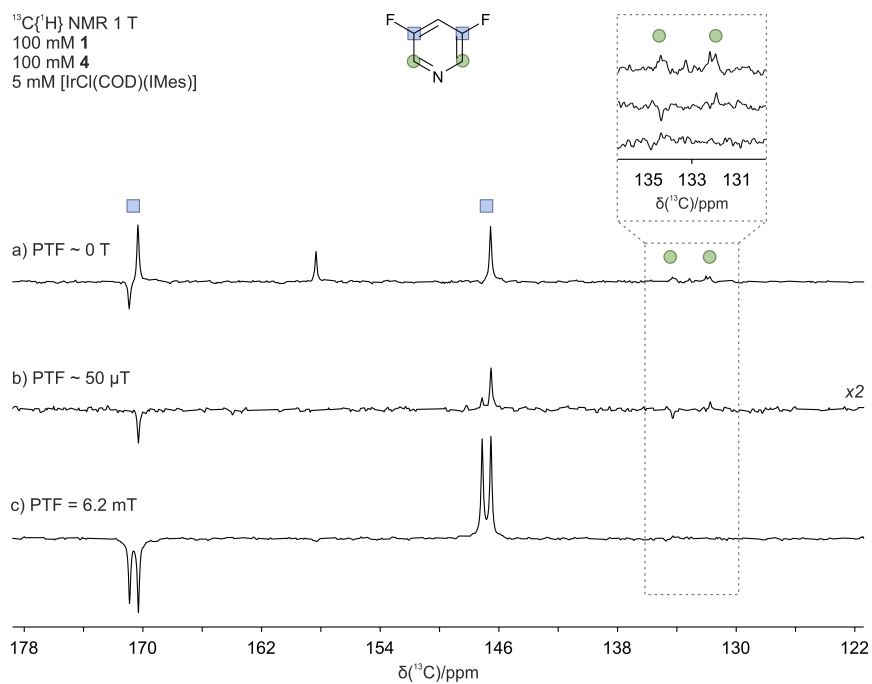


Figure 5.11: SABRE-hyperpolarised proton-decoupled  $^{13}\text{C}$  NMR spectra acquired at a 1 T field of a sample containing 100 mM of DFP, 100 mM of DMSO, and 5 mM of [IrCl(COD)(IMes)] in methanol. Experiments were conducted using PTF values of ~ 0 T (a), ~ 50  $\mu\text{T}$  (b), and 6.2 mT (c). The signals corresponding to  $^{13}\text{C}$  nuclei in *ortho* and *meta* positions are shown with blue squares and green circles, respectively. The inset on the right shows an amplified view of all spectra in the region where *ortho*  $^{13}\text{C}$  can be observed.

were hyperpolarised. This polarisation transfer field favours direct polarisation of  $^1\text{H}$  nuclei,<sup>139,156,218</sup> but as no  $^1\text{H}$  atoms are directly attached to the *meta* carbons,  $^1\text{H}$ -relayed polarisation of  $^{13}\text{C}$  nuclei in this position would not be expected.

The signal profiles observed for each polarisation transfer field suggest that different polarisation transfer pathways are at play.<sup>83</sup> For example, at a polarisation transfer field of 6.2 mT the signal arising from the  $^{13}\text{C}$  in *meta* position is anti-phase relative to a 260 Hz coupling which corresponds to a one bond  $^{13}\text{C}$ - $^{19}\text{F}$  coupling. In contrast, at  $\sim 0$  T this signal is anti-phase to a three bond  $^{13}\text{C}$ - $^{19}\text{F}$  coupling (6 Hz). This suggests that at these polarisation transfer field values, the  $^{13}\text{C}$  signal arises from the hyperpolarisation of different coupled  $^{13}\text{C}$ - $^{19}\text{F}$  two-spin order terms.

These promising results in terms of  $^{13}\text{C}$  signal enhancement for fluorinated molecules could be exploited, particularly in characterisation strategies probing long range  $^{13}\text{C}$ - $^{19}\text{F}$  couplings.<sup>219,220</sup> However, this was not further explored as it was outside the scope of this thesis.

## 5.4 Limits of Detection with SABRE Hyperpolarisation

The previous section examined the advantages of using co-substrates to enhance SABRE efficiency and their role in forming a stable polarisation transfer catalyst under sub-stoichiometric conditions. This section focuses on the application of co-substrates for probing low concentrations of target analytes and determining the minimum concentration that can be reliably detected. This performance parameter is crucial when selecting an appropriate measurement technique for a specific analytical problem. For instance, major component analysis often requires the determination of an analytical target which is present in percentages. In contrast, the analysis of trace or ultra trace components, often crucial in contamination analysis in environmental or food samples, requires measurement systems capable of detecting analytes at concentrations below 100  $\mu\text{g/g}$ .<sup>221,222</sup>

To assess the suitability of a measurement system for a specified concentration range, it is customary to determine its limit of detection (LOD). The International Vocabulary

of Metrology defines limit of detection as a 'measured quantity value, obtained by a given measurement procedure, for which the probability of falsely claiming the absence of a component in a material is  $\beta$ , given a probability  $\alpha$  of falsely claiming its presence', with recommended  $\alpha$  and  $\beta$  values of 5%.<sup>223</sup> In simpler terms, the LOD represents the lowest concentration at which the user can reliably establish the presence of a target analyte.

From a practical point of view, a limit of detection can be assessed in several discipline-specific ways.<sup>188</sup> In the field of NMR, the limit of detection is most commonly estimated as the concentration at which the signal-to-noise ratio equals 3,<sup>4,185–187,224</sup> which is the criteria adopted in this work. Alternative methods using measurement precision as an estimate, a common approach in analytical chemistry, can also be used, but these have been found to overestimate limits of detection.<sup>225</sup>

Limit of detection values for high-field NMR can extend to the low micromolar concentration range, in particular when aided by a cryoprobe.<sup>112,225,226</sup> These values compare rather negatively to those commonly obtained in high-sensitivity analytical techniques. For example, LOD values in high-field NMR were estimated to be 10 orders of magnitude larger than those obtainable by mass spectrometry.<sup>186</sup> Detection limits for benchtop NMR spectroscopy measurements are even higher, with typical LOD values in the low millimolar regime.<sup>112</sup> This is not only a consequence of the lower sensitivity of benchtop NMR instruments, but also the reduction in spectral resolution and the broader peaks commonly observed at lower field. Better resolved and narrower peaks, harder to achieve in low-field NMR, facilitate signal processing<sup>227</sup> which indirectly reduces detection limits.

This was illustrated by the limit of detection for non-hyperpolarised  $^1\text{H}$  and  $^{19}\text{F}$  measurements of DFP at 1 T.  $^1\text{H}$  and  $^{19}\text{F}$  LOD values were estimated by analysing a reference sample containing 8.1 mM of DFP with the same NMR acquisition parameters as hyperpolarised experiments, but substituting single-scan acquisition by signal averaging for 64 scans (*ca.* 10 minutes). LOD values, estimated according to Equation 3.14 (Section 3.7.5, Chapter 3), were 3 mM for  $^1\text{H}$ , and 6 mM for  $^{19}\text{F}$  NMR measurements.

It is well known that signal averaging and receiver gain values have an impact on the obtained signal-to-noise ratio for a measurement.<sup>185,186</sup> In order to allow for a direct

comparison between non-hyperpolarised multiple scan experiments and hyperpolarised experiments, the receiver gain was set to the same value ( $RG = 1$ ) and single-scan SNR ( $SNR_{ss}$ ) and LOD ( $LOD_{ss}$ ) values were calculated for thermal experiments, according to Equations 3.16 and 3.3.  $LOD_{ss}$  values for non-hyperpolarised experiments were 23 mM for  $^1\text{H}$ , and 50 mM for  $^{19}\text{F}$  NMR measurements. As expected, LOD values for  $^1\text{H}$  were lower than for  $^{19}\text{F}$  NMR measurements. This is a reflection of the number of nuclei per molecule producing the signal (3 nuclei in  $^1\text{H}$  and 2 nuclei in  $^{19}\text{F}$  measurements) as well as the higher gyromagnetic ratio for  $^1\text{H}$ .

To showcase the improvement in terms of detection limits introduced by SABRE hyperpolarisation with co-substrates, the LOD was estimated using a sample containing 14  $\mu\text{M}$  of DFP, 25 mM of DMSO, and 5 mM of  $[\text{IrCl}(\text{COD})(\text{IMes})]$ . SABRE experiments conducted as described in the previous section ( $\text{PTF} = 6.2 \text{ mT}$ ) on this sample produced signal-to-noise ratio values of 47 and 6, for  $^1\text{H}$  and  $^{19}\text{F}$ , respectively. From these results, LOD values of  $(890 \pm 20) \text{ nM}$  for  $^1\text{H}$ , and  $(6.84 \pm 0.45) \mu\text{M}$  for  $^{19}\text{F}$  NMR measurements were estimated. These results therefore represent an improvement over non-hyperpolarised experiments by 5 orders of magnitude for  $^1\text{H}$ , and 4 orders of magnitude for  $^{19}\text{F}$  NMR measurements.

It is relevant to highlight that these LOD levels would not be attainable for SABRE experiments without the use of co-substrates, as concentrations in the sub-stoichiometric regime could not be probed. This is clearly illustrated in Figure 5.12, which shows the SABRE activity on samples containing 250  $\mu\text{M}$  of DFP, 5 mM of  $[\text{IrCl}(\text{COD})(\text{IMes})]$ , and either 100 mM of DMSO(a) or no co-substrate at all (b). By comparing these spectra, it is evident that no hyperpolarisation can be seen in the absence of co-substrates. As discussed before, the presence of a co-substrate is crucial to the activation of a stable SABRE complex, without which SABRE hyperpolarisation cannot take place. This finding highlights the fact that SABRE hyperpolarisation in a standard approach may increase the sensitivity of measurements, *i.e.* larger signal gradients can be obtained when concentration is incremented,<sup>228</sup> but, in and of itself, cannot typically improve detection limits without co-substrates.

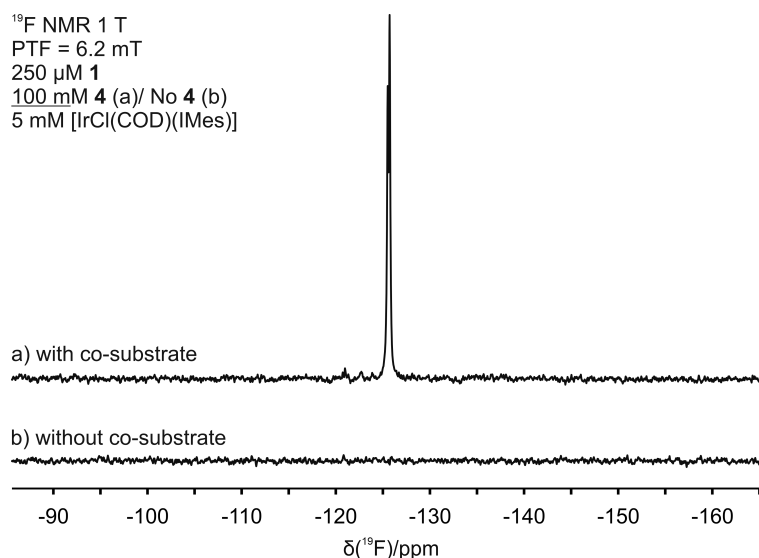


Figure 5.12: SABRE-hyperpolarised  $^{19}\text{F}$  spectra of samples containing 250  $\mu\text{M}$  of DFP, 5 mM of  $[\text{IrCl}(\text{COD})(\text{IMes})]$ , and either 100 mM DMSO (a) or no co-substrate (b) in methanol- $d_4$ . SABRE experiments were conducted using a PTF = 6.2 mT.

Given the link between LOD and SNR values, it follows that by optimising SNR values, lower limits of detection could be achieved. As explored in Chapter 4, 9-fold SNR enhancements can be achieved in SABRE-hyperpolarised measurements for DFP when using SHARPER. This was pursued as a way to lower the limits of detection for this measurement system. Indeed, by applying SHARPER (Section 3.3, Chapter 3) to SABRE-hyperpolarised experiments on the sample containing 14  $\mu\text{M}$  of DFP and 25 mM of DMSO, SNR values improved from 6.1 to 70 (Figure 5.13B and C). This translates to an estimated LOD value of  $(600 \pm 20)$  nM, a 11-fold reduction *versus* normal pulse-and-collect experiments. An example spectrum at sub-micromolar concentrations (800 nM) is shown in Figure 5.13D.

Such limits of detection were facilitated by the use of SHARPER processing strategies, in particular background correction and removal of the imaginary part of the spectrum as discussed in Chapter 4, Section 4.4. To understand the impact of these strategies, a sample containing 221  $\mu\text{M}$  of DFP, 25 mM of DMSO, and 5 mM of  $[\text{IrCl}(\text{COD})(\text{IMes})]$  was prepared and SABRE-SHARPER experiments were conducted as previously discussed. The same

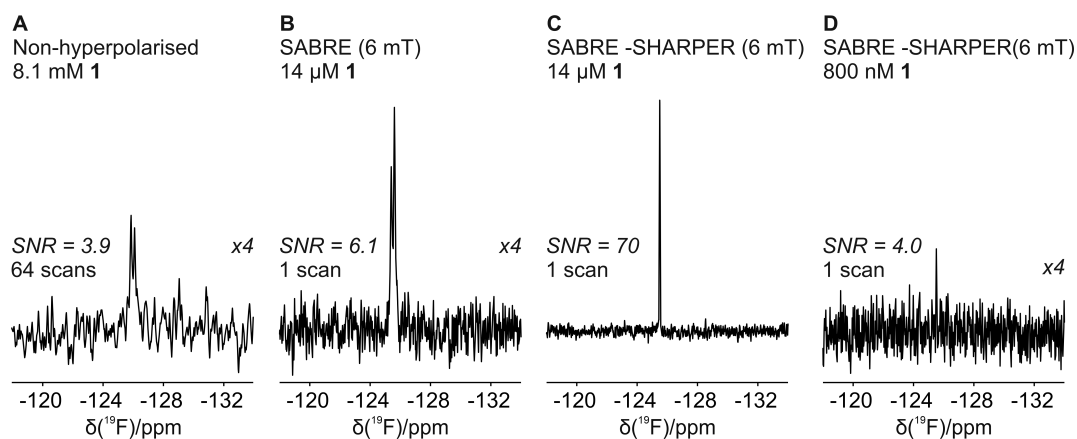


Figure 5.13: Comparison of  $^{19}\text{F}$  spectra for DFP at different concentrations. A) Non-hyperpolarised spectrum for a sample containing 8.1 mM DFP exhibiting a SNR = 3.9 after accumulation of 64 scans. B) SABRE-hyperpolarised spectrum for a sample containing 14  $\mu\text{M}$  of DFP, 25 mM of DMSO, and 5 mM of  $[\text{IrCl}(\text{COD})(\text{IMes})]$ . C) SABRE-SHARPER spectrum on the same sample as B. D) SABRE-SHARPER spectrum for a sample containing 800 nM of DFP, 25 mM of DMSO, and 5 mM of  $[\text{IrCl}(\text{COD})(\text{IMes})]$ . SHARPER spectra were acquired with background correction and the imaginary part of the spectrum was removed. All samples were prepared in methanol, except for A which was prepared in methanol- $d_4$ .

spectrum was then processed with and without the previously mentioned processing steps for comparison.

Table 5.3 shows SNR, standard deviation of the noise ( $s_{noise}$ ), and the height values obtained in each case. When comparing results for spectra with and without the imaginary parts, a drop by a factor of *ca.*  $\sqrt{2}$  in  $s_{noise}$  was seen in the former case, which resulted in an increase of SNR by the same factor. A similar effect was observed when comparing background correction results: a  $\sqrt{2}$ -fold improvement in SNR was observed when no background correction was applied. Interestingly, background correcting the spectrum resulted in a decrease in peak height. This is likely due to the small non-hyperpolarised signal contribution in the reference spectrum which is subtracted during the correction process, therefore decreasing signal intensity. Nevertheless, this contribution was expected to be minimised in the sub-stoichiometric regime as even SHARPER-enhanced signals were very low. In fact, at 221  $\mu\text{M}$ , the drop in height was less than 1%, which was considered an acceptable sacrifice in signal. From these results, it became clear that a potential 2-fold SNR gain could be achieved when the imaginary part of the spectrum was removed but no background correction applied. However, at LOD levels, background correction was deemed necessary as the artefacts arising from the probe signal were considerably larger than the target signal (Figure 5.14).

Limit of detection values could also be potentially lowered by increasing the amount of dissolved  $p\text{-H}_2$  in solution. Larger concentrations of dissolved  $p\text{-H}_2$  favour the exchange pathway that leads to the hyperpolarisation of a new substrate unit, contributing to the build-up of hyperpolarised substrate in solution. One way to do this is to introduce a larger  $p\text{-H}_2$  pressure into the NMR tube.<sup>229</sup> However, modifying the pressure of  $p\text{-H}_2$  to which the sample is subjected to is not trivial in shake-and-drop experiments. The pressure of  $p\text{-H}_2$  is typically set by the  $p\text{-H}_2$ -generating rig and safety concerns may arise when operating at higher pressures. Alternatively, higher  $p\text{-H}_2$  concentrations can be achieved indirectly by decreasing the amount of pre-catalyst in solution to increase the relative amount of dissolved  $p\text{-H}_2$ .<sup>151</sup>

This approach to improve LOD values was investigated with a sample containing 800  $\mu\text{M}$

Table 5.3: Comparison of signal-to-noise (SNR) ratio, standard deviation of the noise ( $s_{noise}$ ) and height values for SABRE-hyperpolarised  $^{19}\text{F}$  NMR signal corresponding to DFP after background correction and/or removing the imaginary part as post-acquisition processing. Experiments were performed on a sample containing 221  $\mu\text{M}$  of DFP, 25 mM of DMSO, and 5 mM of  $[\text{IrCl}(\text{COD})(\text{IMes})]$ . SNR and  $s_{noise}$  values were calculated according to Section 3.7.1 in Chapter 3.

|                          | Imaginary part removed |             |        | Imaginary part not removed |             |        |
|--------------------------|------------------------|-------------|--------|----------------------------|-------------|--------|
|                          | SNR                    | $s_{noise}$ | Height | SNR                        | $s_{noise}$ | Height |
| Not background corrected | 3354                   | 4.32        | 14489  | 2360                       | 6.14        | 14489  |
| Background corrected     | 2500                   | 5.83        | 14581  | 1750                       | 8.33        | 14581  |

of DFP, half the concentration of  $[\text{IrCl}(\text{COD})(\text{IMes})]$  (2.5 mM) and 5 equivalents of DMSO (12.5 mM). The concentration of DMSO was proportionally reduced with the concentration of pre-catalyst to enable a direct comparison with previous results. Additionally, it was hypothesised that reducing the concentration of DMSO would be beneficial in terms of signal enhancement for the substrate. As previously discussed, SABRE complexes with dimethylsulfoxide as a ligand exhibit rapid exchange rates for hydrogen,<sup>202</sup> which would deplete the available pool of dissolved  $p\text{-H}_2$  quickly, thereby reducing its availability for hyperpolarisation of the target substrate.

As seen in Table 5.4 (A *vs.* B), halving the concentration of pre-catalyst and co-substrate introduced significant improvements in SNR and reduced LOD values by a third. This suggests that SABRE efficiency was indeed improved by increasing the concentration of  $p\text{-H}_2$  relative to the catalyst. However, a further reduction of the pre-catalyst concentration to a third of the original value did not yield any improvements (Table 5.4 B *vs.* D). A possible explanation for this is that there is a  $p\text{-H}_2$  pressure above which no improvements in signal enhancement can be detected, *i.e.* a plateau is reached.<sup>229</sup> This saturation is more readily reached at lower  $p\text{-H}_2$  pressures when the concentration of  $[\text{IrCl}(\text{COD})(\text{IMes})]$  is reduced. It may therefore be reasonable to propose that such plateau was reached at

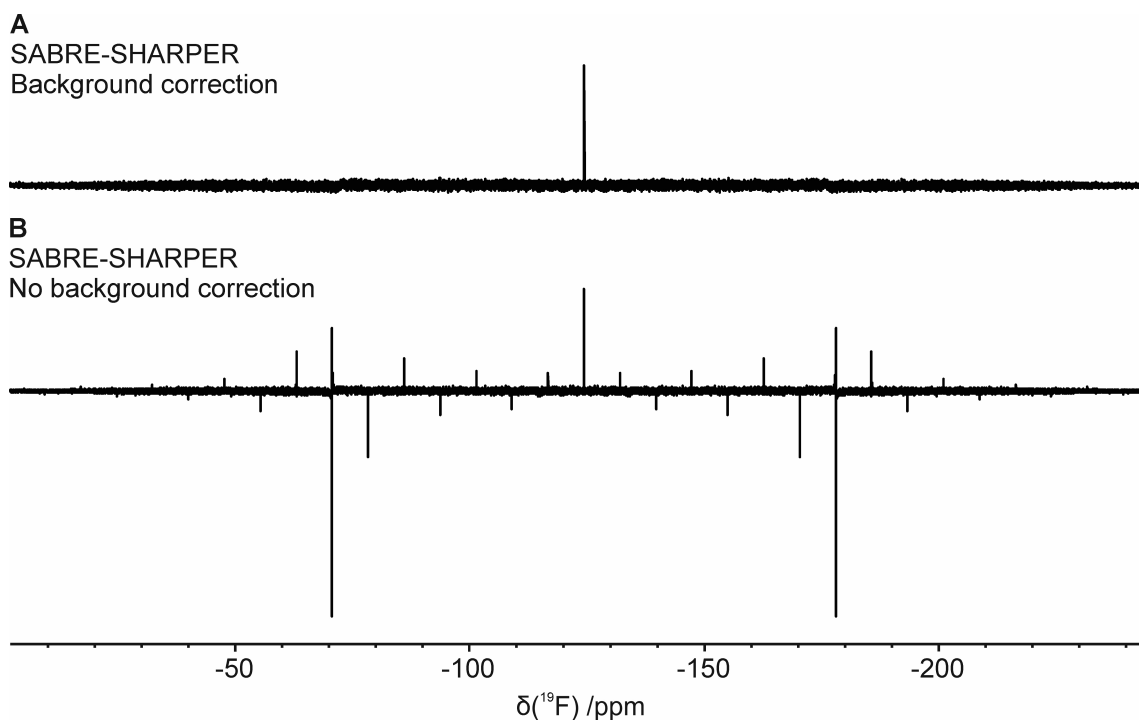


Figure 5.14: Comparison of SABRE-SHARPER  $^{19}\text{F}$  NMR spectra with (A) and without (B) background correction (Section 4.4) in the sub-stoichiometric regime. Artefact signals arising from the probe dominated the spectrum when analysing a low concentration sample containing DFP ( $5\ \mu\text{M}$  of DFP,  $25\ \text{mM}$  of DMSO, and  $5\ \text{mM}$   $[\text{IrCl}(\text{COD})(\text{IMes})]$  in methanol). By using background correction these non-targeted signals were eliminated.

the stated concentration, meaning no improvement of the signal enhancement could be achieved.

Reducing chunk lengths in SHARPER experiments may result in SNR improvements by reducing the effective transverse relaxation time,  $T_2^S$ , as discussed in Chapter 4. To test this strategy, the same sample was tested using a chunk length of  $\tau = 0.4\ \text{ms}$ , 4 times shorter than in the original experiment. As can be observed in Table 5.4 (B *vs.* C), no significant improvement was obtained by decreasing chunk length. It is possible that using longer chunk times would instead be beneficial to SNR, as proposed by Peat and co-workers.<sup>200</sup>

Although halving the concentration of pre-catalyst introduced a marginal improvement

Table 5.4: Variation of limit of detection (LOD) values for  $^{19}\text{F}$  NMR measurements at 1 T with  $[\text{IrCl}(\text{COD})(\text{IMes})]$  concentration and FID chunk length ( $\tau$ , in ms) in SHARPER experiments. Samples were prepared in methanol and contained 25 mM of DMSO and either 14  $\mu\text{M}$  (A) or 800 nM (B-D) of DFP and  $[\text{IrCl}(\text{COD})(\text{IMes})]$  concentrations as listed on the Table.

|   | [Pre-catalyst]<br>/mM | $\tau$ /ms | LOD /nM        |
|---|-----------------------|------------|----------------|
| A | 5.01                  | 1.6        | (600 $\pm$ 20) |
| B | 2.86                  | 1.6        | (410 $\pm$ 80) |
| C | 2.86                  | 0.4        | (430 $\pm$ 30) |
| D | 1.87                  | 1.6        | (440 $\pm$ 60) |

in terms of LOD values (Table 5.4), this strategy was not implemented for quantification studies. By reducing the concentration of pre-catalyst, the stoichiometric upper limit would be reduced. This means that the analytical range, to be explored in the next section, would be reduced.

In this section, limit of detection values in the nanomolar range were demonstrated using  $^{19}\text{F}$  benchtop NMR measurements at a 1 T field conducted using SABRE hyperpolarisation and SHARPER experiments. Similar limit of detection values were reported for a thiazole derivative using photo-CIDNP-hyperpolarised  $^1\text{H}$  NMR experiments at a 1.88 T field.<sup>65</sup> However, it should be noted that signal averaging for 3 minutes was required to reach this value,<sup>65</sup> in contrast to the single-scan approach presented in this work.

## 5.5 Quantification with SABRE Hyperpolarisation

Results from the previous sections highlight how sensitivity gains and low-concentration detection of a target molecule can be achieved by using co-substrates and SABRE-enhanced benchtop NMR spectroscopy. From an analytical perspective, this demonstrates the suitability of this measurement procedure to detect an analyte at low concentrations using a

low-cost platform. Although applications where this kind of qualitative analysis is used are plentiful, there are many more relying on a numerical result. Quantitative analysis can experimentally attribute a numeric value to a quantity, *e.g.* a concentration, through a measurement procedure *via* a suitable calibration system.<sup>228</sup> This quantity value needs to be a good estimate of its true value, a crucial requirement for reliable decisions to be made based on that result.

NMR spectroscopy is intrinsically quantitative in nature, as the integrated signal area is directly proportional to the number of nuclei producing said signal.<sup>2</sup> In fact, NMR has been proposed as primary measurement method,<sup>2,230,231</sup> and as such is considered unbiased and of the highest metrological quality.<sup>232,233</sup> This has been exploited in the last 50 years,<sup>234–237</sup> in simple 1D <sup>1</sup>H or heteronuclear NMR experiments or in 2D and pure shift NMR experiments to improve spectral resolution.<sup>231</sup> Such strategies are particularly useful for benchtop NMR measurements in which spectral crowding is a challenge.

However, the quantitative nature of NMR is lost when using SABRE hyperpolarisation. In conventional NMR experiments, the proportionality constant relating the number of nuclei and the detected integral is fairly constant for each type of nuclei (*e.g.* <sup>1</sup>H or <sup>19</sup>F ) provided the experiment is conducted in quantitative conditions.<sup>2,235,237</sup> However, in SABRE experiments, this relationship changes for each specific hyperpolarised resonance, as signal enhancements can vary for each nucleus in the molecule. This obstacle, although inconvenient, is not insurmountable. Calibration techniques can be used to establish the proportionality constant between the recorded signal and the amount of a specific nucleus. Implementing these calibration techniques requires building a model linking the detected signal, conventionally the peak integral, with the concentration of the target analyte, which can later be used to predict the concentration of an test sample.<sup>238</sup> To produce reliable predictions in a practical way, it is often desirable for this model to be linear, which is not guaranteed when it involves standard SABRE-hyperpolarised measurements.<sup>82</sup>

The lack of linearity of the SABRE-enhanced response under standard conditions can be attributed to several reasons. For instance, the complex interplay of exchange processes during the SABRE polarisation transfer step, particularly when the SABRE-active species

contains units of the target molecule in more than one binding site subject to hyperpolarisation. This situation is further complicated by the presence of several catalyst species. As illustrated in Chapter 4.3, secondary solvent-containing species may form in the absence of a co-substrate. This array of species may contribute to SABRE-enhanced signals with varying efficiencies or exhibiting different peak profiles. Added to the fact that increasing the substrate concentration may lead to the preferential formation of one species over the other, non-proportional signal gains can be expected.

A clever solution to the non-linearity problem was proposed by Tessari and co-workers.<sup>81</sup> In this approach, a co-substrate was used in conjunction with sub-stoichiometric amounts of the target analyte to show a linear dependence between the hyperpolarised  $^1\text{H}$  signal and the analyte concentration in the micromolar regime at 14.1 T.

The use of co-substrates can induce linear responses even in the supra-stoichiometric regime. This was demonstrated by Fekete and co-workers,<sup>151</sup> who reported linear responses for SABRE-hyperpolarised  $^{15}\text{N}$  signals for pyridine, pyrazine, and metronidazole for concentrations ranging from 2.2 mM to 70 mM, using deuterated benzylamine as a co-substrate. This was achieved by dilution of a stock solution containing the co-substrate and pre-catalyst, which would not lead to the construction of a viable calibration curve with prediction capabilities. However, they did demonstrate that a linear signal response could be obtained when co-substrate and pre-catalyst concentration were fixed for pyrazine. Interestingly, they report the formation of two potential polarisation transfer species, either containing a 2:1 or 1:2 co-substrate to substrate ratio. Conveniently, only one of these were found to contribute to the SABRE-enhanced  $^{15}\text{N}$  signal, whilst also being responsive to the amount of substrate present. The authors speculated that if that had not been the case, in other words, if both species contributed to the hyperpolarised signal, a linear response may not have been obtained.

In a later publication, Eshuis *et al.* extended their work to the quantification of several substrates in a multi-component sample. Instead of using a single co-substrate, the authors added low concentrations of 15 substrates with a cumulative supra-stoichiometric concentration.<sup>82</sup> As a consequence of the diversity of substrates in the sample, a large variation of

polarisation transfer catalyst were expected to form for each target analyte. To better address the complexity of this sample, these analytes were quantified *via* the standard addition method. In the standard addition method, aliquots of a standard solution containing the target analyte are added to the unknown sample in progressively increasing amounts.<sup>238–241</sup> Following this, a linear regression model is built to predict the concentration of the sample prior to the additions through extrapolation. This method was proposed to compensate for measurement interference effects, in particular those of a rotational nature,<sup>183</sup> which affect the sensitivity of the measurement most commonly due to analyte-matrix interactions.<sup>241</sup> It seems reasonable to think that this motivated the choice of calibration method in Eshuis' work,<sup>82</sup> as the presence of several competing substrates, which can be thought of as the matrix, would likely reduce the sensitivity of the target analyte.

Although this calibration method is deemed to be effective when strong interference effects are suspected, it can lead to systematic error if adequate tests and corrections are not carried out.<sup>238–241</sup> For instance, the absence of translational interference effects needs to be verified or corrected for through the analysis of blank samples. Additionally, as this method involves model extrapolation, associated uncertainties can be large,<sup>241</sup> and measurement bias may be introduced when the model strays from linearity in that region, or corrections for consecutive dilution steps are not implemented.<sup>238–241</sup> This is illustrated by the relative error values of up to 18% and relative deviations from the reference of up to 12% reported by Eshuis and coworkers in the low micromolar range.<sup>82</sup>

In order to investigate the best achievable analytical performance of SABRE-hyperpolarised quantification using co-substrates at a 1 T field, a simpler test sample, *i.e.* one analyte in the presence of a single co-substrate, was deemed adequate. This less complex sample, in which interference effects are not expected, allowed for the use of a simpler calibration method: external calibration. This method involves the preparation of a series of samples with a known amount of analyte covering a concentration range that includes the test sample. This set of calibration samples is analysed in the same conditions as the test sample to build a model, or calibration curve, relating the concentration of target analyte to the signal response. This model, usually linear, can then be used to predict

the concentration of an unknown sample. Given that no extrapolation takes place, and no assumptions are made in terms of linearity or interference effects, this method can achieve higher levels of accuracy than the standard addition method.<sup>238</sup>

As a first step, the linearity of the calibration method was assessed. To this end, a series of 7 samples containing known amounts of the target analyte, DFP, were gravimetrically prepared. These samples contained DFP in a concentration range covering 15  $\mu\text{M}$  to 1000  $\mu\text{M}$ , 25 mM of DMSO, and 5 mM of  $[\text{IrCl}(\text{COD})(\text{IMes})]$  in methanol. The samples were analysed in triplicate *via* shake-and-drop experiments following the previously described procedure. The signal integrals obtained in this way were plotted against the reference concentration for each sample, determined by gravimetric preparation. To assess the linearity of the calibration curve, and therefore its suitability to quantification, a linear model was determined by ordinary least squares regression and a coefficient of determination was calculated according to Section 3.7.7 in Chapter 3.<sup>238,242</sup> Additionally, the residual error values of the calibration model were plotted against the reference concentration for each calibration sample to visually assess deviations from linearity.<sup>238</sup> Regression analysis and statistics were obtained as described in Section 3.7.7 (Chapter 3).

Figure 5.15 shows the results for the linearity studies for both  $^1\text{H}$  and  $^{19}\text{F}$  hyperpolarised NMR experiments. The coefficient of determination  $R^2$  was used to establish the ‘goodness of fit’ of the proposed linear model to the experimental data.<sup>242</sup> Visual inspection of the data in conjunction with an  $R^2$ -value can be then used to assess the adequacy of the proposed linear model. As shown in Figure 5.15A and C, both nuclei showed  $R^2$  values close to 1, suggesting that the variation in signal relative the concentration of analyte can be mostly explained by the linear regression model. Typically,  $R^2$  values above 0.99 are considered fit for purpose in analytical chemistry although acceptance criteria are field-specific. The residual error plots for  $^1\text{H}$  and  $^{19}\text{F}$  NMR measurements (Figure 5.15 B and D, respectively) were used to further investigate the adequacy of a linear model for these data sets. When the variation of experimental results is insufficiently explained by a linear model, the distribution of residual errors around zero follows a systematic trend.<sup>188,238</sup> This suggests a non-linear model, *e.g.* a polynomial equation, would be better suited as a

calibration curve. In this case, the residual error plots for  $^1\text{H}$  and  $^{19}\text{F}$  show a randomised distribution relative to zero, providing further evidence that a linear model is adequate.

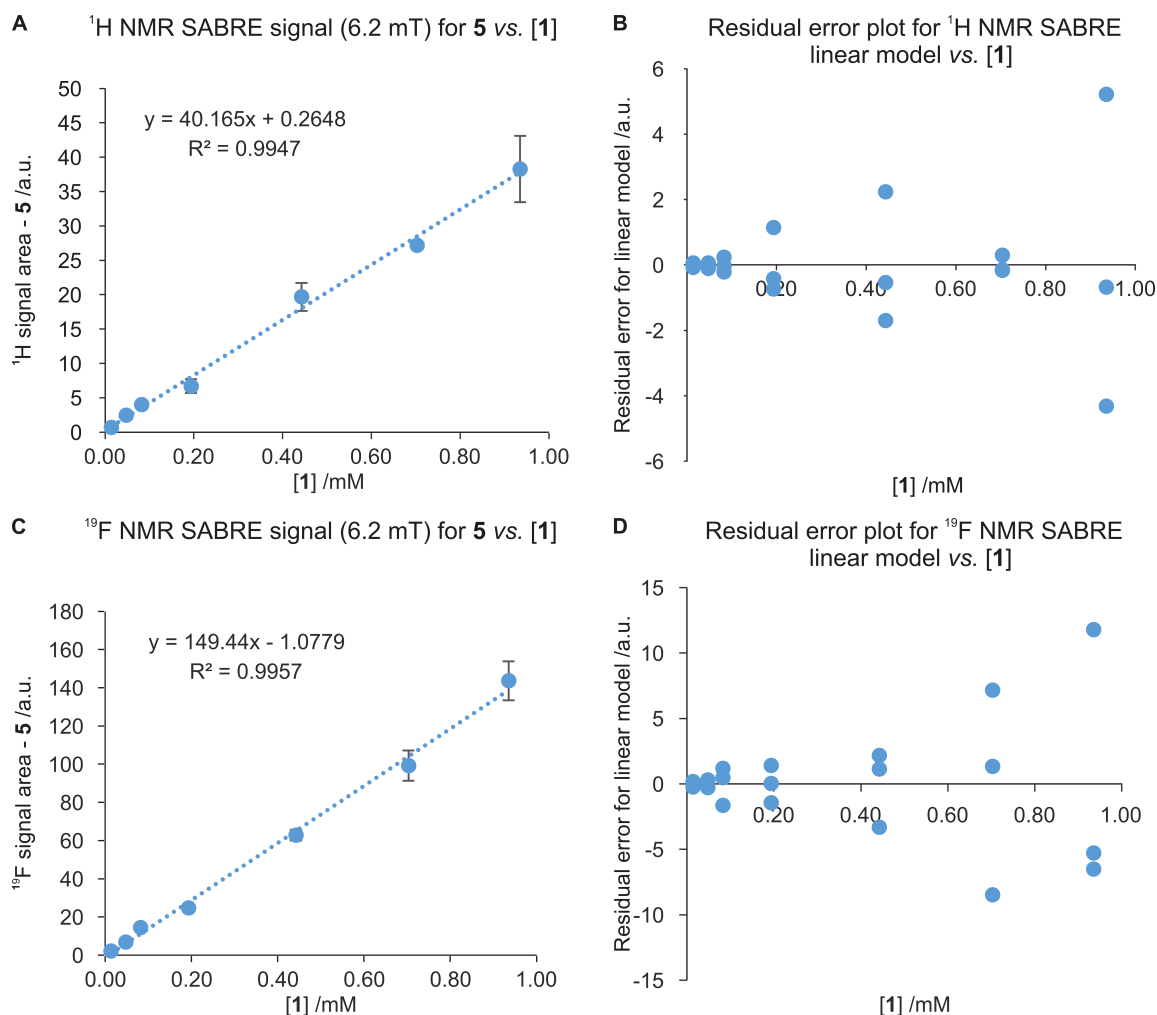


Figure 5.15: Calibration curves for  $^1\text{H}$  (A) and  $^{19}\text{F}$  hyperpolarised (C) NMR measurements of DFP in the  $15\ \mu\text{M}$  to  $1000\ \mu\text{M}$  range. Residual errors of the linear model are plotted against analyte concentration for  $^1\text{H}$  (B) and  $^{19}\text{F}$  (D) hyperpolarised calibration curves.

SABRE-enhanced samples, such as the ones used for calibration, were activated after preparation in order to produce a hyperpolarised NMR signal. During this process, the hyperpolarised signal increases following the formation of the active catalyst species to eventually reach a plateau. It is then pertinent to investigate if the signal remains stable

in time or if variations in signal, for example due to sample degradation or the formation of competing thermodynamic products, result in a limited ‘shelf life’ for these solutions, thus forcing their analysis to be carried out within a restricted time frame. To investigate this, the analysis of the calibration solutions was repeated one week after activation. The samples were aged by keeping them in air-tight conditions at room temperature and in the dark, inside their NMR tubes fitted with J Young’s taps. Re-analysis of all samples was carried out except for the highest concentration (1000 mM) due to a faulty tap, which led to degradation of the sample. As seen in Figure 5.16, the calibration curves obtained for  $^1\text{H}$  SABRE hyperpolarised experiments show no significant variation in slope or coefficient of determination: slope =  $(40.2 \pm 1.3)$  fresh *vs.*  $(39.5 \pm 1.3)$  aged and intercept =  $(0.26 \pm 0.63)$  fresh *vs.*  $(1.02 \pm 0.45)$  aged. However, a slight increase in slope was seen for the  $^{19}\text{F}$  NMR calibration curve: slope =  $(149.4 \pm 3.6)$  fresh *vs.*  $(163.2 \pm 3.6)$  aged and intercept =  $(-1.1 \pm 1.7)$  fresh *vs.*  $(-0.5 \pm 1.3)$  aged. This represented a 9 % increase in sensitivity for  $^{19}\text{F}$  SABRE measurements after ageing the samples for a week. The stability of the  $R^2$ -value for the fresh and aged curves ( $R^2=0.9957$  and  $0.9955$ , respectively) suggests this ageing process took place consistently for all concentrations. From this it is possible to infer that both calibration curves would produce equivalent quantification results, albeit with increased sensitivity after ageing, should the sample be subjected to the same ageing process.

From this linearity study it is possible to establish the working range for this measurement procedure. The working range is defined as the concentration range over which the method can be reliably applied and analytical sensitivity (*i.e.* the slope of the calibration curve) remains largely unchanged.<sup>188</sup> This range is often determined from linearity studies, estimating the working range from the linear range. Based on this approximation, the working range for the quantification of DFP using either SABRE-enhanced  $^1\text{H}$  or  $^{19}\text{F}$  NMR signals at a 1 T field could be established to be  $13.8 \mu\text{M}$  to  $935 \mu\text{M}$ . It is also possible to define the working range as the range bounded by the limit of quantification (LOQ) at the lower end and by the highest concentration contained in the linear range. LOQ can be defined in an analogous way to LOD as the lower concentration that can be

**A**  $^1\text{H}$  NMR SABRE signal (6.2 mT) for **5** vs. **[1]** **B**  $^{19}\text{F}$  NMR SABRE signal (6.2 mT) for **5** vs. **[1]**

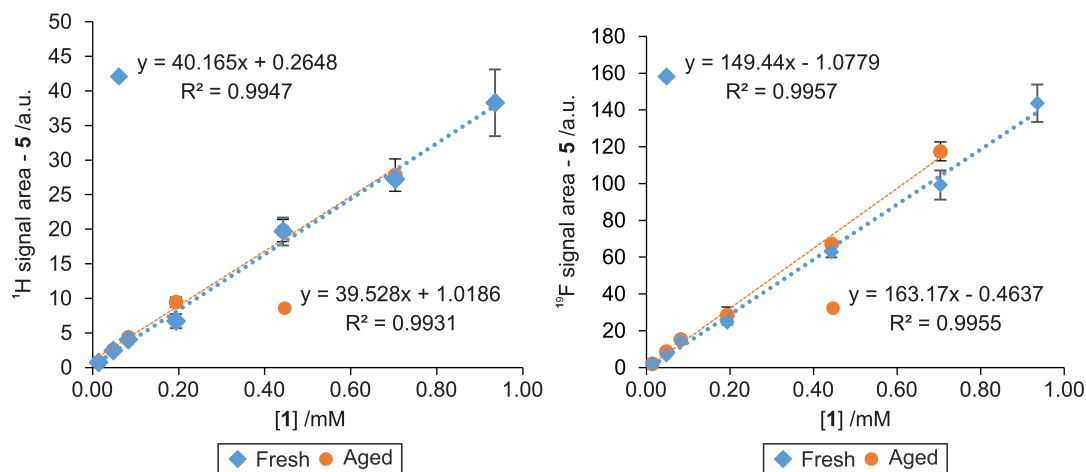


Figure 5.16: Comparison of  $^1\text{H}$  (A) and  $^{19}\text{F}$  (B) NMR SABRE-hyperpolarised calibration curves using fresh (blue diamonds) and aged (orange circles) calibration samples.

reliably quantified by a measurement procedure, and it can be estimated as the concentration at which a signal-to-noise ratio of 10 can be achieved. Following Equation 3.15 (Section 3.7.5, Chapter 3), LOQ values of  $(2.970 \pm 0.060) \mu\text{M}$  for  $^1\text{H}$  NMR measurements and  $(22.8 \pm 1.5) \mu\text{M}$  for  $^{19}\text{F}$  NMR measurements were estimated, and hence represent the lowest limit of the working range. The working range was extended by applying SHARPER to SABRE-hyperpolarised  $^{19}\text{F}$  NMR measurements, resulting in a 10-fold reduction of the LOQ concentration to  $(2.000 \pm 0.080) \mu\text{M}$ . Interestingly, SHARPER also improved the linearity and precision of the calibration curve. This will be discussed further below.

Having demonstrated a good level of linearity for the calibration curves obtained for SABRE-hyperpolarised  $^1\text{H}$  and  $^{19}\text{F}$  NMR measurements, the accuracy of quantification using said calibration curves was investigated. To assess the method's accuracy, or closeness of agreement between the measured and true concentrations,<sup>228</sup> the bias and precision of the quantification results were estimated. The measurement bias was estimated through recovery experiments. In this approach, a test sample of known concentration —  $221 \mu\text{M}$  or  $32 \text{ mg/kg}$  of DFP according to gravimetric preparation results — was quantified in triplicate using calibration curves (4 to 5 levels) covering the concentration range from  $50 \mu\text{M}$  to  $500$

$\mu\text{M}$ . The experimental concentration result was compared to the true value of the test sample (gravimetric value) and the degree of bias was estimated by a recovery value. In order to assess the precision of the method, a relative standard deviation under repeatability conditions was determined. Both parameters were calculated as described in Section 3.7.8 (Chapter 3).

The results of the accuracy assessment are summarised in Table 5.5 and Figure 5.17. All three quantification techniques ( $^1\text{H}$  SABRE,  $^{19}\text{F}$  SABRE and  $^{19}\text{F}$  SABRE-SHARPER) produced results in close agreement with the reference value of  $220.6 \mu\text{M}$ . This is evidenced by the recovery values being close to 100%, which corresponds to a perfectly accurate result. In order to decide whether these recovery results were adequate, it would be necessary to know the analytical performance required to answer a specific analytical problem. Nevertheless, general guidelines for acceptable recovery percentages have been proposed based on analyte concentration.<sup>243,244</sup> According to these guidelines, recovery values should not exceed 107% when the concentration of the target analyte is close to 10 mg/kg. As shown in Table 5.5, all three methods exhibited acceptable recoveries based on these criteria. As for the method's performance in terms of repeatability, RSD values were under the acceptable tolerance of 7.3 % proposed in the literature for values close to 10 mg/kg.<sup>243,244</sup>

Table 5.5: Predicted concentrations, recovery values and relative standard deviation of the samples using  $^1\text{H}$  SABRE,  $^{19}\text{F}$  SABRE and  $^{19}\text{F}$  SABRE-SHARPER measurements using a PTF of 6 mT. Parameters were calculated as described in Sections 3.7.3 and 3.7.8. Recovery values were calculated against the gravimetric reference value  $220.6 \mu\text{M}$

| Analysis                      | Concentration<br>$/\mu\text{M}$ | Recovery<br>$\%$ | RSD<br>$\%$ |
|-------------------------------|---------------------------------|------------------|-------------|
| $^1\text{H}$ SABRE            | $(235 \pm 16)$                  | $(107 \pm 7)$    | 7           |
| $^{19}\text{F}$ SABRE         | $(227.3 \pm 5.4)$               | $(103 \pm 2)$    | 2           |
| $^{19}\text{F}$ SABRE-SHARPER | $(226.0 \pm 3.0)$               | $(102 \pm 1)$    | 1           |

Interestingly,  $^1\text{H}$  SABRE results showed the largest deviation from the reference value

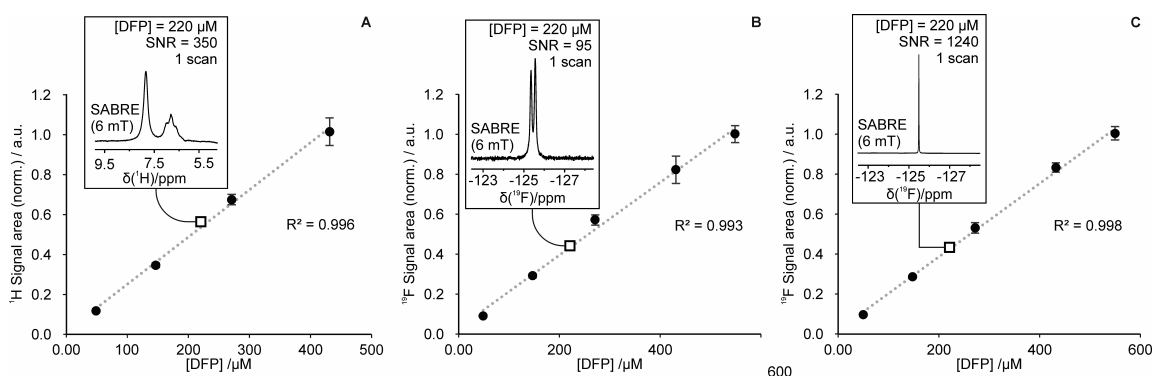


Figure 5.17: Calibration curves for  $^1\text{H}$  SABRE (A),  $^{19}\text{F}$  SABRE (B) and  $^{19}\text{F}$  SABRE-SHARPER (C) experiments and accuracy test. Black markers correspond to the signal arising from calibration solutions and the white squares, those from the test samples. Each sample, either calibration or test, was analysed in triplicate and standard deviation of the mean values were used as error bars. Coefficients of determination,  $R^2$ , are shown for each curve. Insets show the spectra obtained for the test sample in each case, along with its nominal concentration, the signal-to-noise ratio of the measurement and the number of scans.

and the lowest precision. One possible explanation for this is that the  $^1\text{H}$  signals for DFP exhibit complex peak splitting, which, in combination with the apparent peak broadness due to chemical exchange, could make peak integration more challenging and less precise. Conversely, marginally better accuracy and linearity were obtained for  $^{19}\text{F}$  SABRE-SHARPER experiments. Using a similar argument, as the SHARPER experiments yielded a single resonance peak a large signal-to-noise ratio (*e.g.*  $\text{SNR} = 1240$  for the test sample, Figure 5.17C), signal processing would likely lead to more accurate results.

The results presented in this section highlight the quantification potential of SABRE-hyperpolarised and co-substrate assisted  $^1\text{H}$  and  $^{19}\text{F}$  benchtop NMR for DFP. The comparable, or arguably better, performance of  $^{19}\text{F}$  *versus*  $^1\text{H}$  NMR measurements suggests that these nuclei could be used in a complementary fashion as quality assurance. This comparison between results arising from  $^1\text{H}$  and  $^{19}\text{F}$  measurements could be useful to investigate potential  $^1\text{H}$  NMR signal overlap issues. When signal crowding does preclude  $^1\text{H}$  NMR

analysis, a common occurrence at a 1 T field,  $^{19}\text{F}$  NMR would be a viable alternative for a molecule such as DFP.

## 5.6 Conclusion

In this chapter, the application of SABRE-hyperpolarised  $^1\text{H}$  and  $^{19}\text{F}$  NMR in conjunction with co-substrates for the low-concentration detection and quantification of 3,5-difluoropyridine were explored at a 1 T field. When preparing a SABRE sample combining the target substrate and dimethylsulfoxide as a co-substrate, the formation of a mixed species with improved enhancement efficiency was readily observed. This species was shown to be stable even in sub-stoichiometric conditions, allowing for the sub-micromolar probing of 3,5-difluoropyridine when the SNR-enhancing SHARPER pulse sequence was applied. The accurate quantification of this substrate was also demonstrated, through external calibration using linear calibration curves for  $^1\text{H}$  SABRE,  $^{19}\text{F}$  SABRE and  $^{19}\text{F}$  SABRE SHARPER NMR measurements. The greater performance of  $^{19}\text{F}$  over  $^1\text{H}$  NMR measurements, especially when SHARPER was employed, highlights the benefits of analysing samples through this heteronucleus.

The superior analytical performance of SABRE-enhanced benchtop NMR spectroscopy when using co-substrates was here demonstrated on a well-studied and accessible SABRE substrate. However, for this technique to reach its full potential it needs to be applicable to a more extensive and challenging scope of compounds. This will be explored in the next chapter where 2,4,6-trifluorobenzylamine will be the analytical target. This substrate adds complexity as it contains exchangeable protons that may participate in a SABRE-Relay process, which could impact both quantification and limits of detection.

## Chapter 6

# Low Micromolar Detection and Quantification of Fluoroamines

This chapter will expand on the promising results presented in Chapter 5, in which the low-concentration detection and accurate quantification potential of  $^{19}\text{F}$  SABRE-enhanced benchtop NMR was demonstrated. The remarkable analytical performance of this approach was showcased using the SABRE-amenable substrate 3,5-difluoropyridine and dimethylsulfoxide as a co-substrate. This fluoropyridine represented an accessible test subject as it exhibits simple proton and fluorine spectra, and its SABRE performance had been previously demonstrated.<sup>193</sup> Whilst investigating this well-performing system was useful to demonstrate the best analytical performance of the method in a proof-of-concept study, it fails to reflect the complexities of potential real-life analytes.

In this chapter, the robustness of this SABRE-enhanced benchtop NMR technique will be tested using a more challenging: 2,4,6-trifluorobenzylamine. This test subject is representative of the amine chemical group, an ubiquitous moiety in chemistry.<sup>245–248</sup> In addition, this molecule has exchangeable protons, and as such, can participate in SABRE-Relay processes which enables polarisation transfer from an iridium-binding substrate to a second molecule through proton exchange.<sup>78</sup>

Firstly, the  $^1\text{H}$  and  $^{19}\text{F}$  SABRE activity of samples containing 2,4,6-trifluorobenzylamine

as the substrate and dimethylsulfoxide as the co-substrate will be presented. Secondly, the SABRE-Relay activity of this substrate and its impact on enhancement factors, as well as a remediation strategy, will be discussed. This will be followed by a comparison of analytical performance parameters, in particular, limits of detection and quantification accuracy, under both SABRE-Relay active and inactive conditions.

## 6.1 Background Theory

### 6.1.1 SABRE Hyperpolarisation of Amines

Amines are commonly found in industrial pharmaceutical settings, as well as being present in several biologically relevant molecules,<sup>245-248</sup> making them interesting analytical objectives. The hyperpolarisation of substrates through an amine moiety was first reported by Glögler *et al.* using Crabtree's catalyst.<sup>146</sup> More recently, Iali *et al.* investigated the hyperpolarisation of amines such as ammonia and benzylamine using [IrCl(COD)(IMes)] as a pre-catalyst, reaching <sup>1</sup>H signal enhancement levels of up to 154-fold and 194-fold per proton, respectively.<sup>78,79</sup> An aprotic solvent (dichloromethane-*d*<sub>2</sub>) was used in these SABRE experiments in order to prevent the deuteration of the amine group through rapid <sup>2</sup>H exchange in deuterated solvents.

Although direct polarisation of amines, *i.e.* through the formation of a tris-substituted amine complex of structure [Ir(H)<sub>2</sub>(IMes)(amine)<sub>3</sub>]Cl, was shown to be suitable for the hyperpolarisation of some primary amines, it was found to be ineffective for bulkier or electronically-poor primary amines, as well as, secondary amines.<sup>78</sup> For example, when testing the electron-deficient aniline as a substrate using SABRE, no SABRE-active species were observed. As previously discussed, this could be overcome by applying the well-established strategy of using co-substrates to form stable SABRE-active catalyst species. For instance, using acetonitrile as a co-substrate led to signal enhancement levels by a factor of 306 for the amino protons in aniline. However, the same approach proved to be unsuccessful for bulky secondary amines such as dibenzylamine.<sup>78</sup>

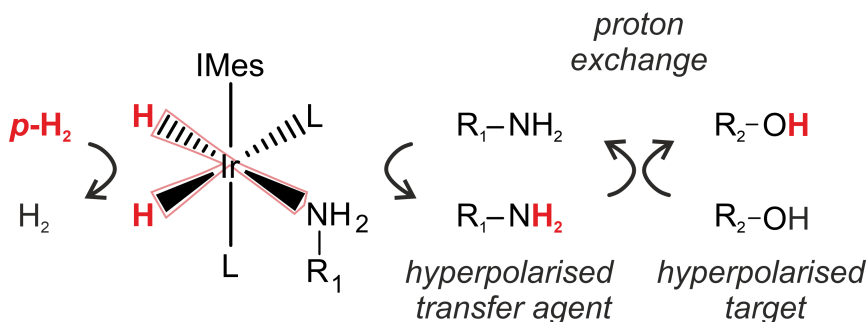


Figure 6.1: Schematic representation of SABRE-Relay hyperpolarisation. Direct hyperpolarisation of a substrate with exchangeable protons, here exemplified by R<sub>1</sub>NH<sub>2</sub>, results in a hyperpolarised transfer agent once released into solution. A second molecule (R<sub>2</sub>OH) then becomes indirectly hyperpolarised after proton exchange with the polarisation transfer agent.

### 6.1.2 SABRE-Relay

SABRE-Relay offers a different approach to the hyperpolarisation of sterically hindered or electron-poor amines by exploiting proton exchange mechanisms as a polarisation redistribution strategy.<sup>78,79</sup> This approach, which is represented schematically in Figure 6.1, involves the relay of polarisation from a SABRE-active molecule with exchangeable protons ('hyperpolarised transfer agent' in Figure 6.1) to a non-SABRE-active molecule *via* proton exchange. This approach proved to be an effective route to hyperpolarise challenging secondary amines,<sup>78</sup> as well as other target molecules with exchangeable protons including alcohols, amides, carboxylic acids, and carbonates.<sup>79,154</sup> SABRE-Relay was also successfully used to hyperpolarise heteronuclei such as <sup>13</sup>C, <sup>19</sup>F, <sup>31</sup>P, and <sup>29</sup>Si.<sup>154,180</sup> In this way, SABRE-Relay can greatly extend the scope of molecules that can be hyperpolarised *via* SABRE.

Work carried out by Rayner *et al.* revealed that a key factor in SABRE-Relay hyperpolarisation efficiency is the chosen polarisation transfer agent.<sup>154</sup> For this molecule to successfully participate in a SABRE-Relay process, it must form an active SABRE complex, and exchange into solution at a suitable rate to yield large signal enhancements. In a

study of several amines, the authors observed that the best performing polarisation carrier was ammonia, followed by benzylamine and ethylamine. These organic amines performed even better when their carbon backbone was deuterated, as spin dilution is minimised.

Equally relevant to an optimum SABRE-Relay process, is the efficiency of proton exchange between the polarisation carrier and the target molecule to be hyperpolarised.<sup>154</sup> The authors proposed that the proton exchange process, which is thought to happen in a bimolecular fashion with  $[R_1-NH_3^+][^-O-R_2]$  as an intermediate,<sup>249,250</sup> needs to happen at a suitable rate that favours efficient polarisation transfer. The relative concentration between polarisation carrier and target molecule should also be considered. They observed that for best results, these concentrations should be similar, as an excess of one over the other would favour proton exchange either amongst carrier molecules or target molecules.

The presence of a competing exchange process, for example, one involving water, may have a negative impact on the signal enhancement of the target molecule. Rayner *et al.* illustrated this by adding 1  $\mu$ L of water to a SABRE-Relay sample, which led to a reduction in the signal enhancement level of the target molecule by a factor of 10, and the observation of hyperpolarised water signals.<sup>154</sup> This was proposed to be a consequence of increased spin dilution and a less efficient proton exchange process between the polarisation carrier and the target molecule. Such an effect could be minimised by performing SABRE-Relay experiments under anhydrous conditions to eliminate this alternative proton exchange pathway.

As illustrated above, successful SABRE-Relay experiments may require more optimisation steps than the direct SABRE hyperpolarisation approach. Nevertheless, this approach greatly extends the scope of molecules that can be probed and, as such, is analytically promising. For example, Alsheri *et al.* employed SABRE-Relay to hyperpolarise complex plant-based oils containing hydroxyl groups ( $-OH$ ) to obtain both  $^1H$  and  $^{13}C$  NMR diagnostic information.<sup>251</sup> This approach enabled the low-concentration detection (*ca.* 30  $\mu$ M) of these compounds in a commercially-sourced essential oil. Further illustrating the analytical usefulness of this technique, Richardson *et al.* demonstrated that quantification using SABRE-Relay is possible.<sup>84</sup> This was shown for the analysis of monosaccharides us-

ing hyperpolarised  $^{13}\text{C}$  NMR, for which a linear relationship between the concentration of analyte and the hyperpolarised signals was obtained.

## 6.2 Choice of Test System

In order to test the robustness and versatility of SABRE-hyperpolarised quantification using benchtop NMR, a more challenging substrate, 2,4,6-trifluorobenzylamine (TFBA, **7**, Figure 6.2), was chosen as a test subject. SABRE-hyperpolarisation of its non-fluorinated analogue, benzylamine, has been reported before,<sup>78,79,154</sup> setting a favourable precedent for TFBA. The added difficulties introduced by this substrate include a more complex  $^{19}\text{F}$  NMR spectrum, as it presents two distinct  $^{19}\text{F}$  resonances with complex splitting patterns. Additionally, SABRE-hyperpolarisation of amines is expected to be less efficient ( $\epsilon_{1\text{H}} < 1000$ <sup>78</sup>) than for pyridine-based substrates ( $\epsilon_{1\text{H}}$  of tens of thousands<sup>76</sup>). An additional complication of this substrate is that it contains exchangeable protons, and has been shown to act as a polarisation transfer carrier in SABRE-Relay process.<sup>78,154</sup> This has the potential to negatively impact enhancement levels as polarisation may be diverted from TFBA to other molecules with exchangeable protons in solution. Each of these challenges is expected to have a detrimental impact on the resulting SNR for this molecule, and, as a consequence, result in a higher limit of detection. Nevertheless, amines are common moieties in molecules such as pharmaceuticals and metabolites,<sup>245–248</sup> making TFBA a relevant and interesting substrate.

SABRE-hyperpolarisation of amines is commonly done in aprotic solvents, *e.g.* dichloromethane or chloroform, in order to prevent proton exchange with the solvent.<sup>78,79,154</sup> However, methanol was chosen as the solvent in this study to avoid using chlorinated solvents with increasing concerns in terms of toxicity and environmental impact, concerns which have now led to a ban on the use of dichloromethane in some countries.<sup>252,253</sup> Using methanol also provided a route to understanding how unwanted SABRE-Relay processes may affect the analysis of proton exchanging molecules, as well as to investigate possible remediation strategies.

As for the choice of co-substrate, the use of dimethyl sulfoxide (DMSO) was maintained due to the advantages discussed in Chapter 5, whilst also allowing for a direct comparison with the fluoropyridine system. Additionally, the lack of exchangeable protons and low reactivity of DMSO was deemed advantageous.

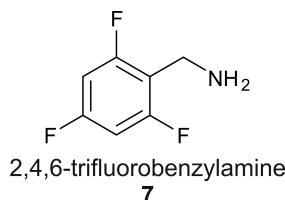


Figure 6.2: Chemical structure of the substrate 2,4,6-trifluorobenzylamine (TFBA, **7**).

### 6.3 SABRE Hyperpolarisation of the Test Molecule

For the proposed system to be suitable for this study, it was necessary to investigate whether a SABRE-active species containing both TFBA and DMSO forms upon mixing. In the first instance, this was tested by comparing the SABRE activity of samples containing TFBA with and without the addition of DMSO, as changes in hyperpolarisation behaviour would be indicative of different species being at play. To test this, a set of samples containing 100 mM of TFBA, 5 mM of [IrCl(COD)(IMes)], and either 100 mM of DMSO, or no co-substrate in methanol- $d_4$  were prepared. Given the air-sensitive nature of TFBA, the samples were prepared inside a glovebox, as described in Section 3.1.2 (Chapter 3). Shake-and-drop experiments followed by  $^1\text{H}$  and  $^{19}\text{F}$  pulse-and-collect NMR acquisition (1 T) were conducted and processed as previously described (Sections 3.2 to 3.4, Chapter 3). Polarisation transfer fields of 6.2 mT for  $^1\text{H}$  measurements and both 6.2 mT and  $\sim 50 \mu\text{T}$  for  $^{19}\text{F}$  measurements were used. Whilst the PTF values of 6.2 mT (for  $^1\text{H}$  nuclei) and  $\sim 50 \mu\text{T}$  (for  $^{19}\text{F}$  nuclei) were chosen as they are expected to yield good results for direct transfer to those nuclei, 6.2 mT was also used for  $^{19}\text{F}$  measurements to investigate the efficiency of proton-relayed polarisation transfer mechanisms. Non-hyperpolarised  $^1\text{H}$  NMR spectra at 1.4 T were acquired according to Section 3.3 (Chapter 3). Enhancement factors and SNR

calculations were done according to Sections 3.7.1 and 3.7.2 (Chapter 3).

Inspection of hyperpolarised and non-hyperpolarised  $^1\text{H}$  NMR spectra (1 T) for samples with and without co-substrate (Figure 6.3) revealed SABRE-active systems in both cases: hyperpolarisation of the methylene ( $\delta$  3.83, purple circles) and aromatic ( $\delta$  6.85, yellow squares) signals in TFBA were observed. When DMSO was used as a co-substrate, its corresponding hyperpolarised signal was also observed ( $\delta$  2.65). As for  $^{19}\text{F}$  signals, hyperpolarisation was observed for *ortho* ( $\delta$  - 116.1) and *para* ( $\delta$  -111.9)  $^{19}\text{F}$  NMR signals for samples with and without co-substrate (Figure 6.6).

Although hyperpolarisation of the target substrate was achieved in both scenarios, it appears to be produced by different polarisation transfer catalyst species, as shown by the hydride ligand signals in the insets of Figure 6.3 (C and D). When no co-substrate was used, a singlet at  $\delta$  -24.5 was observed. The singlet nature of this peak, as well as the lack of a corresponding partner, suggested this was an equatorially symmetric species, likely that corresponding to the tris-substituted species containing TFBA,  $[\text{IrCl}(\text{H})_2(\text{IMes})(\mathbf{7})_3]$ . The chemical shift value for this signal was comparable to that reported for a tris-benzylamine SABRE complex ( $\delta$  -23.95<sup>78</sup>), increasing confidence in the assignment.

In contrast, when DMSO was added as a co-substrate, new hyperpolarised hydride ligand signals were observed, and later on confirmed by non-hyperpolarised experiments at 1.4 T (Figure 6.3, inset D), a field chosen due to the increased sensitivity it affords. These signals included a singlet at  $\delta$  - 22.8 and a pair of signals at  $\delta$  -23.2 and  $\delta$  -24.3. As this pair of signals exhibited a similar intensity, they were thought to correspond to an asymmetric complex, which could correspond to the desired mixed species containing TFBA and DMSO.

In order to confirm that an active species containing both TFBA and DMSO was formed when adding a co-substrate, a high-field NMR characterisation study was carried out as presented in Figure 6.5 and Table 6.1, and described in detail in Chapter 3, Section 3.8.2. Based on this study, the structure shown in Figure 6.4, **8**, is proposed as the species exhibiting hydride ligand signals at  $\delta$  -23.2 and  $\delta$  -24.3. This species is analogous to that observed with the same co-substrate and either 3,5-difluoropyridine (Chapter 5), dichloro-

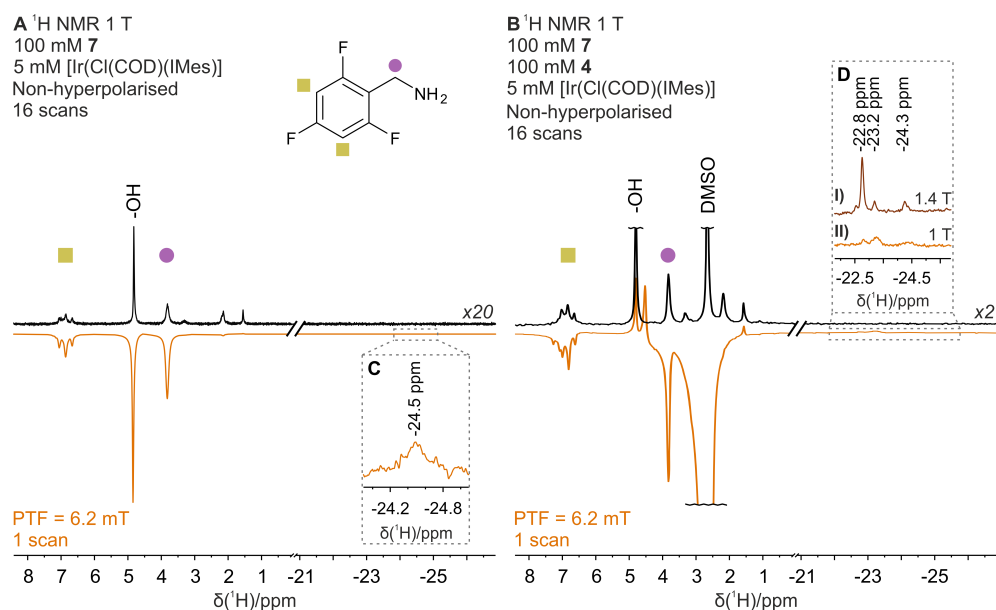


Figure 6.3: Comparison between non-hyperpolarised (top trace) and SABRE- hyperpolarised (bottom trace)  $^1\text{H}$  NMR spectra for samples containing 100 mM of TFBA, 5 mM of  $[\text{IrCl}(\text{COD})(\text{IMes})]$ , and either no co-substrate (A) or 100 mM of DMSO (B) in methanol- $d_4$ . Spectra are zoomed in to show the organic ( $\delta$  8.5 to  $\delta$  0) and hydride ( $\delta$  -21 to  $\delta$  -27) regions. Hyperpolarised experiments were conducted using a polarisation transfer field of 6.2 mT. Signals corresponding to the exchangeable protons ('-OH') and DMSO ('DMSO') are indicated with labels. Inset C shows the hyperpolarised hydride ligand signal detected for this sample, which is thought to correspond to the tris-substituted species  $[\text{IrCl}(\text{H})_2(\text{IMes})(\mathbf{7})_3]$ . Inset D shows a comparison of the hyperpolarised hydride signals detected for the sample with co-substrate (II) and the those detected on a non-hyperpolarised experiment of this sample at 1.4 T by signal averaging for 4096 scans (I).

/dibromopyridine,<sup>189</sup> or 2,5-lutidine<sup>163</sup> as substrates. As discussed in Chapter 5, this structure is advantageous for analytical applications as it contains the target molecule on the equatorial plane, a position which favours signal enhancement. Additionally, the other equatorial position is filled by a chloride ion, which minimises spin dilution as  $^{35}\text{Cl}$  and  $^{37}\text{Cl}$  are spin-3/2 nuclei with low gyromagnetic ratio and therefore are not expected to

participate significantly in the polarisation transfer process.

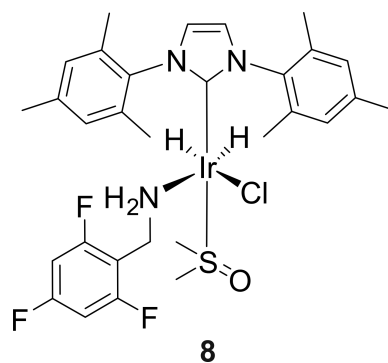


Figure 6.4: Main SABRE-active species (**8**) in samples containing TFBA, DMSO, and 5 mM of  $[\text{IrCl}(\text{COD})(\text{IMes})]$ .

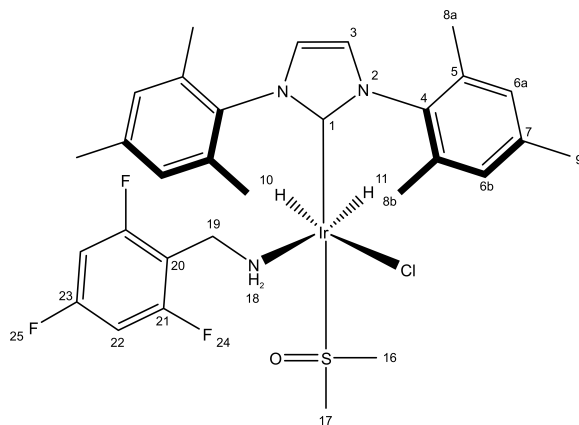


Figure 6.5: Proposed structure for the active SABRE complex containing TFBA and DMSO.

Table 6.1: High-field NMR characterisation results for the SABRE active complex containing TFBA and DMSO.

| Resonance number | $\delta$ $^1\text{H}$ | $\delta$ $^{13}\text{C}$ | $\delta$ $^{19}\text{F}$ |
|------------------|-----------------------|--------------------------|--------------------------|
| 1                | -                     | 160.29                   | -                        |
| 2                | -                     | -                        | -                        |
| 3                | 7.21                  | 122.69                   | -                        |
| 4                | -                     | 139.90                   | -                        |
| 5                | -                     | 136.49/138.44            | -                        |
| 6                | 6.94/6.96             | 128.58/128.72            | -                        |
| 7                | -                     | 140.59                   | -                        |
| 8                | 2.13/2.22             | 18.94/17.95              | -                        |
| 9                | 2.20                  | 20.45                    | -                        |
| 10               | -23.2 (d, J = 7.6 Hz) | -                        | -                        |
| 11               | -24.3 (d, J = 7.6 Hz) | -                        | -                        |
| 16, 17           | 3.19/3.21             | 58.15/46.73              | -                        |
| 18               | 5.15                  | -                        | -                        |
| 19               | 3.90                  | 32.34                    | -                        |
| 20               | -                     | 112.98                   | -                        |
| 21               | -                     | 161.26                   | -                        |
| 22               | 6.97                  | 100.03                   | -                        |
| 23               | -                     | 163.22                   | -                        |
| 24               | -                     | -                        | -112.45                  |
| 25               | -                     | -                        | -106.45/ -110.77         |

In order to assess whether the introduction of a co-substrate improved SABRE efficiency,  $\varepsilon_{^1\text{H}}$  and  $\varepsilon_{^{19}\text{F}}$  values for samples with and without DMSO were compared (Table 6.2). Enhancement factors for  $^1\text{H}$  signals in TFBA were modest for samples without a co-substrate. For instance,  $\varepsilon_{^1\text{H}}$  for signals corresponding to the methylene ( $-\text{CH}_2$ ) and

aromatic ring ( $m$ - $^1\text{H}$ ) resonances were  $\varepsilon_{1\text{H}} = (26.4 \pm 2.6)$  and  $\varepsilon_{1\text{H}} = (28.9 \pm 2.2)$ . It was not possible to establish from these results whether the addition of co-substrates was beneficial, as  $^1\text{H}$  enhancement factors varied in opposite ways:  $\varepsilon_{1\text{H}}$  for the methylene signal doubled ( $\varepsilon_{1\text{H}} = (55.6 \pm 7.7)$ ), whilst that of the aromatic signal decreased by *ca.* 20 % ( $\varepsilon_{1\text{H}} = (23.8 \pm 3.2)$ ).

One notable difference introduced by the use of co-substrates was in the enhancement for the signal corresponding to exchangeable protons ( $\delta$  4.8, ‘-OH’ in Figure 6.3), as hyperpolarisation of this signal was only observed in the absence of DMSO. It is unlikely this signal had a significant contribution of exchangeable protons from the amine group in TFBA, as the preparation of these sample in a solvent with exchangeable deuterium would result in their rapid deuteration. Similar results were reported before by Fekete *et al.*, who observed fast deuteration of the exchangeable protons in benzylamine in deuterated solvent.<sup>151</sup> Therefore, it is reasonable to propose that the hyperpolarised signal observed at  $\delta$  4.8 must have a predominant contribution from protonated methanol- $d_4$  ( $\text{CD}_3\text{OH}$ ). As methanol-containing SABRE species are not expected to lead to hyperpolarisation in methanol- $d_4$  (Chapter 4), this enhanced signal must be the consequence of SABRE-Relay activity, with TFBA acting as a polarisation transfer agent.

The SABRE-Relay activity of samples containing TFBA in methanol- $d_4$  was not expected to be efficient, as the exchangeable protons of the polarisation transfer agent would predominantly be deuterated. However, this behaviour could be explained if the amine was re-protonated whilst bound to the iridium catalyst by H-D exchange with hydrides *cis* to TFBA. This behaviour was observed for species containing fluoropyridines and methanol- $d_4$  (Section 4.3, Chapter 4), as evidenced by the formation of characteristic downfield hydride singlet signals and a triplet at  $\delta$  4.55 corresponding to HD gas (Section 3.8.2, Chapter 3). High-field NMR characterisation studies of samples containing TFBA and DMSO (Section 3.8.2, Chapter 3) revealed similar observations, further supporting the idea that TFBA participates in H-D exchange with neighbouring hydride ligands.

The H-D exchange process between hydrides and TFBA may also account for the difference in SABRE-Relay activity in samples with and without co-substrate. In the absence of

Table 6.2: Proton ( $\varepsilon_{1\text{H}}$ ) and fluorine ( $\varepsilon_{19\text{F}}$ ) enhancement factors for hyperpolarised samples containing 100 mM of TFBA, either no co-substrate or 100 mM of DMSO as a co-substrate, and 5 mM of  $[\text{IrCl}(\text{COD})(\text{IMes})]$  in methanol- $d_4$ . Fluorine enhancement factors were estimated using PTF values of 6.2 mT and  $\sim 50 \mu\text{T}$ . \*ND: signal not detectable.

| PTF                   | No co-substrate           |                       |  |                          | With co-substrate         |                       |  |                          |
|-----------------------|---------------------------|-----------------------|--|--------------------------|---------------------------|-----------------------|--|--------------------------|
|                       | $\varepsilon_{1\text{H}}$ |                       | $\varepsilon_{19\text{F}} (\times 10^1)$ |                          | $\varepsilon_{1\text{H}}$ |                       | $\varepsilon_{19\text{F}} (\times 10^1)$ |                          |
|                       | $-\text{CH}_2$            | $m\text{-}^1\text{H}$ | $o\text{-}^{19}\text{F}$                 | $p\text{-}^{19}\text{F}$ | $-\text{CH}_2$            | $m\text{-}^1\text{H}$ | $o\text{-}^{19}\text{F}$                 | $p\text{-}^{19}\text{F}$ |
| 6.2 mT                | $26.4 \pm$                | $28.9 \pm$            | $140 \pm$                                | $130 \pm$                | $55.6 \pm$                | $23.8 \pm$            | $258 \pm$                                | $295 \pm$                |
|                       | 2.6                       | 2.2                   | 22                                       | 24                       | 7.7                       | 3.2                   | 13                                       | 9                        |
| $\sim 50 \mu\text{T}$ | -                         | -                     | $16.0 \pm$                               | ND*                      | -                         | -                     | 39.85                                    | -63.47                   |
|                       |                           |                       | 1.5                                      |                          |                           |                       | $\pm 0.64$                               | $\pm 0.57$               |

DMSO, SABRE activity is enabled by a tris-substituted species containing TFBA, which means two units of TFBA are on the equatorial plane and may be subject to H-D exchange. In contrast, samples containing DMSO favour the formation of  $[\text{IrCl}(\text{H})_2(\text{IMes})(\mathbf{7})(\mathbf{4})]$ , which means only one unit of TFBA in the complex may undergo H-D exchange. Consequently, re-protonation of deuterated TFBA is expected to be more efficient in samples without DMSO, thus facilitating SABRE-Relay polarisation of the solvent. Furthermore, every substrate dissociation event for the tris-TFBA species releases one unit of polarisation transfer carrier into solution. Conversely, for  $[\text{IrCl}(\text{H})_2(\text{IMes})(\mathbf{7})(\mathbf{4})]$ , substrate dissociation may release either TFBA or chloride. As a result, the concentration of hyperpolarised polarisation carrier at any given time is expected to be lower for samples with DMSO, thus reducing the effectiveness of SABRE-Relay.<sup>154</sup>

Contrary to what was observed in  $^1\text{H}$  experiments, the use of co-substrates led to a clear improvement in  $^{19}\text{F}$  enhancement factors, as seen in Table 6.2. Indeed, the introduction of DMSO has roughly doubled  $\varepsilon_{19\text{F}}$  at both of the tested polarisation transfer fields. The improvement of SABRE performance for TFBA when adding co-substrates is consistent with observations for 3,5-difluoropyridine (Chapter 5), as well as previous reports of sim-

ilar behaviour,<sup>140,163,189</sup> which attributed this improvement to a more efficient substrate dissociation rate. Iali *et al.* argued that polarisation levels achieved for benzylamine were limited by its slow exchange rate, which induces faster relaxation as the residence time of the substrate increases.<sup>78</sup> Therefore, it is possible that the active species containing chloride and DMSO resulted in a faster exchange rate which optimised hyperpolarisation efficiency for TFBA. Since an improvement in hyperpolarisation efficiency was observed for TFBA when using DMSO, a detailed study of the exchange rates was not deemed necessary.

Closer inspection of fluorine enhancement factors for SABRE experiments on TFBA (Table 6.2) revealed that  $\varepsilon_{^{19}\text{F}}$  using a polarisation transfer field of 6.2 mT were larger than those obtained at  $\sim 50 \mu\text{T}$ . This suggests that the proton-relayed polarisation transfer mechanism favoured at this PTF is more efficient than direct polarisation to  $^{19}\text{F}$  nuclei. Such a finding is reasonable as  $^{19}\text{F}$  hyperpolarisation at  $\sim 50 \mu\text{T}$  involves polarisation transfer from the hydrides to the fluorine atoms through a long-range scalar coupling: either a 6-bond coupling (*ortho*- $^{19}\text{F}$ ) or a 8-bond coupling (*para*- $^{19}\text{F}$ ). Polarisation transfer through so many bonds, although enabled by long distance  $^{19}\text{F}$  scalar couplings, would likely be less effective. Notably, at PTF values of  $\sim 50 \mu\text{T}$ , *ortho* and *para*  $^{19}\text{F}$  signals showed opposite phase, suggesting an inter-fluorine polarisation transfer pathway (Figure 6.6). Although this difference in phasing was only evident for samples with co-substrates, it is hypothesised that this would also be present in samples without a co-substrate, with low enhancements precluding its observation in these experiments. Samples with co-substrates tested at  $\sim 50 \mu\text{T}$  also exhibited an anti-phase character relative to a J coupling of *ca.* 9 Hz (Figure 6.6c). This coupling, which was identified as  $^3J_{\text{HF}}$ , indicates that polarisation transfer also occurs between fluorine nuclei in the *ortho* position and the protons in the aromatic ring.

Given the long bond distance between the hydride ligands and the fluorine nuclei, direct polarisation transfer was likely to be most efficient for the closest  $^{19}\text{F}$  nuclei, *i.e.* *o*- $^{19}\text{F}$ , which would be then relayed to *p*- $^{19}\text{F}$ . Although this explains the larger  $\varepsilon_{^{19}\text{F}}$  seen for the *ortho* position in samples without a co-substrate, it fails to account for the *ca.* 50% larger  $\varepsilon_{^{19}\text{F}}$  values for *p*- $^{19}\text{F}$  relative to *o*- $^{19}\text{F}$ , in samples with DMSO. One possible explanation

for this may be based on differences in relaxation times for these nuclei in the systems with and without co-substrate. As previously discussed, changes in the coordination sphere of these catalyst species, particularly in terms of electronic density, are expected to have an impact on ligand exchange rates and substrate residence times. As hyperpolarisation lifetime values are heavily influenced by substrate residence times,  $T_1$  values would likely differ in species with and without co-substrates. In addition, *ortho*  $^{19}\text{F}$  nuclei are expected to have a more complex scalar coupling network which extends to the nuclei in the catalyst, whereas the coupling network for *para* fluorine would involve less nuclei, placing it in relative isolation. As a result, when the substrate is bound to the catalyst, relaxation would be preferentially induced for *ortho* fluorine nuclei, leading to a smaller  $\varepsilon_{^{19}\text{F}}$ . It is possible that the combination of these two factors accounts for the difference in relative  $\varepsilon_{^{19}\text{F}}$  for *ortho* and *para* signals in samples with and without co-substrates. Another explanation would be that as some of the polarisation of the *ortho* fluorine nuclei appeared to be relayed towards the aromatic  $^1\text{H}$  nuclei, the overall enhancement seen for this resonance would be lower.

The results presented so far illustrate the lower SABRE efficiency of fluoroamines when compared to fluoropyridines. For instance, enhancement factors observed for  $^1\text{H}$  nuclei in fluoroamines ( $\varepsilon_{^1\text{H}} < 100$ ) were considerably lower than those for the fluoropyridines discussed in Chapters 4 and 5 ( $\varepsilon_{^1\text{H}} = 700 - 3000$ ). The slow exchange rate reported for benzylamine by Iali *et al.* may provide an explanation for this. Whilst amines have a lone pair of electrons that can readily form a dative bond to act as a ligand, the lone pair of electrons on the nitrogen in pyridine-based molecules is de-localised in the aromatic ring, making it less electron rich. As a result, amine ligands would form a more stable tris-complex,<sup>78</sup> as evidenced by the slower exchange rate constant for ammonia and benzylamine ( $k_D = 1.64 \text{ s}^{-1}$  and  $k_D = 3.33 \text{ s}^{-1}$ , respectively) *versus* pyridine ( $k_D = 13.2 \text{ s}^{-1}$ ) at 298 K.<sup>78</sup>

Another factor leading to the lower SABRE activity of amines *versus* pyridine-based molecules is their higher basicity.<sup>199</sup> The substrate TFBA is expected to be present in solution as a mixture of the amine and its conjugate acid ( $\text{R-NH}_3^+$ ), provided there is a source of  $\text{H}^+$  in solution. The presence of such species was corroborated experimentally

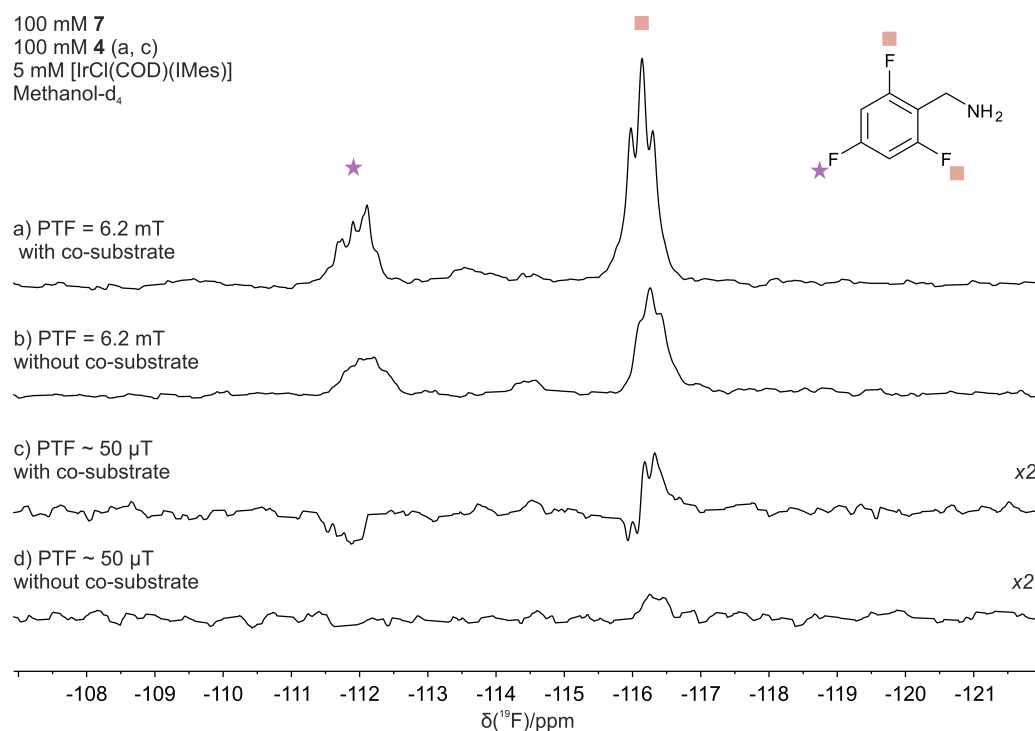


Figure 6.6: Typical 1 T  $^{19}\text{F}$  hyperpolarised spectra for samples with 100 mM TFBA, either 100 mM (a and c) or no (b and d) DMSO and 5 mM [IrCl(COD)(IMes)] in methanol- $d_4$ . SABRE experiments were conducted using a polarisation transfer field of 6.2 mT (a and b) or  $\sim 50 \mu\text{T}$  (c and d).

through high-field NMR experiments (Chapter 3, Section 3.8.2) by the presence of signals in the  $\delta$  8.7 to  $\delta$  7.5 range,<sup>254</sup> which were attributed to protonated amines with different degrees of deuteration (*e.g.*  $\text{R-NH}_3^+$ ,  $\text{R-NDH}_2^+$ , *etc.*). When the substrate is in the conjugate acid form, it cannot act as a ligand in the SABRE complex, as the lone pair of electrons that typically participates in this dative bond would be used in forming a bond with the extra proton. This is believed to have a negative impact on SABRE activity, as a portion of the total amount of TFBA in the sample cannot participate in the SABRE exchange process, thus reducing the effective concentration of substrate in solution. As the largest source of  $\text{H}^+$  in these samples was likely to arise from the residual amounts of  $\text{H}_2\text{O}$  in reagents, particularly through the hygroscopic dimethylsulfoxide, it is expected that

drying the reagents prior to sample preparation would mitigate this problem. Alternatively, pH-controlling measures could be implemented.<sup>196</sup>

The active species  $[\text{IrCl}(\text{H})_2(\text{IMes})(7)(4)]$  was observed even in sub-stoichiometric conditions. This is evidenced by the presence of the characteristic hydride ligand signals corresponding to the active species at  $\delta$  -23.2 and  $\delta$  -24.3 in samples containing TFBA in concentrations below stoichiometric conditions ( $< 5$  mM, Figure 6.7, orange squares). In a similar fashion to that already observed for samples containing 3,5-difluoropyridine and DMSO, the hydride ligand signals decreased in intensity with the concentration of substrate. This observation implies that the formation of this active species is sensitive to the concentration of substrate, which is a key requirement for quantitative applications. These spectra also revealed the presence of  $[\text{IrCl}(\text{H})_2(\text{IMes})(4)_2]$ , evidenced by two broad peaks at  $\delta$  15.5 and  $\delta$  21.5 (Figure 6.7, green triangles).

The hyperpolarised hydride ligand signals for the active species of interest (**8**) occasionally exhibited a further splitting, as shown in Figure 6.7A. As this splitting was not observed when protio methanol was used (Figure 6.7B), this behaviour is linked to the presence of deuterium. It is hypothesised that what appears to be splitting of signals is in fact two different hydride ligand species *trans* to units of TFBA with different degrees of deuteration. Similar results were observed for SABRE samples using ammonia as a substrate in methanol- $d_4$ , in which several hydride ligand signals were detected and attributed to ammonia isotopologues formed through H-D exchange.<sup>79</sup> The use of either protio or deuterated solvent introduced further differences in the performance of the SABRE process, a topic that will be addressed in the next section.

A third SABRE active species was detected in the sub-stoichiometric regime when using DMSO as a co-substrate. This species was observed both in methanol and methanol- $d_4$  samples and exhibited hydride signals at  $\delta$  - 9.5 and  $\delta$  -15.3, as shown in Figure 6.7 (purple circles). The same hydride ligand signals were detected in sub-stoichiometric samples containing 3,5-difluoropyridine and DMSO (Section 5.3.1, Chapter 5). The presence of such hydride ligand signals has been linked to the formation of a trihydride species in samples containing DMSO in basic conditions, for which the formula  $[\text{Ir}(\text{H})_3(\text{IMes})(4)_2]$  was pro-

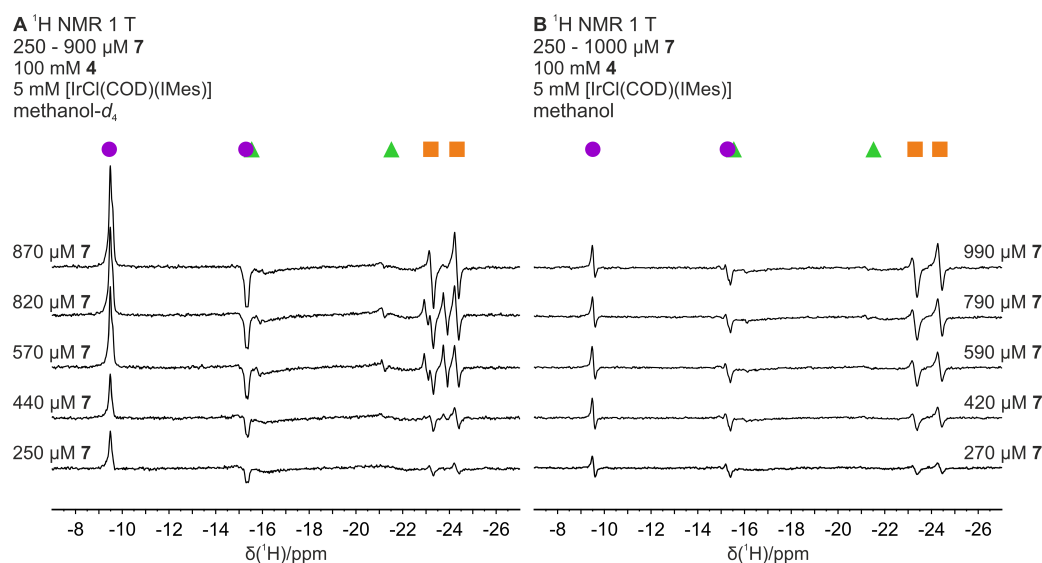


Figure 6.7: SABRE-hyperpolarised  $^1\text{H}$  NMR spectra acquired at 1 T of samples containing 250  $\mu\text{M}$  to 1000  $\mu\text{M}$  of TFBA, 100 mM of DMSO, and 5 mM of  $[\text{IrCl}(\text{COD})(\text{IMes})]$  in methanol- $d_4$  (A) or methanol (B), using a PTF = 6.2 mT. Spectra are zoomed in to show the hydride ligand signal region ( $\delta$  -7 to -27). Orange squares show the main active species containing TFBA (**8**), green triangles show **6**, and purple circles a trihydride species containing DMSO.

posed.<sup>211</sup> As this species does not contain the target analyte, its formation is not expected to affect the accuracy of quantification. However, as this species is SABRE-active, it contributes to the consumption of  $p\text{-H}_2$  from the solution which may reduce the efficiency of hyperpolarisation for TFBA, and as a result, measurement sensitivity.

The hyperpolarised signals observed for TFBA in the sub-stoichiometric regime correspond to those of the bound substrate. This is illustrated in Figure 6.8, in which SABRE samples containing TFBA in the supra-stoichiometric (100 mM) and sub-stoichiometric (0.87 mM) regimes are compared to a concentrated reference sample. Whilst the chemical shifts corresponding to the *ortho* and *para*  $^{19}\text{F}$  nuclei in the supra-stoichiometric regime ( $\delta$  -116.1 and  $\delta$  -111.9, respectively) matched those of the reference sample, these exhibited a shift upon binding. Bound hyperpolarised signals were also observed for the 3,5-

difluoropyridine system with co-substrates in the sub-stoichiometric regime. In both instances, this observation can be attributed to a higher binding affinity to the iridium centre of the substrates *versus* dimethylsulfoxide, which leads to a higher bound-to-free substrate ratio in the sub-stoichiometric regime, according to Eshuis' model (Chapter 5, Equation 5.1).<sup>81</sup>

Another consequence of TFBA being predominantly in its bound form in the sample is that its *ortho*-<sup>19</sup>F signals become chemically non-equivalent and differentiate to give two distinct signals of equal amplitude at  $\delta$  -107 and  $\delta$  -111 (Figure 6.8), which were also observed in high-field NMR characterisation studies at 7 T. These signals were considerably less intense than the signal for the *para* fluorine nuclei, even though these were expected to be in equimolar amounts. This was attributed to the differences in  $T_1$  relaxation for *ortho* and *para* <sup>19</sup>F signal previously discussed, which would be exacerbated in the sub-stoichiometric regime as the substrate is predominantly in its bound form.

Probing this system in the sub-stoichiometric regime using polarisation transfer fields of 6.2 mT and  $\sim 50 \mu\text{T}$  revealed a similar trend to that seen in supra-stoichiometric conditions: experiments at 6.2 mT resulted in equally-phased <sup>19</sup>F signals with larger enhancements. Based on these findings, studies in the sub-stoichiometric regime were conducted at 6.2 mT due to the higher sensitivity it afforded. In addition, results at this PTF were more compatible with SHARPER acquisition, as experiments at  $\sim 50 \mu\text{T}$  resulted in signals with different phases, which would lead to partial or complete signal cancellation upon application of SHARPER.

In the previous chapter, the optimisation of the concentration of DMSO led to higher enhancement factors. Therefore, a similar study was performed for the fluoroamine test system in sub-stoichiometric conditions by comparing samples containing 10 mM of TFBA, either 25 mM or 100 mM of DMSO, and 5 mM of [IrCl(COD)(IMes)] in methanol-*d*<sub>1</sub>. The comparison of <sup>1</sup>H signal enhancement for samples with 25 mM and 100 mM of co-substrate is shown in Figure 6.9 and Table 6.3. Proton signal enhancements were approximately 4 and 6 times larger for the methylene and aromatic resonances, respectively, when higher concentrations of DMSO were used. A similar observation can be made for <sup>19</sup>F enhancements,

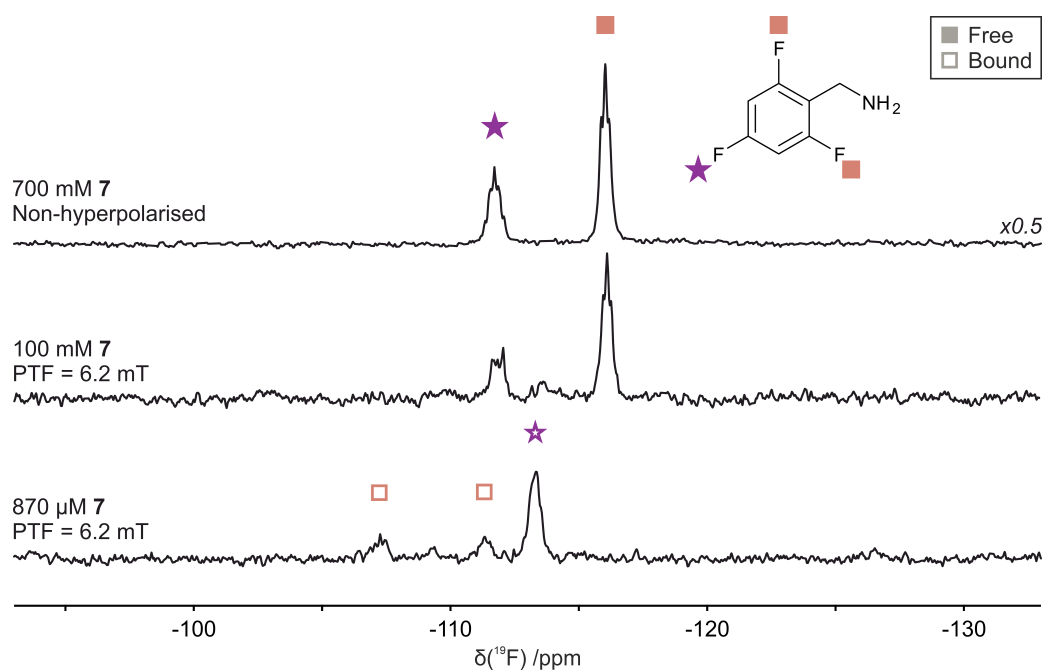


Figure 6.8: Comparison of  $^{19}\text{F}$  spectra of TFBA samples at 1 T. The samples contained 700 mM of TFBA (top), 100 mM of TFBA, 100 mM of DMSO and 5 mM of  $[\text{IrCl}(\text{COD})(\text{IMes})]$  (middle) or 870  $\mu\text{M}$  of TFBA, 100 mM of DMSO and 5 mM of  $[\text{IrCl}(\text{COD})(\text{IMes})]$  (bottom). All samples were prepared in methanol- $d_4$  and all spectra acquired with a single scan.

as shown in Figure 6.10. The low sensitivity of non-hyperpolarised  $^{19}\text{F}$  measurements precluded the determination of  $\epsilon_{^{19}\text{F}}$  for each sample, even at a near-stoichiometric concentration resulting in a mixture of bound and free signals. Nevertheless, a direct comparison of areas showed that the use of a higher concentration of DMSO increased hyperpolarised signal intensity by roughly 50%.

This increase in  $^1\text{H}$  and  $^{19}\text{F}$  enhancement factors at higher co-substrate concentrations may be attributed to an increase in the formation of the active species **8**, as evidenced by its hydride ligand signals in Figure 6.9C. This figure also shows larger signals for the SABRE-active species  $[\text{IrCl}(\text{H})_2(\text{IMes})(\mathbf{4})_2]$  (**6**), which by undergoing fast substrate dissociation,<sup>163,202</sup> may increase the rate of substrate sampling and consequently, hyperpolarisation efficiency. This improvement in performance observed at higher co-substrate

concentration may also be explained by an increase in free-to-bound substrate ratio, as predicted by Equation 5.1. By increasing this ratio, the overall detected hyperpolarisation lifetime would also increase, thus helping overcome one of the signal enhancement limitations of benzylamines.<sup>78</sup> Interestingly, even though samples with higher concentrations of DMSO favoured the formation of  $[\text{Ir}(\text{H})_3(\text{IMes})(\mathbf{4})_2]$ , this did not negatively impact signal enhancements for TFBA, as anticipated.

Table 6.3: Proton ( $\varepsilon_{1\text{H}}$ ) enhancement factors for SABRE-hyperpolarised samples containing 10 mM of TFBA, either 25 mM or 100 mM of DMSO as a co-substrate, and 5 mM of  $[\text{IrCl}(\text{COD})(\text{IMes})]$  in methanol- $d_1$ . Experiments were conducted using a PTF of 6.2 mT.

|                           | 25 mM co-substrate |                           | 100 mM co-substrate |                           |
|---------------------------|--------------------|---------------------------|---------------------|---------------------------|
| Signal                    | –CH <sub>2</sub>   | <i>m</i> - <sup>1</sup> H | –CH <sub>2</sub>    | <i>m</i> - <sup>1</sup> H |
| $\varepsilon_{1\text{H}}$ | 29 ± 16            | 79.5 ± 3.2                | 112.1 ± 7.7         | 497.2 ± 9.6               |

Under optimised condition, typical <sup>1</sup>H and <sup>19</sup>F SABRE spectra in the sub-stoichiometric regime are shown in Figure 6.11. Proton enhancement factors could not be reliably determined at this concentration due to peak overlap, for the aromatic signals, or poor baseline separation for the methylene group. In contrast, <sup>19</sup>F NMR signals were isolated enough to estimate an enhancement factor of 170 ± 20 (Figure 6.11B). This highlights the benefits of probing <sup>19</sup>F signals as an alternative to <sup>1</sup>H. A significant decrease in  $\varepsilon_{19\text{F}}$  was seen in the sub-stoichiometric regime when compared to the supra-stoichiometric regime (Table 6.2). This is likely a consequence of TFBA being mainly in its bound form, leading to increase relaxation and lower signal intensities.

## 6.4 SABRE-Relay Activity of the Test Molecule

As introduced in the previous section (Section 6.3), the test molecule under investigation displayed SABRE-Relay activity, as evidenced by the hyperpolarisation of the exchangeable proton in the solvent ( $\delta$  4.8). It was also observed that using co-substrates led to

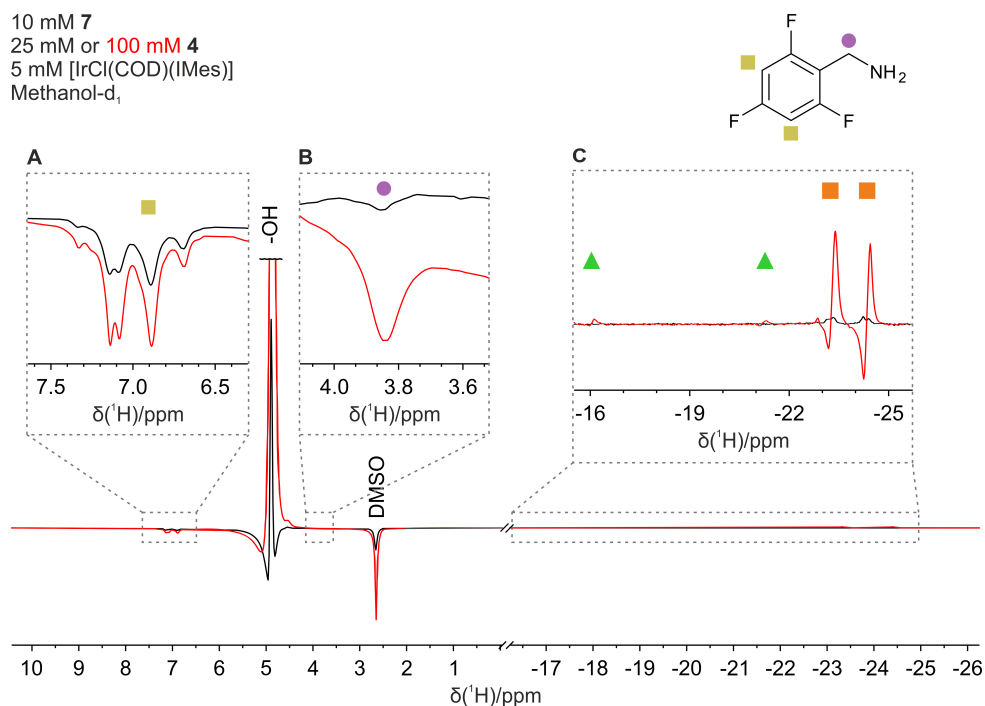


Figure 6.9: SABRE-hyperpolarised  $^1\text{H}$  spectra acquired at 1 T using  $\text{PTF} = 6.2$  mT of samples containing 10 mM of TFBA, either 25 mM (black) or 100 mM (red) of DMSO, and 5 mM of [IrCl(COD)(IMes)] in methanol- $d_4$ . Insets show spectra zoomed in to the aromatic (A, yellow square) and methylene (B, purple circle) signals of TFBA, and the hydride ligand region of the spectra (C). Hydride ligand signals shown in inset C correspond to [IrCl(H) $_2$ (IMes)(**4**) $_2$ ] (green triangles) and [IrCl(H) $_2$ (IMes)(**7**)(**4**)] (orange squares).

a decrease in this activity. As an explanation for this, it was proposed that by halving the number of polarisation transfer carrier molecules (TFBA) in equatorial position, both the occurrence of the H-D exchange process that re-protonated the amine group and the amount of hyperpolarised carrier were reduced.

Upon closer inspection of the activation process for a SABRE sample containing TFBA and DMSO, it is evident that the SABRE-Relay activity did increase with time yielding hyperpolarised solvent molecules, even in deuterated solvent (Figure 6.12, green squares). When comparing the same activation process on a sample prepared in protio methanol, the build up rate of hyperpolarised -OH appeared to be much faster and hyperpolarisation of

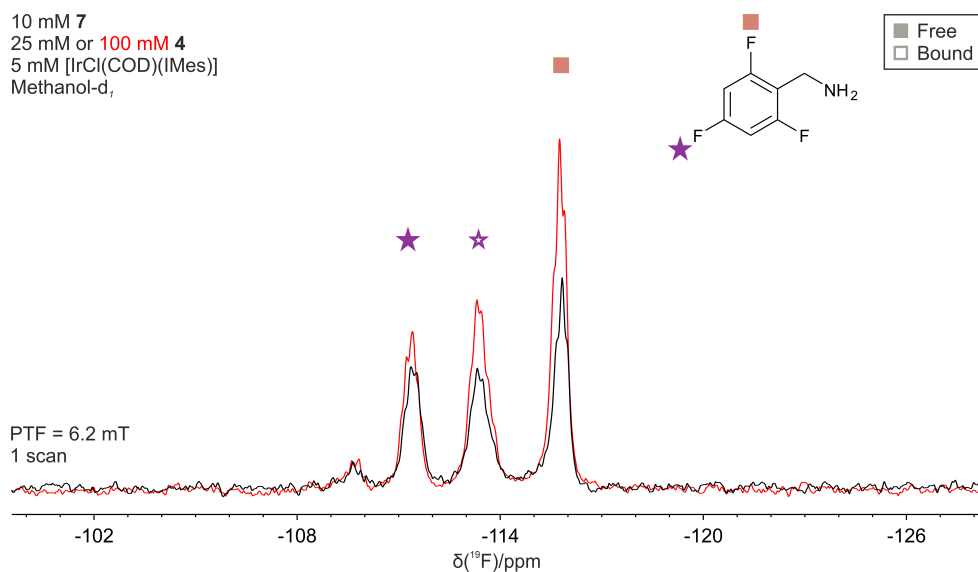


Figure 6.10: SABRE-hyperpolarised  $^{19}\text{F}$  spectra at 1 T of samples containing 10 mM TFBA, either 25 mM (black) or 100 mM (red) DMSO, and 5 mM [IrCl(COD)(IMes)] in methanol- $d_1$ .

the methyl resonance for the solvent was observed (Figure 6.12, orange markers).

As shown in Figure 6.12, deuteration of the exchangeable protons in the amine group of TFBA was effective in reducing the efficiency of SABRE-Relay for this system. This deuteration, achieved by fast H-D exchange with methanol- $d_4$ , drastically reduced the concentration of active polarisation transfer agent, *i.e.* those units that possess at least one proton per amino group to participate in proton exchange with the solvent and result in hyperpolarised -OH signals. This is shown schematically in Figure 6.13. However, the counteracting re-protonation process that takes place when hydrides and deuterium atoms from the amino group in TFBA exchange, limits the effectiveness of this strategy. Furthermore, every repetition of the shake-and-drop experiment eliminates some of the deuterium from solution, as HD or  $\text{D}_2$  gas, and adds new hydrogen in the form of  $p\text{-H}_2$  into solution. That leads to a gradual and steady increase of SABRE-Relay activity and solvent hyperpolarisation.

The correlation between concentration of TFBA and SABRE-Relay activity was inves-

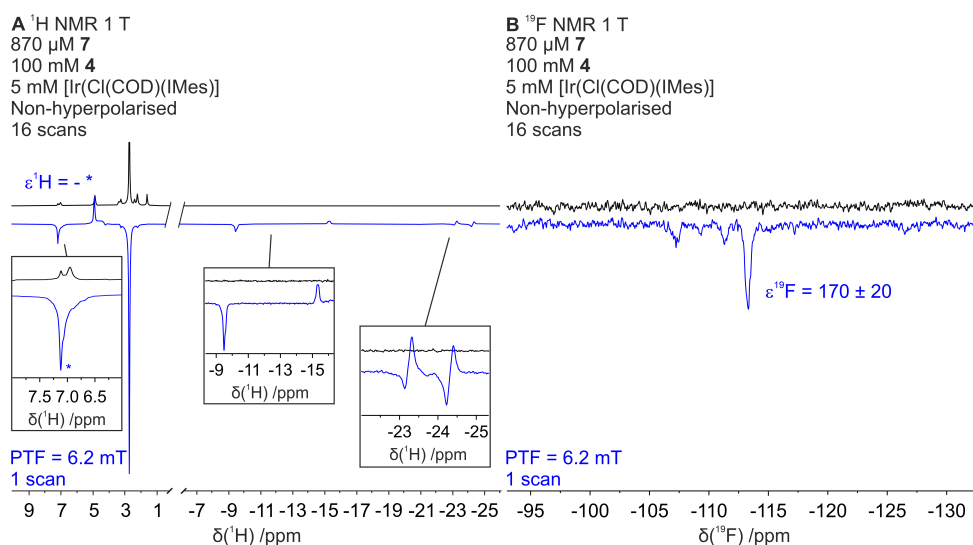


Figure 6.11: Comparison between non-hyperpolarised (black trace) and hyperpolarised (blue)  $^1\text{H}$  (A) and  $^{19}\text{F}$  (B) NMR spectra of TFBA at 1 T. The sample contained  $870\ \mu\text{M}$  TFBA, 100 mM DMSO and 5 mM  $[\text{IrCl}(\text{COD})(\text{IMes})]$  in methanol- $d_4$ . Insets show regions of the spectra zoomed in the aromatic proton region (left), and the hydride ligand region corresponding to  $[\text{Ir}(\text{H})_3(\text{IMes})(\mathbf{4})_2]$  (middle) and the main active species  $[\text{IrCl}(\text{H})_2(\text{IMes})(\mathbf{7})(\mathbf{4})]$  (right). It was not possible to determine an enhancement factor for the aromatic protons of TFBA due to peak overlap with hyperpolarised signals from IMes, shown with an asterisk, or for the methylene signals due to poor baseline separation.

igated by measuring the signal intensity for the hydroxyl signal of methanol in SABRE experiments as a function of the concentration of the polarisation transfer agent, TFBA, using both methanol- $d_4$  and methanol (Figure 6.14). This hydroxyl signal was monitored as an indicator of the level of polarisation that was diverted from the target substrate, TFBA, *via* unwanted SABRE-Relay effects. Sub-stoichiometric concentration levels for TFBA were chosen for this experiment as this would be the range used during quantification studies. SABRE samples with decreasing amounts of TFBA, either in methanol- $d_4$  or methanol, were analysed *via* shake-and-drop experiments performing six replicates to ensure full activation and the production of a stable hydroxyl signal. The last three repeats were averaged and plotted, after visual inspection to confirm that this signal was stable.

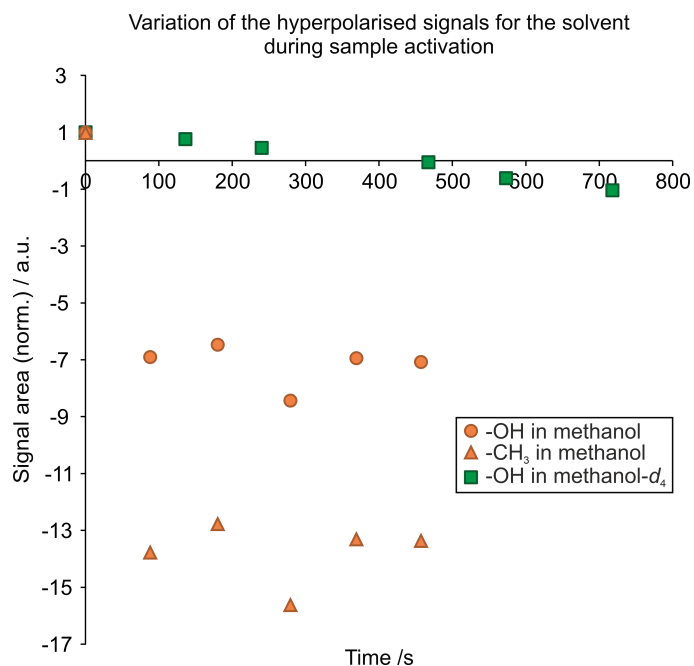


Figure 6.12: Variation of SABRE-hyperpolarised solvent signals in  $^1\text{H}$  NMR (1 T) during sample activation for samples containing either 10 mM of TFBA, 100 mM of DMSO, and 5 mM of  $[\text{IrCl}(\text{COD})(\text{IMes})]$  in methanol- $d_4$  (green marker) or 1.3 mM of TFBA, 100 mM of DMSO, and 5 mM of  $[\text{IrCl}(\text{COD})(\text{IMes})]$  in methanol (orange markers). The first activation step was set as time = 0 s. Hyperpolarised signals are phased negatively.

Spectra were phased so that hyperpolarised signals appeared negative, using the methyl signal from DMSO as a reference. A methanol- $d_4$  sample serving as a negative control was probed following the same shake-and-drop technique, as described in Section 3.5 (Chapter 3). In this way, a typical non-hyperpolarised signal intensity value for the hydroxyl group in methanol- $d_4$  was estimated and is indicated in Figure 6.14A by a triangle.

The resulting plots showed that much larger hyperpolarisation levels were obtained for hydroxyl signals in methanol versus methanol- $d_4$ . In fact, this signal remained positive for methanol- $d_4$  samples in the tested range of TFBA concentrations, showing that the non-hyperpolarised signal was only partially cancelled by the negatively-phased hyperpolarised signal. As previously discussed, this residual SABRE-Relay activity is thought to stem

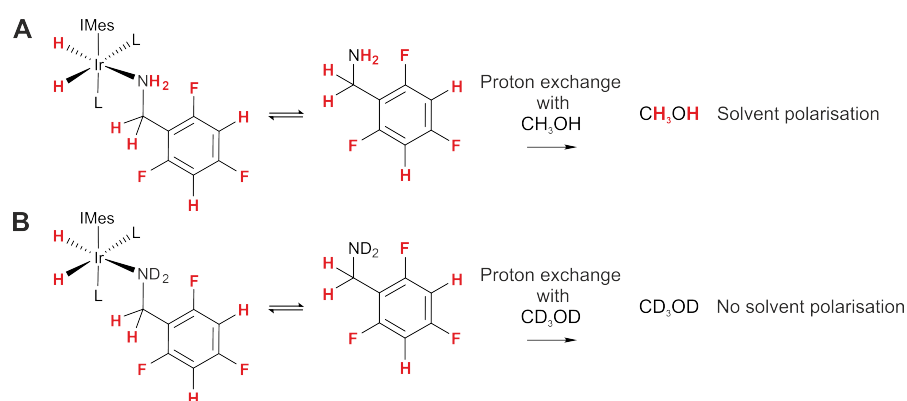


Figure 6.13: Schematic representation of SABRE-Relay hyperpolarisation with TFBA as a polarisation transfer carrier and either methanol (A) or methanol- $d_4$  (B) as recipients of this polarisation. The amine protons in TFBA exchange with the labile protons of methanol, transferring hyperpolarisation to the solvent in a continuous way. In methanol- $d_4$ , TFBA becomes rapidly deuterated and polarisation loss to the solvent is minimised.

from re-protonation of TFBA *via* H-D exchange with the hydrides whilst bound to the active species. These results support the idea that deuteration of the exchangeable protons in the target molecule, TFBA, may be an effective, albeit non-comprehensive, way to prevent polarisation loss to the solvent. Also illustrated by Figure 6.14 is the correlation between the concentration of TFBA and the degree of solvent hyperpolarisation. At lower concentrations of TFBA, hyperpolarisation of the hydroxyl signal was reduced for both methanol- $d_4$  and methanol. Such an observation was in agreement with previous results showing that low concentrations of the polarisation transfer agent limit the efficiency of SABRE-Relay.<sup>154</sup> This was thought to have positive implications for quantification studies as these must necessarily be done in the low concentration levels of the sub-stoichiometric regime, thus reducing polarisation loss to the solvent even in methanol.

To better understand the impact of polarisation loss to the solvent on the sensitivity of fluorine measurements, the same samples were tested using shake-and-drop experiments with fluorine detection. SHARPER acquisition (Sections 3.3.3 and 3.4.1, Chapter 3) was used for these experiments to improve the sensitivity of fluorine detection and allow for

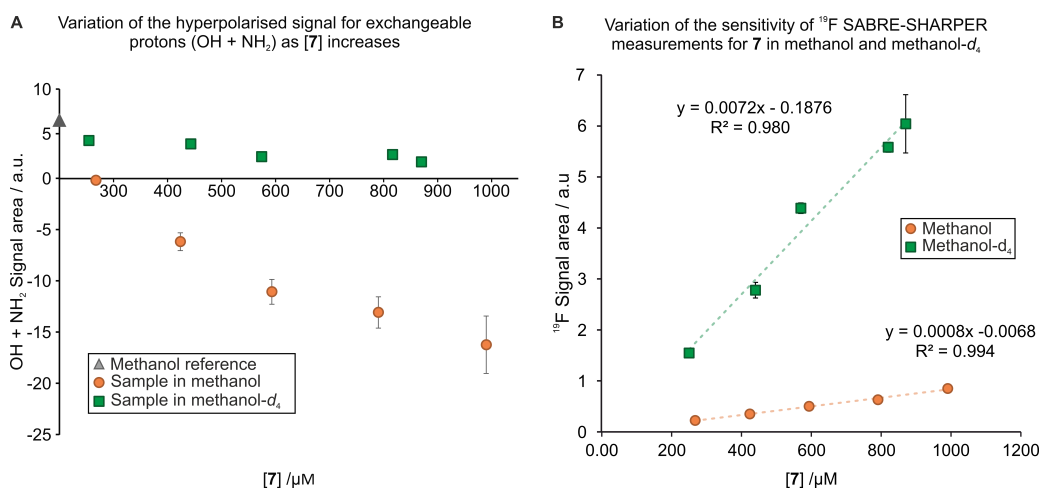


Figure 6.14: A) Variation in the hyperpolarised signal of exchangeable protons (-OH from methanol) as a response to [TFBA] for protio (orange circles) and deuterated methanol (green squares). B) Comparison of <sup>19</sup>F SABRE SHARPER signals for TFBA using protio methanol (orange circles) and deuterated methanol (green squares). Error bars for protio methanol measurements are present but smaller than markers (square), therefore not visible.

the comparison of samples in methanol-*d*<sub>4</sub> and methanol even when the low concentration of TFBA prevented direct SABRE detection in methanol. This experiment facilitated the discovery of a correlation between the level of diversion of polarisation to the solvent and fluorine enhancement levels. The results of this experiment are shown in Figure 6.14B. Hyperpolarisation of fluorine signals in TFBA was observed both for methanol-*d*<sub>4</sub> and methanol samples, implying that although significant polarisation loss to the solvent could be observed for in methanol, this did not preclude fluorine hyperpolarisation. Nevertheless, the sensitivity of fluorine measurements, *i.e.* the slope of the curve, was approximately ten times larger for samples in methanol-*d*<sub>4</sub>. This behaviour can be rationalised in the following way. The amount of dissolved *p*-H<sub>2</sub> in solution sets a finite amount of potential polarisation that can be transferred to the analyte. If some polarisation is diverted to the solvent by proton exchange, a smaller amount would remain in the target analyte, TFBA, and redistributed to <sup>19</sup>F nuclei. By reducing the loss of polarisation to the solvent, *e.g.* by deuteration of exchangeable protons in TFBA, higher fluorine polarisation levels would be

expected, and were in fact observed.

The results presented so far illustrate that although SABRE-hyperpolarised  $^{19}\text{F}$  measurements of TFBA using protio methanol are possible, there is an associated sensitivity penalty which is expected to be detrimental to the analytical performance of the technique. Nevertheless, such a concession might be deemed reasonable when the use of deuterated solvents is to be avoided, due to economical or practical reasons. In light of this, the analytical performance of SABRE-hyperpolarised measurements of TFBA in the sub-stoichiometric regime, particularly in terms of detection limits and quantification, were evaluated in both methanol- $d_4$  and methanol. These results will be presented in the following sections.

## 6.5 Analytical Performance in Inactive SABRE-Relay Conditions

Following the same analysis performed on SABRE samples with 3,5-difluoropyridine and dimethylsulfoxide, the analytical performance of SABRE-enhanced  $^{19}\text{F}$  benchtop NMR determinations were evaluated in terms of its limits of detection and quantification, and quantification accuracy. The results of these assessments are presented below for samples prepared in methanol- $d_4$ , in which SABRE-Relay activity was minimised, here termed ‘inactive SABRE-Relay conditions’.

### 6.5.1 Limits of Detection and Quantification

As discussed in Chapter 5, the limits of detection and quantification are fundamental performance parameters when considering the suitability of a measurement technique to a specific analytical problem. These parameters are often assessed by analysing low-concentration samples, and estimated as the concentration at which SNR values are 3 (LOD) and 10 (LOQ). However, the large variability in SNR values for hyperpolarised signals in samples containing TFBA made this single-sample approach (Section 3.7.5, Chapter 3) unreliable. Instead, LOD and LOQ values were estimated using a set of six samples containing between 250 and 870  $\mu\text{M}$  of TFBA (sub-stoichiometric regime) and an average value and

standard deviation were calculated from these, as detailed in Section 3.7.6 (Chapter 3). Each SABRE sample contained 100 mM of DMSO and 5 mM of [IrCl(COD)(IMes)] and was prepared according to the described procedure (Chapter 3, Section 3.1.2), followed by shake-and-drop experiments (Chapter 3, Section 3.2) with fluorine detection using both pulse-and-collect and SHARPER acquisition, as previously described. Although more than one distinct fluorine resonance could be integrated for this analysis, these were collectively integrated as one in order to increase the sensitivity of the measurement. Similarly, the non-selective version of SHARPER was used to collapse all resonances into a single peak to the same effect. Whilst *sel*SHARPER acquisition would be necessary in the presence of more than one analyte, it is noted that this approach would not be suitable in the case of overlapping resonances. To minimise the appearance of artefacts arising from the probe signal, SHARPER spectra were acquired using the background correction strategy described in Chapter 5, Section 5.4. The imaginary part of the spectrum was removed in SHARPER spectra to improve SNR values and obtain the lowest possible LOD and LOQ values (Chapter 5, Section 5.4).

Typical  $^{19}\text{F}$  NMR SABRE and SABRE SHARPER spectra at 254  $\mu\text{M}$  of TFBA are shown in Figure 6.15. Through the analysis of these samples, a limit of detection of  $(162 \pm 28)$   $\mu\text{M}$  and a limit of quantification of  $(540 \pm 92)$   $\mu\text{M}$  were estimated for  $^{19}\text{F}$  NMR SABRE measurements. The large dispersion associated with these values (17% relative standard deviation) was a result of inter-sample variation. When comparing to the single-scan LOD value of 194 mM for non-hyperpolarised spectra (Chapter 3, Section 3.7.5, 25 mM of TFBA, 2048 scans), this represented an improvement in  $LOD_{ss}$  by 4 orders of magnitude. It is relevant to mention that  $^1\text{H}$  signals could not be reliably processed due to peak overlap (Figure 6.11), highlighting the benefits of probing this molecule through  $^{19}\text{F}$  NMR measurements. By combining SABRE with SHARPER, a further improvement of SNR by a factor of 9 resulted in lower limits of detection,  $(17.5 \pm 2.0)$   $\mu\text{M}$ , and quantification,  $(58.2 \pm 6.8)$   $\mu\text{M}$ , thus extending the working range of this technique to low micromolar concentrations. In this case, the dispersion of LOD and LOQ results decreased to 12%, which was likely due to the increased repeatability afforded by SHARPER measurements.

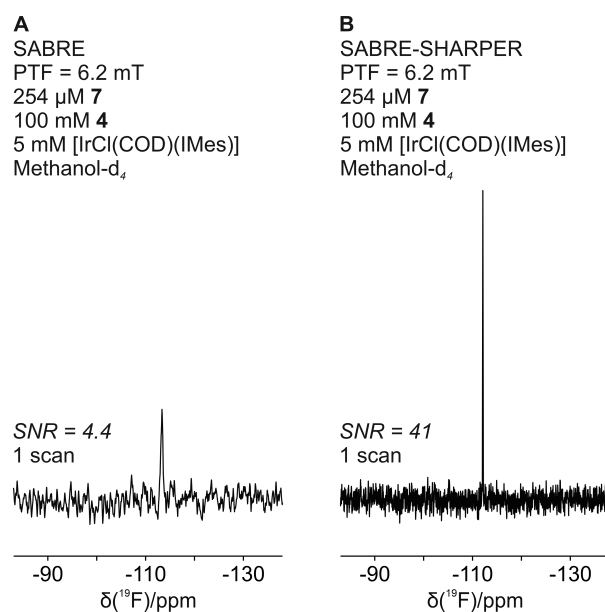


Figure 6.15: SABRE (A) and SABRE-SHARPER (B)  $^{19}\text{F}$  NMR spectra acquired at 1 T for a sample containing 254  $\mu\text{M}$  of TFBA, 100 mM of DMSO, and 5 mM of [IrCl(COD)(IMes)] in methanol- $d_4$ .

The limits of detection presented for this system in SABRE-Relay inactive conditions were higher than those obtained for the simpler case of 3,5-difluoropyridine, for which a limit of detection in the nanomolar range was obtained using SABRE-SHARPER. As the loss of polarisation *via* SABRE-Relay was minimised through deuteration of the amino group in TFBA, the best explanation for the higher LOD of this system is a less efficient SABRE process. This idea is supported by the *ca.* 5 times lower  $\varepsilon_{^{19}\text{F}}$  value for TFBA in the sub-stoichiometric regime:  $\varepsilon_{^{19}\text{F}} = (940 \pm 40)$  for 3,5-difluoropyridine (Figure 5.10, Chapter 5) *vs.*  $\varepsilon_{^{19}\text{F}} = (170 \pm 20)$  for TFBA (Figure 6.11).

### 6.5.2 Quantification

As a first step to assess the quantification capabilities of the technique on the fluoroamine system, a six-level calibration curve (250  $\mu\text{M}$  to 870  $\mu\text{M}$  of TFBA) was prepared gravimetrically and SABRE experiments were conducted as described in the previous section. The

NMR signal areas obtained from these experiments were plotted against the concentration of TFBA and then fitted to a straight line through ordinary least squares regression (Chapter 3, Section 3.7.7). The residual fitting error for each measurement was plotted against the concentration of TFBA (Chapter 3, Section 3.7.7).

Results for  $^{19}\text{F}$  SABRE and  $^{19}\text{F}$  SABRE SHARPER measurements are presented in Figure 6.16. In contrast to 3,5-difluoropyridine,  $^1\text{H}$  results were not obtained as peak overlap prevented this analysis. Coefficient of determination values ( $R^2$ ) were used to assess the degree to which the experimental data fits the proposed linear model.  $R^2$  values for both SABRE and SABRE SHARPER calibration curves were similar ( $R^2 = 0.95$  and  $0.96$ , respectively), but lower than those obtained for measurements of 3,5-difluoropyridine ( $R^2 = 0.993$  and  $0.998$ , Section 5.5, Chapter 5). A low coefficient of determination sometimes suggests an alternative model may better describe the behaviour of the experimental data. However, as the residual errors of the calibration curves appeared to be randomly distributed around zero (Figure 6.16B and D), an alternative model (*e.g.* a higher-degree polynomial) was therefore not proposed. This behaviour could also be explained by a lower repeatability of results, which for  $^{19}\text{F}$  SABRE measurements reached a relative standard deviation of 11%. However, a similar deviation from linearity was seen for SHARPER results, despite the fact that these showed a lower intra-level dispersion of results when compared to SABRE-enhanced pulse-and-collect experiments (Figure 6.16B and D). Having ruled out those common explanations, and after observing larger  $R^2$  values in previous experiments (Figure 6.14), it was hypothesised that this mild deviation from linearity was a consequence of operator variability during sample preparation. In particular, the gravimetric preparation of samples inside a glovebox was found to be non-trivial. By improving the sample preparation conditions, for example by improving the precision of the balance inside the glovebox or weighing outside the glovebox altogether, the linearity of these calibration curves could be improved.

Having established a linear calibration curve for both  $^{19}\text{F}$  SABRE and  $^{19}\text{F}$  SABRE SHARPER measurements, the quantification accuracy of those models was investigated. A test sample containing  $443\ \mu\text{M}$  of TFBA ( $80\ \text{mg}/\text{kg}$ ) was prepared and its reference value

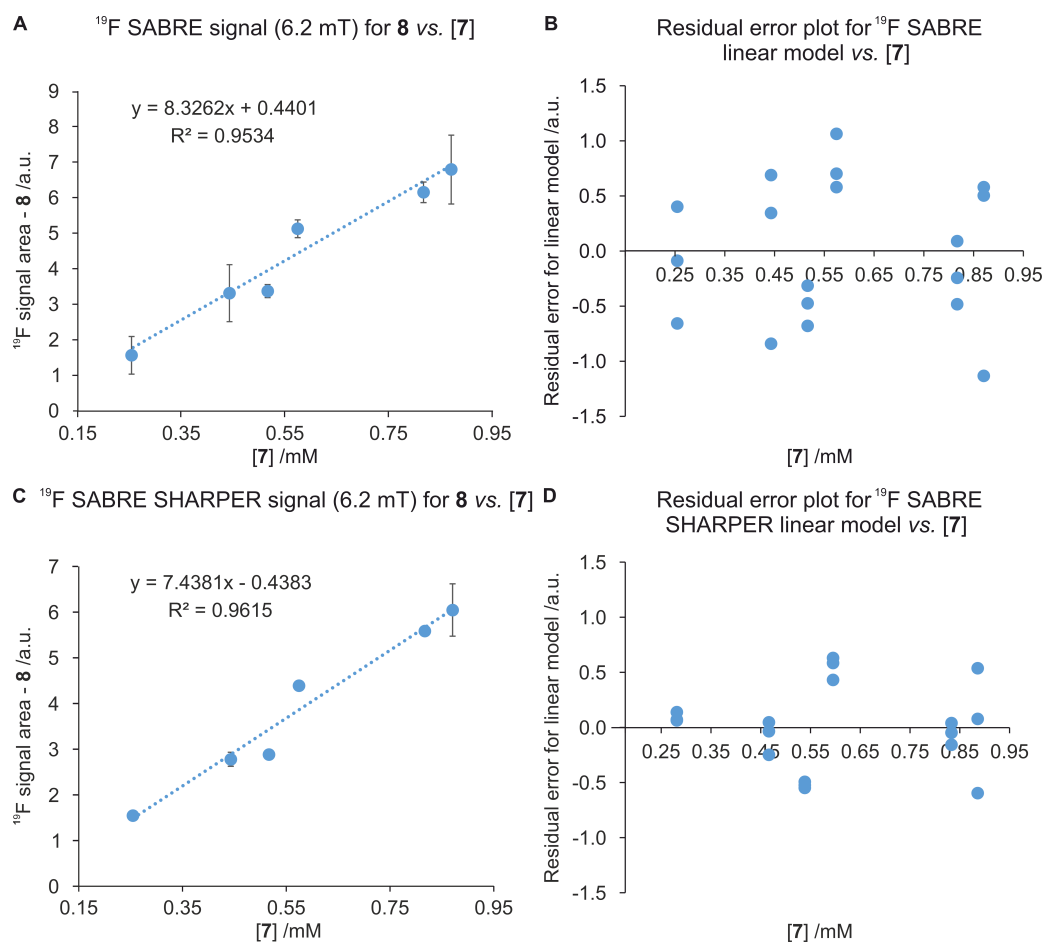


Figure 6.16: Calibration curves for  $^{19}\text{F}$  SABRE (A) and  $^{19}\text{F}$  SABRE SHARPER (C) measurements of TFBA in the  $250\ \mu\text{M}$  to  $900\ \mu\text{M}$  range in SABRE-Relay inactive conditions (methanol- $d_4$ ). Residual errors of the linear model are plotted against analyte concentration for  $^{19}\text{F}$  SABRE (B) and  $^{19}\text{F}$  SABRE SHARPER (D) hyperpolarised calibration curves.

assigned gravimetrically. This sample was analysed with the calibration curve, and the linear models were used to predict a concentration. It should be noted that the concentration of reference sample was at the lower end of the LOQ range for  $^{19}\text{F}$  SABRE measurements estimated in the previous section, but as its SNR was close to 10, quantification accuracy was evaluated at this level nonetheless.  $^{19}\text{F}$  SABRE and  $^{19}\text{F}$  SABRE SHARPER calibration curves and test samples are shown in Figure 6.17. The values predicted by the

linear models were averaged and compared to the reference value to estimate a recovery percentage value ( $R$ ) and its associated relative standard deviation ( $RSD$ ), as described in Chapter 3, Sections 3.7.3 and 3.7.8. Mean, recovery, and relative standard deviation results for  $^{19}\text{F}$  SABRE and  $^{19}\text{F}$  SABRE SHARPER measurements are presented in Table 6.4.

As discussed in Chapter 5, recovery values close to 100% show a good level of agreement between the concentration predicted by the model and the reference value. Results in Table 6.4 show that this is the case for both  $^{19}\text{F}$  SABRE and  $^{19}\text{F}$  SABRE SHARPER measurements. Taking as reference the acceptance criteria proposed in the literature at a concentration of analyte close to 100 mg/kg (90 to 107%,<sup>243,244</sup>), the recovery values obtained in this accuracy study can be considered to be fit for purpose. However, it must be noted that this test sample represented the best possible performance out of the set of samples in the calibration curve. In other words, if the sample containing 517  $\mu\text{M}$  of TFBA was used as a test sample to assess the accuracy of this linear model instead, recovery values would fall outside the proposed acceptable range:  $(86 \pm 4)\%$  and  $(83 \pm 1)\%$  for  $^{19}\text{F}$  SABRE and SABRE SHARPER measurements, respectively. This variability in recovery values can be explained by the deviation from linearity of the calibration curve, which as previously discussed, is likely a consequence of the complexity of the sample preparation procedure.

Table 6.4: Predicted concentrations, recovery values and relative standard deviation of the samples analysed *via*  $^{19}\text{F}$  SABRE and  $^{19}\text{F}$  SABRE-SHARPER measurements using a PTF of 6.2 mT. Parameters were calculated as described in Sections 3.7.3 and 3.7.8. Recovery values were calculated against the gravimetric reference value 443  $\mu\text{M}$ .

| Analysis                      | Concentration<br>/ $\mu\text{M}$ | Recovery<br>/% | RSD<br>/% |
|-------------------------------|----------------------------------|----------------|-----------|
| $^{19}\text{F}$ SABRE         | $(453 \pm 55)$                   | $(102 \pm 13)$ | 12        |
| $^{19}\text{F}$ SABRE-SHARPER | $(429 \pm 12)$                   | $(97 \pm 3)$   | 3         |

In terms of method repeatability, only  $^{19}\text{F}$  SABRE SHARPER results were under the

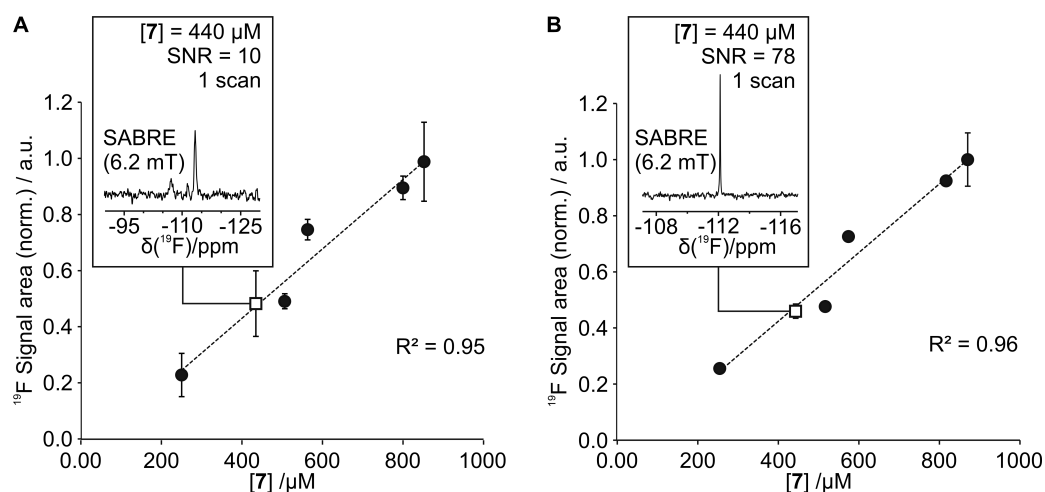


Figure 6.17: Calibration curves for  $^{19}\text{F}$  SABRE (A) and  $^{19}\text{F}$  SABRE SHARPER (B) experiments and accuracy test. Black markers correspond to the signal arising from calibration solutions and the white squares, those from the test samples. Each sample, either calibration or test, was analysed in triplicate and the standard deviation of the mean values were used as error bars. Coefficients of determination,  $R^2$ , are shown for each curve. Insets show the spectra obtained for the test sample in each case, along with its nominal concentration, the signal-to-noise ratio of the measurement and the number of scans.

acceptable tolerance of 5.3% proposed in the literature for values close to 100 mg/kg.<sup>243,244</sup> In general, the repeatability of measurements for TFBA were larger than those for 3,5-difluoropyridine at similar concentrations. This decline in repeatability was particularly severe for  $^{19}\text{F}$  SABRE measurements (12% *vs.* 3%), whilst only moderate for  $^{19}\text{F}$  SABRE SHARPER measurements (3% *vs.* 1%). It is hypothesised that a key contributor to signal variability was additional competing chemical exchange processes in samples containing TFBA and DMSO, namely proton/deuterium exchange with the solvent and re-protonation of the amine group by the hydrides. Such processes would likely produce broader signals, which at the low SNR values observed for this system, were expected to complicate signal integration and thus introduce variability. This argument is further supported by the improvement in repeatability observed for SHARPER results, as this pulse sequence significantly reduces peak broadness, thus making integration more precise. It is possible

that increasing the repeatability of shake-and-drop experiments would also result in better precision of non-SHARPER results, for example, through an automated SABRE approach such as the ones reported previously.<sup>255</sup>

## 6.6 Analytical Performance in Active SABRE-Relay Conditions

For applications in which the benefits of using non-deuterated solvents prevail over sensitivity requirements, and chlorinated alternatives are to be avoided for health and safety concerns,<sup>252</sup> experiments in SABRE-Relay active conditions might be preferred. In this last section, the analytical performance parameters associated with detection and quantification limits, and quantification accuracy will be explored for the test system using protio methanol.

### 6.6.1 Limits of Detection and Quantification

Following the same strategy to that presented for SABRE-Relay inactive conditions, a set of samples containing TFBA in sub-stoichiometric concentrations (270 to 990  $\mu\text{M}$ ), 100 mM of DMSO, and 5 mM of  $[\text{IrCl}(\text{COD})(\text{IMes})]$  were prepared in protio methanol and analysed using shake-and-drop experiments using fluorine detection with pulse-and-collect and SHARPER acquisition. Experimental conditions used in the SABRE-Relay inactive case were replicated for this system (Section 6.5.1).

Typical  $^{19}\text{F}$  SABRE and SABRE-SHARPER spectra at the lowest tested concentration is shown in Figure 6.18. From the SNR values obtained for these samples, a limit of detection of  $(368 \pm 63) \mu\text{M}$  was estimated for  $^{19}\text{F}$  SABRE measurements, as well as an associated limit of quantification of  $(1.23 \pm 0.21) \text{mM}$ . Although SABRE hyperpolarisation has yet again improved the limit of detection by 3 orders of magnitude (*versus*  $LOD_{ss} = 194 \text{mM}$ , non-hyperpolarised), the use of SABRE-Relay active conditions has resulted in an increase of the limits of detection and quantification by over a factor of 2 when compared to SABRE-Relay inactive conditions ( $LOD = (162 \pm 28) \mu\text{M}$  and  $LOQ = (540 \pm 92) \mu\text{M}$

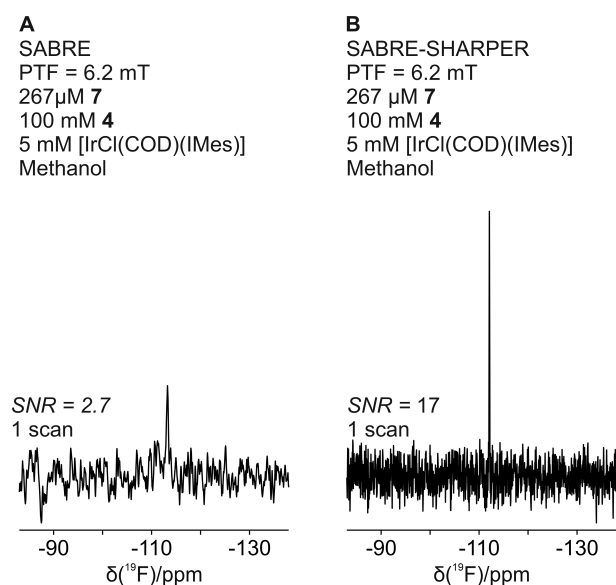


Figure 6.18: SABRE (A) and SABRE-SHARPER (B)  $^{19}\text{F}$  NMR spectra acquired at 1 T for a sample containing 267  $\mu\text{M}$  of TFBA, 100 mM of DMSO, and 5 mM of [IrCl(COD)(IMes)] in methanol.

in methanol- $d_4$ , Section 6.5.1). Estimation of a limit of detection for  $^1\text{H}$  measurements was once again not possible due to peak overlap. A similar penalty in sensitivity was observed when SABRE-SHARPER experiments were carried out in methanol, resulting in a limit of detection of  $(42.6 \pm 3.6) \mu\text{M}$  and a limit of quantification of  $(142 \pm 12) \mu\text{M}$ . Nevertheless, the use of SHARPER enables the analysis of this system at low micromolar concentrations even in the non-optimal sensitivity conditions introduced by the use of protio methanol.

### 6.6.2 Quantification

Prior to assessing the quantification potential of SABRE-hyperpolarised benchtop  $^{19}\text{F}$  NMR for the system containing TFBA and DMSO in SABRE-Relay active conditions, the linearity of the signal response relative to the concentration of analyte was tested. The same steps described for methanol- $d_4$  samples (Section 6.5.2) were followed for a set of samples containing 270 to 990  $\mu\text{M}$  of TFBA in protio methanol. The results of the linearity study are presented in Figure 6.19. Visual inspection of the calibration curve constructed with  $^{19}\text{F}$

SABRE signals (Figure 6.19A) reveals a certain degree of deviation from linearity, further supported by a  $R^2$  value of 0.93, which is the lowest value seen out of the calibration curves presented in Chapter 5 and 6. The hypothesis of an alternative model better describing the data was discarded based on the random distribution of residuals around zero, as displayed in Figure 6.19B. This residual error plot also reveals a large dispersion of results at each concentration level, with relative standard deviation values reaching up to 20 % for this measurement approach.

In contrast,  $^{19}\text{F}$  SABRE-SHARPER measurements exhibited a better repeatability, as evidenced by the error bars of the corresponding calibration curve and the dispersion of intra-level residual errors (Figure 6.19C and D). The SABRE-SHARPER measurement approach also displayed a better adherence to a linear model, with a  $R^2$  value of 0.98 and a roughly three-fold reduction in the magnitude of residual errors. Based on this, it is proposed that the observed deviation from linearity for  $^{19}\text{F}$  SABRE measurements could be explained by poor repeatability of results. This was likely further exacerbated by the low signal-to-noise ratio of  $^{19}\text{F}$  SABRE-enhanced measurements for this system in methanol, a consequence of the reduced sensitivity observed due to polarisation loss to the solvent. In fact, all the processed signals used to construct the  $^{19}\text{F}$  SABRE curve presented in Figure 6.19A had SNR values less than 10, and as such were below the limit of quantification for this system. This comparison of linearity between  $^{19}\text{F}$  SABRE and  $^{19}\text{F}$  SABRE SHARPER systems highlights the impact of repeatability in linearity, and more broadly, in the accuracy of results. Although repeatability could be improved using SHARPER, exploring the use of internal standards or implementing an automated SABRE setup rendering manual operation unnecessary and enabling signal averaging, higher SNR values are thought to be necessary to ensure reliable measurements. In light of this, quantification accuracy studies using  $^{19}\text{F}$  SABRE non-SHARPER measurements were not pursued in SABRE-Relay active conditions.

A sample containing 420  $\mu\text{M}$  of TFBA, 100 mM of DMSO, and 5 mM of  $[\text{IrCl}(\text{COD})(\text{IMes})]$  was used to test the accuracy of quantification using a  $^{19}\text{F}$  SABRE SHARPER calibration curve, following the same procedure described for SABRE-Relay

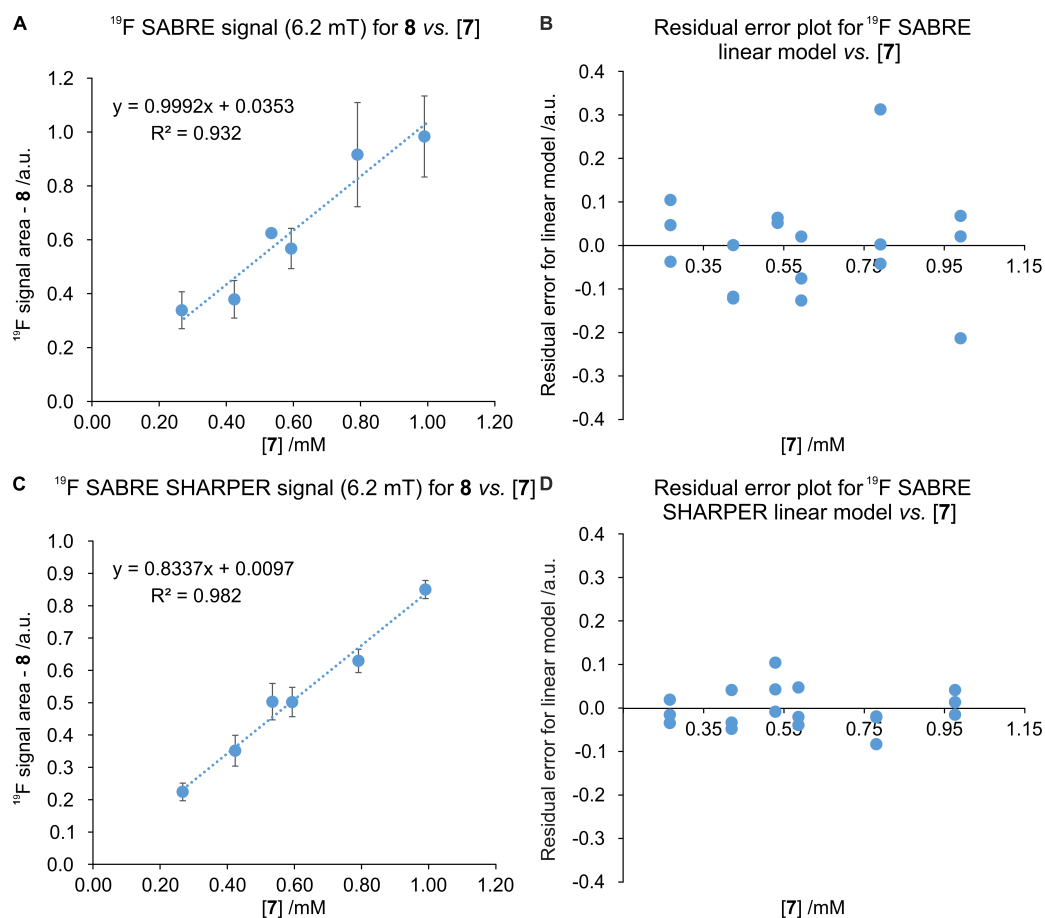


Figure 6.19: Calibration curves for  $^{19}\text{F}$  SABRE (A) and  $^{19}\text{F}$  SABRE SHARPER (C) measurements of TFBA in the  $270\ \mu\text{M}$  to  $990\ \mu\text{M}$  range in SABRE-Relay active conditions (protio methanol). Residual errors of the linear model are plotted against analyte concentration for  $^{19}\text{F}$  SABRE (B) and  $^{19}\text{F}$  SABRE SHARPER (D) hyperpolarised calibration curves.

inactive conditions (Section 6.5.2). This concentration was chosen to be similar to the sample used during accuracy studies for SABRE-Relay inactive conditions, thus allowing for a direct comparison. The predicted concentration, as well as the recovery percentage and its associated relative standard deviation are presented in Table 6.5.

As shown in Figure 6.20, the test sample presented a SNR suitable for quantification (*i.e.* above the LOQ), but it was still approximately 2.5 times lower than what was observed

in SABRE-Relay inactive conditions. The recovery value,  $(96 \pm 14) \%$ , was comparable in magnitude to samples in methanol- $d_4$  ( $(97 \pm 3) \%$ , Section 6.5.2) and well within the acceptable range for a concentration close to 100 mg/kg (90 to 107%,<sup>243,244</sup>). However, the relative standard deviation exceeded the maximum acceptable value proposed in the literature of 5.3%,<sup>243,244</sup> as it was more than double the RSD observed in SABRE-Relay inactive conditions (8% *vs.* 3%). This greater variation in signal areas was once again linked to the low sensitivity of measurements in methanol.

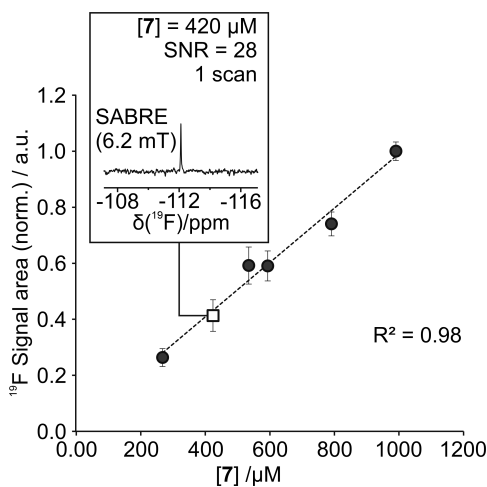


Figure 6.20: Calibration curves for  $^{19}\text{F}$  SABRE SHARPER experiments and accuracy test in SABRE-Relay active conditions. Black markers correspond to the signal arising from calibration solutions and the white squares, those from the test samples. Each sample, either calibration or test, was analysed in triplicate and the standard deviation of the mean values were used as error bars. Coefficients of determination,  $R^2$ , are shown for each curve. The inset shows the spectrum corresponding to the test sample, along with its nominal concentration, the signal-to-noise ratio of the measurement and the number of scans.

In summary, although the use of protio methanol and SABRE-Relay active conditions did not, in and of itself, preclude the detection and accurate quantification of samples at a low micromolar level, the reduction in sensitivity has a significant impact on the working range and precision of these measurements. Furthermore, it was found that for this analysis to be possible, the use of the pulse sequence SHARPER was crucial as it greatly improved

Table 6.5: Predicted concentration, recovery value and relative standard deviation of the sample analysed *via*  $^{19}\text{F}$  SABRE-SHARPER measurements using a PTF of 6.2 mT. Parameters were calculated as described in Sections 3.7.3 and 3.7.8. The recovery value was calculated against the gravimetric reference value  $424 \mu\text{M}$ .

| Analysis                      | Concentration<br>/ $\mu\text{M}$ | Recovery<br>/% | RSD<br>/% |
|-------------------------------|----------------------------------|----------------|-----------|
| $^{19}\text{F}$ SABRE-SHARPER | $(405 \pm 33)$                   | $(96 \pm 14)$  | 8         |

SNR values, and as a result, decreased limits of detection and quantification. In addition, the use of SHARPER improved measurement repeatability, likely by facilitating more robust processing of signals broadened by chemical exchange, which indirectly improved linearity results.

## 6.7 Conclusions

This chapter explored the analytical performance of SABRE-hyperpolarised  $^{19}\text{F}$  bench-top NMR measurements on a substrate presenting significant challenges: 2,4,6-trifluorobenzylamine. This test subject is representative of a group of molecules for which SABRE activity is facilitated by an amine ligand, which are reported to hyperpolarise less efficiently than the pyridine-based test molecules explored in Chapters 4 and 5. Once again, the use of co-substrates improved enhancement factors of the molecule under consideration. In addition, 2,4,6-trifluorobenzylamine is a prime example of substrates which can participate in proton exchange processes with the solvent, as well as undergo deuteration of the amine group. Both processes were expected to impact SABRE efficiency, and in the former case this was confirmed experimentally by comparing the signal enhancements when polarisation loss was inhibited through deuteration. This process, rationalised as an unwanted SABRE-Relay pathway, was found to be responsible for polarisation loss from the substrate to the solvent, thus decreasing the efficiency of SABRE on the target molecule and measurement sensitivity.

It was shown that this polarisation loss process could be largely inactivated by deuteration of the exchangeable proton sites in the amine group of 2,4,6-trifluorobenzylamine, which is rapidly achieved by using a deuterated solvent capable of proton exchange, such as methanol- $d_4$ . To understand the full impact of this polarisation loss pathway on the analytical performance demonstrated for 3,5-difluoropyridine in Chapter 5, the limit of detection and quantification accuracy of SABRE-enhanced  $^{19}\text{F}$  benchtop NMR measurements using co-substrates were investigated when this process was either active, in methanol, or inactive, in methanol- $d_4$ .

Results showed that the use of methanol can be associated with a sensitivity penalty, which results in higher limits of detection and quantification (mid- $\mu\text{M}$  and low mM, respectively), as well as a decrease in repeatability (RSD of up to 20 %). It was observed that using the pulse sequence SHARPER led to improved limits of detection and quantification in the low micromolar range, even when polarisation loss effects were present. This pulse sequence also improves measurement repeatability, which is attributed to a reduction of peak broadening effects induced by chemical exchange, and enabled the accurate quantification of micromolar test samples irrespective of the solvent.

In the next chapter, the applicability of this methodology will be further challenged by exploring carboxylic acids as substrates. In particular, this chapter will explore strategies to analyse difluoro- and trifluoroacetic acid, to pave the way to the analysis of environmentally concerning perfluorocarboxylic acids.

## Chapter 7

# Analysis of Fluorocarboxylic Acids with SABRE Hyperpolarisation

In this final experimental chapter, the SABRE-hyperpolarised benchtop NMR technique is applied to a novel class of fluorinated substrates: carboxylic acids. The focus on these molecules stems from the analytical importance of perfluoroalkyl carboxylic acids, which hold significant environmental relevance.<sup>256,257</sup> To evaluate the feasibility of studying these environmental targets using SABRE-hyperpolarised benchtop NMR, the simplest representatives of this group, di- and trifluoroacetic acid, were selected as test subjects.

First, a range of ultimately unsuccessful attempts to directly hyperpolarise difluoroacetic acid, both on its own and with co-substrates, are presented. This is followed by a discussion covering potential explanations for the negative outcome, including chemical interactions between substrate and co-substrate. Secondly, the hyperpolarisation of difluoroacetate, the conjugate base, is examined, focusing on co-substrate optimisation and transitioning into the sub-stoichiometric regime to determine the limits of detection.

Finally, trifluoroacetic acid and trifluoroacetate hyperpolarisation studies are presented and similarities with the difluoroacetate systems are discussed, including the formation of active SABRE species, as well as the observed differences. In particular, a comparison of hyperpolarisation efficiency for difluoroacetate and trifluoroacetate is presented to gain

insights into the role of hydrogen atoms as a pathway for hyperpolarising fluorine nuclei.

## 7.1 Background Theory

### 7.1.1 Environmental Relevance of Fluorinated Carboxylic Acids

Carboxylic acids are naturally occurring compounds that play essential roles in biological processes, including carbon metabolic pathways and fermentation.<sup>258–260</sup> Additionally, anthropogenic activities contribute significantly to the presence of carboxylic acids in the environment, as seen in their use in herbicides,<sup>261</sup> their formation as atmospheric pollutants from combustion and motor exhaust emissions,<sup>262,263</sup> and their occurrence as perfluorocarboxylic acids.<sup>264</sup> Carboxylic acids are also integral to various industrial processes, including the production of polymers, pharmaceuticals, cosmetics, and as additives in the food industry.<sup>260,265–267</sup> Consequently, the analysis of carboxylic acids holds substantial importance across industrial, environmental, and clinical applications.

Within the field of environmental analysis, perfluorocarboxylic acids (PFCAs) have drawn a lot of attention after their introduction in the 1940s.<sup>256,257</sup> PFCAs have the general formula  $C_nF_{2n+1}COOH$  and they are a subset of a class of compounds known as per- and polyfluoroalkyl substances (PFAS). The common motif in these molecules is the presence fully fluorinated carbon backbones, with the strength of C-F bonds conferring stability and chemical inertness on these molecules.<sup>256,257</sup> This property has led to the use of PFAS for applications in which thermal resistance and low reactivity is needed. For example, coated cookware, fire-fighting foams, flame retardants, and waterproof textiles are amongst the 200 reported applications.<sup>257</sup> In particular, PFCAs have been found in personal care products,<sup>268</sup> and are widely used as in the textile industry as water and oil repellents.<sup>269–271</sup> The widespread use of these chemicals in everyday consumer goods has led to their occurrence and hence their detection in the environment,<sup>272–274</sup> as well as in food and water samples.<sup>275–278</sup>

The remarkable chemical resistance of PFAS contributes to their environmental persistence, with an estimated half-life of approximately 100 years in aqueous environments.<sup>279</sup>

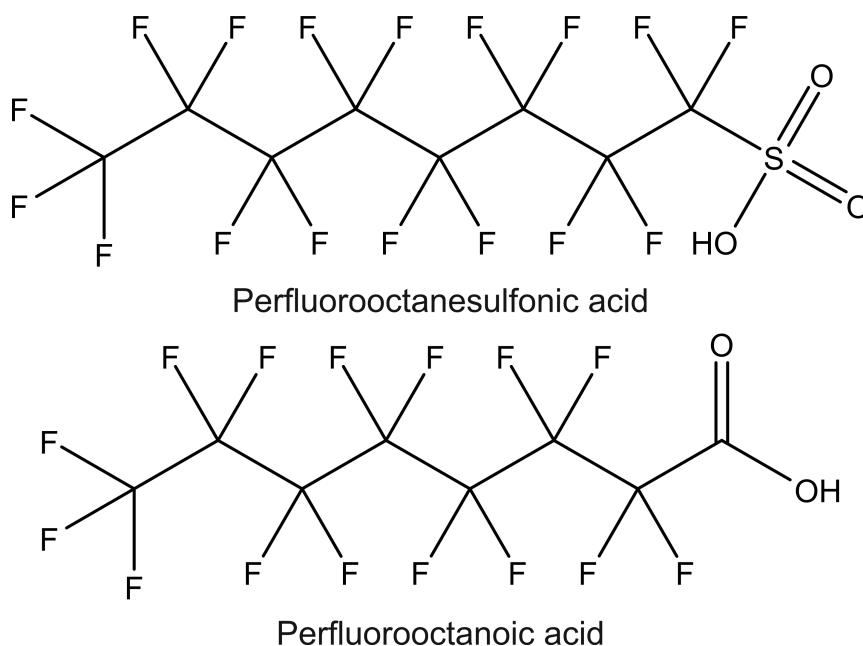


Figure 7.1: Chemical structures of perfluorooctanesulfonic acid and perfluorooctanoic acid, two commonly encountered perfluoroalkyl substances.

This persistence facilitates bioaccumulation within the food chain. In fact, studies report the presence of PFAS in human samples from environmental and food sources, with perfluorooctanesulfonic acid (PFOS) and perfluorooctanoic acid (PFOA) being the most commonly encountered (Figure 7.1).<sup>280-282</sup> Growing concerns have emerged regarding the toxicity of these chemicals, as they have been linked to liver toxicity, prenatal and neonatal toxicity, immunotoxicity, and adverse effects on fertility and pregnancy outcomes.<sup>281,283</sup> In particular, PFOA has recently been classified as carcinogenic to humans by the International Agency for Research on Cancer.<sup>284</sup>

Daily intake of PFAS from contaminated drinking water is considered to be one of the largest sources of exposure in non-occupational settings.<sup>283,285</sup> This has promoted authorities to establish increasingly conservative regulations on PFAS.<sup>281</sup> For instance, the UK's Drinking Water Inspectorate recently issued guidelines for water supply companies, setting an actionable maximum concentration for 47 PFAS in drinking water at 100 ng/L, applicable to both individual and combined measurements of PFAS compounds.<sup>286</sup> Whilst the

European Union has established similar limits, setting a maximum of 100 ng/L for the sum of concentrations of a set of 20 critical PFAS,<sup>287</sup> the US has recently set more stringent regulations: a 4 ng/L limit for six PFAS, including PFOS and PFOA.<sup>288</sup>

In order to assess conformity with these guidelines, PFAS monitoring schemes must use analytical techniques which are able to detect, identify and quantify these target molecules at concentrations of ng/L or parts per trillion (ppt).<sup>285,289</sup> This targeted analysis is commonly done using solid-phase extraction (SPE) as a sample cleaning and concentration strategy, followed by liquid chromatography with tandem mass spectrometry (LC/MS/MS), as stipulated by standardised methodologies such as US EPA 537.1, US EPA 533, and ISO 21675:2019.<sup>290-292</sup> While this approach enables accurate and sensitive quantification at the required low concentration, it often fails to encompass the extensive array of newly emerging PFAS compounds. In contrast, suspect and non-targeted analyses facilitate the identification and characterization of unknown PFAS, generally employing high-resolution mass spectrometers, such as high-resolution time-of-flight, orbitrap, and Fourier transform ion cyclotron resonance instruments.<sup>285</sup> However, this approach can be time-intensive and requires costly instrumentation, rendering it less suitable for monitoring laboratories.<sup>285,289</sup> A third analytical approach, known as surrogate indicators, estimates the overall PFAS burden by measuring general fluorine content, using techniques such as total organic fluorine (TOF) and total oxidisable precursor (TOP). This serves as an indicator of anthropogenic activity given the rarity of organofluorines in nature.<sup>289</sup> Although it cannot identify or quantify specific PFAS compounds, this approach facilitates the rapid detection of contamination events, making it a highly valuable tool for initiating early-response remediation campaigns.<sup>289</sup>

Amongst other surrogate indicator techniques, <sup>19</sup>F NMR presents an attractive option due to its non-discriminating quantitative nature for assessing total PFAS concentrations, while also allowing the characterization of unknown PFAS compounds.<sup>293,294</sup> This capability was first demonstrated by Moody *et al.*,<sup>295</sup> and since expanded by several research groups.<sup>296-299</sup> In a recent study, Camdzic *et al.* compared <sup>19</sup>F NMR results with those obtained from widely used techniques, such as LC-MS/MS and TOP, finding that total PFAS

concentrations measured by  $^{19}\text{F}$  NMR were approximately 65% higher. This increase was attributed to a better performance of  $^{19}\text{F}$  NMR in detecting short-chain PFAS, like trifluoroacetic acid.<sup>298</sup> Despite its comprehensive analytical power,  $^{19}\text{F}$  NMR faces limitations in sensitivity, with detection limits in the  $\mu\text{g/L}$  range,<sup>295,298</sup> and accessibility due to the high cost of instrumentation.<sup>285</sup> Heerah *et al.* explored the use of lower-cost benchtop NMR spectrometers for PFOA analysis, particularly in the context of investigating remediation strategies. Although benchtop NMR was highlighted as a ‘quick and reliable tool’ for such studies, its lower sensitivity limits the application potential to the analysis of samples with low PFAS concentrations.<sup>300</sup> Similarly, Chen *et al.* employed a 1.4 T benchtop instrument to analyse PFAS in wastewater samples, albeit at concentrations approaching 1%.<sup>299</sup>

### 7.1.2 SABRE Hyperpolarisation of Carboxylic Acids

The use of benchtop NMR spectroscopy and hyperpolarisation could provide an accessible and sensitive platform for the analysis of PFAS. The hyperpolarisation of unsaturated perfluoroalkyl compounds has been attempted in the past by Plaumann *et al.* using hydrogenative PHIP.<sup>301</sup> Although this resulted in SNR enhancement factors of up to 26-fold for  $^{19}\text{F}$  NMR measurements, this solution is only applicable to a very small subset of PFAS containing double or triple bonds. Moreover, sensitivity improvement may be limited by the non-reversible nature of the hyperpolarisation step.

Hyperpolarisation of PFAS *via* SABRE would remove such limitations. Although this has not been attempted to date, SABRE hyperpolarisation of molecules containing carboxylic acid motifs has been reported before, setting a favourable precedent for PFCA compounds. For instance, Gemeinhardt *et al.* investigated the hyperpolarisation of 1- $^{13}\text{C}$ -acetic acid and 1- $^{13}\text{C}$ -acetate as potential MRI contrast agents. In this study, pyridine was used as a co-substrate to facilitate the formation of a stable SABRE complex, which yielded  $^{13}\text{C}$  enhancement factors up to 108-fold for 1- $^{13}\text{C}$ -acetate.<sup>302</sup> Indirect hyperpolarisation of acetate has also been demonstrated using SABRE-Relay, a technique presented in the previous chapter. Following this approach, a  $^{13}\text{C}$  enhancement factor of 48 per unit of carbon was obtained for 1- $^{13}\text{C}$ -acetate.<sup>79</sup>

Carboxylate binding was also observed in hyperpolarisation studies concerning amino acids, which revealed that these molecules bind in a bidentate fashion, with the oxygen donor from the carboxylate group binding equatorially, and the nitrogen donor from the amine binding axially.<sup>167</sup> The formation of this active species was also facilitated by the use of pyridine as a co-substrate. Given the strength of the oxygen bond to the catalyst, exchange into free solution was proposed to be slow, leading to inefficient hyperpolarisation. However, hyperpolarisation was enabled by the exchange of a suitable co-substrate, which facilitated  $p$ -H<sub>2</sub> replenishing. Such a strategy allowed the detection of sub-micromolar concentrations through the hyperpolarised hydride ligand signals.<sup>167</sup> Alternative co-substrates have also successfully led to the hyperpolarisation of molecules containing carboxylate motifs. In particular, dimethylsulfoxide has been used to hyperpolarise bidentate ligands such as pyruvate<sup>207,208</sup> and carboxyimines.<sup>173</sup>

Successful direct SABRE-hyperpolarisation of molecules containing carboxylic acids appears to rely on deprotonation of this group, to form the corresponding carboxylate species. Gemeinhardt *et al.*<sup>302</sup> reported that when acetic acid was probed by SABRE and using pyridine as a co-substrate, signal enhancements were not observed for either acetic acid or pyridine, which they attributed to catalyst deactivation. In contrast, the analysis of an acetate salt under similar conditions resulted in <sup>13</sup>C hyperpolarisation of acetate and <sup>1</sup>H hyperpolarisation of pyridine. Sellies and co-workers observed a similar phenomenon during the analysing of amino acids. When probing alanine under basic conditions (pH = 11.1), the authors detected a 6-fold increase in the hydride ligand signals corresponding to the active catalyst species *versus* non pH-corrected conditions.<sup>167</sup> Having observed the sensitivity of their system to pH variations, the authors opted for deprotonating the amino acids under investigation at a constant pH by using either KOH/HCl or a piperidine/piperidinium buffer.<sup>167</sup>

## 7.2 Choice of Test Systems

Difluoroacetic acid (DFA, **9**, Figure 7.2) was chosen as the simplest example of a fluorinated carboxylic acid that contains both proton and fluorine resonances. The mono fluorinated analogue, although equally suitable for this test, was not selected due to its higher toxicity.<sup>303</sup> Trifluoroacetic acid (TFA, **10**, Figure 7.2) was also tested as it better represents perfluoroalkyl compounds lacking hydrogen substituents on the carbon chain. The  $^{19}\text{F}$  NMR spectra for DFA and TFA reveals a doublet ( $^2J_{\text{HF}} = 53$  Hz between  $^{19}\text{F}$  and  $^1\text{H}$  in  $-\text{CF}_2\text{H}$  group) and a singlet, respectively, as determined by pulse-and-collect  $^1\text{H}$  and  $^{19}\text{F}$  NMR experiments at 1.4 T (Chapter 3, Section 3.3). The deprotonated analogues of these carboxylic acids, di- and trifluoroacetate ( $[\text{DFA-H}]^-$ , **14** and  $[\text{TFA-H}]^-$ , **15**, Figure 7.4) were also investigated, their  $^{19}\text{F}$  NMR spectra revealing a doublet ( $^2J_{\text{HF}} = 56$  Hz between  $^{19}\text{F}$  and  $^1\text{H}$  in  $-\text{CF}_2\text{H}$  group) and a singlet, respectively. Comparing the results for both of these molecules provides insight into the role of proton-relayed mechanisms in fluorine hyperpolarised experiments. In addition to providing a simple yet representative test system, difluoroacetic and trifluoroacetic acids are themselves an analytical target as ultra-short PFAs, which have come into use as an alternative to their longer chain analogues due to new regulations.<sup>304</sup> Trifluoroacetic acid has also been reported as a degradation product of fluoroorganics, including hydrofluorocarbon and hydrochlorofluorocarbon refrigerants,<sup>305</sup> making it an attractive pollution marker in environmental monitoring.<sup>306</sup>

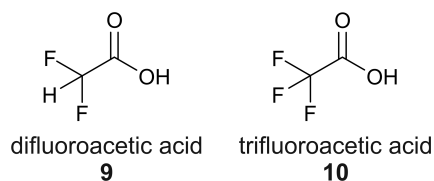


Figure 7.2: Chemical structures of fluorinated carboxylic acids under investigation in Chapter 7: difluoroacetic acid (DFA, **9**) and trifluoroacetic acid (TFA, **10**).

In terms of the co-substrate, both dimethylsulfoxide and selected N-heterocycles were tested. The former (DMSO, **4**, Figure 7.3) was selected as its low binding affinity and chemical reactivity proved to be effective for fluoropyridines and fluoroamines, as shown in

Chapters 5 and 6. Additionally, this enables the exploration of a potential single, all-purpose co-substrate, an attractive idea in analytical chemistry as it would eliminate the need to use analyte-specific co-substrates. Pyridine-based molecules were also studied following reports of hyperpolarisation of carboxylic acids employing pyridine,<sup>167,302</sup> suggesting this was likely to be a successful class of co-substrates. As a result, pyridine and 4-methylpyridine were proposed as co-substrates (PYR, **11** and 4MPYR, **12**, Figure 7.3), as well as the versatile 1-methyl-1,2,3-triazole (MTZ, **13**, Figure 7.3).<sup>81,168,307,308</sup>

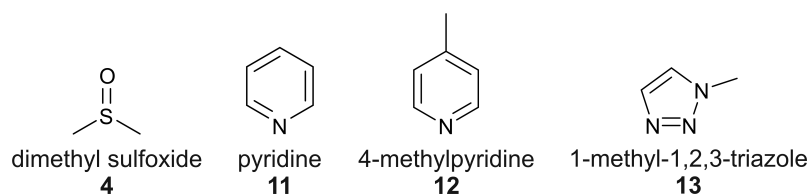


Figure 7.3: Chemical structure of the co-substrates dimethylsulfoxide (DMSO, **4**), here shown again for convenience, pyridine (PYR, **11**), 4-methylpyridine (4MPYR, **12**), and 1-methyl-1,2,3-triazole (MTZ, **13**).

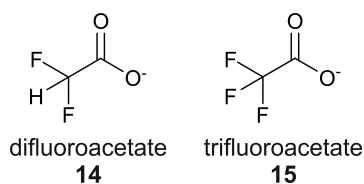


Figure 7.4: Chemical structures of fluorinated carboxylates under investigation in Chapter 7: difluoroacetate ( $[\text{DFA-H}]^-$ , **14**) and trifluoroacetate ( $[\text{TFA-H}]^-$ , **15**).

As for the choice of solvent, both methanol and methanol- $d_4$  were tested as these substrates have exchangeable protons. As shown in Chapter 6, the use of methanol- $d_4$  may be an effective way to minimise SABRE-Relay driven polarisation loss mechanisms. Performing experiments in both solvents enables a comparison of both active and inactive SABRE-Relay conditions.

## 7.3 SABRE Hyperpolarisation of Difluoroacetic Acid and Difluoroacetate

### 7.3.1 Hyperpolarisation of Difluoroacetic Acid

Although the literature suggests that efficient SABRE hyperpolarisation of carboxylic acids can only be achieved through the formation of conjugated carboxylate species,<sup>167,302</sup> initial studies focused on the protonated forms. These studies aimed to uncover the reasons behind this lack of SABRE activity, as this may lead to the proposal of solutions. Studies pertaining to the hyperpolarisation of difluoroacetic acid under different co-substrate and solvent conditions are presented in this section.

As a starting point, the hyperpolarisation of difluoroacetic acid was attempted on its own. To achieve this, a sample containing 100 mM of difluoroacetic acid and 5 mM of [IrCl(COD)(IMes)] was prepared and shake-and-drop experiments performed as described in Chapter 3, Sections 3.1.1 and 3.2. SABRE experiments were conducted at polarisation transfer fields of 6.2 mT (<sup>1</sup>H and <sup>19</sup>F),  $\sim 50 \mu\text{T}$ , and  $\sim 0 \text{ T}$  (<sup>19</sup>F) to explore different polarisation transfer pathways as described in Chapters 4 to 6. The sample was prepared in methanol-*d*<sub>4</sub> in order to deuterate the exchangeable proton on the carboxylic group, so as to reduce the occurrence of SABRE-Relay processes. In this way, signal enhancements for DFA, if observed, would be evidence of direct hyperpolarisation mechanisms.

These experiments revealed no hyperpolarised signals for difluoroacetic acid, either in <sup>1</sup>H or <sup>19</sup>F NMR measurements. This outcome was unsurprising as the bulky nature of this substrate was unlikely to lead to a stable tris-substituted species without the aid of a co-substrate. This rationale is likely to have motivated Gemeinhardt *et al.* to use pyridine as a co-substrate in order to hyperpolarise acetic acid.<sup>302</sup> This study did not lead to favourable results, which the authors attributed to catalyst deactivation in the presence of the acid. For completeness, the hyperpolarisation of difluoroacetic acid using pyridine as a co-substrate was tested.

SABRE experiments performed on a sample containing 100 mM of difluoroacetic acid, 100 mM of pyridine, and 5 mM of [IrCl(COD)(IMes)] in methanol-*d*<sub>4</sub> were conducted as

previously described. These experiments revealed neither  $^1\text{H}$  nor  $^{19}\text{F}$  NMR signals for DFA displayed observable hyperpolarisation, in agreement with Gemeinhardt's results.<sup>302</sup> The only hyperpolarised signal observed in these experiments was that corresponding to PYR, which was thought to arise from the tris-pyridine active species as evidenced by its characteristic singlet hydride ligand signal at  $\delta$  -22.8.<sup>155,157</sup>

Comparing hyperpolarised  $^1\text{H}$  NMR spectra for samples containing pyridine with and without difluoroacetic acid, revealed differences in SABRE efficiency and chemical shift values for the resonances corresponding to pyridine (Figure 7.5, dashed rectangle). The lack of hyperpolarisation for DFA, as well as the absence of new hydride ligand  $^1\text{H}$  NMR signals, implies that the decrease in signal enhancement for PYR is not a consequence of catalyst competition. Instead, direct interaction between pyridine and difluoroacetic acid, probably of acid-base nature, is the most likely explanation. Such a reaction between pyridine and carboxylic acids has been reported to produce pyridinium cations and carboxylate anions, the former presenting chemical shifts in  $^1\text{H}$  NMR similar to those observed in these experiments (Figure 7.5a).<sup>309</sup> As the pyridinium ions would not be expected to act as a ligand, this would inhibit its hyperpolarisation, and the indirect hyperpolarisation of difluoroacetic acid aided by pyridine as a co-substrate. These findings propose an alternative explanation to that presented by Gemeinhardt *et al.* for the lack of hyperpolarisation in SABRE samples containing carboxylic acids and pyridine.<sup>302</sup>

This theory is further supported by results from SABRE experiments on difluoroacetic acid using dimethylsulfoxide as a co-substrate. Dimethylsulfoxide was proposed as an alternative as it is not expected to participate in acid/base interactions with difluoroacetic acid. In addition, sulfoxide co-substrates have been employed to hyperpolarise compounds with carboxylic moieties.<sup>207,208</sup> A SABRE sample was prepared following the same procedure as described previously but using 100 mM of DMSO instead of PYR. These experiments revealed  $^1\text{H}$  NMR hyperpolarised signals for dimethylsulfoxide, thus providing evidence that catalyst deactivation does not take place when adding difluoroacetic acid. Nevertheless, the use of dimethylsulfoxide proved to be ineffective: hyperpolarisation of  $^1\text{H}$  NMR resonances in DFA was not observed and only modest signal enhancements ( $\epsilon_{^{19}\text{F}} < 2$ ) were detected

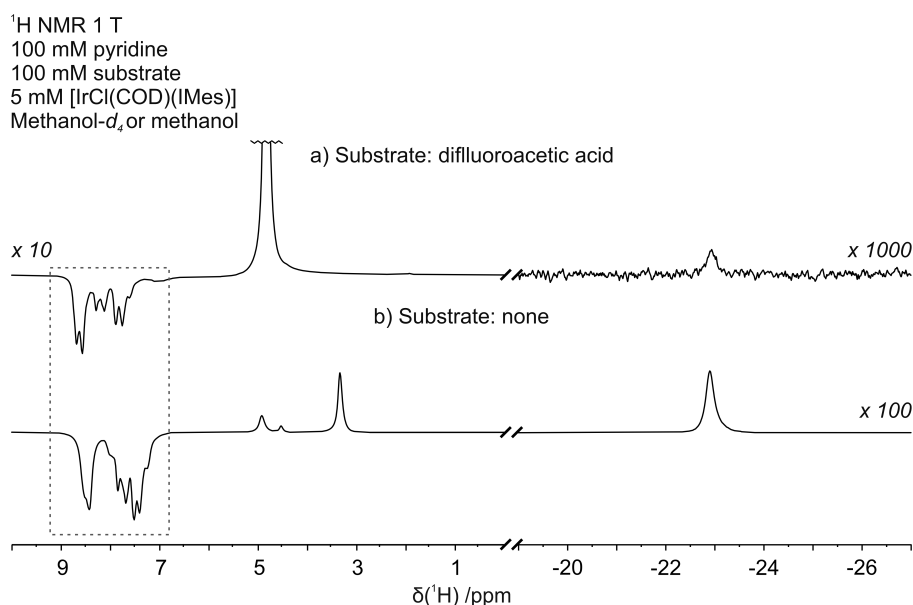


Figure 7.5: Comparison of SABRE-enhanced <sup>1</sup>H spectra for samples containing 100 mM of pyridine and either 100 mM of difluoroacetic acid (a) or no additional substrate (b), and 5 mM of [IrCl(COD)(IMes)]. Spectra is zoomed in to show the organic ( $\delta$  1 to 10) and the hydride ligand ( $\delta$  -19 to -27) regions of the spectra. Hyperpolarised signals corresponding to pyridine and pyridinium are highlighted in the dashed box, other signals correspond to the hydroxyl and methyl signals of methanol ( $\delta$  3 to 5) and the hydride ligands of a symmetric iridium complex containing pyridine ( $\delta$  - 22.8). Spectra was amplified as specified to aid visualisation.

in <sup>19</sup>F NMR experiments.

Lastly, SABRE hyperpolarisation of DFA using dimethylsulfoxide as a co-substrate was tested in protio methanol. This experiment was designed to test whether the deuteration of difluoroacetic acid when samples were prepared in methanol-*d*<sub>4</sub> hinders hyperpolarisation due to isotopic effects. It would also reveal any SABRE-Relay processes that could take place, for example involving methanol. Results revealed no significant difference when using protio solvent instead of methanol-*d*<sub>4</sub> either in enhancement factors ( $\epsilon_{^{19}\text{F}} < 2$ ) or peak profile.

These results demonstrate that the lack of direct hyperpolarisation for DFA was not a

consequence of catalyst inactivation, as previously proposed.<sup>302</sup> However, additional tests conducted with alternative co-substrates or solvents did not yield efficient hyperpolarisation for this target. This suggests that SABRE hyperpolarisation is inhibited either by its inability to form a stable SABRE complex or, if such a complex is indeed formed, by rates of exchange of dihydrogen or substrate(s) that do not promote hyperpolarisation. As the hyperpolarisation of carboxylate groups has been reported to lead to more successful outcomes,<sup>167,207,208,302</sup> difluoroacetate hyperpolarisation was then pursued, as discussed in the next section.

### 7.3.2 Hyperpolarisation of Difluoroacetate

Having established that the hyperpolarisation of difluoroacetic acid was unsuccessful under the tested conditions, the hyperpolarisation of the associated carboxylate species was pursued. Based on successful reports of the hyperpolarisation of acetate with pyridine,<sup>302</sup> this molecule was tested as a co-substrate. A sample containing 100 mM of difluoroacetate ( $[\text{DFA-H}]^-$ , lithium salt), 100 mM of PYR, and 5 mM of  $[\text{IrCl}(\text{COD})(\text{IMes})]$  in methanol- $d_4$  was analysed by shake-and-drop experiments, as described in the previous sections. Whilst studies of the carboxylate form of this target were conducted by acquiring a difluoroacetate salt for convenience, it is noted that the use of buffers could also have been used to achieve the same goal, as previously reported.<sup>167</sup>

Although hyperpolarisation of the proton resonance corresponding to the difluoromethyl group ( $\text{CF}_2\text{H-}$ ) was not clearly identified due to peak overlap, hyperpolarised  $^{19}\text{F}$  signals ( $\delta$  -125.8) were observed at 6.2 mT (Figure 7.6a), with a moderate  $\varepsilon_{^{19}\text{F}}$  of  $(7.05 \pm 0.38)$ . In contrast, experiments conducted at  $\sim 50 \mu\text{T}$  and  $\sim 0 \text{ T}$  did not result in significant signal enhancements relative to non-hyperpolarised spectra, as illustrated by Figure 7.6b to d. Closer inspection of the  $^{19}\text{F}$  spectrum at  $\sim 50 \mu\text{T}$  reveals that only one of the signals from the doublet was present. This suggests that an anti-phase doublet was produced at this PTF which resulted in the cancellation of one side of the non-hyperpolarised doublet. The comparatively better  $^{19}\text{F}$  signal enhancements observed at 6.2 mT are indicative of a proton-relayed polarisation transfer mechanism, as suggested by Chukanov *et al.*,<sup>134</sup> highlighting

the role of the hydrogen atom in facilitating  $^{19}\text{F}$  hyperpolarisation for this substrate.

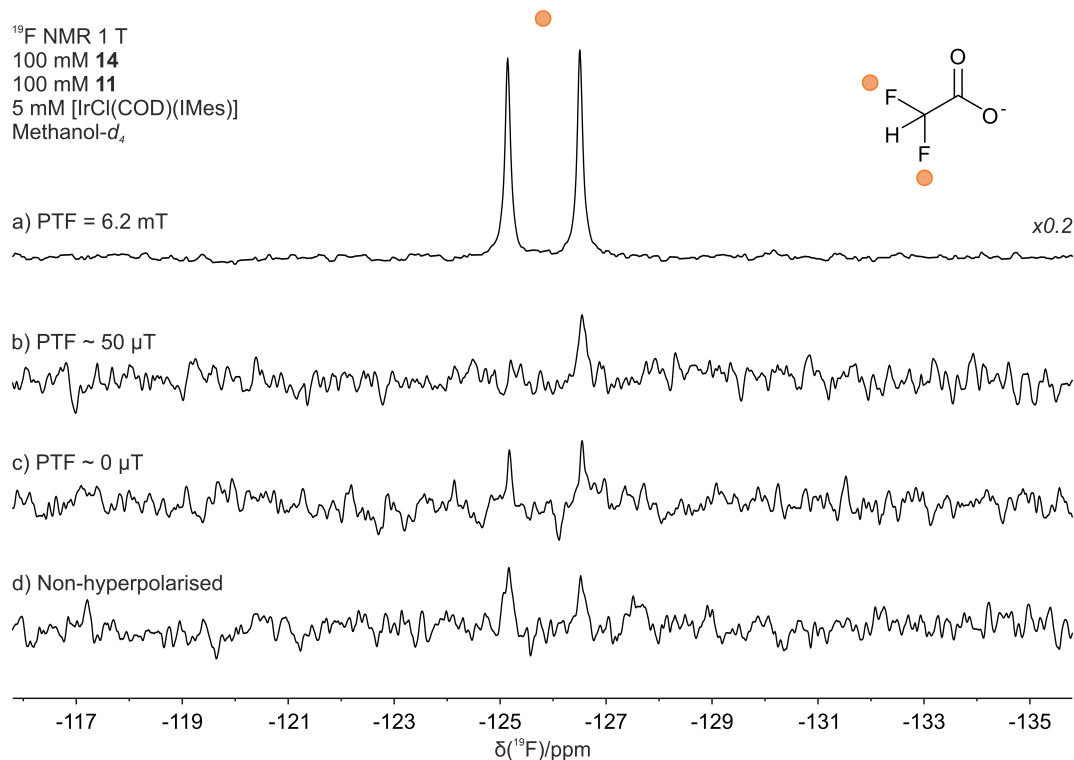


Figure 7.6: Comparison of SABRE-enhanced  $^{19}\text{F}$  spectra for difluoroacetate at polarisation transfer fields of 6.2 mT (a),  $\sim 50 \mu\text{T}$  (b) and  $\sim 0 \text{T}$  (c) with non-hyperpolarised spectra (d). The sample contained 100 mM of  $[\text{DFA-H}]^-$  (as a lithium salt), 100 mM of PYR, and 5 mM of  $[\text{IrCl}(\text{COD})(\text{IMes})]$  in methanol- $d_4$ . The doublet at  $\delta -125.8$  corresponds to the fluorine resonance in the difluoromethyl group.

Inspection of the hydride ligand region of the  $^1\text{H}$  NMR spectra for these experiments revealed a single hyperpolarised signal corresponding to the tris-pyridine species observed in Figure 7.5, which was thought to be responsible for the observed enhancement of pyridine signals. In contrast, no hyperpolarised hydride ligand signals were observed to which the modest  $^{19}\text{F}$  signals enhancements for  $[\text{DFA-H}]^-$  could be attributed, suggesting the SABRE-active species that drives this hyperpolarisation forms in small amounts. Taken together, these results suggest that pyridine may have a stronger binding affinity to the iridium centre *versus*  $[\text{DFA-H}]^-$ , hence limiting the formation of the mixed SABRE active species

containing both ligands, or that if this species does form in large quantities, it leads to inefficient hyperpolarisation.

This theory motivated the investigation of dimethylsulfoxide as a co-substrate based on its lower binding affinity to the iridium centre and the performance of dimethylsulfoxide-containing SABRE complexes demonstrated in Chapters 5 and 6. To test this, a SABRE sample containing 100 mM of [DFA-H]<sup>-</sup>, 100 mM of DMSO, and 5 mM of [IrCl(COD)(IMes)] in methanol-*d*<sub>4</sub> was studied. Figure 7.7 shows a comparison of SABRE-hyperpolarised and non-hyperpolarised <sup>1</sup>H NMR spectra obtained for this sample at 1 T. On first inspection, a hyperpolarised signal corresponding to the exchangeable proton of methanol ( $\delta$  4.8), and a partially anti-phase hyperpolarised signal for DMSO ( $\delta$  2.65) were observed. As methanol-*d*<sub>4</sub> was used in this experiment, and [DFA-H]<sup>-</sup> did not present exchangeable hydrogens, the hyperpolarisation of the hydroxyl signal ('-OH') was unexpected.

Protonation of methanol-*d*<sub>4</sub> could be attributed to proton exchange with residual water in the sample, likely stemming from the hygroscopic lithium difluoroacetate salt. However, this explanation was refuted by comparing non-hyperpolarised spectra pre- and post-activation, which revealed a significant increase in intensity for the exchangeable proton of methanol-*d*<sub>4</sub> after activation. In light of this, protonation of methanol-*d*<sub>4</sub> was attributed to hydrogen/deuterium exchange mechanisms for methanol-containing SABRE complexes, as explored in Chapter 4. Further evidence for this hypothesis was provided by the chemical shift of the main active species' hydride ligand signals: a doublet pair at  $\delta$  -15.3 and  $\delta$  -24.5. These shifts are consistent with a species containing hydride ligands *trans* to DMSO ( $\delta$  -15.3) and methanol-*d*<sub>4</sub>/methanol ( $\delta$  -24.5) in the equatorial positions, as observed in the SABRE complexes explored in Chapters 4 to 6. Not only would this species facilitate H/D exchange between adjacent hydrides and methanol-*d*<sub>4</sub> ligands, but it would also explain the hyperpolarisation of the -OH signals.

It has been found in the literature that hydrides *trans* to negatively charged oxygen atoms in carboxyimines and amino acids when pyridine is used as a co-substrate appear at *ca.*  $\delta$  -28,<sup>167,310</sup> whilst hydrides *trans* to pyruvate with dimethylsulfoxide in the equatorial

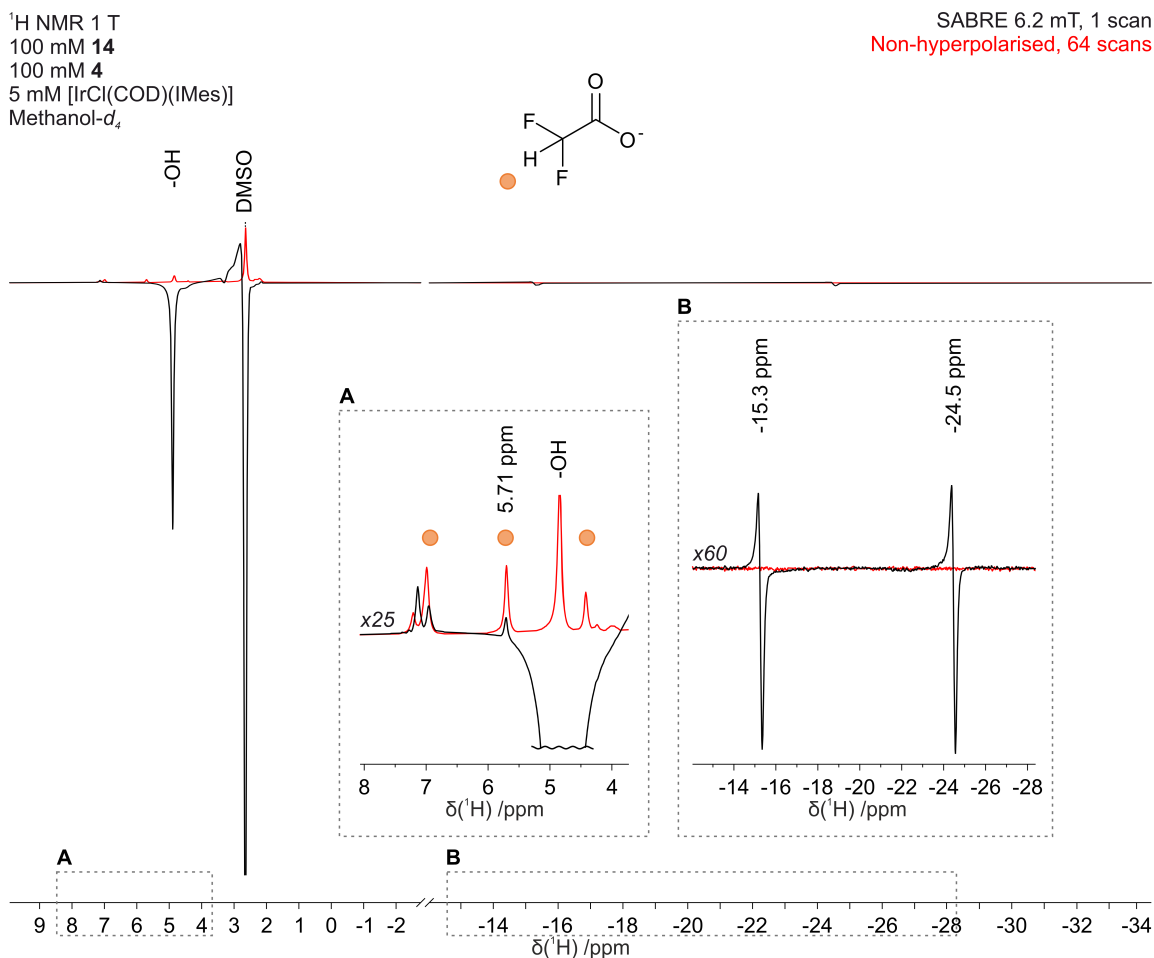


Figure 7.7: Comparison of SABRE-enhanced (black trace) and non-hyperpolarised (red trace) <sup>1</sup>H NMR spectra for difluoroacetate at 1 T using dimethylsulfoxide (‘DMSO’) as a co-substrate. The sample contained 100 mM of lithium difluoroacetate, 100 mM of dimethylsulfoxide, and 5 mM [IrCl(COD)(IMes)] in methanol-*d*<sub>4</sub>. Insets show an expanded view within the organic region of the spectra ( $\delta$  4 to 8, A) showing the signal for the proton resonance in the difluoromethyl group of [DFA-H]<sup>-</sup> at  $\delta$  5.71, and the hydride region of the spectra ( $\delta$  -12 to -28, B).

position appear at  $\delta$  -24.<sup>207</sup> Although, the formation of a species containing DMSO and methanol-*d*<sub>4</sub> in an equatorial position appears to be more reasonable, as it explains the hyperpolarisation of the hydroxyl signal, the formation of an equatorially asymmetric species

containing DMSO and [DFA-H]<sup>-</sup> cannot be discarded without full characterisation studies.

The signal corresponding to the difluoromethyl group in [DFA-H]<sup>-</sup> ( $\delta$  5.71) did not exhibit clear signs of hyperpolarisation (Figure 7.7, inset A). The lower signal intensity detected in SABRE experiments could be due to an overlap of signals of opposite phase (*i.e.* hyperpolarised and non-hyperpolarised) which could partially cancel. However, this could also be explained by a shorter residence time of the sample inside the spectrometer before FID acquisition, meaning polarisation build-up at the detection field would be incomplete, hence producing a smaller signal. Gemeinhardt *et al.* reported that no <sup>1</sup>H hyperpolarisation was observed for acetate even if hyperpolarised <sup>13</sup>C signals were detected.<sup>302</sup> A similar observation was made in this case: <sup>19</sup>F signal enhancements were detected for difluoroacetate when using dimethylsulfoxide as a co-substrate even when no enhancement was observed for <sup>1</sup>H signals in [DFA-H]<sup>-</sup>.

SABRE experiments using <sup>19</sup>F detection revealed signal enhancements at all tested polarisation transfer fields of 6.2 mT,  $\sim 50 \mu\text{T}$ , and  $\sim 0$  T, as shown in Figure 7.8. Similarly to samples using pyridine as a co-substrate, the largest enhancements were observed at 6.2 mT,  $\varepsilon_{19\text{F}} = (49.54 \pm 0.82)$  which after application of SHARPER (Section 3.3.3, Chapter 3) resulted in a SNR enhancement factor of  $(62.0 \pm 4.8)$ . Observing the largest <sup>19</sup>F signal enhancement at 6.2 mT was not anticipated, as this usually signals a polarisation transfer mechanism from proton to fluorine nuclei, and as discussed before, <sup>1</sup>H hyperpolarisation was not evident at this PTF. However, a similar behaviour was observed for 3-(difluoromethyl)pyridine, which exhibited the largest enhancement levels at this PTF (Chapter 4, Section 4.3). As the strong <sup>2</sup>J<sub>H,F</sub> coupling ( $\sim 55$  Hz) in the difluoromethyl group is the commonality in both cases, it is likely that this acts as the effective coupling of the system, to which the difference in frequencies in the hydride/substrate spin system needs to be matched.<sup>77,157,218</sup> As a consequence, a larger magnetic field such as 6.2 mT may facilitate a more efficient polarisation transfer to the substrate, leading to higher enhancement factors.

<sup>19</sup>F enhancements at  $\sim 50 \mu\text{T}$  and  $\sim 0$  T were 60% lower than at 6.2 mT, indicating less efficient polarisation transfer mechanisms at those fields (Figure 7.8b and c). Experiments

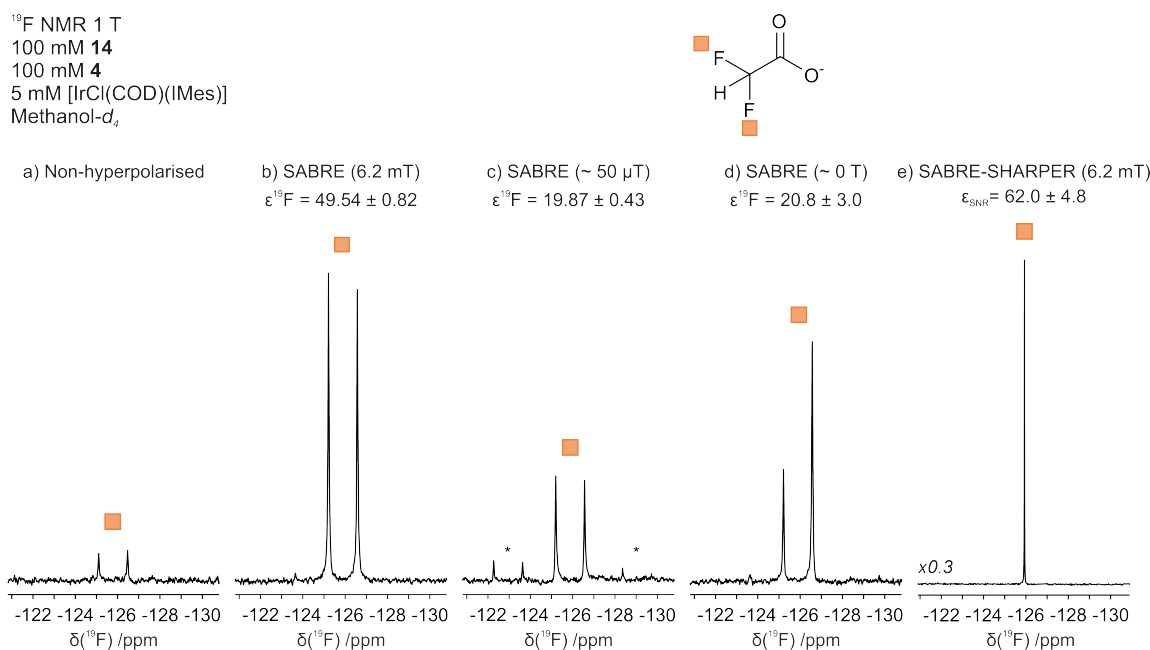


Figure 7.8: Comparison of <sup>19</sup>F NMR non-hyperpolarised (a) and hyperpolarised spectra acquired at 6.2 mT (b,e), ~ 50 μT (c) or ~ 0 T (d) using pulse-and-collect (a-d) or SHARPER (e) acquisition of a sample containing 100 mM of difluoroacetate (as a lithium salt), 100 mM of DMSO, and 5 mM of [IrCl(COD)(IMes)] in methanol-*d*<sub>4</sub>. All spectra were acquired with a single scan. Main doublet signal (orange square) corresponds to the difluoromethyl group ( $\delta$  -125.8), signals shown with asterisks in c) correspond to carbon satellites.

conducted at ~ 50 μT also exhibited some minor signals which were interpreted to be carbon satellites, appearing as a doublet of doublets with scalar couplings of 249 Hz and 55 Hz, corresponding to <sup>1</sup>J<sub>C,F</sub> and <sup>2</sup>J<sub>H,F</sub>, respectively. The observation of carbon satellites, corresponding to ~ 1% of the substrate concentration yet showing a signal roughly ten times larger, suggests that some <sup>19</sup>F -<sup>13</sup>C polarisation transfer mechanism could be at play.

The potential presence of <sup>13</sup>C -<sup>19</sup>F polarisation transfer mechanisms was deemed interesting, as this could be an exploitable route for indirect hyperpolarisation of <sup>19</sup>F nuclei by harnessing the typically long *T*<sub>1</sub> values for <sup>13</sup>C resulting in longer-lived observable polarisation. To further investigate this <sup>13</sup>C -<sup>19</sup>F polarisation transfer mechanism, SABRE

experiments were conducted with proton-decoupled  $^{13}\text{C}$  detection and results are shown in Figure 7.9. From this figure it is evident that only a  $\sim 0$  T field produced detectable  $^{13}\text{C}$  hyperpolarisation in a single-scan acquisition. The hyperpolarised signal in this case corresponds to a triplet at  $\delta$  108.7 with a  $J$  coupling of 249 Hz, corresponding to the carbon in the difluoromethyl group. This suggests that  $^{13}\text{C}$  polarisation was facilitated by the strong  $J$  coupling with the fluorine atoms. The remarkable  $^{13}\text{C}$  signal enhancement achieved in a single scan at 1 T for samples in natural abundance presents a promising avenue for investigating fluorinated carboxylic acids, or their carboxylate analogues, due to its specificity to this  $^{13}\text{C}$  -  $^{19}\text{F}$  coupling. This enhancement could potentially be further amplified by removing the peak splitting due to said heteronuclear scalar coupling through the application of SHARPER. However, while intriguing, this approach was not explored further as it fell outside the scope of this thesis.

Interestingly, fluorine enhancement values when using DMSO were *ca.* 7 times larger than when using PYR ( $\epsilon_{^{19}\text{F}} = 7.05 \pm 0.38$ ) at the best performing PTF, demonstrating that dimethylsulfoxide exhibits a better performance as a co-substrate when compared to pyridine. This is hypothesised to be a result of dimethylsulfoxide binding more weakly to the iridium centre, thus not outcompeting the substrate. Although the enhancements seen when using DMSO were larger than with pyridine, they are still considerably lower than those observed for previously studied substrates using this co-substrate ( $\epsilon_{^{19}\text{F}} \sim 2400 - 3000$ , Chapter 5 and 6). As explored in previous chapters, the concentration of co-substrates may affect signal enhancements for the target substrate, so optimisation studies were carried out for the difluoroacetate and dimethylsulfoxide system.

Samples were prepared containing 50 mM of  $[\text{DFA-H}]^-$ , either 100 mM or 25 mM of DMSO, and 5 mM of  $[\text{IrCl}(\text{COD})(\text{IMes})]$  in methanol- $d_4$ . The concentration of  $[\text{DFA-H}]^-$  was chosen as a compromise between testing at a level closer to the sub-stoichiometric regime and being able to obtain enough signal intensity to compare results. SABRE-enhanced fluorine experiments revealed that higher  $\epsilon_{^{19}\text{F}}$  values are obtained when decreasing the concentration of co-substrate, as shown in Figure 7.10. This observation applied to all of the tested polarisation transfer fields, with fluorine enhancement factors between 2.5 to 4.3

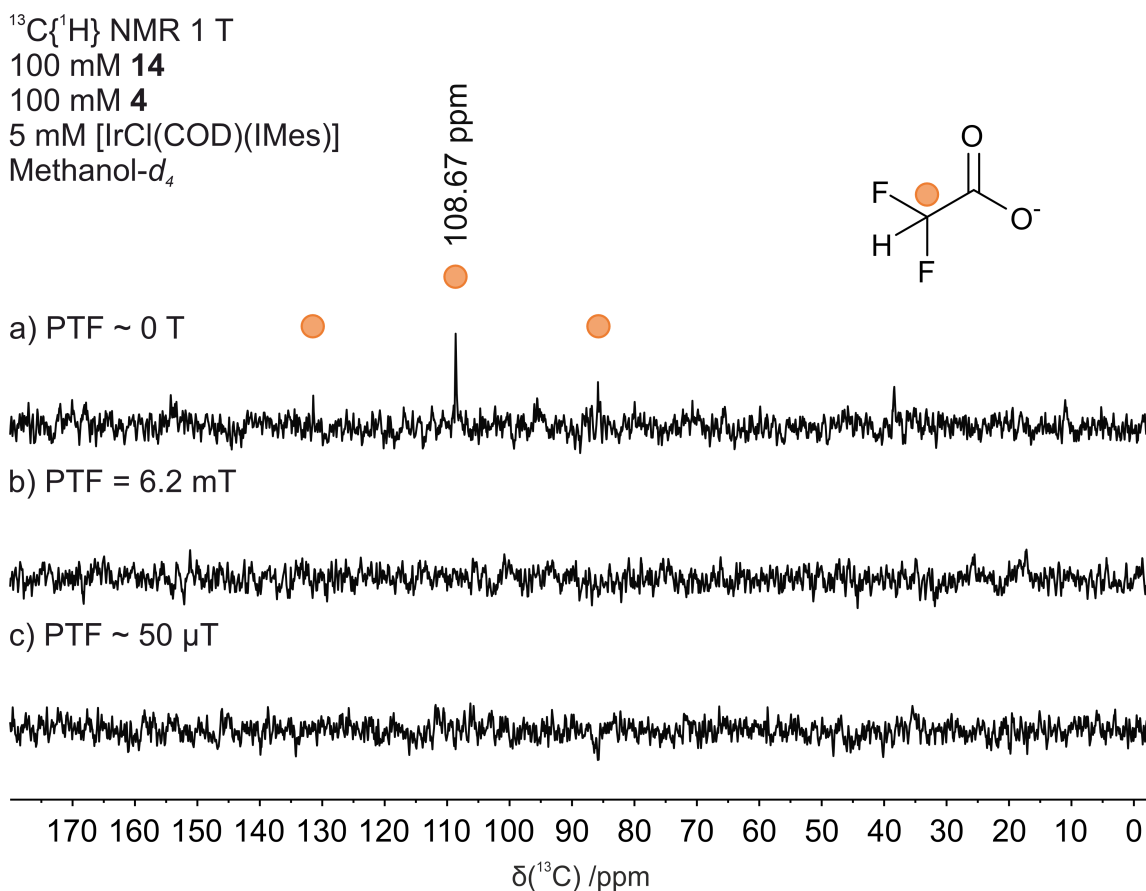


Figure 7.9: Comparison of  $^{13}\text{C}\{^1\text{H}\}$  NMR SABRE-hyperpolarised spectra acquired using a polarisation transfer field of  $\sim 0$  T (a), 6.2 mT (b), or  $\sim 50$   $\mu\text{T}$  (c). The sample contained 100 mM  $[\text{DFA-H}]^-$ , 100 mM of DMSO, and 5 mM of  $[\text{IrCl}(\text{COD})(\text{IMes})]$  in methanol- $d_4$ . The highlighted signal at  $\delta -108.7$  (t,  $J=249$  Hz) corresponds to the carbon in the difluoromethyl group ( $-\text{CF}_2\text{H}$ ) of difluoroacetate.

times larger when using lower concentrations of DMSO (Table 7.1). Based on these results, SABRE experiments on the difluoroacetate and dimethylsulfoxide system were conducted using 25 mM of co-substrate and a PTF of 6.2 mT. By performing SABRE experiments under these optimised conditions in combination with SHARPER (Figure 7.11), SNR values were boosted by a factor of *ca.* 63 *versus* non-hyperpolarised pulse-and-collect experiments.

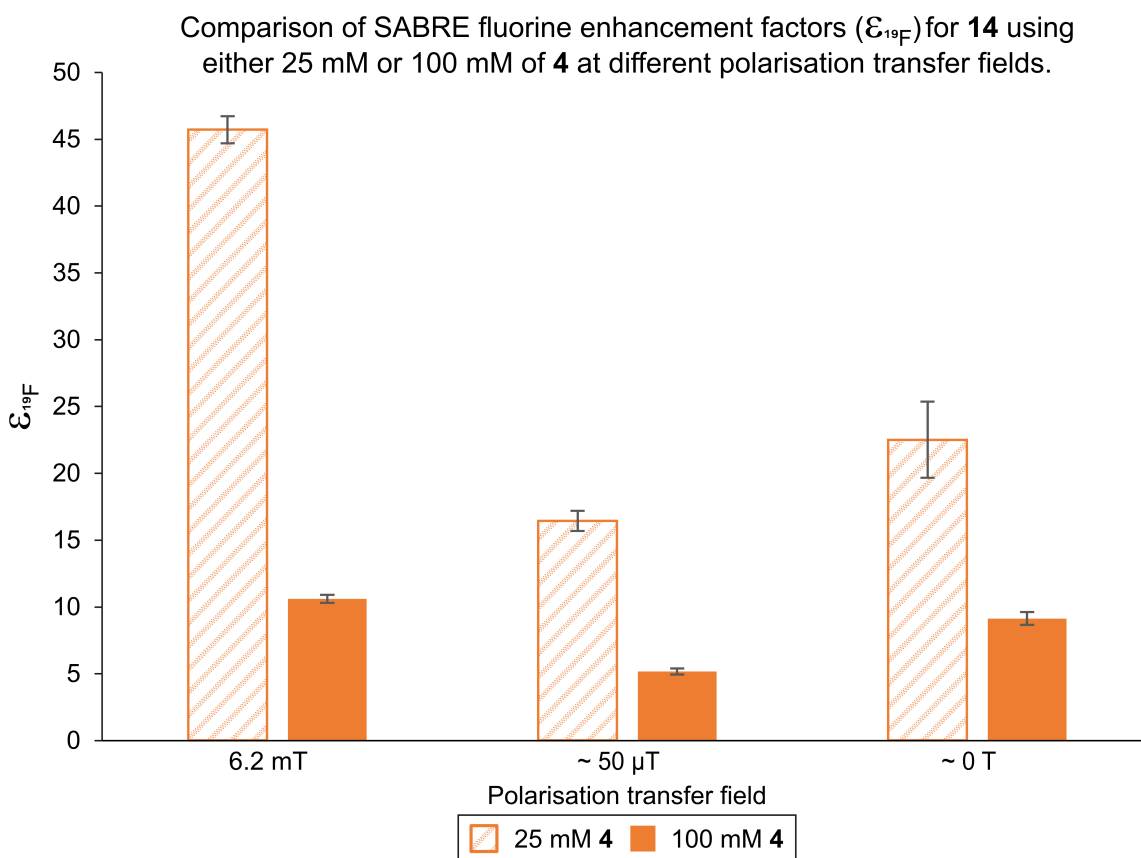


Figure 7.10: Comparison of fluorine enhancement factors ( $\epsilon_{19F}$ ) for SABRE experiments on samples containing 50 mM of [DFA-H]<sup>-</sup> (**14**), either 25 mM or 100 mM of DMSO (**4**), and 5 mM of [IrCl(COD)(IMes)] at PTF values of 6.2 mT, ~ 50  $\mu$ T, and ~ 0 T.  $\epsilon_{19F}$  were estimated as the average of triplicate measurements, with the standard deviation shown as error bars.

Proton experiments for both co-substrate levels showed no significant change in terms of difluoroacetate enhancement. However, it was observed that when lower concentrations of DMSO were added to the sample, the hydride pair described previously (doublet pair at  $\delta$  -15.3 and  $\delta$  -24.5) decreased in intensity, both in hyperpolarised and non-hyperpolarised spectra (Figure 7.12). This provides further validation of the proposed structure for this species, *i.e.* containing DMSO and methanol-*d*<sub>4</sub>/methanol equatorially, as a decrease in overall dimethylsulfoxide concentration would likely limit its formation. Likewise, if this

Table 7.1: Fluorine enhancement factors ( $\epsilon_{^{19}\text{F}}$ ) for SABRE-hyperpolarised samples containing 50 mM of  $[\text{DFA-H}]^-$ , either 25 mM or 100 mM of DMSO, and 5 mM of  $[\text{IrCl}(\text{COD})(\text{IMes})]$ , at three polarisation transfer fields: 6.2 mT,  $\sim 50 \mu\text{T}$ , and  $\sim 0 \text{ T}$ .

| [Co-substrate] | $\epsilon_{^{19}\text{F}}$ |                           |                        |
|----------------|----------------------------|---------------------------|------------------------|
|                | PTF = 6.2 mT               | PTF $\sim 50 \mu\text{T}$ | PTF $\sim 0 \text{ T}$ |
| 25 mM          | $45.7 \pm 1.0$             | $16.42 \pm 0.75$          | $22.5 \pm 2.8$         |
| 100 mM         | $10.59 \pm 0.30$           | $5.15 \pm 0.39$           | $9.11 \pm 0.47$        |

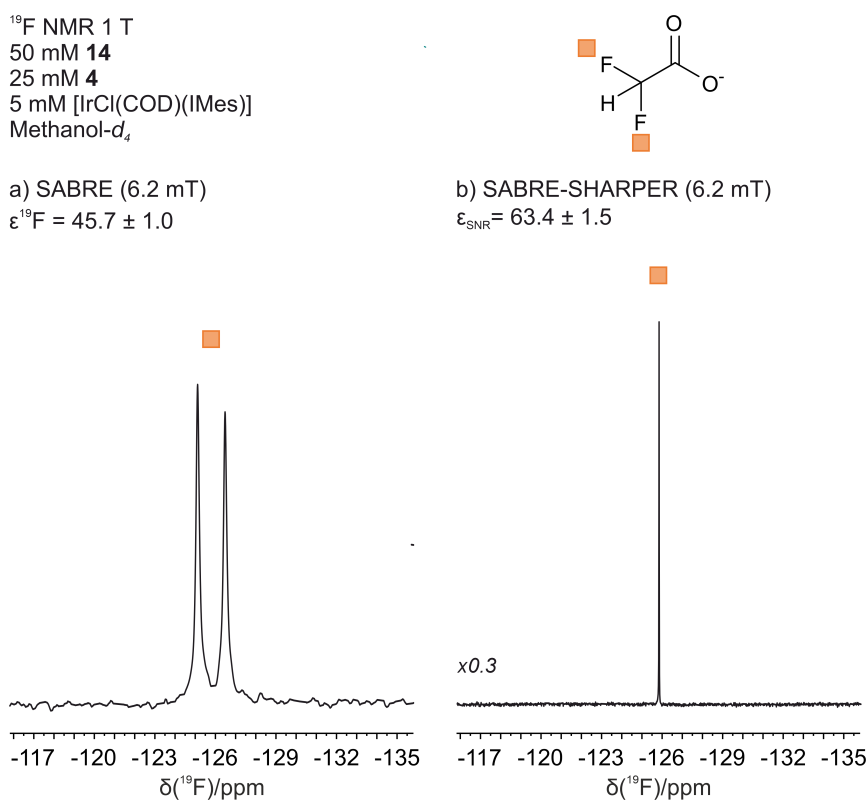


Figure 7.11: Comparison of  $^{19}\text{F}$  NMR hyperpolarised spectra acquired at 6.2 mT using pulse-and-collect (a) or SHARPER (b) acquisition of a sample containing 50 mM of difluoroacetate (as a lithium salt), 25 mM of DMSO, and 5 mM of  $[\text{IrCl}(\text{COD})(\text{IMes})]$  in methanol- $d_4$ . All spectra were acquired with a single scan. Main doublet signal (orange square) corresponds to the difluoromethyl group ( $\delta$  -125.8).

active species did have difluoroacetate in its structure, signal enhancements would decrease at lower concentrations of DMSO, and its associated complex, which is contrary to what was observed. It is therefore proposed that the main hyperpolarised hydride signals observed at  $\delta$  -15.3 and  $\delta$  -24.5 are not the main active species containing  $[\text{DFA-H}]^-$ , with its likely structure being  $[\text{Ir}(\text{H})_2(\text{IMes})(\text{L})(\text{MeOD}/\text{H})(\mathbf{4})]^+$ , with MeOD and MeOH being methanol- $d_4$  and methanol, respectively and L being an unknown ligand in axial position, such as DMSO.

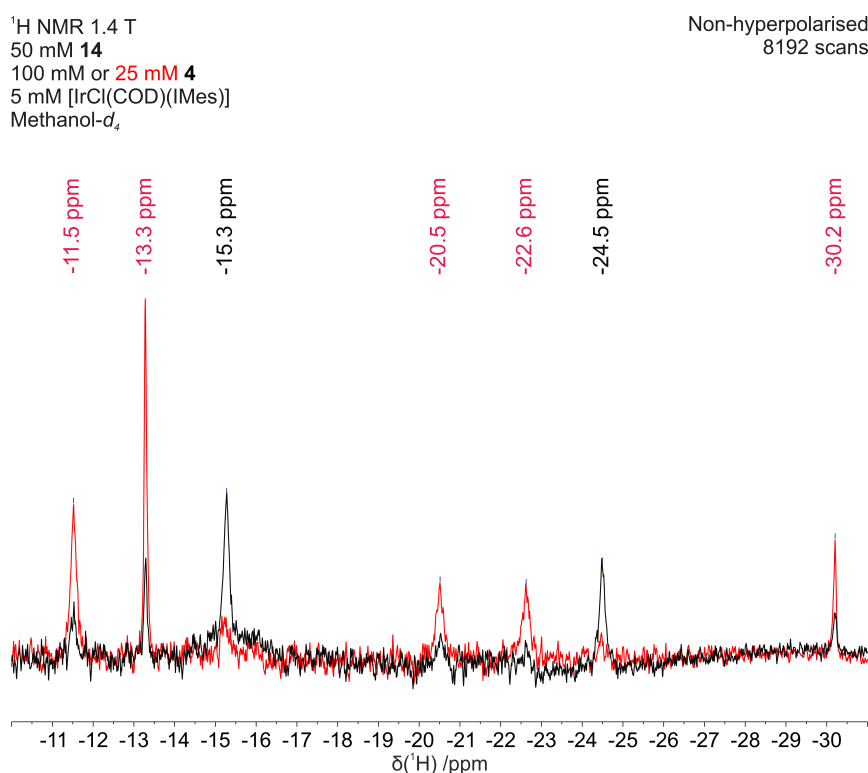


Figure 7.12: Comparison of post activation non-hyperpolarised <sup>1</sup>H NMR spectra at 1.4 T of samples containing 50 mM of  $[\text{DFA-H}]^-$ , either 25 mM (red trace) or 100 mM (black trace) of DMSO, and 5 mM of  $[\text{IrCl}(\text{COD})(\text{IMes})]$  in methanol- $d_4$ . Spectra are zoomed in to show the hydride region of the spectra ( $\delta$  - 10 to  $\delta$  -31). Chemical shift values for detected hydride signals are shown above each peak.

It is likely the case that the main active species containing  $[\text{DFA-H}]^-$  and leading to its

hyperpolarisation was present in very small amounts or in fast exchange leading to broad peaks, precluding the observation of its hydrides when hyperpolarised. As shown in Figure 7.12, several additional hydride signals were observed in non-hyperpolarised experiments conducted at 1.4 T, which were undetected in hyperpolarised spectra. Given that these hydride signals intensified upon the reduction of [DMSO] in a manner consistent with the SABRE-hyperpolarised  $^{19}\text{F}$  signals for  $[\text{DFA-H}]^-$ , they are strong candidates for the active species containing this substrate.

Having obtained a promising test system and optimised conditions, experiments decreasing the concentration of  $[\text{DFA-H}]^-$  were conducted in order to approach the analytically-relevant sub-stoichiometric regime. Samples containing 50 mM, 10 mM, and 1 mM of  $[\text{DFA-H}]^-$ , 25 mM of DMSO, and 5 mM of  $[\text{IrCl}(\text{COD})(\text{IMes})]$  were analysed. Upon inspection of the resulting SABRE-hyperpolarised  $^1\text{H}$  NMR spectra (Figure 7.13), it was observed that lower concentrations of  $[\text{DFA-H}]^-$  resulted in a decrease in intensity of the hyperpolarised hydride ligand signals previously attributed to  $[\text{Ir}(\text{H})_2(\text{IMes})(\text{L})(\text{MeOD}/\text{H})(\mathbf{4})]^+$ . Seemingly linked to this, it was also observed that hyperpolarised signals for DMSO and the exchangeable proton in methanol ( $\delta$  2.65 and  $\delta$  4.8, respectively) also decreased in intensity with  $[[\text{DFA-H}]^-]$ .

Based on this correlation between the concentrations of  $[\text{DFA-H}]^-$  and the main active hydrides ( $\delta$  -15.3 and  $\delta$  -24.5), one could reasonably argue that  $[\text{DFA-H}]^-$  is either part of its structure or that it indirectly facilitates its formation. Building on the hypothesis that this species contains DMSO and methanol- $d_4$ /methanol in equatorial positions, a hypothesis further substantiated by the correlation between their hyperpolarised signals and those of the aforementioned hydride ligands, it follows that  $[\text{DFA-H}]^-$  could occupy the axial position. However, this would not be consistent with the observation of hyperpolarised signals for  $[\text{DFA-H}]^-$ , a position to which hyperpolarisation is not favoured.<sup>77,155,159</sup>

Alternatively, difluoroacetate may be linked to the formation of the main active species by acting as a counter ion to the positively charged  $[\text{Ir}(\text{H})_2(\text{IMes})(\text{L})(\text{MeOD}/\text{H})(\mathbf{4})]^+$  complex. The close proximity of  $[\text{DFA-H}]^-$  to the iridium centre in the active species would place it in an advantageous position for substrate exchange, indirectly facilitating  $[\text{DFA-H}]^-$

hyperpolarisation. This hypothesis would also explain why this species was not observed for other samples containing DMSO, such as the ones investigated in Chapters 5 and 6. It was additionally observed that at the lowest tested concentration of  $[\text{DFA-H}]^-$  (1 mM), two new sets of hydride ligand signals became visible: an anti-phase doublet at  $\delta$  -18.9 and  $\delta$  -25.0 ( $J = 8$  Hz) and a very broad anti-phase doublet at  $\delta$  -15.5 and  $\delta$  -21.5, the latter of which corresponds to the previously reported  $[\text{IrCl}(\text{H})_2(\text{IMes})(\mathbf{4})_2]$  (**6**, Chapter 5).<sup>202</sup> This species containing dimethylsulfoxide and chloride was not observed at higher concentrations of  $[\text{DFA-H}]^-$ , lending additional support to the idea that for  $[\text{Ir}(\text{H})_2(\text{IMes})(\text{L})(\text{MeOD}/\text{H})(\mathbf{4})]^+$  to form, it relies on the presence of  $[\text{DFA-H}]^-$  as a counter ion.

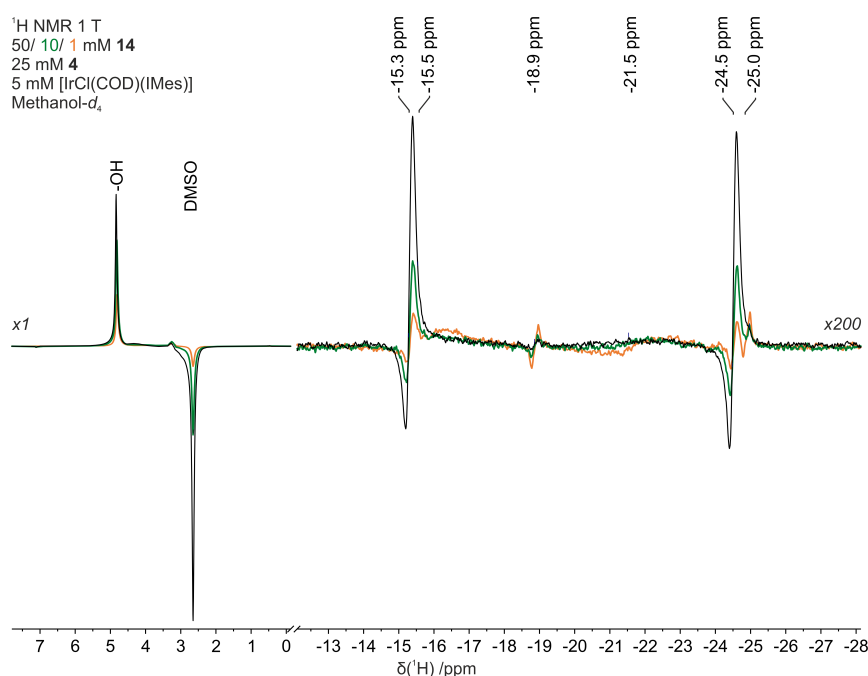


Figure 7.13: Comparison of SABRE-hyperpolarised  $^1\text{H}$  spectra for samples containing 50 mM (black), 10 mM (green), or 1 mM (orange) of  $[\text{DFA-H}]^-$ , 25 mM of DMSO, and 5 mM of  $[\text{IrCl}(\text{COD})(\text{IMes})]$  in methanol- $d_4$ . Inset shows a zoom in portion of the spectra in the  $\delta$  -12 to  $\delta$  -27 region.

Fluorine enhancements at low concentrations were tested using a polarisation transfer field of 6.2 mT, as it proved to yield the largest signal amplification. At this polarisation

transfer field, enhancement factors were estimated to be  $\varepsilon_{^{19}\text{F}} = (45.7 \pm 1.0)$  at 50 mM and  $\varepsilon_{^{19}\text{F}} = (68.0 \pm 1.9)$  at 10 mM. Taking into consideration the SNR values obtained for SABRE-hyperpolarised  $^{19}\text{F}$  spectra at 50 mM of  $[\text{DFA-H}]^-$  under optimised conditions, limit of detection values for SABRE and SABRE SHARPER measurements were estimated to be  $(1007 \pm 12) \mu\text{M}$  and  $(263.8 \pm 6.2) \mu\text{M}$ , respectively. SABRE experiments performed on the sample containing 1 mM of  $[\text{DFA-H}]^-$  did not produce a detectable  $^{19}\text{F}$  NMR signal, which was consistent with the estimated LOD value for this approach. SABRE-SHARPER experiments at the same concentration, however, did not yield detectable signals, despite the tested concentration being significantly above the estimated LOD of 264  $\mu\text{M}$ .

Linking this result to the hydride ligand signal analysis previously discussed, it would be reasonable to propose that the reduced amount of  $[\text{Ir}(\text{H})_2(\text{IMes})(\text{L})(\text{MeOD}/\text{H})(\mathbf{4})]^+$  observed at 1 mM may explain the lack of SABRE activity at this level. At such low concentrations of difluoroacetate, the formation of the neutral dimethylsulfoxide complex (**6**) is favoured over that of the positively charged  $[\text{Ir}(\text{H})_2(\text{IMes})(\text{L})(\text{MeOD}/\text{H})(\mathbf{4})]^+$  species. Under the assumption that  $[\text{DFA-H}]^-$  does indeed act as a counterion of the latter case, the preferential formation of the neutral species would likely be detrimental for SABRE activity at lower concentrations, precluding sub-stoichiometric measurements. Based on this hypothesis, a set of alternative co-substrates were tested: 4-methylpyridine, pyridine and 1-methyl-1,2,3-triazole. These were chosen as they were expected to form positively charged tris-substituted species, which may act as the hyperpolarisation machinery, regardless of the concentration of  $[\text{DFA-H}]^-$ .

To test the previously stated theory, samples containing  $[\text{DFA-H}]^-$  at 10 mM were tested using 25 mM of co-substrate and 5 mM of  $[\text{IrCl}(\text{COD})(\text{IMes})]$  in methanol- $d_4$  following the same described procedure. This concentration of  $[\text{DFA-H}]^-$  was chosen as it was the lowest concentration that could be detected *via* SABRE experiments, whilst the co-substrate concentration was maintained from experiments with DMSO to minimise displacement of difluoroacetate by these more strongly binding co-substrates. Fluorine enhancement factors obtained in these experiments are detailed in Table 7.2. When using 4-methylpyridine,  $^{19}\text{F}$  hyperpolarised signals were observed with an estimated  $\varepsilon_{^{19}\text{F}}$  at 6.2 mT of  $(29.0 \pm 3.2)$ .

Table 7.2: Fluorine enhancement factors ( $\epsilon_{19\text{F}}$ ) for SABRE experiments on samples containing 10 mM of  $[\text{DFA-H}]^-$ , 25 mM of co-substrate, and 5 mM of  $[\text{IrCl}(\text{COD})(\text{IMes})]$  using a PTF of 6.2 mT.

| Co-substrate            | $\epsilon_{19\text{F}}$ |
|-------------------------|-------------------------|
| dimethylsulfoxide       | $68.0 \pm 1.9$          |
| 4-methylpyridine        | $29.0 \pm 3.2$          |
| pyridine                | $27.6 \pm 2.8$          |
| 1-methyl-1,2,3-triazole | ND                      |

This result was under half of what was reported at the same concentration of  $[\text{DFA-H}]^-$  when using DMSO as a co-substrate ( $\epsilon_{19\text{F}} = (68.0 \pm 1.9)$ ). Once again, hyperpolarised hydride ligand signals for the species responsible for the signal enhancement of  $[\text{DFA-H}]^-$  were not observed. Instead, the only hyperpolarised hydride ligand signals observed in these experiments corresponded to the tris-4-methylpyridine species at  $\delta - 22.83$ . Similar results were obtained for pyridine as a co-substrate, yielding  $\epsilon_{19\text{F}} = (27.6 \pm 2.8)$  at 10 mM of  $[\text{DFA-H}]^-$  with the only visible hyperpolarised hydride species corresponding to that of the tris-pyridine species ( $\delta - 22.8$ ). The lower enhancement factors observed when using pyridine and 4-methylpyridine as co-substrates were attributed to their stronger binding affinity *versus* dimethylsulfoxide, thus outcompeting the target molecule. The co-substrate 1-methyl-1,2,3-triazole, which was expected to show weaker binding than pyridine due to the steric hinderance introduced by the methyl substituent, did not result in any detectable hyperpolarisation. Based on these results, it can be concluded that even if these alternative co-substrate would facilitate probing  $[\text{DFA-H}]^-$  at lower concentrations, the reduced SABRE efficiency observed for these systems may result in high limits of detection.

The results presented in this section demonstrate that although the hyperpolarisation of difluoroacetate was more successful than for difluoroacetic acid, it is not without its challenges. It was found that the best co-substrate for this system was dimethylsulfoxide, which allowed  $^{19}\text{F}$  NMR detection of  $[\text{DFA-H}]^-$  at as low as 10 mM using a single scan at

1 T. When this approach was combined with SHARPER detection, an SNR enhancement factor of  $\varepsilon_{SNR} = (53.5 \pm 1.9)$  was obtained. In practical terms, an estimated 4 hours of signal averaging would be needed to achieve similar SNR values as those obtained with a single-scan SABRE-SHARPER experiment, a high time commitment for routine analysis. Nevertheless, the challenges in forming a stable SABRE species acting as the hyperpolarisation machinery for this system result in high operational limits of detection, restricting its use to high-concentration analysis, and therefore, its potential for analytical applications.

## 7.4 SABRE Hyperpolarisation of Trifluoroacetic Acid and Trifluoroacetate

In the previous section, the hyperpolarisation of difluoroacetic acid and difluoroacetate was explored under various co-substrate and PTF conditions. These results showed that whilst hyperpolarisation of difluoroacetic acid was unsuccessful, that of difluoroacetate yielded  $^{19}\text{F}$  signal enhancements that were optimised when using 25 mM of dimethylsulfoxide as a co-substrate and a polarisation transfer field of 6.2 mT. This PTF is believed to facilitate proton-relayed polarisation transfer mechanisms, which in this case was enabled by the hydrogen atom in the difluoromethyl group in  $[\text{DFA-H}]^-$ . However, this proton-facilitated polarisation transfer mechanism would not be possible in many perfluorocarboxylic acids, most notably perfluorooctanoic acid, one of the most targeted compounds within the PFAS group. To evaluate the performance of SABRE hyperpolarisation for perfluorocarboxylic acids lacking hydrogen atoms, trifluoroacetic acid and its conjugate base, trifluoroacetate, were examined.

### 7.4.1 Hyperpolarisation of Trifluoroacetic Acid

The hyperpolarisation of carboxylic acids in their protonated form has proved to be unsuccessful, as demonstrated by attempts made for difluoroacetic acid (Section 7.3) and acetic acid.<sup>302</sup> However, as trifluoroacetic acid samples would naturally present a larger amount of trifluoroacetate in solution due to its lower pKa (0.23 for TFA *vs.* 1.24 for DFA,

respectively<sup>311</sup>), it was speculated that SABRE experiments may indeed exhibit hyperpolarisation.

The hyperpolarisation of trifluoroacetic acid was tested using dimethylsulfoxide as a co-substrate, which proved to be the best for difluoroacetate. To this end, SABRE experiments were conducted on a sample containing 100 mM of TFA, 100 mM of DMSO, and 5 mM of [IrCl(COD)(IMes)] in methanol-*d*<sub>4</sub>. <sup>1</sup>H NMR spectra exhibited several similarities to those obtained for low concentration difluoroacetate samples with the same co-substrate. For instance, hyperpolarised signals corresponding to DMSO and the exchangeable proton in methanol-*d*<sub>4</sub> were observed, as well as a very similar pattern in hydride ligand <sup>1</sup>H NMR signals, as seen in Figure 7.14. The main species in samples containing TFA exhibited hydride ligand <sup>1</sup>H NMR signals at  $\delta$  -15.3 and  $\delta$  -25.1, chemical shift values which were in close proximity to those of the main active species when [DFA-H]<sup>-</sup> was probed. This suggests that these species are indeed similar and based on the discussion presented in the previous section, it is proposed to be the same [Ir(H)<sub>2</sub>(IMes)(L)(MeOD/H)(4)]<sup>+</sup> species with trifluoroacetate as a counter ion. The small amount of this species in solution, as hinted by the intensity of its hyperpolarised signal, is likely a consequence of the small amount of trifluoroacetate in a sample prepared with trifluoroacetic acid.

Such a small amount of the active SABRE species was not expected to yield large <sup>19</sup>F NMR signal enhancements. Indeed, no evidence of <sup>19</sup>F hyperpolarisation was observed for the tested polarisation transfer fields (6.2 mT,  $\sim$  50  $\mu$ T and  $\sim$  0 T) with the exception of experiments conducted at  $\sim$  50  $\mu$ T. Under those conditions, the singlet signal corresponding to deuterated trifluoroacetic acid ( $\delta$  -78.5) exhibited a 35 % decrease in area, which was attributed to partial cancellation of the thermally-polarised signal with a hyperpolarised signal of opposite phase. Although this result shows promise for the hyperpolarisation of fluorinated carboxylic acid without a proton in their alkyl chain to relay polarisation, the low abundance of the carboxylate species in solution renders this process inefficient.

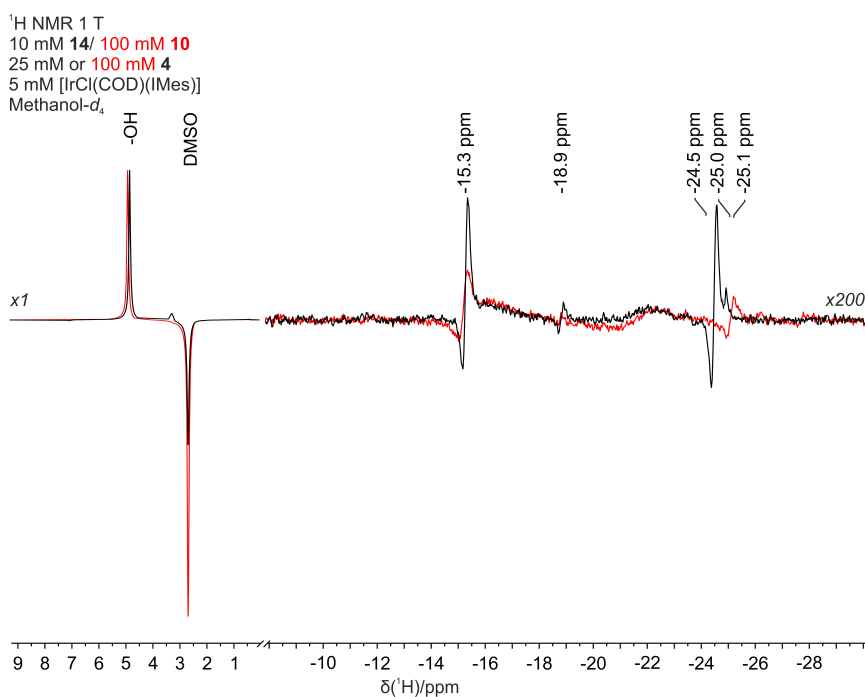


Figure 7.14: Comparison of SABRE-hyperpolarised spectra corresponding to samples containing either 10 mM of  $[\text{DFA-H}]^-$ , 25 mM of DMSO (black trace) or 100 mM of TFA, 100 mM of DMSO (red trace), and 5 mM of  $[\text{IrCl}(\text{COD})(\text{IMes})]$  in methanol- $d_4$ . The left side of the figure shows the organic region of the spectra ( $\delta$  9 to 0) whilst the right side is zoomed in to show the hydride region ( $\delta$  - 8 to - 30) and is amplified by a factor of 200 to aid visualisation. Chemical shift values for the main hyperpolarised hydride signals are shown above the spectra.

#### 7.4.2 Hyperpolarisation of Trifluoroacetate

As demonstrated in the previous section, the hyperpolarisation of trifluoroacetic acid in samples containing dimethylsulfoxide as a co-substrate was unsuccessful, despite it being a stronger acid compared to difluoroacetic acid. Consequently, the direct hyperpolarisation of trifluoroacetate samples was explored, as tests with difluoroacetate indicated that this approach was more likely to succeed. This investigation also enabled a comparison of SABRE performance between difluoroacetate and trifluoroacetate, providing insights into

how the chemical structure of fluorocarboxylic targets influences signal enhancement.

Following the successful results obtained for difluoroacetate and dimethylsulfoxide systems, a sample containing 100 mM of trifluoroacetate ( $[\text{TFA-H}]^-$ , as a sodium salt), 100 mM of DMSO, and 5 mM of  $[\text{IrCl}(\text{COD})(\text{IMes})]$  in methanol- $d_4$  was analysed. SABRE-enhanced  $^1\text{H}$  NMR spectra resembled those detected for trifluoroacetic acid samples. Hyperpolarised  $^1\text{H}$  NMR signals from both the solvent and dimethylsulfoxide were observed, as well as two pairs of hyperpolarised hydride ligand signals: one at  $\delta$  -15.3 and  $\delta$  -25.1, present in the trifluoroacetic acid/dimethylsulfoxide samples (Figure 7.14), and one at  $\delta$  -15.5 and  $\delta$  -21.5, corresponding to  $[\text{IrCl}(\text{H})_2(\text{IMes})(\mathbf{4})_2]$ .<sup>202</sup> The main active signal ( $\delta$  -15.3 and  $\delta$  -25.1), previously proposed to be  $[\text{Ir}(\text{H})_2(\text{IMes})(\text{L})(\text{MeOD}/\text{H})(\mathbf{4})]^+$ , exhibited a much larger intensity in samples containing trifluoroacetate than in those containing trifluoroacetic acid, as shown in Figure 7.15.

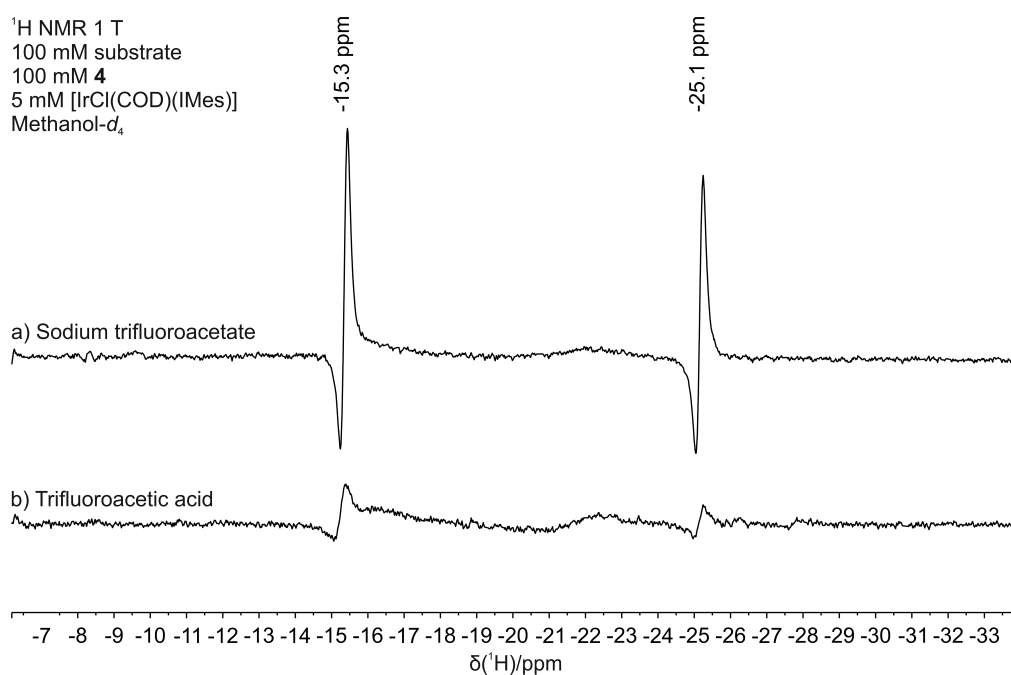


Figure 7.15: Comparison of SABRE-enhanced  $^1\text{H}$  spectra for samples containing 100 mM of either sodium trifluoroacetate (a) or trifluoroacetic acid (b), 100 mM of dimethylsulfoxide, and 5 mM of  $[\text{IrCl}(\text{COD})(\text{IMes})]$  in methanol- $d_4$ . Spectra are zoomed in to display the relevant hydride region ( $\delta$  -6 to  $\delta$  -34).

Linked to the increase in the amount of the active species is an improvement in SABRE efficiency for  $^{19}\text{F}$  NMR measurements on the singlet signal for  $[\text{TFA-H}]^-$ . Notably, whilst experiments conducted at 6.2 mT and  $\sim 0$  T yielded clear  $^{19}\text{F}$  NMR signal enhancements ( $\varepsilon_{^{19}\text{F}} = (2.908 \pm 0.056)$  and  $\varepsilon_{^{19}\text{F}} = (2.78 \pm 0.36)$ , respectively), those performed using the Earth's magnetic field ( $\sim 50 \mu\text{T}$ ) as a PTF did not result in hyperpolarisation. This was contrary to expectation as it was believed that this magnetic field would be efficient for direct polarisation transfer to the fluorine atoms, a pathway which was anticipated to be the most effective in the absence of hydrogen atoms in the alkyl chain. This observation is promising for future applications using SABRE hyperpolarisation to probe perfluorocarboxylic acids, as it suggests that the commonly-occurring fully perfluorinated alkyl chains can be enhanced by this approach.

When SABRE experiments conducted at the best performing PTF (6.2 mT) were combined with SHARPER detection, an SNR enhancement factor of  $\varepsilon_{\text{SNR}} = (7.40 \pm 0.23)$  was obtained. This improvement in SNR would enable a theoretical limit of detection of  $(992 \pm 30) \mu\text{M}$ , which whilst lower than the estimated LOD for non-SHARPER SABRE experiments ( $\text{LOD} = (3.160 \pm 0.098) \text{mM}$ ), it is still the highest LOD value amongst the investigated substrates in this thesis. It is however understood that in practice the limit of detection for this system would be determined by the ability to form the active species facilitating SABRE hyperpolarisation ( $[\text{Ir}(\text{H})_2(\text{IMes})(\text{L})(\text{MeOD}/\text{H})(\mathbf{4})]^+$ ), as demonstrated by low-concentration difluoroacetate experiments.

The enhancement factors observed for fluorine measurements on trifluoroacetate were lower than those for difluoroacetate in equal conditions (100 mM substrate and co-substrate, each), as illustrated in Figure 7.16. This 7- to 19-fold reduction in  $\varepsilon_{^{19}\text{F}}$  highlights a less efficient SABRE process for trifluoroacetate. Two potential explanations are proposed for this behaviour. Firstly, it is possible that the hydrogen atom in the alkyl chain in difluoroacetate may provide a more efficient polarisation transfer pathway, especially as the largest enhancements for  $[\text{DFA-H}]^-$  were detected at 6.2 mT. Secondly, the additional fluorine atom in the methyl group of trifluoroacetate is expected to have an electron-withdrawing inductive effect on the carboxylate group which decreases the electron density of this moi-

ety. This would presumably affect the efficiency of SABRE as it might have a detrimental effect on the exchange process or the stability of the active SABRE complex. The reduced performance of SABRE for  $[\text{TFA-H}]^-$  is likely to hinder its suitability for analytical applications, given that PFCAs typically lack hydrogen atoms in their carbon backbones.

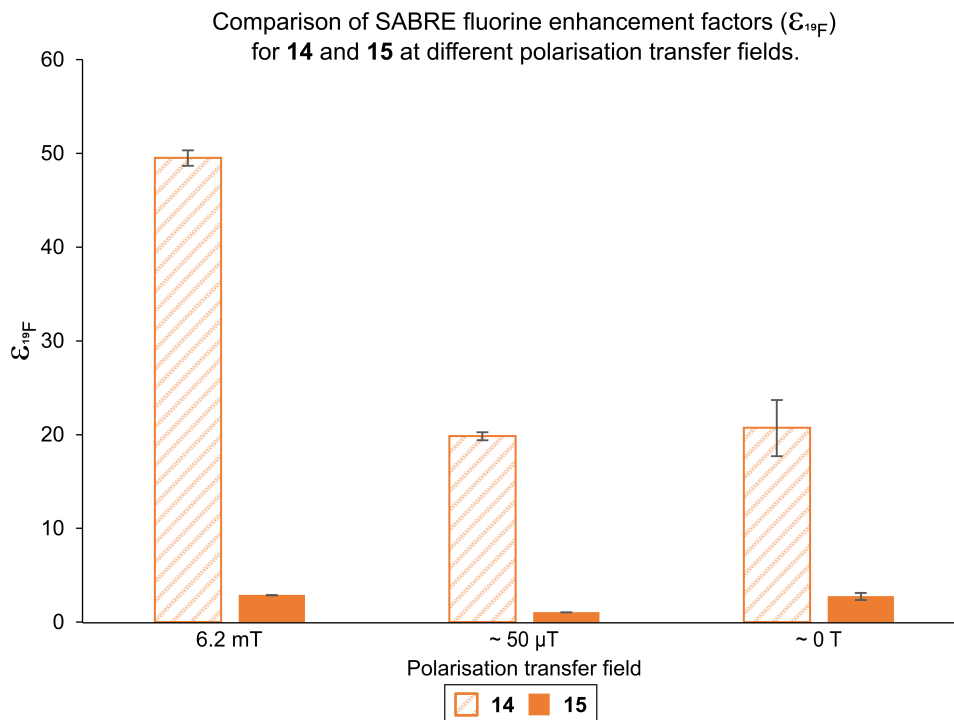


Figure 7.16: Comparison of fluorine enhancement factors ( $\epsilon_{19\text{F}}$ ) for SABRE experiments on samples containing 100 mM of either difluoroacetate ( $[\text{DFA-H}]^-$ , **14**, stripes) or trifluoroacetate ( $[\text{TFA-H}]^-$ , **15**, filled), 100 mM of DMSO, and 5 mM of  $[\text{IrCl}(\text{COD})(\text{IMes})]$  in methanol- $d_4$ . Enhancement factors were compared at three polarisation transfer fields: 6.2 mT,  $\sim 50 \mu\text{T}$ , and  $\sim 0 \text{ T}$ , and were estimated as the average of triplicate measurements, with the standard deviation shown as error bars.

## 7.5 Conclusions

This chapter presents results from direct hyperpolarisation attempts for fluorocarboxylic acids *via* SABRE. This investigation was conducted on difluoroacetic and trifluoroacetic

acids as the simplest models that could be investigated. These test molecules also enabled the comparison of SABRE efficiency for systems with and without hydrogen atoms in the alkyl chain.

Results showed that SABRE experiments of the carboxylic acids did not lead to hyperpolarisation of fluorine signals, in agreement with what was reported in similar studies covering acetic acid.<sup>302</sup> Instead, the conjugated carboxylates, *i.e.* difluoroacetate and trifluoroacetate, did show signal enhancement *via* SABRE. Whilst hyperpolarisation of non-fluorinated carboxylate species was previously reported using pyridine as a co-substrate,<sup>167,302</sup> here it is demonstrated that dimethylsulfoxide can outperform pyridine and pyridine-related co-substrates. This improved performance was attributed to the lower binding affinity of dimethylsulfoxide, which reduces binding competition.

It was observed that for both di- and trifluoroacetate, the highest enhancements were obtained at 6.2 mT, a polarisation transfer field often associated with proton- relayed transfer, even in the absence of a proton in the alkyl chain for trifluoroacetate. When comparing these fluorinated carboxylates under identical conditions, difluoroacetate exhibited greater signal enhancements than trifluoroacetate across all tested polarisation transfer fields, with differences reaching a factor of up to 19. Notably, no signal enhancements were observed for trifluoroacetate when a polarisation transfer field favouring direct fluorine hyperpolarisation was used.

The hyperpolarisation of difluoroacetate and trifluoroacetate is believed to be facilitated by a SABRE complex containing dimethylsulfoxide and methanol or methanol- $d_4$  in equatorial positions, with the fluorinated acetates potentially acting as a counter ion for the positively charged complex. As the formation of this species exhibited a dependency with the amount of carboxylate present in solution, low-concentration detection of this substrate was hindered, as well as its quantification. As a result, the lowest concentration of difluoroacetate that could be detected was 10 mM, a concentration on the upper threshold of the sub-stoichiometric regime. This concentration was above the estimated limit of detection of 1 mM for SABRE experiments or 300  $\mu$ M when in combination with SHARPER detection. It is anticipated that the addition of auxiliary carboxylates such as acetate may stabilise the

formation of the auxiliary species containing dimethylsulfoxide and methanol/methanol- $d_4$ , thus enabling lower detection limits.

## Chapter 8

# Conclusions and Future Work

This thesis investigated the potential of SABRE-enhanced  $^{19}\text{F}$  benchtop NMR measurement systems for analytical applications. By combining SABRE hyperpolarisation with the multiplet-refocusing pulse sequence SHARPER, the limits of detection of benchtop NMR measurements were significantly improved, with the use of a co-substrate enabling the analysis of samples with a concentration as low as 400 nM. This work explores the optimal analytical performance of this technique across a range of test molecules with increasing complexity, providing insight into its scope of application.

The application of the SHARPER pulse sequence played a key role in the success of SABRE-enhanced  $^{19}\text{F}$  benchtop NMR analysis. The combined power of SABRE and SHARPER was demonstrated on three fluoropyridines exhibiting homonuclear and heteronuclear scalar couplings of up to 55 Hz, thus highlighting its robustness. This pulse sequence minimised the effects of field inhomogeneity, as evidenced by the exceptionally narrow linewidths of hyperpolarised signals, reaching values below 0.2 Hz. The application of SHARPER also resulted in the refocusing of chemical shift for substrates with multiple  $^{19}\text{F}$  resonances. In this case, the use of short FID chunk times proved to be crucial to achieve optimal SNR gains. Additional sensitivity enhancement and spectral quality improvements were shown to be possible by the use of matched filters and post-acquisition processing tools. These included the removal of the imaginary component of the FID signal, as proposed by Dickson *et al.* for non-hyperpolarised samples,<sup>104</sup> and background correction to

suppress artefacts. By suppressing peak splitting and sharpening signals under optimised conditions, the use of SHARPER resulted in signal-to-noise ratio enhancements of up to a factor of 17. Interestingly, the highest enhancement achieved with SABRE-SHARPER, a 5700-fold increase, was observed for the most complex test molecule, where a combination of homo- and heteronuclear scalar couplings and chemical shift differences would otherwise hinder sensitive detection.

A comparison of SABRE-SHARPER results with those obtained by SABRE-enhanced  $^1\text{H}$ -decoupled  $^{19}\text{F}$  NMR experiments, a strategy commonly employed to remove peak splitting due to heteronuclear coupling, highlighted the benefits of the former approach. While SABRE-SHARPER delivered significant signal-to-noise ratio enhancements and completely eliminated peak splitting,  $^{19}\text{F}\{^1\text{H}\}$  NMR spectra showed no improvement in SNR and only partial peak splitting removal, alongside baseline and peak signal distortion. This comparison emphasised one of the key benefits of SHARPER: it only requires pulses on the active spin channel, and so can refocus all heteronuclear couplings as well as line broadening due to field inhomogeneity. In addition, it simplifies spectra without sacrificing sensitivity, unlike other techniques such as pure-shift and selective detection methods, which incur a sensitivity penalty,<sup>98,99</sup> even when combined with hyperpolarisation.<sup>100–102</sup>

An adaptation of the existing selective variation of SHARPER,<sup>103,104</sup> termed *sel*SHARPER HPT, was developed. The variation proposed in this thesis offered a more sensitive approach to the previously reported *sel*SHARPER pulse sequence by minimising the use of long selective pulses inside the loop, which induce signal loss due to relaxation. The effectiveness of this pulse sequence was demonstrated through the analysis of a binary sample, achieving simultaneous isolation and up to 4300-fold signal enhancements for each target signal. As only one signal could be isolated per experiment, this approach may prove to be time-consuming when several signals need to be isolated. It is envisaged that combining this approach with automated SABRE hyperpolarisation systems<sup>255</sup> may facilitate such analyses. Alternatively, the selective variation of the multi-resonance SHARPER pulse sequence<sup>312</sup> could be employed to isolate multiple signals simultaneously, improving the efficiency of this analysis. It should be noted that *sel*SHARPER variations fail to

isolate overlapped signals, compromising its suitability for complex samples. Whilst the occurrence of such issues is minimised by probing  $^{19}\text{F}$  nuclei, as opposed to  $^1\text{H}$ , the analysis of samples exhibiting severe spectral congestion may require the use of pure-shift and selective excitation techniques such as GEMSTONE,<sup>96,99</sup> even at the cost of sensitivity.

The analysis of low-concentration samples, aided by the significant improvement in signal-to-noise ratio introduced by SABRE-SHARPER, was explored in Chapter 5. Central to probing analytes at sub-stoichiometric concentrations relative to the catalyst (typically below 1 mM), was the use of a co-substrate to facilitate the formation of a stable hexacoordinated SABRE complex, acting as the ‘hyperpolarisation machinery’ for the system. This was exemplified by probing 3,5-difluoropyridine, a well-studied SABRE-amenable molecule,<sup>193</sup> using dimethylsulfoxide as a co-substrate. The introduction of this co-substrate led to substantial improvements in SABRE efficiency for 3,5-difluoropyridine, as the signal enhancement factors resulting from the formation of this mixed complex were approximately 10-fold greater compared to samples without a co-substrate. Remarkably, this improved performance also enabled the observation of hyperpolarised  $^{13}\text{C}$  NMR signals in a single scan for a 100 mM sample at natural abundance.

The formation of a mixed species, containing 3,5-difluoropyridine and dimethylsulfoxide, was demonstrated at sub-stoichiometric concentrations, a critical requirement for low-concentration analysis. Indeed, samples containing as low as 14  $\mu\text{M}$  of 3,5-difluoropyridine were detected *via* a single scan on a 1 T benchtop NMR, with an associated limit of detection of *ca.* 7  $\mu\text{M}$ . This represented an improvement of the limit of detection by 4 orders of magnitude *versus* non-hyperpolarised experiments. Importantly, this limit of detection was comparable to the those typically obtained in high-field NMR measurements,<sup>112,225,226</sup> in a single scan and using low-cost, portable instrumentation, thus demonstrating the potential of this approach. By applying SHARPER acquisition, a limit of detection of *ca.* 400 nM was demonstrated, thus surpassing the performance of standard high-field NMR experiments. Although a similar limit of detection was demonstrated on 2-(2-aminothiazol-4-yl)propan-2-ol using photo-CIDNP hyperpolarisation on a NMR spectrometer operating at a 1.88 T field,<sup>65</sup> this required signal averaging for several minutes, in contrast to the single scan

approach investigated in this thesis. It is anticipated that incorporating automated setups enabling scan averaging<sup>83,86,129,255</sup> would further improve the detecting capabilities of this SABRE-enhanced benchtop NMR approach.

A linear relationship ( $R^2=0.993$ ) between hyperpolarised signal area and analyte concentration in the micromolar range, facilitated by the use of co-substrates,<sup>81,82</sup> was demonstrated for low-field  $^{19}\text{F}$  NMR measurements for the first time. This was applied in the quantification of 3,5-difluoropyridine *via* external calibration, offering a potentially more reliable alternative to the standard addition method applied in a previous publication.<sup>82</sup> This approach enabled the accurate quantification of 3,5-difluoropyridine at low micromolar concentrations using SABRE-enhanced  $^{19}\text{F}$  NMR measurements at 1 T, exhibiting low bias ( $R = 103\%$ ) and result dispersion ( $\text{RSD} = 2\%$ ), outperforming the 5 to 20% relative error reported with the standard addition method.<sup>82</sup> A high level of comparability was observed between  $^{19}\text{F}$  and  $^1\text{H}$  NMR results under identical conditions, highlighting the potential for cross-validation of results as a quality control tool. The application of SHARPER further improved the performance of quantitative measurements, both in terms of linearity ( $R^2=0.998$ ) and accuracy ( $R = (102 \pm 1)\%$ ).

A natural progression for this line of research would be to investigate the analytical performance of SABRE-enhanced  $^{19}\text{F}$  benchtop NMR in the presence of either more than one hyperpolarisable analyte, or non-targeted sample components which may interfere with the measurement process. In such situations, the use of the standard addition method,<sup>241</sup> matrix-matched calibration,<sup>313</sup> or an internal standard may prove advantageous. Given the remarkable hyperpolarisation efficiency demonstrated for  $^{13}\text{C}$  NMR measurements in this system, the investigation of this heteronucleus as either an alternative or complementary route to analytical determinations would be a worthwhile pursuit. Further signal enhancement, as provided by  $^{13}\text{C}$  SHARPER or radiofrequency-driven polarisation transfer from  $^{19}\text{F}$  nuclei, is expected to facilitate this study.

To determine the applicability scope for SABRE-hyperpolarised  $^{19}\text{F}$  benchtop NMR analysis, the same process was repeated on the more challenging substrate 2,4,6-trifluorobenzylamine. This analyte represents a class of molecules which binds *via* an amino moi-

ety, which is known to hyperpolarise less efficiently than pyridine-based molecules.<sup>76,78</sup> By using dimethylsulfoxide as a co-substrate, <sup>19</sup>F signal enhancements again showed improvement, albeit more modest than for 3,5-difluoropyridine, with an increase by a factor of 2. Another characteristic of this analyte is its exchangeable protons, making it susceptible to SABRE-Relay<sup>78,79</sup> interactions with the solvent, methanol. Indeed, SABRE experiments probing 2,4,6-trifluorobenzylamine demonstrated SABRE-Relay activity, as evidenced by the hyperpolarisation of signals corresponding to the solvent. This led to a reduction of <sup>19</sup>F signal enhancements for this system, which resulted in a limit of detection of 370  $\mu$ M, or 43  $\mu$ M upon application of SHARPER acquisition.

This unwanted polarisation redistribution process was found to significantly reduce when deuterated methanol was used as a solvent, due to the fast deuteration of the exchangeable protons in the amino group.<sup>151</sup> This resulted in substantial improvements in sensitivity, translating to a *ca.* 50 % reduction of the associated limit of detection, both for SHARPER and non-SHARPER acquisition modes. The inhibition of this SABRE-Relay process in methanol-*d*<sub>4</sub> also proved beneficial during the quantification of low-micromolar samples, reducing bias ( $R = (97 \pm 3) \%$  *vs.*  $R = (96 \pm 14) \%$  in methanol) and measurement variability ( $RSD = 3 \%$  *vs.*  $RSD = 8 \%$  in methanol). In light of these findings, the use of deuterated methanol for the analysis of molecules with exchangeable hydrogens is generally recommended, except where financial or practical constraints necessitate an alternative. The application of SHARPER during quantification studies had a similar effect in samples prepared in methanol-*d*<sub>4</sub>, reducing RSD values from 12 % to 3 %. Moreover, SHARPER proved to be essential for methanol samples, as non-SHARPER experiments resulted in SNR values too low to enable reliable processing. Although the analytical performance demonstrated for this substrate was not as good as that observed for 3,5-difluoropyridine, the results were within the acceptable range for samples at this concentration level,<sup>243,244</sup> demonstrating the robustness of this technique even in protonated solvents. Nevertheless, it is anticipated that the analytical performance for 2,4,6-trifluorobenzylamine could be improved by introducing pH-correcting measures or by removing residual water in samples, to prevent amine protonation and minimise the occurrence of SABRE-Relay activity. In

addition, automated sample preparation and hyperpolarisation steps may further reduce result variability and, in the latter case, enable further signal enhancements through signal averaging.

Finally, the analysis of a third class of molecules was explored *via* SABRE-hyperpolarised benchtop NMR: fluorinated carboxylic acids. In particular, di- and trifluoroacetic acid were tested as they are the simplest representatives of the perfluorocarboxylic acids group, which are analytically significant due to their associated environmental concerns. Experiments revealed no hyperpolarisation for these analytes, even when co-substrates were employed, in line with previous reports.<sup>167,302</sup> A new explanation is offered for this lack of SABRE activity, which was previously attributed to catalyst deactivation. Instead, this was found to be a problem specific to the use of pyridine as a co-substrate, due to the formation of pyridinium ions under acidic conditions, which cannot bind to the iridium centre. Nevertheless, hyperpolarisation attempts using alternative co-substrates did not yield positive results, as previously stated, suggesting that carboxylic acids cannot form stable iridium complexes, or if they do form, these complexes do not lead to efficient SABRE hyperpolarisation processes.

Hyperpolarisation studies proved to be fruitful when the carboxylate species were tested instead. Experiments conducted on difluoroacetate using dimethylsulfoxide and pyridine-based co-substrates revealed better results for the former option, with a 2-fold improvement in fluorine enhancement factors. Despite the increase in SABRE performance introduced by dimethylsulfoxide, enhancement factors for this system were still lower than those observed for the fluoropyridine and fluoroamine systems. Similar to previous observations for 3,5-difluoropyridine, hyperpolarised  $^{13}\text{C}$  NMR signals were also detected for this system. Interestingly, the enhancement factors observed for trifluoroacetate were 10 to 20 times lower than those observed for difluoroacetate. This difference in performance was attributed to the lack of hydrogen atoms in the carbon backbone, which are thought to facilitate more efficient  $^1\text{H}$ -relayed polarisation transfer mechanisms.

The iridium complex species linked to the observed SABRE activity was found to be different to that involved in the hyperpolarisation of 3,5-difluoropyridine and 2,4,6-

trifluorobenzylamine, even when the same co-substrate was used in all three cases. It is believed that the presence of a charged analyte, a first in this thesis, favoured the formation of a different species acting as the hyperpolarisation machinery. Unlike 3,5-difluoropyridine and 2,4,6-trifluorobenzylamine systems, the formation of this hyperpolarisation machinery was not observed at concentrations of difluoroacetate below 10 mM, suggesting that high concentrations of the acetate species are needed for its formation. This prevented the detection of hyperpolarised  $^{19}\text{F}$  NMR signals below that concentration, and as a result, their quantification.

These results demonstrate that although SABRE hyperpolarisation of fluorinated carboxylic acids can be achieved, as first demonstrated in this thesis, its applicability in analytical applications is limited. This limitation may be overcome by using a different system to facilitate sub-stoichiometric analysis, for example, by adding acetate to the sample to stabilise the species acting as the hyperpolarisation machinery, or by exploring alternative co-substrates. Alternatively, the analysis of fluorinated carboxylic acids could be attempted *via* SABRE-Relay, whose quantification potential has been demonstrated before.<sup>84</sup> In this approach, the polarisation transfer agent would stabilise the active complex in order to probe sub-stoichiometric concentrations. For this to be successful, the polarisation transfer agent, typically ammonia or an amine, would need to be carefully selected as to avoid unwanted reactions with the carboxylic moiety, such as amidation reactions. This test system would be particularly well suited for SABRE-Relay investigations, as direct hyperpolarisation of the carboxylic acid species under investigation proved unsuccessful. Therefore, any hyperpolarisation observed for this system when adding a suitable polarisation transfer agent, *e.g.* benzylamine,<sup>154</sup> would be solely attributed to SABRE-Relay effects.

The presented results have illustrated the analytical performance of SABRE-hyperpolarised  $^{19}\text{F}$  benchtop NMR measurements, highlighting both the challenges introduced by different analyte classes as well as strategies to mitigate them. It is expected that the new knowledge presented in this thesis would be a useful reference for analysts, informing the development of real-life applications using SABRE-enhanced benchtop NMR.

# Appendices

# Appendix A

## List of Compounds

| Compound number          | Name  |
|--------------------------|---|
| 1, DFP                   | 3,5-difluoropyridine                                    |
| 2, DFMP                  | 3-(difluoromethyl)pyridine                              |
| 3, TFP                   | 3,4,5-trifluoropyridine                                 |
| 4, DMSO                  | dimethylsulfoxide                                       |
| 5                        | [IrCl(H) <sub>2</sub> (IMes)( <b>1</b> )( <b>4</b> )]   |
| 6                        | [IrCl(H) <sub>2</sub> (IMes)( <b>4</b> ) <sub>2</sub> ] |
| 7, TFBA                  | 2,4,6-trifluorobenzylamine                              |
| 8                        | [IrCl(H) <sub>2</sub> (IMes)( <b>7</b> )( <b>4</b> )]   |
| 9, DFA                   | difluoroacetic acid                                     |
| 10, TFA                  | trifluoroacetic acid                                    |
| 11, PYR                  | pyridine  |
| 12, 4MPYR                | 4-methylpyridine  |
| 13, MTZ                  | 1-methyl-1,2,3-triazole                                 |
| 14, [DFA-H] <sup>-</sup> | difluoroacetate   |
| 15, [TFA-H] <sup>-</sup> | trifluoroacetate  |

Table A.1: Number and name of the compounds mentioned throughout this thesis.

# Bibliography

- (1) B. King, *Accreditation and Quality Assurance*, 2000, **5**, 429–436.
- (2) F. Malz and H. Jancke, *Journal of Pharmaceutical and Biomedical Analysis*, 2005, **38**, 813–823.
- (3) B. Gouilleux, J. Farjon and P. Giraudeau, *Journal of Magnetic Resonance*, 2020, **319**, 106810.
- (4) A. Ciampa, L. Laghi and G. Picone, *Journal of Food Quality*, 2022, **2022**, 3612095.
- (5) B. Blümich and K. Singh, *Angewandte Chemie International Edition*, 2018, **57**, 6996–7010.
- (6) Q Magnetics, *QM-125 Features | 125 MHz Benchtop NMR*, Q Magnetics, <https://www.qmagnetics.com/qm-125-features> (visited on 12/01/2025).
- (7) P. Giraudeau and F.-X. Felpin, *Reaction Chemistry & Engineering*, 2018, **3**, 399–413.
- (8) T. Maschmeyer, L. P. E. Yunker and J. E. Hein, *Reaction Chemistry & Engineering*, 2022, **7**, 1061–1072.
- (9) L. Tadiello, M. E. Halse and T. Beweries, *Analytical Methods*, 2024, **16**, 5399–5402.
- (10) M. Leutzsch, A. J. Sederman, L. F. Gladden and M. D. Mantle, *Magnetic Resonance Imaging*, 2019, **56**, 138–143.
- (11) A. Friebel, E. von Harbou, K. Münnemann and H. Hasse, *Industrial & Engineering Chemistry Research*, 2019, **58**, 18125–18133.

- (12) T. Maschmeyer, D. J. Russell, J. G. Napolitano and J. E. Hein, *Magnetic Resonance in Chemistry*, 2024, **62**, 310–322.
- (13) M. Rubens, J. Van Herck and T. Junkers, *ACS Macro Letters*, 2019, **8**, 1437–1441.
- (14) A. I. Leonov, A. J. S. Hammer, S. Lach, S. H. M. Mehr, D. Caramelli, D. Angelone, A. Khan, S. O’Sullivan, M. Craven, L. Wilbraham and L. Cronin, *Nature Communications*, 2024, **15**, 1240.
- (15) B. C. Percival, M. Grootveld, M. Gibson, Y. Osman, M. Molinari, F. Jafari, T. Sahota, M. Martin, F. Casanova, M. L. Mather, M. Edgar, J. Masania and P. B. Wilson, *High-Throughput*, 2018, **8**, 2.
- (16) P. Alonso-Moreno, I. Rodriguez and J. L. Izquierdo-Garcia, *Metabolites*, 2023, **13**.
- (17) K. Meyer, S. Kern, N. Zientek, G. Guthausen and M. Maiwald, *TrAC Trends in Analytical Chemistry*, 2016, **83**, 39–52.
- (18) S. Kern, K. Meyer, S. Guhl, P. Gräfer, A. Paul, R. King and M. Maiwald, *Analytical and Bioanalytical Chemistry*, 2018, **410**, 3349–3360.
- (19) S. Kern, L. Wander, K. Meyer, S. Guhl, A. R. G. Mikkula, M. Holtkamp, M. Salge, C. Fleischer, N. Weber, R. King, S. Engell, A. Paul, M. P. Remelhe and M. Maiwald, *Analytical and Bioanalytical Chemistry*, 2019, **411**, 3037–3046.
- (20) A. Siddhantakar, J. Santillán-Saldivar, T. Kippes, G. Sonnemann, A. Reller and S. B. Young, *Resources, Conservation and Recycling*, 2023, **193**, 106935.
- (21) B. M. Goodson, *Journal of Magnetic Resonance*, 2002, **155**, 157–216.
- (22) A. W. Overhauser, *Physical Review*, 1953, **89**, 689–700.
- (23) J. H. Ardenkjær-Larsen, B. Fridlund, A. Gram, G. Hansson, L. Hansson, M. H. Lerche, R. Servin, M. Thaning and K. Golman, *Proceedings of the National Academy of Sciences*, 2003, **100**, 10158–10163.
- (24) J. Hore and R. Broadhurst, *Progress in Nuclear Magnetic Resonance Spectroscopy*, 1993, **25**, 345–402.
- (25) C. R. Bowers and D. P. Weitekamp, *Physical Review Letters*, 1986, **57**, 2645–2648.

- (26) R. W. Adams, J. A. Aguilar, K. D. Atkinson, M. J. Cowley, P. I. P. Elliott, S. B. Duckett, G. G. R. Green, I. G. Khazal, J. López-Serrano and D. C. Williamson, *Science*, 2009, **323**, 1708–1711.
- (27) J. Eills, D. Budker, S. Cavagnero, E. Y. Chekmenev, S. J. Elliott, S. Jannin, A. Lesage, J. Matysik, T. Meersmann, T. Prisner, J. A. Reimer, H. Yang and I. V. Koptuyug, *Chemical Reviews*, 2023, **123**, 1417–1551.
- (28) D. M. L. Lilburn, G. E. Pavlovskaya and T. Meersmann, *Journal of Magnetic Resonance*, 2013, **229**, 173–186.
- (29) L. Schröder, T. J. Lowery, C. Hilty, D. E. Wemmer and A. Pines, *Science*, 2006, **314**, 446–449.
- (30) C. Witte, V. Martos, H. M. Rose, S. Reinke, S. Klippel, L. Schröder and C. P. R. Hackenberger, *Angewandte Chemie International Edition*, 2015, **54**, 2806–2810.
- (31) E. Weiland, M.-A. Springuel-Huet, A. Nossov and A. Gédéon, *Microporous and Mesoporous Materials*, 2016, **225**, 41–65.
- (32) K. Chighine, E. Léonce, C. Boutin, H. Desvaux and P. Berthault, *Magnetic Resonance*, 2021, **2**, 409–420.
- (33) W. Kilian, S. Gulich, T. Riemer and L. Mitschang, *Journal of Magnetic Resonance Open*, 2025, **22**, 100179.
- (34) T. R. Carver and C. P. Slichter, *Physical Review*, 1953, **92**, 212–213.
- (35) A. W. Overhauser, *Physical Review*, 1953, **92**, 411–415.
- (36) M. Abraham, R. W. Kedzie and C. D. Jeffries, *Physical Review*, 1957, **106**, 165–166.
- (37) B. Corzilius, A. A. Smith and R. G. Griffin, *The Journal of Chemical Physics*, 2012, **137**, 054201.
- (38) C. F. Hwang and D. A. Hill, *Physical Review Letters*, 1967, **19**, 1011–1014.
- (39) M. Borghini, *Physical Review Letters*, 1968, **20**, 419–421.
- (40) W. T. Wenckebach, *Journal of Magnetic Resonance*, 2019, **299**, 124–134.

- (41) W. T. Wenckebach, *Journal of Magnetic Resonance*, 2019, **299**, 151–167.
- (42) K. R. Thurber and R. Tycko, *The Journal of Chemical Physics*, 2012, **137**, 084508.
- (43) D. A. Hall, D. C. Maus, G. J. Gerfen, S. J. Inati, L. R. Becerra, F. W. Dahlquist and R. G. Griffin, *Science*, 1997, **276**, 930–932.
- (44) J. R. Biller, R. Barnes and S. Han, *Current Opinion in Colloid & Interface Science*, 2018, **33**, 72–85.
- (45) B. Gizatullin, C. Mattea and S. Stapf, *Journal of Magnetic Resonance*, 2021, **322**, 106851.
- (46) F. A. Gallagher, M. I. Kettunen, D.-E. Hu, P. R. Jensen, R. i. t. Zandt, M. Karlsson, A. Gisselsson, S. K. Nelson, T. H. Witney, S. E. Bohndiek, G. Hansson, T. Peitersen, M. H. Lerche and K. M. Brindle, *Proceedings of the National Academy of Sciences*, 2009, **106**, 19801–19806.
- (47) H. Gutte, A. E. Hansen, H. H. Johannesen, A. E. Clemmensen, J. H. Ardenkjær-Larsen, C. H. Nielsen and A. Kjær, *American Journal of Nuclear Medicine and Molecular Imaging*, 2015, **5**, 548–560.
- (48) F. A. Gallagher, R. Woitek, M. A. McLean, A. B. Gill, R. Manzano Garcia, E. Provenzano, F. Riemer, J. Kaggie, A. Chhabra, S. Ursprung, J. T. Grist, C. J. Daniels, F. Zaccagna, M.-C. Laurent, M. Locke, S. Hilborne, A. Frary, T. Torheim, C. Boursnell, A. Schiller, I. Patterson, R. Slough, B. Carmo, J. Kane, H. Biggs, E. Harrison, S. S. Deen, A. Patterson, T. Lanz, Z. Kingsbury, M. Ross, B. Basu, R. Baird, D. J. Lomas, E. Sala, J. Wason, O. M. Rueda, S.-F. Chin, I. B. Wilkinson, M. J. Graves, J. E. Abraham, F. J. Gilbert, C. Caldas and K. M. Brindle, *Proceedings of the National Academy of Sciences*, 2020, **117**, 2092–2098.
- (49) S. Tang, M. V. Meng, J. B. Slater, J. W. Gordon, D. B. Vigneron, B. A. Stohr, P. E. Z. Larson and Z. J. Wang, *Cancer*, 2021, **127**, 2693–2704.

- (50) A. Bornet, M. Maucourt, C. Deborde, D. Jacob, J. Milani, B. Vuichoud, X. Ji, J.-N. Dumez, A. Moing, G. Bodenhausen, S. Jannin and P. Giraudeau, *Analytical Chemistry*, 2016, **88**, 6179–6183.
- (51) A. Dey, B. Charrier, E. Martineau, C. Deborde, E. Gandriau, A. Moing, D. Jacob, D. Eshchenko, M. Schnell, R. Melzi, D. Kurzbach, M. Ceillier, Q. Chappuis, S. F. Cousin, J. G. Kempf, S. Jannin, J.-N. Dumez and P. Giraudeau, *Analytical Chemistry*, 2020, **92**, 14867–14871.
- (52) V. Ribay, C. Praud, M. P. Letertre, J.-N. Dumez and P. Giraudeau, *Current Opinion in Chemical Biology*, 2023, **74**, 102307.
- (53) Y. Su, L. Andreas and R. G. Griffin, *Annual Review of Biochemistry*, 2015, **84**, 465–497.
- (54) Q. Z. Ni, E. Daviso, T. V. Can, E. Markhasin, S. K. Jawla, T. M. Swager, R. J. Temkin, J. Herzfeld and R. G. Griffin, *Accounts of Chemical Research*, 2013, **46**, 1933–1941.
- (55) A. G. M. Rankin, J. Trébosc, F. Pourpoint, J.-P. Amoureux and O. Lafon, *Solid State Nuclear Magnetic Resonance*, 2019, **101**, 116–143.
- (56) A. J. Rossini, A. Zagdoun, M. Lelli, A. Lesage, C. Copéret and L. Emsley, *Accounts of Chemical Research*, 2013, **46**, 1942–1951.
- (57) S. Jannin, A. Bornet, R. Melzi and G. Bodenhausen, *Chemical Physics Letters*, 2012, **549**, 99–102.
- (58) K. Kouřil, M. Gramberg, M. Jurkutat, H. Kouřilová and B. Meier, *Magnetic Resonance*, 2021, **2**, 815–825.
- (59) T. Prisner, V. Denysenkov and D. Sezer, *Journal of Magnetic Resonance*, 2016, **264**, 68–77.
- (60) T. Orlando, R. Dervişoğlu, M. Levien, I. Tkach, T. F. Prisner, L. B. Andreas, V. P. Denysenkov and M. Bennati, *Angewandte Chemie International Edition*, 2019, **58**, 1402–1406.

- (61) R. Kircher, H. Hasse and K. Münnemann, *Analytical Chemistry*, 2021, **93**, 8897–8905.
- (62) C. Bocquelet, N. Rougier, H.-N. Le, L. Veyre, C. Thieuleux, R. Melzi, A. Porea, D. Banks, J. G. Kempf, Q. Stern, E. Vaneeckhaute and S. Jannin, *Science Advances*, 2024, **10**, eadq3780.
- (63) J. Bernarding, C. Bruns, I. Prediger and M. Plaumann, *Applied Magnetic Resonance*, 2022, **53**, 1375–1398.
- (64) K. F. Sheberstov, L. Chuchkova, Y. Hu, I. V. Zhukov, A. S. Kiryutin, A. V. Esh-tukov, D. A. Cheshkov, D. A. Barskiy, J. W. Blanchard, D. Budker, K. L. Ivanov and A. V. Yurkovskaya, *The Journal of Physical Chemistry Letters*, 2021, **12**, 4686–4691.
- (65) G. R. Stadler, T. F. Segawa, M. Bütikofer, V. Decker, S. Loss, B. Czarniecki, F. Torres and R. P. Riek, *Angewandte Chemie (International Ed. in English)*, 2023, e202308692.
- (66) F. Torres, A. Sobol, J. Greenwald, A. Renn, O. Morozova, A. Yurkovskaya and R. Riek, *Physical Chemistry Chemical Physics*, 2021, **23**, 6641–6650.
- (67) F. Torres, A. Renn and R. Riek, *Magnetic Resonance*, 2021, **2**, 321–329.
- (68) F. Torres, M. Bütikofer, G. R. Stadler, A. Renn, H. Kadavath, R. Bobrovs, K. Jaudzems and R. Riek, *Journal of the American Chemical Society*, 2023, **145**, 12066–12080.
- (69) M. Bütikofer, G. R. Stadler and F. Torres, *Chemistry–Methods*, 2024, **4**, e202400009.
- (70) C. R. Bowers and D. P. Weitekamp, *Journal of the American Chemical Society*, 1987, **109**, 5541–5542.
- (71) A. Gamliel, H. Allouche-Arnon, R. Nalbandian, C. M. Barzilay, J. M. Gomori and R. Katz-Brull, *Applied Magnetic Resonance*, 2010, **39**, 329–345.
- (72) F. Ellermann, A. Pravdivtsev and J.-B. Hövener, *Magnetic Resonance*, 2021, **2**, 49–62.

- (73) B. Chapman, B. Joalland, C. Meersman, J. Ettetdgui, R. E. Swenson, M. C. Krishna, P. Nikolaou, K. V. Kovtunov, O. G. Salnikov, I. V. Koptuyug, M. E. Gemeinhardt, B. M. Goodson, R. V. Shchepin and E. Y. Chekmenev, *Analytical Chemistry*, 2021, **93**, 8476–8483.
- (74) J. R. Birchall, A. M. Coffey, B. M. Goodson and E. Y. Chekmenev, *Analytical Chemistry*, 2020, **92**, 15280–15284.
- (75) P. M. Richardson, S. Jackson, A. J. Parrott, A. Nordon, S. B. Duckett and M. E. Halse, *Magn. Reson. Chem.*, 2018, **56**, 641–650.
- (76) P. J. Rayner, P. Norcott, K. M. Appleby, W. Iali, R. O. John, S. J. Hart, A. C. Whitwood and S. B. Duckett, *Nature Communications*, 2018, **9**, 4251.
- (77) D. A. Barskiy, S. Knecht, A. V. Yurkovskaya and K. L. Ivanov, *Progress in Nuclear Magnetic Resonance Spectroscopy*, 2019, **114-115**, 33–70.
- (78) W. Iali, P. J. Rayner, A. Alshehri, A. J. Holmes, A. J. Ruddlesden and S. B. Duckett, *Chemical Science*, 2018, **9**, 3677–3684.
- (79) W. Iali, P. J. Rayner and S. B. Duckett, *Science Advances*, 2018, **4**, eaa0625.
- (80) A. I. Silva Terra, D. A. Taylor and M. E. Halse, *Progress in Nuclear Magnetic Resonance Spectroscopy*, 2024, **144-145**, 153–178.
- (81) N. Eshuis, N. Hermkens, B. J. A. van Weerdenburg, M. C. Feiters, F. P. J. T. Rutjes, S. S. Wijmenga and M. Tessari, *J. Am. Chem. Soc.*, 2014, **136**, 2695–2698.
- (82) N. Eshuis, B. J. A. vanWeerdenburg, M. C. Feiters, F. P. J. T. Rutjes, S. S. Wijmenga and M. Tessari, *Angew. Chem., Int. Ed.*, 2015, **54**, 1481–1484.
- (83) P. M. Richardson, A. J. Parrott, O. Semenova, A. Nordon, S. B. Duckett and M. E. Halse, *Analyst*, 2018, **143**, 3442–3450.
- (84) P. M. Richardson, W. Iali, S. S. Roy, P. J. Rayner, M. E. Halse and S. B. Duckett, *Chemical Science*, 2019, **10**, 10607–10619.
- (85) R. Kircher, J. Xu and D. A. Barskiy, *Journal of the American Chemical Society*, 2024, **146**, 514–520.

- (86) A. D. Robinson, P. M. Richardson and M. E. Halse, *Appl. Sci.*, 2019, **9**, 1173.
- (87) P. W. Howe, *Prog. Nucl. Magn. Reson. Spectrosc.*, 2020, **118-119**, 1–9.
- (88) J. Gracia-Vitoria, M. Rubens, E. Feghali, P. Adriaensens, K. Vanbroekhoven and R. Vendamme, *Industrial Crops and Products*, 2022, **176**, 114405.
- (89) K. Montgomery, A. Elhabashy, G. Chen, Q.-H. Chen and V. V. Krishnan, *Journal of Fluorine Chemistry*, 2023, **266**, 110084.
- (90) K. E. Arntson and W. C. K. Pomerantz, *Journal of Medicinal Chemistry*, 2016, **59**, 5158–5171.
- (91) Y. Hu, K. Cheng, L. He, X. Zhang, B. Jiang, L. Jiang, C. Li, G. Wang, Y. Yang and M. Liu, *Analytical Chemistry*, 2021, **93**, 1866–1879.
- (92) A. M. Gronenborn, *Structure*, 2022, **30**, 6–14.
- (93) K. Zangger, *Progress in Nuclear Magnetic Resonance Spectroscopy*, 2015, **86-87**, 1–20.
- (94) R. W. Adams, in *eMagRes*, John Wiley & Sons, Ltd, 2014, vol. 3, pp. 295–310.
- (95) L. Castañar, *Magnetic Resonance in Chemistry*, 2017, **55**, 47–53.
- (96) P. Kiraly, N. Kern, M. P. Plesniak, M. Nilsson, D. J. Procter, G. A. Morris and R. W. Adams, *Angewandte Chemie International Edition*, 2021, **60**, 666–669.
- (97) A. Jenne, W. Bermel, C. A. Michal, O. Gruschke, R. Soong, R. Ghosh Biswas, M. Bastawrous and A. J. Simpson, *Angewandte Chemie International Edition*, 2022, **61**, e202110044.
- (98) T. Castaing-Cordier, D. Bouillaud, P. Bowyer, O. Gonçalves, P. Giraudeau and J. Farjon, *ChemPhysChem*, 2019, **20**, 736–744.
- (99) K. Downey, W. Bermel, R. Soong, D. H. Lysak, K. Ronda, K. Steiner, P. M. Costa, W. W. Wolff, V. Decker, F. Busse, B. Goerling, A. Haber, M. J. Simpson and A. J. Simpson, *Magnetic Resonance in Chemistry*, 2024, **62**, 345–360.
- (100) D. A. Taylor, L. S. Natrajan, M. Nilsson and R. W. Adams, *Magnetic Resonance in Chemistry*, 2021, **59**, 1244–1252.

- (101) P. L. Norcott, *Physical Chemistry Chemical Physics*, 2022, **24**, 13527–13533.
- (102) K. J. Donovan and L. Frydman, *Angewandte Chemie International Edition*, 2015, **54**, 594–598.
- (103) A. B. Jones, G. C. Lloyd-Jones and D. Uhrín, *Anal. Chem.*, 2017, **89**, 10013–10021.
- (104) C. L. Dickson, G. Peat, M. Rossetto, M. E. Halse and D. Uhrín, *Chem. Commun.*, 2022, **58**, 5534–5537.
- (105) M. H. Levitt, *Spin dynamics: basics of nuclear magnetic resonance*, John Wiley & Sons, Chichester, 2nd ed., 2008, 714 pp.
- (106) P. J. Hore, *Nuclear Magnetic Resonance*, Google-Books-ID: L9umCAAAQBAJ, Oxford University Press, 2nd ed., 2015, 121 pp.
- (107) J. Keeler, *Understanding NMR spectroscopy*, Wiley, Chichester, 2nd ed., 2010, xiii+511.
- (108) T. D. W. Claridge, *High-Resolution NMR Techniques in Organic Chemistry*, Elsevier, 3rd ed., 2016.
- (109) H. Günther, *NMR Spectroscopy: Basic Principles, Concepts and Applications in Chemistry*. Wiley-VCH, 3rd ed., 2013.
- (110) B. Blümich, *Journal of Magnetic Resonance*, 2019, **306**, 27–35.
- (111) M. Grootveld, B. Percival, M. Gibson, Y. Osman, M. Edgar, M. Molinari, M. L. Mather, F. Casanova and P. B. Wilson, *Anal. Chim. Acta*, 2019, **1067**, 11–30.
- (112) T. Castaing-Cordier, D. Bouillaud, J. Farjon and P. Giraudeau, *Annual Reports on NMR Spectroscopy*, 2021, **103**, ed. G. A. Webb, 191–258.
- (113) J. Giberson, J. Scicluna, N. Legge and J. Longstaffe, in *Annual Reports on NMR Spectroscopy*, Elsevier, 2021, vol. 102, pp. 153–246.
- (114) W. Pauli, *Physical Review*, 1940, **58**, 716–722.
- (115) J. Natterer and J. Bargon, *Progress in Nuclear Magnetic Resonance Spectroscopy*, 1997, **31**, 293–315.

- (116) P. Atkins and R. S. Friedman, *Molecular Quantum Mechanics. 3rd edition*, Oxford University Press, Oxford, 3rd ed., 1997, 545 pp.
- (117) M. Matsumoto and J. H. Espenson, *Journal of the American Chemical Society*, 2005, **127**, 11447–11453.
- (118) S. Wijnans, R. Zietara, E. Pearson, M. Boele and M. A. Reynolds, *Industrial & Engineering Chemistry Research*, 2024, **63**, 20065–20078.
- (119) C. Aroulanda, L. Starovoytova and D. Canet, *The Journal of Physical Chemistry A*, 2007, **111**, 10615–10624.
- (120) L. Buljubasich, M. B. Franzoni and K. Münnemann, in *Hyperpolarization Methods in NMR Spectroscopy*, ed. L. T. Kuhn, Springer, Berlin, Heidelberg, 2013, pp. 33–74.
- (121) S. Nantogma, B. Joalland, K. Wilkens and E. Y. Chekmenev, *Analytical chemistry*, 2021, **93**, 3594–3601.
- (122) J.-B. Hoevener, S. Baer, J. Leupold, K. Jenne, D. Leibfritz, J. Hennig, S. B. Duckett and D. von Elverfeldt, *NMR in Biomedicine*, 2013, **26**, 124–131.
- (123) B. Feng, A. M. Coffey, R. D. Colon, E. Y. Chekmenev and K. W. Waddell, *Journal of Magnetic Resonance*, 2012, **214**, 258–262.
- (124) T. C. Eisenschmid, R. U. Kirss, P. P. Deutsch, S. I. Hommeltoft, R. Eisenberg, J. Bargon, R. G. Lawler and A. L. Balch, *Journal of the American Chemical Society*, 1987, **109**, 8089–8091.
- (125) M. G. Pravica and D. P. Weitekamp, *Chemical Physics Letters*, 1988, **145**, 255–258.
- (126) H. J. Bernstein, J. A. Pople and W. G. Schneider, *Canadian Journal of Chemistry*, 1957, **35**, 67–83.
- (127) F. Reineri, T. Boi and S. Aime, *Nature Communications*, 2015, **6**, 5858.
- (128) K. Them, F. Ellermann, A. N. Pravdivtsev, O. G. Salnikov, I. V. Skovpin, I. V. Koptuyug, R. Herges and J.-B. Hövener, *Journal of the American Chemical Society*, 2021, **143**, 13694–13700.

- (129) S. Alcicek, E. Van Dyke, J. Xu, S. Pustelny and D. A. Barskiy, *Chemistry–Methods*, 2023, **3**, e202200075.
- (130) S. R. Muhammad, R. B. Greer, S. B. Ramirez, B. M. Goodson and A. R. Fout, *ACS Catalysis*, 2021, **11**, Publisher: American Chemical Society, 2011–2020.
- (131) V. V. Zhivonitko, H. Beer, D. O. Zakharov, J. Bresien and A. Schulz, *ChemPhysChem*, 2021, **22**, 813–817.
- (132) T. Theis, M. L. Truong, A. M. Coffey, R. V. Shchepin, K. W. Waddell, F. Shi, B. M. Goodson, W. S. Warren and E. Y. Chekmenev, *J. Am. Chem. Soc.*, 2015, **137**, 1404–1407.
- (133) V. Daniele, F.-X. Legrand, P. Berthault, J.-N. Dumez and G. Huber, *ChemPhysChem*, 2015, **16**, 3413–3417.
- (134) N. V. Chukanov, O. G. Salnikov, R. V. Shchepin, A. Svyatova, K. V. Kovtunov, I. V. Koptuyug and E. Y. Chekmenev, *J. Phys. Chem. C*, 2018, **122**, 23002–23010.
- (135) K. M. Appleby, R. E. Mewis, A. M. Olaru, G. G. R. Green, I. J. S. Fairlamb and S. B. Duckett, *Chemical Science*, 2015, **6**, 3981–3993.
- (136) S. Glöggler, M. Emondts, J. Colell, R. Müller, B. Blümich and S. Appelt, *The Analyst*, 2011, **136**, 1566.
- (137) J.-B. Hövener, N. Schwaderlapp, T. Lickert, S. B. Duckett, R. E. Mewis, L. A. R. Highton, S. M. Kenny, G. G. R. Green, D. Leibfritz, J. G. Korvink, J. Hennig and D. von Elverfeldt, *Nature Communications*, 2013, **4**, 2946.
- (138) J. F. P. Colell, A. W. J. Logan, Z. Zhou, R. V. Shchepin, D. A. Barskiy, G. X. Ortiz, Q. Wang, S. J. Malcolmson, E. Y. Chekmenev, W. S. Warren and T. Theis, *J. Phys. Chem. C*, 2017, **121**, 6626–6634.
- (139) E. B. Dücker, L. T. Kuhn, K. Münnemann and C. Griesinger, *Journal of Magnetic Resonance*, 2012, **214**, 159–165.
- (140) M. Fekete, P. J. Rayner, G. G. R. Green and S. B. Duckett, *Magnetic Resonance in Chemistry*, 2017, **55**, 944–957.

- (141) M. Fekete, O. Bayfield, S. B. Duckett, S. Hart, R. E. Mewis, N. Pridmore, P. J. Rayner and A. Whitwood, *Inorganic Chemistry*, 2013, **52**, Publisher: American Chemical Society, 13453–13461.
- (142) R. E. Mewis, R. A. Green, M. C. R. Cockett, M. J. Cowley, S. B. Duckett, G. G. R. Green, R. O. John, P. J. Rayner and D. C. Williamson, *The Journal of Physical Chemistry B*, 2015, **119**, 1416–1424.
- (143) K. MacCulloch, A. Browning, P. TomHon, S. Lehmkuhl, E. Y. Chekmenev and T. Theis, *Analytical Chemistry*, 2023, **95**, 7822–7829.
- (144) A. W. J. Logan, T. Theis, J. F. P. Colell, W. S. Warren and S. J. Malcolmson, *Chemistry – A European Journal*, 2016, **22**, %, 10777–10781.
- (145) P. J. Rayner, M. Fekete, C. A. Gater, F. Ahwal, N. Turner, A. J. Kennerley and S. B. Duckett, *Journal of the American Chemical Society*, 2022, **144**, 8756–8769.
- (146) S. Glöggler, R. Müller, J. Colell, M. Emondts, M. Dabrowski, B. Blümich and S. Appelt, *Physical Chemistry Chemical Physics*, 2011, **13**, 13759–13764.
- (147) L. Dreisewerd, R. L. E. G. Aspers, M. C. Feiters, F. P. J. T. Rutjes and M. Tessari, *Journal of the American Chemical Society*, 2023, **145**, 1518–1523.
- (148) E. Vaneeckhaute, J.-M. Tyburn, J. G. Kempf, J. A. Martens and E. Breynaert, *Advanced Science*, 2023, **10**, 2207112.
- (149) R. V. Shchepin, D. A. Barskiy, A. M. Coffey, B. M. Goodson and E. Y. Chekmenev, *ChemistrySelect*, 2016, **1**, 2552–2555.
- (150) V. V. Zhivonitko, I. V. Skovpin and I. V. Koptuyug, *Chemical Communications*, 2015, **51**, 2506–2509.
- (151) M. Fekete, F. Ahwal and S. B. Duckett, *The Journal of Physical Chemistry B*, 2020, **124**, 4573–4580.
- (152) R. V. Shchepin, B. M. Goodson, T. Theis, W. S. Warren and E. Y. Chekmenev, *ChemPhysChem*, 2017, **18**, 1961–1965.

- (153) D. A. Barskiy, R. V. Shchepin, C. P. N. Tanner, J. F. P. Colell, B. M. Goodson, T. Theis, W. S. Warren and E. Y. Chekmenev, *ChemPhysChem*, 2017, **18**, 1493–1498.
- (154) P. J. Rayner, B. J. Tickner, W. Iali, M. Fekete, A. D. Robinson and S. B. Duckett, *Chemical Science*, 2019, **10**, 7709–7717.
- (155) M. L. Truong, F. Shi, P. He, B. Yuan, K. N. Plunkett, A. M. Coffey, R. V. Shchepin, D. A. Barskiy, K. V. Kovtunov, I. V. Koptug, K. W. Waddell, B. M. Goodson and E. Y. Chekmenev, *The Journal of Physical Chemistry B*, 2014, **118**, 13882–13889.
- (156) K. L. Ivanov, A. N. Pravdivtsev, A. V. Yurkovskaya, H.-M. Vieth and R. Kaptein, *Prog. Nucl. Magn. Reson. Spectrosc.*, 2014, **81**, 1–36.
- (157) A. N. Pravdivtsev, K. L. Ivanov, A. V. Yurkovskaya, P. A. Petrov, H.-H. Limbach, R. Kaptein and H.-M. Vieth, *Journal of Magnetic Resonance*, 2015, **261**, 73–82.
- (158) E. V. Stanbury, P. M. Richardson and S. B. Duckett, *Catalysis Science & Technology*, 2019, **9**, 3914–3922.
- (159) D. A. Barskiy, A. N. Pravdivtsev, K. L. Ivanov, K. V. Kovtunov and I. V. Koptug, *Physical Chemistry Chemical Physics*, 2015, **18**, 89–93.
- (160) S. Knecht, A. N. Pravdivtsev, J.-B. Hövener, A. V. Yurkovskaya and K. L. Ivanov, *RSC Advances*, 2016, **6**, 24470–24477.
- (161) L. S. Lloyd, A. Asghar, M. J. Burns, A. Charlton, S. Coombes, M. J. Cowley, G. J. Dear, S. B. Duckett, G. R. Genov, G. G. R. Green, L. A. R. Highton, A. J. J. Hooper, M. Khan, I. G. Khazal, R. J. Lewis, R. E. Mewis, A. D. Roberts and A. J. Ruddlesden, *Catal. Sci. Technol.*, 2014, **4**, 3544–3554.
- (162) B. J. A. van Weerdenburg, N. Eshuis, M. Tessari, F. P. J. T. Rutjes and M. C. Feiters, *Dalton Transactions*, 2015, **44**, 15387–15390.
- (163) P. J. Rayner, J. P. Gillions, V. D. Hannibal, R. O. John and S. B. Duckett, *Chemical Science*, 2021, **12**, 5910–5917.

- (164) J. F. P. Colell, A. W. J. Logan, Z. Zhou, J. R. Lindale, R. Laasner, R. V. Shchepin, E. Y. Chekmenev, V. Blum, W. S. Warren, S. J. Malcolmson and T. Theis, *Chemical Communications*, 2020, **56**, 9336–9339.
- (165) C. Min Wong, M. Fekete, R. Nelson-Forde, M. R. D. Gatus, P. J. Rayner, A. C. Whitwood, S. B. Duckett and B. A. Messerle, *Catalysis Science & Technology*, 2018, **8**, 4925–4933.
- (166) R. Mandal, P. Pham and C. Hilty, *ChemPhysChem*, 2020, **21**, 2166–2172.
- (167) L. Sellies, R. L. E. G. Aspers, M. C. Feiters, F. P. J. T. Rutjes and M. Tessari, *Angewandte Chemie International Edition*, 2021, **60**, 26954–26959.
- (168) L. Sellies, I. Reile, R. L. E. G. Aspers, M. C. Feiters, F. P. J. T. Rutjes and M. Tessari, *Chemical Communications*, 2019, **55**, 7235–7238.
- (169) I. Reile, N. Eshuis, N. K. J. Hermkens, B. J. A. v. Weerdenburg, M. C. Feiters, F. P. J. T. Rutjes and M. Tessari, *Analyst*, 2016, **141**, Publisher: The Royal Society of Chemistry, 4001–4005.
- (170) R. Mandal, P. Pham and C. Hilty, *Analytical Chemistry*, 2022, **94**, 11375–11381.
- (171) H. de Maissin, P. R. Groß, O. Mohiuddin, M. Weigt, L. Nagel, M. Herzog, Z. Wang, R. Willing, W. Reichardt, M. Pichotka, L. Heß, T. Reinheckel, H. J. Jessen, R. Zeiser, M. Bock, D. von Elverfeldt, M. Zaitsev, S. Korchak, S. Glöggler, J.-B. Hövener, E. Y. Chekmenev, F. Schilling, S. Knecht and A. B. Schmidt, *Angewandte Chemie International Edition*, 2023, **62**, e202306654.
- (172) K. MacCulloch, A. Browning, D. O. Guarin Bedoya, S. J. McBride, M. B. Abdulmojeed, C. Dedesma, B. M. Goodson, M. S. Rosen, E. Y. Chekmenev, Y.-F. Yen, P. TomHon and T. Theis, *Journal of Magnetic Resonance Open*, 2023, **16-17**, 100129.
- (173) B. J. Tickner, P. J. Rayner and S. B. Duckett, *Analytical Chemistry*, 2020, **92**, 9095–9103.
- (174) R. Fraser, F. P. J. T. Rutjes, M. C. Feiters and M. Tessari, *Accounts of Chemical Research*, 2022, **55**, 1832–1844.

- (175) M. E. Halse, *TrAC Trends in Analytical Chemistry*, 2016, **83**, 76–83.
- (176) T. Tennant, M. Hulme, T. Robertson, O. Sutcliffe and R. Mewis, *Magn. Reson. Chem.*, 2020, **58**, 1151–1159.
- (177) T. B. R. Robertson, N. Gilbert, O. B. Sutcliffe and R. E. Mewis, *Chemphyschem*, 2021, **22**, 1059–1064.
- (178) A. I. Silva Terra, M. Rossetto, C. L. Dickson, G. Peat, D. Uhrín and M. E. Halse, *ACS Measurement Science Au*, 2023, **3**, 73–81.
- (179) O. Torres, M. Martín and E. Sola, *Organometallics*, 2009, **28**, 863–870.
- (180) P. M. Richardson, R. O. John, A. J. Parrott, P. J. Rayner, W. Iali, A. Nordon, M. E. Halse and S. B. Duckett, *Phys. Chem. Chem. Phys.*, 2018, **20**, 26362–26371.
- (181) A. J. Shaka, J. Keeler, T. Frenkiel and R. Freeman, *Journal of Magnetic Resonance (1969)*, 1983, **52**, 335–338.
- (182) O. Semenova, P. M. Richardson, A. J. Parrott, A. Nordon, M. E. Halse and S. B. Duckett, *Anal. Chem.*, 2019, **91**, 6695–6701.
- (183) J. N. Miller and J. C. Miller, *Statistics and chemometrics for analytical chemistry*, Prentice Hall, Harlow, 6th ed., 2010, xvi+278.
- (184) S. L. R. Ellison and A. Williams (Eds.), *Eurachem/CITAC guide: Quantifying Uncertainty in Analytical Measurement*, 3rd ed., 2012.
- (185) G. Maniara, K. Rajamoorthi, S. Rajan and G. W. Stockton, *Analytical Chemistry*, 1998, **70**, 4921–4928.
- (186) M. E. Lacey, R. Subramanian, D. L. Olson, A. G. Webb and J. V. Sweedler, *Chemical Reviews*, 1999, **99**, 3133–3152.
- (187) T Schönberger, R Bachmann, N Gerhardt, J Panzer, K Meyer, M Romoth, J Teipel, A Scharinger, M Weber, T Kuballa, M Maiwald, S Esslinger, C Fauhl-Hassek, B Horn, J Riedl, R Becker, E Annweiler, M Meier, M Ohmenhäuser, H U Waiblinger, V Schilling, J Maier, V Gottstein, J Keller, D W Lachenmeier, M Mahler, T Rajcic De Rezende, K Sommerfeld, S Weber, B Gutsche, C Decker, J Geisser, C Kunz,

W Behrens, M Friesen, D Jansen, M Kronen, B Salzmann, H Zipper, T Resler, F Ulberth, C Loerchner, V Bäumer, P Kürbel, C Patz, A Ferner, S Weiß, M Last, J Riehle, M Burre, A Mohring, J Zahlbach, M Bunzel, U Jost, J P Schroer, M Kaufmann, L Wagner, M Schmidt, O Krenz, A Hermann, T Sonntag, S Wetzel, R Preissler, D Kern, J Ammon, K Kaltenbach, I Haase, K Speer, J Liermann, S Schwarzingler, T Hackl, M Buchweitz and M Stoyke, *Guide to NMR Method Development and Validation – Part I: Identification and Quantification (update 2023)*, No 01/2023, 2023.

- (188) B. Magnusson and Örnemark, U., *The fitness for purpose of analytical methods : A laboratory guide to method validation and related topics*, Eurachem, 2nd ed., 2014.
- (189) B. J. Tickner, M. Dennington, B. G. Collins, C. A. Gater, T. F. N. Tanner, A. C. Whitwood, P. J. Rayner, D. P. Watts and S. B. Duckett, *ACS Catalysis*, 2024, **14**, 994–1004.
- (190) H. Y. Carr and E. M. Purcell, *Physical Review*, 1954, **94**, 630–638.
- (191) G. A. Morris and A. Gibbs, *J. Magn. Reson.*, 1988, **78**, 594–596.
- (192) R. G. Spencer, *Concepts in Magnetic Resonance Part A*, 2010, **36A**, 255–265.
- (193) A. M. Olaru, T. B. R. Robertson, J. S. Lewis, A. Antony, W. Iali, R. E. Mewis and S. B. Duckett, *ChemistryOpen*, 2018, **7**, 97–105.
- (194) P. J. Rayner, M. J. Burns, E. J. Fear and S. B. Duckett, *Magnetic Resonance in Chemistry*, 2021, **59**, 1187–1198.
- (195) K. X. Moreno, K. Nasr, M. Milne, A. D. Sherry and W. J. Goux, *Journal of Magnetic Resonance (San Diego, Calif.: 1997)*, 2015, **257**, 15–23.
- (196) A. M. Olaru, M. J. Burns, G. G. R. Green and S. B. Duckett, *Chemical Science*, 2017, **8**, 2257–2266.
- (197) D. A. Barskiy, K. V. Kovtunov, I. V. Koptuyug, P. He, K. A. Groome, Q. A. Best, F. Shi, B. M. Goodson, R. V. Shchepin, A. M. Coffey, K. W. Waddell and E. Y. Chekmenev, *Journal of the American Chemical Society*, 2014, **136**, 3322–3325.

- (198) O. Semenova, Ph.D. Thesis, University of York, 2020.
- (199) J. Clayden, N. Greeves and S. Warren, *Organic Chemistry*, University Press, Oxford, 2012.
- (200) G. Peat, P. J. Boaler, C. L. Dickson, G. C. Lloyd-Jones and D. Uhrin, *Nature Communications*, 2023, **14**, 4410.
- (201) M. H. Levitt and R. Freeman, *Journal of Magnetic Resonance (1969)*, 1981, **43**, 502–507.
- (202) B. J. Tickner, J. S. Lewis, R. O. John, A. C. Whitwood and S. B. Duckett, *Dalton Transactions*, 2019, **48**, 15198–15206.
- (203) B. J. Tickner, Y. Borozdina, S. B. Duckett and G. Angelovski, *Dalton Transactions*, 2021, **50**, 2448–2461.
- (204) B. J. A. v. Weerdenburg, A. H. J. Engwerda, N. Eshuis, A. Longo, D. Banerjee, M. Tessari, C. F. Guerra, F. P. J. T. Rutjes, F. M. Bickelhaupt and M. C. Feiters, *Chemistry – A European Journal*, 2015, **21**, 10482–10489.
- (205) B. J. Tickner, S. Komulainen, S. Palosaari, J. Heikkinen, P. Lehenkari, V. V. Zhivonitko and V.-V. Telkki, *RSC Advances*, 2022, **12**, 1479–1485.
- (206) R. V. Shchepin, M. L. Truong, T. Theis, A. M. Coffey, F. Shi, K. W. Waddell, W. S. Warren, B. M. Goodson and E. Y. Chekmenev, *J. Phys. Chem. Lett.*, 2015, **6**, 1961–1967.
- (207) W. Iali, S. S. Roy, B. J. Tickner, F. Ahwal, A. J. Kennerley and S. B. Duckett, *Angewandte Chemie International Edition*, 2019, **58**, 10271–10275.
- (208) B. J. Tickner, O. Semenova, W. Iali, P. J. Rayner, A. C. Whitwood and S. B. Duckett, *Catalysis Science & Technology*, 2020, **10**, 1343–1355.
- (209) B. J. Tickner, F. Ahwal, A. C. Whitwood and S. B. Duckett, *ChemPhysChem*, 2021, **22**, 13–17.

- (210) M. J. Cowley, R. W. Adams, K. D. Atkinson, M. C. R. Cockett, S. B. Duckett, G. G. R. Green, J. A. B. Lohman, R. Kerssebaum, D. Kilgour and R. E. Mewis, *J. Am. Chem. Soc.*, 2011, **133**, 6134–6137.
- (211) B. J. Tickner and S. B. Duckett, *Chemical Science*, 2025, **16**, 1396–1404.
- (212) M. Calligaris, *Croatica Chemica Acta*, 1999, **72**, 147–169.
- (213) P. J. Rayner, M. J. Burns, A. M. Olaru, P. Norcott, M. Fekete, G. G. R. Green, L. A. R. Highton, R. E. Mewis and S. B. Duckett, *Proceedings of the National Academy of Sciences*, 2017, **114**, E3188–E3194.
- (214) F. Fernandez Diaz-Rullo, F. Zamberlan, R. E. Mewis, M. Fekete, L. Broche, L. A. Cheyne, S. Dall’Angelo, S. B. Duckett, D. Dawson and M. Zanda, *Bioorganic & Medicinal Chemistry*, 2017, **25**, 2730–2742.
- (215) R. L. Vold and R. R. Vold, *Progress in Nuclear Magnetic Resonance Spectroscopy*, 1978, **12**, 79–133.
- (216) T. Meersmann and G. Bodenhausen, *Journal of Magnetic Resonance, Series A*, 1995, **115**, 277–282.
- (217) T. F. Segawa and G. Bodenhausen, *Journal of Magnetic Resonance*, 2013, **237**, 139–146.
- (218) A. N. Pravdivtsev, A. V. Yurkovskaya, H.-M. Vieth, K. L. Ivanov and R. Kaptein, *ChemPhysChem*, 2013, **14**, 3327–3331.
- (219) A. J. R. Smith, R. York, D. Uhrín and N. G. A. Bell, *RSC Advances*, 2022, **12**, 10062–10070.
- (220) A. J. R. Smith, R. York, D. Uhrín and N. G. A. Bell, *Chemical Science*, 2022, **13**, 3766–3774.
- (221) International Union of Pure and Applied Chemistry, *IUPAC Compendium of Chemical Terminology*, 3rd ed., 2006.
- (222) R. J. C. Brown and M. J. T. Milton, *TrAC Trends in Analytical Chemistry*, 2005, **24**, 266–274.

- (223) Joint Committee for Guides in Metrology, *Evaluation of measurement data — Supplement 1 to the “Guide to the expression of uncertainty in measurement” — Propagation of distributions using a Monte Carlo method*, 2008.
- (224) D. A. Armbruster and T. Pry, *The Clinical Biochemist Reviews*, 2008, **29**, S49–S52.
- (225) M. Schleiff, C. Sommers, J. Yang, X. Shen, J. D. Rodriguez and Q. Shu, *Journal of Pharmaceutical and Biomedical Analysis*, 2023, **222**, 115073.
- (226) R. Martino, V. Gilard, F. Desmoulin and M. Malet-Martino, *Journal of Pharmaceutical and Biomedical Analysis*, 2005, **38**, 871–891.
- (227) A. Krunić and J. Orjala, *Magnetic Resonance in Chemistry*, 2015, **53**, 1043–1050.
- (228) Joint Committee for Guides in Metrology (JCGM), *International Vocabulary of Metrology – Basic and general concepts and associated terms (VIM), 3rd edition*, JCGM 200:2012(E/F), 2012.
- (229) A. Duchowny, J. Denninger, L. Lohmann, T. Theis, S. Lehmkuhl and A. Adams, *International Journal of Molecular Sciences*, 2023, **24**, 2465.
- (230) B. King, in *Traceability in Chemical Measurement*, ed. P. De Bièvre and H. Günzler, Springer Berlin Heidelberg, Berlin, Heidelberg, 2005, pp. 85–92.
- (231) P. Giraudeau, *Magnetic Resonance in Chemistry*, 2017, **55**, 61–69.
- (232) M. J. T. Milton and T. J. Quinn, *Metrologia*, 2001, **38**, 289–296.
- (233) P. Taylor, H. Kipphardt and P. De Bièvre, *Accreditation and Quality Assurance*, 2001, **6**, 103–106.
- (234) D. P. Hollis, *Analytical Chemistry*, 1963, **35**, 1682–1684.
- (235) G. F. Pauli, B. U. Jaki and D. C. Lankin, *Journal of Natural Products*, 2005, **68**, 133–149.
- (236) G. F. Pauli, T. Gödecke, B. U. Jaki and D. C. Lankin, *Journal of Natural Products*, 2012, **75**, 834–851.
- (237) S. K. Bharti and R. Roy, *TrAC Trends in Analytical Chemistry*, 2012, **35**, 5–26.

- (238) K. Danzer and L. A. Currie, *Pure and Applied Chemistry*, 1998, **70**, 993–1014.
- (239) R. J. Brown, M. R. Roberts and M. J. Milton, *Analytica Chimica Acta*, 2007, **587**, 158–163.
- (240) A.-L. Hauswaldt, O. Rienitz, R. Jährling, N. Fischer, D. Schiel, G. Labarraque and B. Magnusson, *Accreditation and Quality Assurance*, 2011, **17**, 129–138.
- (241) J. E. T. Andersen, *TrAC Trends in Analytical Chemistry*, 2017, **89**, 21–33.
- (242) J. N. Miller, *Analyst*, 1991, **116**, Publisher: The Royal Society of Chemistry, 3–14.
- (243) A. Gustavo González and M. Ángeles Herrador, *TrAC - Trends Anal. Chem.*, 2007, **26**, 227–238.
- (244) AOAC International, *Guidelines for Standard Method Performance Requirements AOAC Official Methods of Analysis. Appendix F*. AOAC International, 2016, pp. 1–18.
- (245) S. D. Roughley and A. M. Jordan, *Journal of Medicinal Chemistry*, 2011, **54**, 3451–3479.
- (246) D. Ghislieri and N. J. Turner, *Topics in Catalysis*, 2014, **57**, 284–300.
- (247) W. Zawodny and S. L. Montgomery, *Catalysts*, 2022, **12**, 595.
- (248) A. R. Patel, I. Patel and S. Banerjee, *Current Organic Chemistry*, 2024, **28**, 375–389.
- (249) T. B. McMahon and J. L. Beauchamp, *The Journal of Physical Chemistry*, 1977, **81**, 593–598.
- (250) G. S. Denisov and N. S. Golubev, *Journal of Molecular Structure*, 1981, **75**, 311–326.
- (251) A. Alshehri, B. J. Tickner, W. Iali and S. B. Duckett, *Chemical Science*, 2023, **14**, 9843–9853.
- (252) A. Jordan, P. Stoy and H. F. Sneddon, *Chemical Reviews*, 2021, **121**, 1582–1622.

- (253) EPA Press Office, *Biden-Harris Administration Finalizes Ban on Most Uses of Methylene Chloride, Protecting Workers and Communities from Fatal Exposure | US EPA*, <https://www.epa.gov/newsreleases/biden-harris-administration-finalizes-ban-most-uses-methylene-chloride-protecting>, 2024, <https://www.epa.gov/newsreleases/biden-harris-administration-finalizes-ban-most-uses-methylene-chloride-protecting> (visited on 10/01/2024).
- (254) Q. Liu and M. Zhu, *Polymer Testing*, 2016, **56**, 174–179.
- (255) F. Ellermann, P. Saul, J.-B. Hövener and A. N. Pravdivtsev, *Analytical Chemistry*, 2023, **95**, 6244–6252.
- (256) R. C. Buck, J. Franklin, U. Berger, J. M. Conder, I. T. Cousins, P. De Voogt, A. A. Jensen, K. Kannan, S. A. Mabury and S. P. Van Leeuwen, *Integrated Environmental Assessment and Management*, 2011, **7**, 513–541.
- (257) J. Glüge, M. Scheringer, I. T. Cousins, J. C. DeWitt, G. Goldenman, D. Herzke, R. Lohmann, C. A. Ng, X. Trier and Z. Wang, *Environmental Science: Processes & Impacts*, 2020, **22**, 2345–2373.
- (258) N. P. Mira, R. Marshall, M. J. F. Pinheiro, R. Dieckmann, S. A. Dahouk, N. Skroza, K. Rudnicka, P. A. Lund and D. De Biase, *International Journal of Infectious Diseases*, 2024, **140**, 119–123.
- (259) X. Li, Y. Yang, B. Zhang, X. Lin, X. Fu, Y. An, Y. Zou, J.-X. Wang, Z. Wang and T. Yu, *Signal Transduction and Targeted Therapy*, 2022, **7**, 1–22.
- (260) L. Liu, Y. Zhu, J. Li, M. Wang, P. Lee, G. Du and J. Chen, *Critical Reviews in Biotechnology*, 2012, **32**, 374–381.
- (261) H. Cai, X. Gan, Z. Jin and G. Hao, *Journal of Agricultural and Food Chemistry*, 2023, **71**, 9973–9993.
- (262) A. Chebbi and P. Carlier, *Atmospheric Environment*, 1996, **30**, 4233–4249.
- (263) M. Löflund, A. Kasper-Giebl, B. Schuster, H. Giebl, R. Hitzenberger and H. Puxbaum, *Atmospheric Environment*, 2002, **36**, 1553–1558.

- (264) P. Dewapriya, L. Chadwick, S. G. Gorji, B. Schulze, S. Valsecchi, S. Samanipour, K. V. Thomas and S. L. Kaserzon, *Journal of Hazardous Materials Letters*, 2023, **4**, 100086.
- (265) M. Djas and M. Henczka, *Separation and Purification Technology*, 2018, **201**, 106–119.
- (266) C. S. López-Garzón and A. J. J. Straathof, *Biotechnology Advances*, 2014, **32**, 873–904.
- (267) G. Dhillon, S. Brar, M. Verma and R. Tyagi, *Food and Bioprocess Technology*, 2011, **4**, 505–529.
- (268) Y. Fujii, K. H. Harada and A. Koizumi, *Chemosphere*, 2013, **93**, 538–544.
- (269) K. Prevedouros, I. T. Cousins, R. C. Buck and S. H. Korzeniewski, *Environmental Science & Technology*, 2006, **40**, Publisher: American Chemical Society, 32–44.
- (270) C. Wang, W. Li, Y. Lv, H. Bai, P. Zhao, L. Wen, C. Wang and Q. Ma, *Microchemical Journal*, 2020, **155**, 104773.
- (271) J. J. Lim, Y. Suh, E. M. Faustman and J. Y. Cui, *Drug Metabolism and Disposition*, 2022, **50**, 1396–1413.
- (272) J. R. Lang, B. M. Allred, J. A. Field, J. W. Levis and M. A. Barlaz, *Environmental Science & Technology*, 2017, **51**, 2197–2205.
- (273) I. Ericson Jogsten, M. Nadal, B. van Bavel, G. Lindström and J. L. Domingo, *Environment International*, 2012, **39**, 172–180.
- (274) C. Bach, X. Dauchy, V. Boiteux, A. Colin, J. Hemard, V. Sagres, C. Rosin and J.-F. Munoz, *Environmental Science and Pollution Research*, 2017, **24**, 4916–4925.
- (275) J. L. Domingo, *Environment International*, 2012, **40**, 187–195.
- (276) J. L. Domingo and M. Nadal, *Journal of Agricultural and Food Chemistry*, 2017, **65**, 533–543.
- (277) J. L. Domingo and M. Nadal, *Environmental Research*, 2019, **177**, 108648.

- (278) R. Akhbarizadeh, S. Dobaradaran, T. C. Schmidt, I. Nabipour and J. Spitz, *Journal of Hazardous Materials*, 2020, **392**, 122271.
- (279) United States Environmental Protection Agency, *Emerging Contaminants Perfluorooctane Sulfonate (PFOS) and Perfluorooctanoic Acid (PFOA)*, EPA 505-F-14-001, Elsevier, 2014, pp. 1–10.
- (280) M. K. So, N. Yamashita, S. Taniyasu, Q. Jiang, J. P. Giesy, K. Chen and P. K. S. Lam, *Environmental Science & Technology*, 2006, **40**, 2924–2929.
- (281) Z. Dong, M. M. Bahar, J. Jit, B. Kennedy, B. Priestly, J. Ng, D. Lamb, Y. Liu, L. Duan and R. Naidu, *Environment International*, 2017, **105**, 86–94.
- (282) G. M. Sinclair, S. M. Long and O. A. H. Jones, *Chemosphere*, 2020, **258**, 127340.
- (283) K. Sznajder-Katarzyńska, M. Surma and I. Cieślik, *Journal of Chemistry*, 2019, **2019**, 2717528.
- (284) S. Zahm, J. P. Bonde, W. A. Chiu, J. Hoppin, J. Kanno, M. Abdallah, C. R. Blystone, M. M. Calkins, G.-H. Dong, D. C. Dorman, R. Fry, H. Guo, L. S. Haug, J. N. Hofmann, M. Iwasaki, M. Machala, F. R. Mancini, S. S. Maria-Engler, P. Møller, J. C. Ng, M. Pallardy, G. B. Post, S. Salihovic, J. Schlezinger, A. Soshilov, K. Steenland, I.-L. Steffensen, V. Tryndyak, A. White, S. Woskie, T. Fletcher, A. Ahmadi, N. Ahmadi, L. Benbrahim-Tallaa, W. Bijoux, S. Chittiboyina, A. de Conti, C. Facchin, F. Madia, H. Mattock, M. Merdas, E. Pasqual, E. Suonio, S. Viegas, L. Zupunski, R. Wedekind and M. K. Schubauer-Berigan, *The Lancet Oncology*, 2024, **25**, 16–17.
- (285) Royal Society of Chemistry, *Evidence report. PFAS in UK waters – presence, detection, and remediation*, 2023.
- (286) DWI, *Guidance on the Water Supply (Water Quality) Regulations 2016 (as amended) for England and Water Supply (Water Quality) Regulations 2018 for Wales specific to PFAS (per- and polyfluoroalkyl substances) in drinking water*, Drinking Water Inspectorate, 2024.

- (287) European Parliament, *Directive (EU) 2020/2184 of the European Parliament and the Council of 16 December 2020 on the quality of water intended for human consumption (recast)*. 2020.
- (288) United States Environmental Protection Agency, *Proposed PFAS National Primary Drinking Water Regulation*. 2023.
- (289) A. O. De Silva, J. M. Armitage, T. A. Bruton, C. Dassuncao, W. Heiger-Bernays, X. C. Hu, A. Kärrman, B. Kelly, C. Ng, A. Robuck, M. Sun, T. F. Webster and E. M. Sunderland, *Environmental Toxicology and Chemistry*, 2021, **40**, 631–657.
- (290) J.A. Shoemaker and D.R. Tettenhorst, *Method 537.1: Determination of Selected Per- and Polyfluorinated Alkyl Substances in Drinking Water by Solid Phase Extraction and Liquid Chromatography/Tandem Mass Spectrometry (LC/MS/MS)*, version 2.0, Washington, DC, 2020.
- (291) L. Rosenblum and S. C. Wendelken, *Method 533: Determination of Per- and Polyfluoroalkyl Substances in Drinking Water by Isotope Dilution Anion Exchange Solid Phase Extraction and Liquid Chromatography/Tandem Mass Spectrometry*, Washington, DC, 2019.
- (292) ISO, *Water quality – determination of perfluoroalkyl and polyfluoroalkyl substances (PFAS) in water – method using solid phase extraction and liquid chromatography-tandem mass spectrometry (LC-MS/MS)*. Geneva, Switzerland, 2019.
- (293) T. Ruan and G. Jiang, *TrAC Trends in Analytical Chemistry*, 2017, **95**, 122–131.
- (294) S. Joudan, R. Liu, J. C. D’eon and S. A. Mabury, *TrAC Trends in Analytical Chemistry*, 2020, **124**, 115431.
- (295) C. A. Moody, W. C. Kwan, J. W. Martin, D. C. G. Muir and S. A. Mabury, *Analytical Chemistry*, 2001, **73**, 2200–2206.
- (296) D. Camdzic, R. A. Dickman and D. S. Aga, *Journal of Hazardous Materials Letters*, 2021, **2**, 100023.
- (297) J. R. Gauthier and S. A. Mabury, *Analytical Chemistry*, 2022, **94**, 3278–3286.

- (298) D. Camdzic, R. A. Dickman, A. S. Joyce, J. S. Wallace, P. L. Ferguson and D. S. Aga, *Analytical Chemistry*, 2023, **95**, 5484–5488.
- (299) P. Chen, S. Zhuang, W. Chen, Z. Chen, R. Li, F. Chen, T. Jiang and X. Fu, *Magnetic Resonance Letters*, 2024, **4**, 100097.
- (300) K. Heerah, S. Waclawek, J. Konzuk and J. G. Longstaffe, *Magn. Reson. Chem.*, 2020, **58**, 1160–1167.
- (301) M. Plaumann, U. Bommerich, T. Trantzschel, D. Lego, S. Dillenberger, G. Sauer, J. Bargon, G. Buntkowsky and J. Bernarding, *Chemistry – A European Journal*, 2013, **19**, 6334–6339.
- (302) M. E. Gemeinhardt, M. N. Limbach, T. R. Gebhardt, C. W. Eriksson, S. L. Eriksson, J. R. Lindale, E. A. Goodson, W. S. Warren, E. Y. Chekmenev and B. M. Goodson, *Angewandte Chemie International Edition*, 2020, **59**, 418–423.
- (303) L. Liu, F. Li, Z. Dong, G. Dong, J. Xu, W. Liu, X. Wang, X. Hai and K. Yu, *Human & Experimental Toxicology*, 2020, **39**, 634–641.
- (304) M. Ateia, A. Maroli, N. Tharayil and T. Karanfil, *Chemosphere*, 2019, **220**, 866–882.
- (305) H. P. H. Arp, A. Gredelj, J. Glüge, M. Scheringer and I. T. Cousins, *Environmental Science & Technology*, 2024, **58**, Publisher: American Chemical Society, 19925–19935.
- (306) D. A. Ellis, J. W. Martin, D. C. Muir and S. A. Mabury, *Analytical Chemistry*, 2000, **72**, 726–731.
- (307) N. Reimets, K. Ausmees, S. Vija and I. Reile, *Analytical Chemistry*, 2021, **93**, 9480–9485.
- (308) K. Ausmees, N. Reimets and I. Reile, *Molecules*, 2022, **27**, 802.
- (309) J. A. Gowland and R. A. McClelland, *Canadian Journal of Chemistry*, 1979, **57**, 2140–2144.

- (310) B. J. Tickner, R. O. John, S. S. Roy, S. J. Hart, A. C. Whitwood and S. B. Duckett, *Chemical Science*, 2019, **10**, 5235–5245.
- (311) R. S. Forgan, *Chemical Science*, 2020, **11**, 4546–4562.
- (312) M. Davy, C. L. Dickson, R. Wei, D. Uhrin and C. P. Butts, *Analyst*, 2022, **147**, 1702–1708.
- (313) C. Rimayi, D. Odusanya, F. Mtunzi and S. Tsoka, *Chemosphere*, 2015, **118**, 35–43.